

https://dspace.org/

Investigation into energy manipulation in reactive components using transmission line modelling

Mofu, Mubanga

2019

https://hdl.handle.net/10539/29572

Mofu, Mubanga Charles (2019) Investigation into energy manipulation in reactive components using transmission line modelling, University of the Witwatersrand, Johannesburg, <http://hdl.handle.net/10539/29572>

Downloaded from a DSpace repository. https://dspace.org/

Investigation into Energy Manipulation in Reactive Components Using Transmission Line Modelling



UNIVERSITY OF THE
WITWATERSRAND,
JOHANNESBURG

Mubanga Mofu

Faculty of Engineering & Built Environment

University of the Witwatersrand

A thesis submitted for the degree of

Master of Science Engineering

March 2019

Declaration of Authorship

I, Mubanga Mofu declare that this dissertation is my own unaided work. It is being submitted for the Degree of Master of Science in Engineering in the University of the Witwatersrand, Johannesburg. It has not been submitted before for any degree or examination in any other University.

Signed: 

Date: 26 March 2019

Dedicated to Chilambwe "Chi-Chi" Mofu

Acknowledgments

Firstly, I would like to thank Prof Ivan Hofsajer for the many vital consultation and contact hours he afforded me during the tenure of this research. His knowledge and insight were invaluable during the research endeavor.

Secondly, I would like to thank my parents and siblings Mukuka Mofu, Musonda Mofu and Chilambwe Mofu for providing me with great support and council during the arduous writing process.

Thirdly, I would like to thank Tinashe Chingozha, Musonda Mofu, Molefi Alfred Makuebu, Sean Muzoka,Yuval Genga and Charlotte Mosimane for their various contributions towards the research effort.

Finally, I would like to thank Jeannine Davids and Mumtaz Adams for everything they do for the undergraduate and postgraduate students in the school of Electrical and Information engineering. They are truly inspirational and tremendous assets to the school.

The financial assistance of the National Research Foundation (NRF) towards this research is hereby acknowledged. Opinions expressed and conclusions arrived at, are those of the author and are not necessarily to be attributed to the NRF.

Abstract

The principle objectives of this research are to seek alternative avenues to enhance qualitative and quantitative understanding at a fundamental level of the internal electromagnetic environment in reactive components during energy flow, conversion and transfer processes. That can be seen, for example in power electronic converters. The study of these fundamental energy processes is necessary, as it has been documented in literature that the adoption of wide-bandgap (WBG) semiconductors and the increased switching frequencies they enable, are facilitating the miniaturisation of components which leads to increased power densities. Consequently, this means that multiple components or converter functions can be packaged in discrete or integrated power modules. The spatial arrangement of the components in these densely populated power modules means that greater emphasis needs to be placed on the internal electromagnetic structure and environment of the various components. The ramifications of these environmental conditions are seen as fundamental switching limits or bottlenecks to the maximum realisable switching frequency. The implications of these limits are seen as increases in switching frequency passed a certain threshold provide diminishing returns in terms of power density as well as negatively affecting converter efficiency. From these observations and the ones made in contemporary literature, it has been established that a more wholistic approach to improving power electronic converters that is not solely dependent on the switching function is necessary for improvements in contemporary as well as future converters. Consensus from various sources in literature suggest that a fundamental breakthrough is required in the power passives i.e. reactive components of the converter before appreciable performance gains are established. In this work the fundamental energy manipulation interactions between electric and magnetic energies in these power passives i.e. reactive components will be analysed as a potential means of providing this paradigm shift. Increased insight and understanding of the energy manipulations processes in reactive components may provide the foundational framework for improved power passives to be developed in future

These energy manipulation processes are examined by considering the common LC Resonant tank and *Twin Capacitor* topologies. These topologies are selected because they are fundamental examples of electric to magnetic and electric to electric energy manipulation processes respectively. It is shown in this work that analysing the *Twin Capacitor Paradox* with conventional circuit theory leads to the violation of conservation of energy, highlighting the limitations in circuit theory in modelling energy manipulations. In this research, the reactive components are modelled using lossless 1-D TLM Link-Line equivalent transmission line models. The implications of this mean that the interconnection of two components effectively forms a cascaded transmission line with three principle nodes. The *Energy Conversion Efficacy* (ECE) quantification metric is coined to establish the quality of an energy manipulation process. ECE is principally concerned with establishing the maximum amount of energy that can be transferred from a primary energy store to a secondary energy store and the maximum amount of energy that can be reconstituted back into the primary energy store in the original form. Additionally, the term *Fragmentation* is coined to better explain some of the *diffusion* and *scattering* effects that may take place at the interface or junction of the transmission lines segments with arbitrary lengths. Consequently, the implications this imposes on ECE are subsequently analysed.

The nature of this research is purely theoretical and as a direct consequence; the contributions arising as a result are purely theoretical. A major contribution arising from this work is the derivation of an alternative solution to the *Twin Capacitor Paradox* in which the perceived loss or deficit in energy is found to be present in the self-inductors of the respective capacitors. It is also shown in this work that a condition for maximum ECE can only be achieved provided both transmission line segments have identical impedances and propagation delays. If the ratio of propagation delays in the cascaded transmission line structure is increased an accompanying increase in generated noise will also be seen.

CONTENTS

Acknowledgments 4
Abstract 5
CONTENTS vi
List of Figures ix
List of Tables xiii
List of Abbreviations xiv
1 Introduction 1
1.1 Background 1
1.2 Research Motivation 3
1.2.1 Electric to Electric Energy Manipulation 5
1.2.2 Electric to Magnetic Energy Manipulation 6
1.3 Research Objectives, Question and Methodology 8
1.3.1 Research Objectives 8
1.3.2 Research Question 8
1.4 Research Scope 8
1.5 Contributions 9
1.6 Dissertation Overview 9
1.7 Conclusion 10
2 Literature Review 11
2.1 Overview 11
2.2 Current and Future Trends In Power Electronics 11
2.3 Limitations of Circuit Theory 12
2.4 Transmission Line Modelling of Reactive Components 14
2.4.1 Discrete structures 14
2.4.2 Integrated structures 17
2.5 Electromagnetic Energy Flow 21
2.5.1 Energy Flux Density Vector 21
2.5.2 Charge Potentials 23
2.5.3 Discussion 24
2.6 Conclusion 25
3 System Modelling 26
3.1 Overview 26
3.2 Electromagnetic Modelling Hierarchy 26
3.3 Transmission Line Theory Fundamentals 27

3.3.1 Preliminaries 27
3.3.2 Transmission Line Equations 28
3.4 TLM Simulation of Reactive Components 30
3.4.1 History of TLM Modelling 30
3.4.2 TLM Modelling Technique 30
3.4.3 Stub Model 31
3.4.4 Link-Line Model 35
3.4.5 Decoupling Systems Using TLM Link-Lines 39
3.5 Limitations of Current Modelling 43
3.5.1 Twin Capacitor Paradox 43
3.5.2 LC Resonator Tank 54
3.6 Conclusion 62
4 Fragmentation 63
4.1 Overview 63
4.2 Formal Definitions 63
4.2.1 Fragmentation 63
4.2.2 Propagating Waveform Characteristics 64
4.2.3 Fragmentation Ratio 64
4.3 Fragment Generation 65
4.3.1 Fragmentation Generation Case Hierarchy 66
4.3.2 Fragmentation Generation Algorithm 67
4.3.3 Finite Fragment Generation Non-Integer Multiple Delays 74
4.3.4 Infinite Irrational Fragment Generation 77
4.3.5 Finite Fragment Generation Integer Multiple Delays 79
4.3.6 Finite Fragment Generation Matched Delays 83
4.4 Conclusion 85
5 Fragmentation Simulator Realisation 86
5.1 Overview 86
5.2 Pre-Processing 87
5.2.1 Parameter Initialisation 87
5.2.2 Determine Fragmentation Ratio 88
5.2.3 Create Origin Waves 90
5.3 Processing 91
5.3.1 Cycle Initialisation 93
5.3.2 Create New Waves 94
5.3.3 Recombination and Transmission 96

5.4 Post Processing....97
5.4.1 Time Discretisation....97
5.4.2 Spatial Discretisation....99
5.5 Conclusion....102
6 Energy Manipulation....103
6.1 Overview....103
6.2 Similar Transmission Lines....103
6.2.1 Energy Implications....109
6.2.2 Noise Implications....114
6.3 Dissimilar Transmission Lines....121
6.3.1 Energy Implications....122
6.3.2 Noise Implications....130
6.4 Conclusion....137
7 Conclusions and Recommendations....138
7.1 Recommendations....139
References....141

LIST OF FIGURES

Figure 1-1: Internal functions of a Power Electronic Converter (adapted from [5]) 2
Figure 1-2: Switched-Capacitor Converter 5
Figure 1-3: Ideal Buck-Boost Converter (Adapted from [12]) 6
Figure 2-1: Twin Capacitor a) Initial State b) Equilibrium State 13
Figure 2-2: Models of MLC Capacitor a) Physical Structure b) Distributed Parameter Model (Adapted from [21]) 15
Figure 2-3: Transmission Line Capacitor Model 16
Figure 2-4: General $\lambda/4$ Transmission Line terminated by load ZL (Adapted from [20]) 18
Figure 2-5: Parallel Planar LC Resonant Structure (Adapted from [20]) 19
Figure 2-6: Transmission Line Model of Parallel LC Resonant Structure (Adapted from [20]) 20
Figure 3-1: Electromagnetic Modelling Hierarchy 27
Figure 3-2: Per-Unit Length Distributed Parameter Segment 28
Figure 3-3: Capacitor Models a) Lumped Element b) TLM Stub c) Thevenin Equivalent Circuit 31
Figure 3-4: Inductor Models a) Lumped Element b) TLM Stub c) Thevenin Equivalent Circuit 33
Figure 3-5: Series Inductor Models a) Lumped Element b) Self-Capacitance c) Link-Line d) Thevenin Equivalent 36
Figure 3-6: Shunt Capacitor Models a) Lumped Element b) Self-Inductance c) Link-Line d) Thevenin Equivalent 38
Figure 3-7: Decoupled Systems via a) Link-Line model b) Thevenin Equivalent model (Adapted from [39]) 39
Figure 3-8: SMPS Converter System a) Coupled System b) Decoupled System 40
Figure 3-9: Switched Capacitor Converter System a) Coupled System b) Decoupled System 42
Figure 3-10: Twin Capacitor Paradox a) Initial Charged State b) Equilibrium State 44
Figure 3-11: Twin Capacitor Link-Line Equivalent Model (Switch Open) 45
Figure 3-12: Twin Capacitor Link-Line Model (Switch Closed) 45
Figure 3-13: Energy Interactions on CA Wave Propagation Towards a) $zA0$ b) zAf 47
Figure 3-14: Energy Interactions on CB Wave Propagation Towards a) $zA0$ b) zAf 48
Figure 3-15: Line A (CA) Voltage and Current Progressions a) Voltage b) Current 51
Figure 3-16: Line B (CB) Voltage and Current Progressions a) Voltage b) Current 51
Figure 3-17:Line A (CA) Energy Progressions a) UEA b) $ULeA$ 53
Figure 3-18: Line B (CB) Energy Progressions a) UEB b) $ULeB$ 54
Figure 3-19: Resonator Tank Link-Line Equivalent Model (Switch Open) 55

Figure 3-20: Resonator Tank Link-Line Equivalent Model (Switch Closed) 56
Figure 3-21: Electromagnetic Energy Interactions on Cr, Wave Propagation Towards (a) $zA0$ (b) zAf. 56
Figure 3-22: Line A (Cr) Voltage and Current Progressions (a) Voltage ($VA \to 0$) (b) Current ($IA \to -I0$) 57
Figure 3-23: Normalized Energy Progressions Line A (a) UEA (b) $ULeA$ 59
Figure 3-24 Electromagnetic Energy Interactions on Lr, Wave Propagation Towards (a) zBf (b) $zB0$ 59
Figure 3-25: Line B Voltage and Current Progressions (a) Voltage ($VB \to 0$) (b) Current ($IB \to I0$) 60
Figure 3-26: Normalized Energy Progressions Line B (a) UHB (b) $UCeB$ 61
Figure 4-1: Fragmentation Bounce Diagram 63
Figure 4-2: Propagating Waveform Characteristics 64
Figure 4-3: Fragmentation Generation Case Hierarchy 66
Figure 4-4:High Level Algorithm for Establishing Fragmentation Generation Cases 67
Figure 4-5:Algorithm Determining Fragment Creation At The Junction Or Discontinuity 68
Figure 4-6:Algorithm Detailing Recombination Effects At The Junction Or Discontinuity 71
Figure 4-7: Finite Fragment Generation $FRA{:}\,FRB$ (FFGNIMD) 76
Figure 4-8: Finite Fragment Generation $1{:}\,k$ (FFGIMD) 82
Figure 4-9: Finite Fragment Generation $1{:}\,1$ (FFGMD) 84
Figure 5-1: Fragmentation Generation Algorithm 86
Figure 5-2: Determine Fragmentation Ratio ($FRA{:}\,FRB$) 88
Figure 5-3: State Of Fragment Generation Process 89
Figure 5-4: Processing Activities Overview 92
Figure 6-1: FFGMD Line A Distributions ($CA = CB$) a) Voltage b) Current 106
Figure 6-2: FFGMD Line B Distributions ($CA = CB$) a) Voltage b) Current 106
Figure 6-3: Max Electrical and Min Magnetic Line Energies Vs. Capacitance 110
Figure 6-4: Min Electrical and Max Magnetic Line Energies Vs. Capacitance 110
Figure 6-5: Energy Conversion Efficacy Vs. Capacitance 111
Figure 6-6: Maximum Electrical Energies vs. Changing Capacitance (FFGIMD) a) $UEAMax$ b) $UEBMax$ 112
Figure 6-7: Energy Conversion Efficacy vs. Changing Capacitance (FFGIMD) 113
Figure 6-8: Line A Voltage at $zA0$ terminals ($FRA = 1, FRB = 1$) 114
Figure 6-9: Line B Voltage at zBf terminals ($FRA = 1, FRB = 1$) 114
Figure 6-10: Current at zJ Junction terminal ($FRA = 1, FRB = 1$) 115
Figure 6-11: Voltage at zJ Junction Terminal ($FRA = 1, FRB = 1$) 115
Figure 6-12: Terminal Voltages a) $v(zA0, t)$ b) $v(zBf, t)$ ($FRA = 1, FRB = 10$) 117
Figure 6-13: Junction Voltage and Current a) $v(zJ, t)$ b) $i(zJ, t)$ ($FRA = 1, FRB = 10$) 118
Figure 6-14: Terminal Voltages a) $v(zA0, t)$ b) $v(zBf, t)$ ($FRA = 1, FRB = 100$) 118
Figure 6-15: Junction Voltage and Current a) $v(zJ, t)$ b) $i(zJ, t)$ ($FRA = 1, FRB = 100$) 119

Figure 6-16: Terminal Voltage Variance a) $Var(v(zA0,t))$b) $Var(v(zBf,t))$ ($FRA = 1, FRB = 1,2,10,50,100$).....119
Figure 6-17: Junction Current Variance $Var(i(zJ,t))$ ($FRA = 1, FRB = 1,2,10,50,100$) 120
Figure 6-18: Junction Voltage Variance $Var(v(zJ,t))$ ($FRA = 1, FRB = 1,2,10,50,100$) 120
Figure 6-19: LC Resonator Terminal and Junction Voltages a) $vA(zA0,t)$ b) $vA(zJ,t)$ 124
Figure 6-20: LC Resonator Junction and Terminal Currents a) $iB(zJ,t)$ b) $iB(zBf,t)$ 124
Figure 6-21: LC Resonator Line A Voltage and Current @ $T0$ ($vA(z,T0), iA(z,T0)$).....124
Figure 6-22: LC Resonator Line A Electric and Magnetic Energies @ $T0$ ($UEA(z,T0), UHA(z,T0)$) 125
Figure 6-23: LC Resonator Line B Voltage and Current @ $T0$ ($vB(z,T0), iB(z,T0)$).....125
Figure 6-24: LC Resonator Line B Electric and Magnetic Energies @ $T0$ ($UEB(z,T0), UHB(z,T0)$) 125
Figure 6-25: LC Resonator Max Electrical and Min Magnetic Line Energies Vs. Self-Capacitance.....126
Figure 6-26: LC Resonator Min Electrical and Max Magnetic Line Energies Vs. Self-Capacitance.....127
Figure 6-27: LC Resonator Energy Conversion Efficacy Vs. Self-Capacitance..127
Figure 6-28: LC Resonator Max Electrical Energies vs. Self-Capacitance (FFGIMD) a) $UEAMax$ b) $UEBMax$ 128
Figure 6-29: LC Resonator Max Magnetic Line Energies vs. Self-Capacitance (FFGIMD) a) $UHAMAX$ b)$UHBMax$.....129
Figure 6-30: Energy Conversion Efficacy vs. Self-Capacitance (FFGIMD) 129
Figure 6-31: Generated Voltage Waveforms a) $vA(zA0,t)$ b)$v(zJ,t)$ ($FRA = 1, FRB = 1$).....131
Figure 6-32: Generated Current Waveforms a) $iB(zBf,t)$ b) $i(zJ,t)$ ($FRA = 1, FRB = 1$).....131
Figure 6-33: Voltage Differences at $zA0$ and zJ a)$\Delta v(zA0,t)$ b)$\Delta v(zBf,t)$ ($FRA = 1, FRB = 1$).....132
Figure 6-34: Current Differences at zBf and zJ a)$\Delta v(zBf,t)$ b) $\Delta v(zJ,t)$ ($FRA = 1, FRB = 1$).....132
Figure 6-35: Generated Voltage waveforms a)$vA(zA0,t)$ b)$v(zJ,t)$ ($FRA = 1, FRB = 10$) 133
Figure 6-36: Generated Current Waveforms a) $i(zJ,t)$ b) $iB(zBf,t)$ ($FRA = 1, FRB = 10$) 133
Figure 6-37: Voltage Differences at $zA0$ and zJ a)$\Delta v(zA0,t)$ b)$\Delta v(zBf,t)$ ($FRA = 1, FRB = 10$) 134
Figure 6-38: Current Differences at zBf and zJ a)$\Delta v(zBf,t)$ b) $\Delta v(zJ,t)$ ($FRA = 1, FRB = 10$) 134
Figure 6-39: Generated Voltage waveforms a)$vA(zA0,t)$ b)$v(zJ,t)$ ($FRA = 1, FRB = 100$) 135

Figure 6-40: Generated Current Waveforms a) $iB(zBf,t)$ b) $i(zJ,t)$ ($FRA = 1, FRB = 100$) 135
Figure 6-41: Voltage Differences at $zA0$ and zJ a)$\Delta v(zA0,t)$ b)$\Delta v(zBf,t)$ ($FRA = 1, FRB = 100$) 136
Figure 6-42: Current Differences at zBf and zJ a)$\Delta v(zBf,t)$ b) $\Delta v(zJ,t)$ ($FRA = 1, FRB = 100$) 136

LIST OF TABLES

Table 1: 3Φ Vienna Rectifier Generational Parameters 1
Table 3.1: Time intervals for energy interaction states in CA and CB 48
Table 6.1: Twin Capacitor FFGMD Simulation Parameters 105
Table 6.2: Instantaneous Line Energies ($CA = CB$) 109
Table 6.3: Twin Capacitor Variance Simulation Parameters 117
Table 6.4: LC Resonator FFGMD Simulation Parameters 122
Table 6.5: LC Resonator FFGIMD Simulation Parameters 130

LIST OF ABBREVIATIONS

AIST-PERC	Japan National Institute of Science and Technology
CPES	Center for Power Electronic Systems
ECE	Energy Conversion Efficacy
ECPE	European Center of Power Electronics
eGaN	Enhancement Mode Galium Nitride
EMC	Electromagnetic Compatibility
EMI	Electromagnetic Interference
FDTD	Finitie Difference Time Difference
FFGIMD	Finite Fragmentation Generation Integer Matched Delays
FFGMD	Finite Fragmentation Generation Matched Delays
FFGNIMD	Finite Fragmentation Generation Non Integer Matched Delays
GaN	Galium Nitride
IIFG	Infinite Irrational Fragment Generation
KCL	Kirchoff's Current Law
KVL	Kirchoff's Voltage Law
LTI	Linear Time Invariant
MF	Medium Frequency
MIM	Metal Insulator Metal
OOP	Object Orientated Programming
SCC	Switched Capacitor Converter
SHM	Simple Harmonic Motion
SHO	Simple Harmonic Oscillation
TEM	Transverse electromagnetic
TL	Transmission Line
TLM	Transmission Line Matrix
UHF	Ultra High Frequency
VF	Velocity Factor
VHF	Very High Frequency
VLF	Very Low Frequency
WBG	Wideband Gap

Semper in animo semper in corde meo

This page is intentionally left blank

1 INTRODUCTION

1.1 Background

Power electronics can formally be defined as a collection of technologies associated with the efficient conversion, control and conditioning of electric power by static means from its available input form into the desired electrical output form [1]. Historically the advancements in power electronic technology have been heavily driven by advancements in semiconductor materials and switching devices [2].The effects of the improvements in semiconductor switching technology and devices are demonstrated by the increases in power densities across various converter applications and power levels. These advancements in power densities are made possible by increases in the switching frequency of the power electronic converter. In order to facilitate these increased switching frequencies, it is necessary to ensure that the semiconductor switching device possesses an appreciably high transitional switching speed during *"turn-on"* and *"turn-off"* state transients in the switching waveform. This is necessary in order to ameliorate the switching losses that will be experienced as a consequence of switching at higher frequencies.

Table 1: 3Φ Vienna Rectifier Generational Parameters

$3\Phi\ Vienna\ Rectifier$ $P_O = 10kW$			
	$F_s\ [kHz]$	$\rho_d\ [kW/dm^3]$	$\eta[\%]$
$1^{st}\ Generation$	72	4.6	97.5
$2^{nd}\ Generation$	250	10	97
$3^{rd}\ Generation$	500	13	95
$4^{th}\ Generation$	1000	14.1	93

To illustrate the effects of increasing switching frequency on power density, four generations of a 3Φ-Vienna rectifier are shown in Table 1 . It is readily apparent that with each subsequent generation, increases in the switching frequency (F_s) and power density (ρ_d) of the rectifier are seen whilst a decline in the converter efficiency (η) is observed.

The emergence and incorporation of SiC, GaN and eGaN and other Wide Band Gap (WBG) semiconductor materials in contemporary SMPS devices means that the transitional switching speeds (slew rate) of the switching waveforms are approaching near idealised "*Heaviside unit-step*" conditions with nano and sub-nano second transition times being reported [3]. These vastly increased transitional speeds in turn facilitates an appreciable reduction in switching losses per cycle, which greatly raises the potential for increased power-frequency products of contemporary power electronic converters. The increased power-frequency product makes it an attractive option to integrate many of the converter components and functions into a singular or discrete package. The spatial arrangements of the various components in this integrated power module increases the coupling between the electromagnetic, thermal and mechanical aspects of the various components and interconnects in the converter. As a consequence of the increased interaction between components the environmental circuit conditions are becoming a principle concern [2],[4].

The implications of the increased interaction between components in power modules are effectively imposing a fundamental limit or a bottleneck, with regards to the practical achievable switching frequencies that can be employed in contemporary SMPS. Subsequent increases in switching frequency are yielding diminishing returns with respect to power density. This is exemplified by the 3Φ-Vienna rectifier. In order to increase the power density from $13kW/dm^3$ to $14.1kW/dm^3$ from the 3rd to 4th generation requires an effective doubling of the switching frequency from $500kHz$ to $1MHz$. The relationship between power density and switching frequency at this stage is not a linear one.

It is therefore readily apparent from these observations and those present in literature [2], [5],[6] that advancements in the semiconductor technology cannot be the sole impetus driving advancements in power electronic technology for current as well as future generations of power electronic converters. A more holistic approach to improving converter performance that is focused on not only improving the switching function but the other converter functions 2 through 5 (Figure 1-1) should be employed. This work will predominantly focus on the electromagnetic energy storage function in hopes of gaining increased qualitative and quantitative understanding of fundamental energy flow, transfer and conversion (i.e. energy manipulation) processes that constitute the internal electromagnetic nature of reactive components in converters.

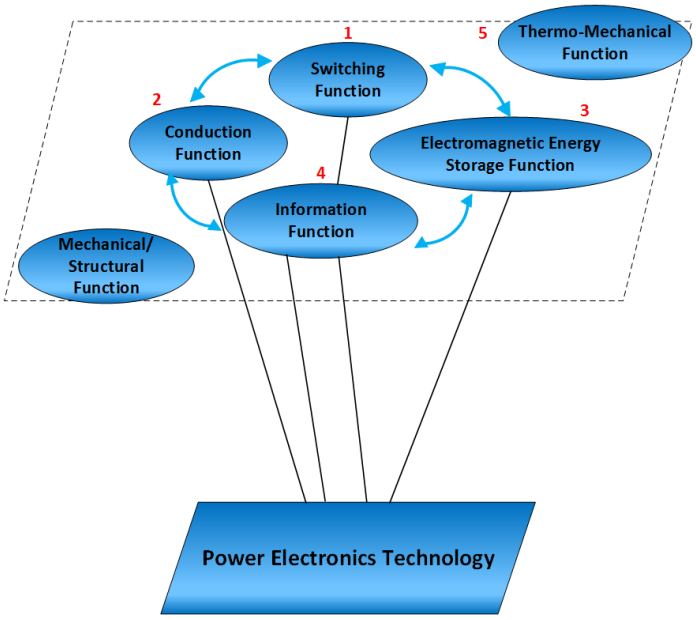


Figure 1-1: Internal functions of a Power Electronic Converter (adapted from [5])

1.2 Research Motivation

In order to facilitate a generic discussion about power electronic converters devoid of a particular application, power level or topology, the power electronic converter will be abstracted into the various functions and activities that are crucial for its operation. The abstraction of the converter yields five internal functions as depicted in Figure 1-1. The internal functions (1 through 5) are seen to have an interdependency with one another. All 5 functions are required in order to ensure functional operation of the power electronic converter. Current trends have been predominantly focused on improving the individual functions through the use of better materials, manufacturing processes and packaging technologies [5]. All the functions (1 through 5) facilitate energy manipulations from a primary store to a secondary store. In order to accomplish this, energy has to be intrinsically transported, converted and stored i.e. manipulated. The 5 internal functions essentially facilitate this energy manipulation (transfer, conversion and storage).

As stated in Chapter 1.1 for future advancements in power electronic technology a holistic approach to approving all internal converter functions must be adopted. At present a very real impediment or barrier to further increases in power densities are being caused by the component interactions and environmental conditions that the power modules are subjected to. Consequently, this increased interaction means that the potential power-frequency product enabled by WBG semiconductor switching devices cannot fully be realised [4], [7]. This is due to the fact that further increases in switching frequency exacerbate undesirable effects such as high frequency oscillations.

This poses an interesting conundrum to the power electronic engineer where further increases in power density will result in a decrease in efficiency. In this instance the power electronic converter is in a state called *Pareto Efficiency*. *Pareto Efficiency* essentially speaks to the fact that a significant or appreciable change in one performance metric cannot occur or take place without an accompanying decrease in another [7]. This is exemplified by the inherent dichotomy that exists between power density and switching losses. For example, increases in power density past a certain point for a particular power level will require higher switching frequencies which will exacerbate switching losses which ultimately lowers the efficiency of the converter. Conversely if efficiency is prioritised and a switching device with fast transitional switching speeds and a lower switching frequency is utilised, this effectively lowers the switching losses whilst an accompanying increase in the spectral content or generated EMI in the converter will be seen.

In order to be complicit with the various EMC standards a bulkier more robust EMI filter will be required. This will essentially occupy a significant portion of real estate in the converter which will reduce the power density. In efforts to reduce the bulkier nature of the EMI filters that will be required planar integration of the EMI filter can be employed [8].

In accordance with the heavy technologically based advancement strategy, little to no new fundamental concepts or advancements are taking place regarding the power passives (capacitors and inductors). Consequently, this means that advancements in material science are the principle means to developing the power passives. As a result, the expected technological progress of the power passives i.e. reactive components is quite slow. It is suggested that a fundamental breakthrough in the physical properties of power passives is required before any significant advancements in converter performance are seen [7].

In this work, the fundamental energy manipulation interactions between electric and magnetic energies in these power passives i.e. reactive components will be undertaken as a potential means of providing this paradigm shift. Increased insight and understanding of the energy manipulations processes in reactive components may provide the foundational framework for improved power passives to be developed in future. For the purposes of this research, it is necessary to define *Fragmentation*, *Energy Conversion Efficacy* (ECE) and *Energy Manipulation Processes* as these are three quintessential terms that are used extensively throughout the dissertation. The *Fragmentation* and *Energy Conversion Efficacy* terms are stated here for brevity but are more formally defined in Chapters 4 and 6 respectively. *Fragmentation*, *Energy Conversion Efficacy* and *Energy Manipulation Processes* are defined as follows:

- ***Fragmentation*** - Describes the effective splitting or fissioning of an incident propagating travelling waveform at an interface or discontinuity between two cascaded or adjoining transmission line segments. This effective fissioning gives rise to new propagating travelling waveforms. If a propagating travelling waveform is successfully transmitted through the interface or junction it is referred to as a fragment of the incident waveform, or merely just a fragment for brevity.

- ***Energy Conversion Efficacy*** - A novel metric designed for the sole purpose of measuring the quality of an energy conversion process. This is done by assessing the energy manipulation process according to two principal attributes. The first attribute is a quantification of the maximum energy that can be transferred/converted from a primary energy store to a secondary energy store. The second attribute establishes the reversibility of the given energy manipulation process.

- ***Energy Manipulation Processes*** – All associated activities pertaining to the flow, transfer and conversion of energies between energy stores.

Results presented in [4] show that in electromagnetically integrated structures and components the principle energy exchange that occurs in reactive components can also be a potential source of EMI. This is antithetical to the conventionally adopted wisdom that fast voltage and current transitions (i.e. the switching edge) are the principle sources of EMI generation in SMPS. As a consequence of the close spatial proximity that the reactive components in integrated electromagnetic structures are operating in, the energy flux of the transport path is effectively minimised. The principle benefit of this is that the subsequent EMI generation that occurs as a result of the energy exchange can be isolated or confined to a particular part of the converter [9].

However, even though the energy flux path is minimised resulting in an optimisation of energy propagation little to no fundamental research or theories have been derived to explain the nuances of the interactions that this energy flux is subjected to. Particularly when energy is converted, transferred and stored i.e. fundamental energy manipulation. An avenue that has not been explored in literature are the effects and implications of potential *Fragmentation* of this energy flux during the energy manipulation processes in reactive components. The consequences of *Fragmentation* generation and the implications on the fundamental energy manipulation processes will be assessed in terms of generated or produced noise as well as *Energy Conversion Efficacy*.

The effects of *Fragmentation* and *Energy Conversion Efficacy* will be explored by examining the common LC Resonant tank topology as well as the *Twin Capacitor* topology. The LC Resonant tank topology represents the most fundamental exchange of electric and magnetic energies and so represents one of the purest forms of electric to magnetic energy manipulations in reactive components.

On account of the LC Resonant tank being a ubiquitous fundamental building block found in almost every conventional power electronic converter topology, results obtained from its study form the necessary foundational research that can later be leveraged to evaluate or predict energy manipulation interactions in resonant, buck and boost converters as well as EMI filters in the future.

In [4] it is documented that the properties of dielectric materials at increased frequencies make it easier to store energy in electric fields, and so alternative topologies that make use of purely capacitive energy storage elements should also be explored. The interconnection of two capacitors represents a fundamental exchange or transfer of electric energies and subsequently represents a pure form of electric to electric energy manipulation. Various Switched Capacitor Converter (SCC) topologies exemplify this type of energy manipulation [10], [11]. The principle building block in these types of converters is the interconnection of at least two capacitors i.e. the *Twin Capacitor* topology. Results obtained from this study can be used to better understand the fundamental energy manipulations that take place in charge-pumps as well as more advanced SCC topologies.

The assessment of *Fragmentation* and *Energy Conversion Efficacy* will be carried out by representing the reactive components in the LC Resonant tank and *Twin Capacitor* topologies with 1-D Transmission Line Modelling or Matrix (TLM) Link-Line equivalent models in a cascaded transmission line configuration. *Energy Conversion Efficacy* will principally be examined by assessing the electric and magnetic energies on the transmission lines in terms of spatial and temporal discretisation. Similarly, the noise implications will be assessed by examination of the spatial and temporal voltage and current distributions.

1.2.1 Electric to Electric Energy Manipulation

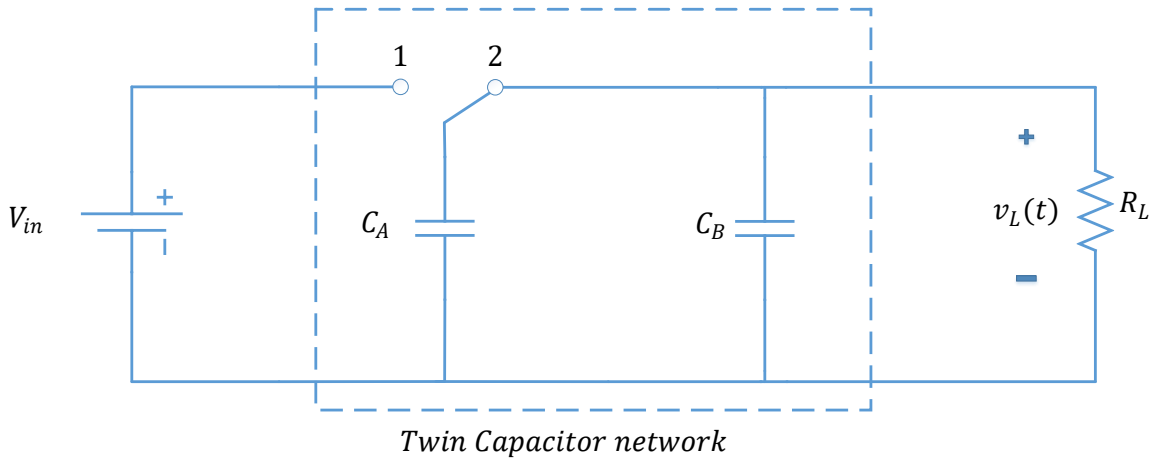


Figure 1-2: Switched-Capacitor Converter

In order to explore the energy manipulation processes involved in transferring purely electrical energy (U_E) between capacitive elements a SCC or Charge-Pump may be used as a case study. The basic operation of a SCC involves charging the primary energy storage capacitor C_A to either a portion of or the full rated voltage V_{in} with the switch in position 1. Once C_A is appropriately charged the switch is moved to position 2 effectively connecting C_A to the initially discharged secondary capacitor C_B.

In practice the energy stored in C_A replenishes the energy store in C_B which subsequently supplies the load R_L.In this work we wish to explore the fundamental energy manipulation processes that take place between the capacitors C_A and C_B as energy is transferred between them. This will be done in an ideal environment with no dissipative elements to ensure that energy loss in the system cannot obfuscate the process. This is achieved by removing the resistive load i.e. setting $R_L = \infty$.

Before the implications due to multiple switching events or *Fragmentation Initiation* events are studied, it is prudent to examine the energy interactions due to a singular switching or *Fragmentation Initiation* event. As this will form the necessary foundational building block for examining multiple switching or *Fragmentation Initiation* events in future work. In order to accomplish this the interconnection of the two capacitors in a *Twin Capacitor* topology will be examined. In examining only one switching or *Fragmentation Initiation* event the system is effectively represented by the *Twin Capacitor* network which forms the basis for the *Twin Capacitor* paradox. A brief description of the *Twin Capacitor* paradox is detailed in Chapter 2.3 with full examination presented in Chapter 3.5.1.

1.2.2 Electric to Magnetic Energy Manipulation

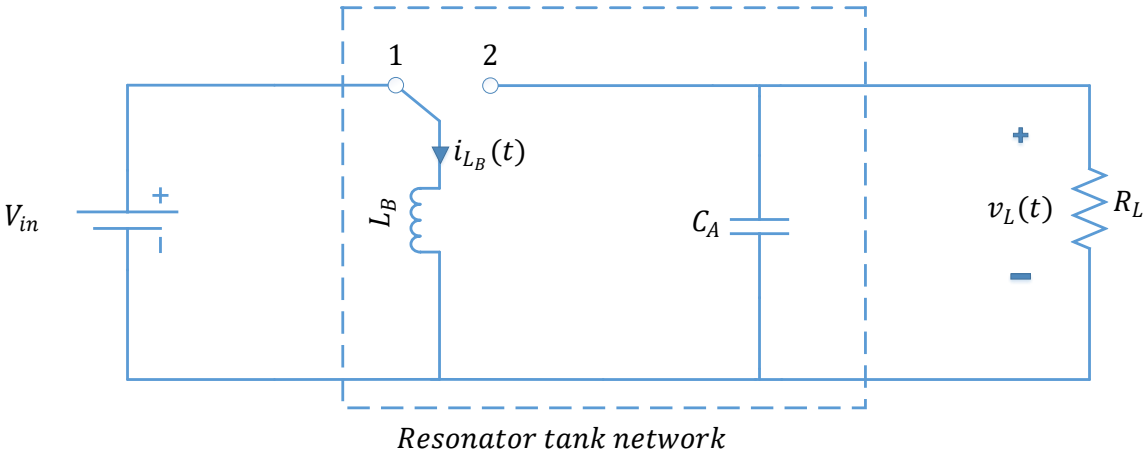


Figure 1-3: Ideal Buck-Boost Converter (Adapted from [12])

In order to explore fundamental energy manipulations between electric (U_E) and magnetic energies (U_H) an ideal Buck-Boost converter will be examined. Observing Figure 1-3 when the switch is in position 1, magnetic energy (U_H) is built up and stored in the inductor L_B. Assuming the output capacitor C_A is charged it supplies the necessary current drawn by the load R_L. Once the desired peak inductor current i_{LB} or maximum magnetic energy (U_H) is reached the switch is connected to position 2. The built-up magnetic energy (U_H) in L_B is now subsequently converted to electrical energy (U_E) stored in C_A, which then ultimately supplies the desired load current to R_L. Now if ideal components are used the expected efficiency in the system is 100% i.e. $\eta = 100\%$. The efficiency metric here speaks to the fact no energy has been lost in the system due to dissipative means (that are not the load). In order to initiate the transfer of the magnetic energy in the inductor (U_H) to electrical energy in the capacitor (U_E) a switching or *Fragmentation Initiation* event is required. This leads to the subsequent generation of EMI in the system.

Now if the system is 100% efficient and can be considered completely closed, then a portion of the converted energy ($U_H \rightarrow U_E$) must be attributed to the EMI. This EMI can be considered as a form of ill-behaved energy that is not useable by the output and cannot be reconstituted back into the system in a well-behaved manner.

If we constrain the study of the energy manipulations to a singular switching or *Fragmentation Initiation* event (the switch moving from position 1 to 2 and staying there). The Buck-Boost converter seen in Figure 1-3 effectively reduces to a resonant tank network with the load resistor. The presence of the load resistor effectively provides a means of damping in the newly formed damped resonator tank network. In order to study the fundamental energy manipulation processes that take place between electric and magnetic energies it is necessary to remove the damping effects of the load resistor R_L i.e. $R_L = \infty$.

The transfer of electric to magnetic energies ($U_E \rightarrow U_H$) does not represent an energy paradox like when energy is transferred purely between electric energy storage elements like in the *Twin Capacitor* paradox. It is readily seen in the system that a 100% energy conversion between electric and magnetic energies will persist *ad infinitum* if zero damping is present in the system. However, this is only under the assumption of idealised lumped element capacitor and inductor models. From conventional circuit theory and lumped element representations, the fundamental nature of how these energy conversion processes take place internally in the reactive components is not readily apparent.

This is seen in the extraction of electrical energy from a capacitor. If an external load or reactive component is connected to a charged capacitor, in order for energy transfer to take place it is readily apparent that an associated current will be required. Now in order to facilitate this current flow this means that intrinsically a portion of the electric energy stored in the capacitor must be converted to magnetic energy. In order to accommodate this magnetic energy storage in the capacitor an associated inductance is a principle requirement.

Similarly, before magnetic energy can be deposited into the inductor there is an associated voltage that is established across the inductor. As a consequence of this, a portion of the energy must be stored in an electric field in order to facilitate the storage of the magnetic energy. In order to further explore the energy manipulation processes in the LC Resonant tank as well as the *Twin Capacitor* topology it is evident that a more fundamental electromagnetic paradigm is necessary to obtain increased insight. In this work this will be achieved through the use of transmission line modelling. A hitherto unexploited feature of transmission line modelling is that the actual energy flow and propagation in the reactive components can be investigated, and hence the nuances of the various energy manipulation processes can be explored [9].

Ferreira in [13] details the movement of energy flux propagation in capacitive and inductive components from a qualitative perspective. It is found that by examining the energy flux vector (Poynting) the point at which energy conversion takes place in the component can be identified. In [4], Ferreira again explores the flow of electromagnetic energy in capacitors and inductors using planar geometric structures. However, this time a qualitative as well as a quasi-static quantitative analysis are performed. The subsequent mapping of the energy flux allows one to obtain a more precise picture of not only how the energy propagates between reactive components but also how it is distributed spatially and the spots at which the conversion of energy to different forms takes place.

Understanding how energy is manipulated at a fundamental level between reactive components will allow for effective energy optimisation. Exploring the nuances of the fundamental energy manipulation processes associated with electric and magnetic energies is paramount to obtaining increased understanding of the internal electromagnetic environment of current and future converters. It is believed that this missing piece of knowledge obtained from this research effort may lay the foundational work for a paradigm shift that considers energy manipulations in capacitive and inductive passive components in power electronic converters.

1.3 Research Objectives, Question and Methodology

1.3.1 Research Objectives

The research objectives are listed as follows:

- To quantify the quality of the energy conversion process between reactive components, in the *Twin Capacitor* and LC Resonant tank topologies. This is assessed in terms of ECE and generated or produced noise.

- Establish a relationship or formula (empirical or otherwise) that is capable of determining the total number of new fragments generated subject to specific design parameters.

- Establish if a proportional relationship exists between *Fragmentation* generation and produced or generated noise exists.

1.3.2 Research Question

The formal problem statement or research question was developed based on preliminary results obtained in the research proposal for the dissertation as well as the literature review (highlighted in Chapter 2). The formal problem statement or research question is given below.

"Utilising transmission line equivalent models for reactive components, what effect do multiple successive internal reflections and transmissions at an interface or discontinuity have on the quality of the energy manipulation processes?"

1.4 Research Scope

The research will be constrained to and by the following:

- Only lossless 1-D TLM Link-Line transmission line segments (no stub transmission line segments) will be used to model the inductors and capacitors in the examined topologies.

- Only two transmission line segments will be used in the modelling of the examined topologies. This is done in efforts to reduce complexity in the *Fragmentation* generation processes.

- Only a solitary switching or *Fragmentation Initiation* event will be modelled.

- Only the *Twin Capacitor* and LC Resonant tank topologies are considered.

.

- Only homogenous materials will be considered for the transmission line segments. In addition, the velocity of propagation on the transmission lines will be considered ideal i.e. the speed of light (velocity factor of 1).

- All propagating travelling waveforms on the transmission line segments must be capable of being represented by linear combinations of Heaviside unit step functions.

1.5 Contributions

The principle focus of the research is in the modelling, analysis and quantification of energy flow, transfer and conversion (i.e. energy manipulation) processes in reactive components. This will be done using the LC Resonant tank and *Twin Capacitor* topologies. A general quantification metric for establishing the quality of a particular energy conversion process (*Energy Conversion Efficacy*) is provided. In addition, the term *Fragmentation* is coined to better explain some of the *diffusion* and *scattering* effects that take place at the interface or junction of two adjoining transmission line segments with arbitrarily defined propagation delays. Consequently, the implications this imposes on *Energy Conversion Efficacy* are subsequently analysed. The concepts of *Energy Conversion Efficacy* and *Fragmentation* are applied to the well-known *Twin Capacitor Paradox* and an alternative solution to the paradox is discovered.

A summary of the major contributions arising from this work are as follows:

1. Implementation of arbitrary transit times in 1-D TLM - In Chapter 4 a novel implementation of the 1-D TLM method that is capable of utilising two arbitrary transit times for two adjoining or cascaded transmission line segments, essentially removing potential limitations on the required propagation delays by not enforcing model synchronism as a principle requirement.

2. Development of a criterion (*Fragmentation Ratio*) based on the propagation delays of the adjoining transmission line segments that is capable of predicting when fragments will come into contact at the junction or interface. In addition, the number of generated fragments (in totality) that will ultimately propagate on both transmission line segments is also established. This is shown in Chapter 4.

3. Alternative solution to *Twin Capacitor Paradox* - An alternative solution to the *Twin Capacitor Paradox* is first presented in Chapter 3 with further exploration following in Chapter 6 . The alternative solution establishes that the *"Missing Energy"* actually converts to magnetic field energy in the respective self-inductors of both capacitors.

4. Derivation of the *Energy Conversion Efficacy* metric and its viability in providing increased understanding into various energy manipulation processes is demonstrated by examining maximum energy transfer and maximum energy reconstitution in the LC Resonant tank and *Twin Capacitor* topologies. The application of the *Energy Conversion Efficacy* metric is shown in Chapter 6.

5. Noise produced by the LC Resonant and the *Twin Capacitor* topologies is shown to increases with successive *Fragmentation* generation until what appears to be a fundamental limit is approached were subsequent noise generation plateaus. This is shown in Chapter 6.

1.6 Dissertation Overview

The remainder of the dissertation is structured as follows. Chapters 2 and 3 provide the necessary foundational context for the research. Chapter 2 provides a literature review on current and future trends in power electronics. After which the limitations of conventional circuit theory in modelling energy manipulations are highlighted by the classical energy paradox in physics known as the *Twin Capacitor* paradox. Various explanations for the paradox are discussed and critiqued and a potential avenue towards solving the paradox is identified. Following this is a section on the

geometric representation of reactive components in discrete as well as integrated multi-layered planar structures and their equivalent transmission line models. Lastly the chapter concludes with a section on electromagnetic energy propagation and flow in reactive components. Chapter 3 details various electromagnetic modelling paradigms and a brief discussion on the applicability of each are presented. This is subsequently followed by the derivation of the 1-D TLM Stub and Link-Line models for reactive components. The chapter concludes by exploring the implications of the cascaded Link-Line model representation in the LC Resonant tank and *Twin Capacitor* topologies, thus facilitating qualitative exploration of the energy manipulation processes. Chapter 4 provides a formal definition for *Fragmentation* as well as establishing the necessary framework for the various *Fragmentation* generation methods. Chapter 5 provides necessary algorithms and procedures for realising the various *Fragmentation* generation techniques in a simulation environment. Chapter 6 presents the energy manipulation processes in the *Twin Capacitor* and LC Resonant tank topologies. The *Energy Conversion Efficacy* metric is formally defined and used to assess the topologies under various *Fragmentation* generation methods. An extensive investigation into the relationships between *Energy Conversion Efficacy*, *Fragmentation* generation and produced or generated EMI is undertaken through various simulated scenarios. Chapter 7 offers concluding remarks on the research as well as future recommendations for the work going forward.

1.7 Conclusion

The principle advancement strategy in power electronics has been largely technologically based since its inception. At the forefront of these technological advancements have been advancements and developments in semiconductor materials and switching devices. By increasing the switching frequency component sizes and dimensions in the converter have been greatly reduced. This reduction in component size makes it feasible to integrate one or more converter functions and components into singular discretised power modules, which subsequently increases the power density of the converter. However, in these power modules greater potential for interaction between components exists. Consequently, what is now being observed is that the traditional avenue of increasing switching frequencies to obtain increased power densities cannot be employed without exacerbating undesirable effects such as high frequency oscillations i.e. ringing which not only effect converter efficiency but produce unwanted EMI. This effectively means that the full potential of contemporary WBG semiconductor switching devices and their near idyllic transitional switching speeds cannot fully be realised.

In order to prepare for future power electronic converters, it is necessary to seek out alternative more fundamental methods rooted in increasing qualitative and quantitative understanding of the internal electromagnetic environment of reactive components. This is required in order to potentially provide the necessary paradigm shift to ensure that advancements in power electronic technology are not solely dependent on advancements in material science of semiconductor devices. In efforts to provide this paradigm shift increased fundamental understanding of the energy flow, transfer and conversion (i.e. energy manipulation) processes in reactive components is required. The analysis of the energy manipulation processes are assessed against the *Energy Conversion Efficacy* metric and potential implications on noise generation established. *Energy Conversion Efficacy* is a novel metric designed to quantify the quality of the energy manipulation processes between reactive components. The analysis will be achieved by modelling the components with 1-D TLM Link-Line transmission line equivalent models. As transmission lines represent a more fundamental electromagnetic modelling paradigm that allows the analysis of wave and energy propagation.

2 LITERATURE REVIEW

2.1 Overview

This chapter details a broad review of some current and future trends in power electronics with specific reverence being placed on road mapping and the identification of potential avenues in order to facilitate increased performance in contemporary as well as future power electronic converters. This is followed by a brief look at the limitations facing conventional circuit theory and lumped element representations in modelling energy manipulation interactions in reactive components. It is established that in order to find ways to address these limitations the reactive components should be replaced with transmission line equivalent models. Consequently, a brief overview of transmission line representations of reactive components in discrete as well as integrated electromagnetic structures follows. Lastly, a brief look at how electromagnetic energy flow and propagation is modelled in classical and contemporary literature is presented. The objectives of this literature review are to ascertain possible limitations in literature specifically pertaining to energy manipulations (transfer, storage and conversion) in reactive components. This literature review thus provides the contextual basis for the specific areas that this research will be primarily focused on.

2.2 Current and Future Trends In Power Electronics

In attempts to better understand and map the current as well as future landscape of power electronics, initiatives such as the European Center of Power Electronics (ECPE), Japan National Institute of Science and Technology (AIST-PERC),Center for Power Electronic Systems (CPES) and international *"think-tank"* workshops such as the Future of Electronic Power Processing and Conversion (FEPPCON) have been formed in recent years in attempts to get industrial professionals and academic researchers to come together to roadmap the future of the power electronic industry [7], [14]. Such initiatives are necessary to identify potential technological barriers and prepare adequate research and development strategies in order to circumvent them.

Principle conclusions arising from these conference proceedings are the following: WBG semiconductor switching devices will become prevalent in the future due to their high transitional switching speeds and their potential to ameliorate switching losses at higher switching frequencies; The prevalence of integrated power modules/processing units will drive the future of power electronic applications; Functional and electromagnetic integration will produce a paradigm shift in the internal structure of power electronic modules [14].

In order to fully exploit the potential of various constituent component technologies in power electronics (manufacturing, packaging and thermal management etc.) a quantifiable mathematical procedure is required. The developed mathematical procedure is in the form of a multi-objective optimisation. This multi-objective optimisation is centred around various performance indices (power density, efficiency and cost etc.). In order to meet the specified design goals specific weightings are attributed to the various performance indices in order to facilitate the optimisation process.

After the optimisation process by the model a *Pareto Front* envelope is established. A *Pareto Front* envelope essentially speaks to the boundary between what is achievable within the confines of the feasible performance space using current technologies and manufacturing procedures in the power electronic converter.

If the desired performance requirements of a system lay outside of the *Pareto Front* envelope (this also represents the boundary of the feasible performance space) a principle technological breakthrough in the landscape of current technologies is required in order to realise the desired performance design goals. Such a fundamental breakthrough in the technological landscape is known as a "*disruptive technology*" [7].

Utilising the multi-objective optimisation and *Pareto Front* envelope detailed in [7] it is readily shown that performance benefits due to increases in transitional switching speeds will eventually yield diminishing returns (eluded to in [4] as well). These diminishing returns are indicated by a zero gradient on the *Pareto Front* boundary or envelope. The zero gradient speaks to the fact that the system is in a state termed *Pareto Efficiency*. *Pareto Efficiency* can be defined as the state of a given system where further increases in any performance metric cannot be achieved without adversely effecting another performance metric. For example, increases in switching frequencies and hence power density will result in a reduction in efficiency [7]. From these observations it is clear that advancements in semiconductor technology and switching frequencies alone cannot be the sole driving force of the power electronic converter of the future.

Leading on from the work established in [4], It is argued that there will be a concerted push to achieve physical integration of the internal converter functions (shown in Figure 1-1) in contemporary as well as future power electronic converters [4]. This subsequent integration essentially forms an integrated electromagnetic processor. Additionally, the subsequent integration of these converter functions/components leads to increases in power densities of converters.

However, principle challenges that arise due to the close spatial proximity of the components in the integrated environment are due to increased component interaction and environmental conditions. Effects due to increased component interaction and environmental conditions will become the new limiting factor for future power electronic converters. This is principally due to the fact that further increases in switching frequencies in efforts to further reduce component sizes to increase power densities will exacerbate undesirable effects such as high frequency oscillations i.e. ringing. In addition, increased coupling and spatial proximity makes it impossible to differentiate between individual reactive components and a lumped element representation becomes inept. Thus, it is necessary to analyse and model the reactive components using more fundamental electromagnetic paradigms that are capable of addressing some of the inadequacies and limitations of conventional circuit theory and lumped element representations. As stated in [7], it has been established that what is necessary for the development of future power electronics is a paradigm shift that focuses on the internal electromagnetic structure of the power electronics module. In this work, the fundamental energy manipulation processes in reactive components will be examined in order to provide the necessary foundational basis for such a paradigm shift.

2.3 Limitations of Circuit Theory

Circuit theory and several network paradigms have become the preferred method of modelling and analysis in power electronics because of their simplicity, which has led to their wide spread adaptation.

Network paradigms and circuit theory have since even expanded to deal with the analysis of systems that lay outside the realm of electromagnetics provided an analogous relationship between the lumped element quantities ($R, L\ and\ C$) and the examined quantities exists [4]. At low frequencies (frequency in this context is w.r.t electrical length) these lumped element abstractions can be modelled as concentrated quantities.

However, at higher frequencies this simple lumped element representation requires augmentation with auxiliary components forming various "*Hidden Schematic*" representations in order to better model the behaviour of the components [15]. Additionally, if components are operating in close spatial proximity the traditional one-to-one mapping between the modelled quantity and the lumped element representation that conventional circuit theory tacitly assumes is violated thus presenting another principle limitation.

Further limitations are demonstrated if energy manipulations in reactive components are considered. In examining energy manipulation processes the limitations of lumped elements and conventional circuit theory becomes glaringly apparent. This is exemplified by the classic *Twin Capacitor* paradox as seen in Figure 2-1.

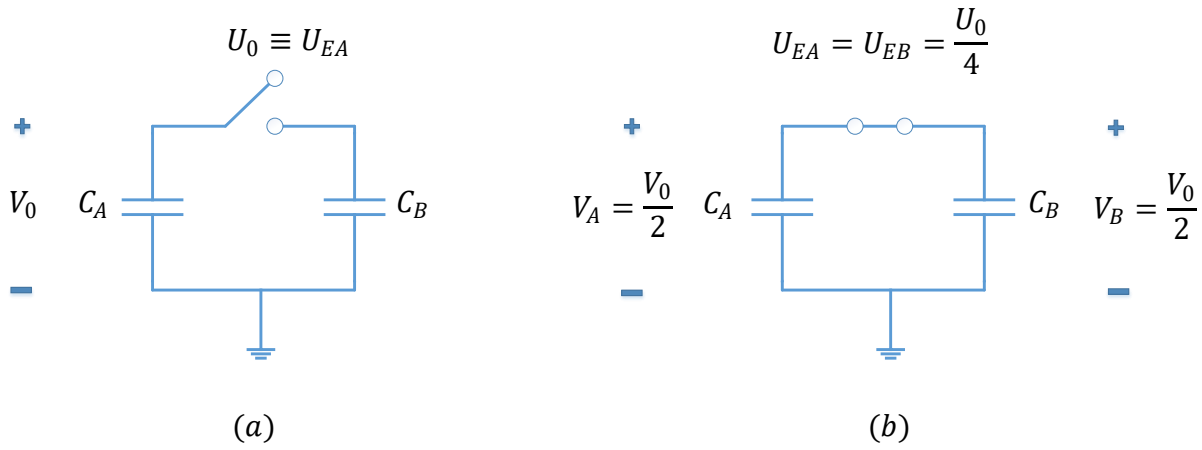


Figure 2-1: Twin Capacitor a) Initial State b) Equilibrium State

The simplest version of this classical energy paradox involves the use of two identical ideal capacitors C_A and C_B. A primary capacitor C_A is initially charged to an arbitrary voltage V_0 by an external source (not shown in Figure 2-1a). Once C_A is appropriately charged it is then subsequently disconnected from the external source and connected to a secondary capacitor C_B that is initially discharged. It is important to note that the interconnecting conductors between C_A and C_B are considered ideal so there can be no loss of energy due to ohmic losses (heat) or any other form of energy dissipation in the capacitors. After the subsequent connection of the capacitors and given a finite amount of time the system will reach an equilibrium state with equal voltage distribution across both capacitors i.e. $V_A = V_B = V_0/2$ (Figure 2-1b). Considering the voltage distribution between capacitors is equal and sums to the initial charge voltage V_0 it is assumed that the energies in both capacitors U_{EA} and U_{EB} sum to the initial energy U_0 before equilibrium. This assumption is in fact erroneous (i.e. $U_{EA} + U_{EB} = \frac{U_0}{2}$) and a *perceived* energy deficit known as *"Missing Energy"* is observed in the system. Since the system is assumed closed and no dissipative elements are present this *"Missing Energy" ipso facto* (by the very fact) represents a violation of conservation of energy [16].

In attempting to analyse or assess the system energy manipulations using purely conventional circuit theory and lumped elements renders this system as an energy paradox. In literature, this *"Missing Energy"* has been attributed to a gain in kinetic energy of the conducting charge carriers required to transport charge from C_A to the C_B [16]. In order to resolve the paradox, the capacitance of C_A is effectively altered by stretching the conducting plates.

In solving the paradox in this manner, the author is artificially manipulating the system by altering the capacitance of C_A. In [17], it is postulated that even though a system may be completely devoid of any ohmic losses it may still contain a radiation resistance. The *"Missing Energy"* in the system is then attributed to the fact that this radiation resistance causes a voltage drop to appear across the conducting wire. This solution like the one given in [16] artificially contaminates the purity of the ideal closed system by introducing a mechanism (radiation resistance) for energy to be dissipated effectively rendering the once closed system now open.

In a truly closed system devoid of any damping or dissipative elements, conservation of energy will always hold. Conventional circuit theory and lumped element representations inadequacy in providing a rigorous explanation for the energy paradox speaks to the limitations in analysing energy manipulation interactions using circuit and network paradigms. This simplistic energy paradox speaks to the nuances of the energy conversion processes that take place in capacitive components that are not readily apparent when viewed with circuit theory and lumped elements. In order to provide a more robust explanation for the energy paradox, a more fundamental approach steeped in electromagnetic propagation and energy flow will therefore be sought out. It is therefore suggested that the lumped element representation of the capacitors is discarded in favour of a transmission line model. The transmission line representation will enable the TEM propagation of the voltage and current waves as well as energy flux in reactive components to be examined.

2.4 Transmission Line Modelling of Reactive Components

The notion of modelling reactive components as transmission lines is not a novel or new concept in electromagnetics or power electronics. Various works in [18]–[20] speak to this fact. This section will explore how transmission line modelling is utilised in modelling discrete reactive components such as Multilayer Ceramic Capacitors (MLC) as well as electromagnetically integrated structures such as multilayer planar LC Resonant tanks. This transmission line representation enables the study of electromagnetic energy flow and propagation aspects in the reactive components. This in turn facilitates the study of the fundamental energy manipulation processes in the reactive components.

2.4.1 Discrete structures

Conventionally capacitors in power electronic applications are modelled as lumped element RLC networks. The inductance associated with the capacitor (usually represented as ESL) is given by the inductance of the capacitor leads as well as the current path through the capacitor itself. In [21] the lumped element representation of the capacitor is shown to be accurate provided that the lead inductance in the capacitor is dominant. However, if the interconnect distance and leads are short, this leads to the inductance path through the capacitor (associated or self-inductance) becoming the dominant inductance in the capacitor. Consequently, the capacitor is now more accurately represented by a model based on distributed capacitance and inductance. In [21], it is experimentally verified that the distributed model i.e. the transmission line model has approximately one fifth of the error when compared to its lumped element counterpart. From this evidence it is apparent that in applications where accuracy in the modelling of the capacitor is paramount, a distributed or transmission line model should be favoured [21].

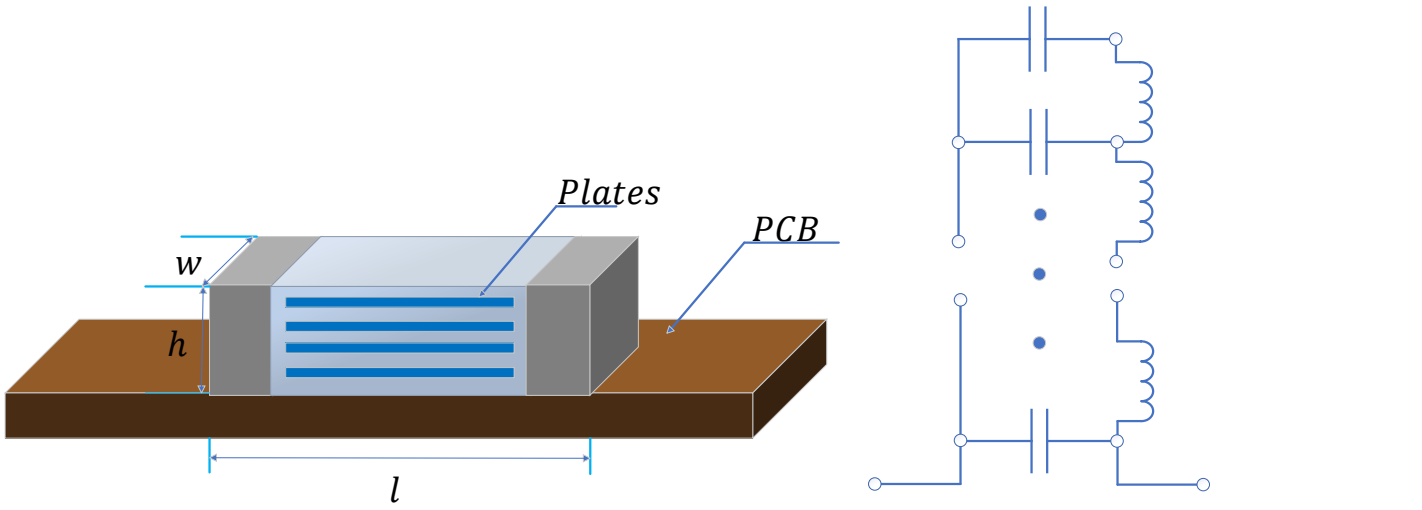
In this work, the transmission line model that will be adopted is that of a lossless transmission line. This is done because the principle objectives of this work are to examine fundamental energy manipulations that take place in reactive components (capacitors and inductors) and the introduction of dissipative elements would obfuscate this process.

In addition to the transmission line representation being not only a more accurate model for capacitors the wave propagation attributes can be leveraged in order to obtain increased qualitative and quantitative understanding of energy manipulation processes that take place in the capacitor particularly when energy is extracted or deposited.

For each layer in the MLC structure an individual capacitor will be used to represent the energy storage capabilities. The series inductors are used to represent the inductance between individual layers in the capacitor [21]. The inductance is given by the equation

$$L = \mu_0 \frac{hl}{w} \tag{2.1}$$

Where $h = Height; l = length; w = width$ and $\mu_0 = Permeability\ of\ free\ space$. The length ($l$) is taken in a direction that is perpendicular to the direction of current flow and the width (w) of the capacitor.



a) Physical Structure of MLC Capacitor *b) Distributed Parameter Model of MLC Capacitor*

Figure 2-2: Models of MLC Capacitor a) Physical Structure b) Distributed Parameter Model (Adapted from [21])

The developed model structure as seen in Figure 2-2b is effectively a distributive model and as such can be represented by a transmission line. In modern MLC capacitors the number of plates is appreciably large enough such that an individual capacitor is not required to represent each layer in the MLC structure. The large number of plates allows for a continuous approximation which means that the spacing between distinct layers is not explicitly required [21].

The continuous approximation effectively spatially discretises the capacitance and inductance of the MLC capacitor in space. This spatial discretisation inherently gives rise to per-unit length quantities. In the presented geometry in Figure 2-2a the discretisation takes place along the height dimension.

The per-unit capacitance (C_{pu}) is given by the specified capacitance (C) divided by the height (h) of the capacitor. Equation (2.2) represents the per-unit capacitance:

$$C_{pu} = \frac{C}{h} \tag{2.2}$$

The per-unit inductance is merely just equation (2.1) divided by the height (h) of the capacitor. The per-unit inductance is thus represented by equation (2.3)

$$L_{pu} = \mu_0 \frac{l}{w} \tag{2.3}$$

The distributed model in Figure 2-2b can now be replaced with its equivalent transmission line model given in Figure 2-3.

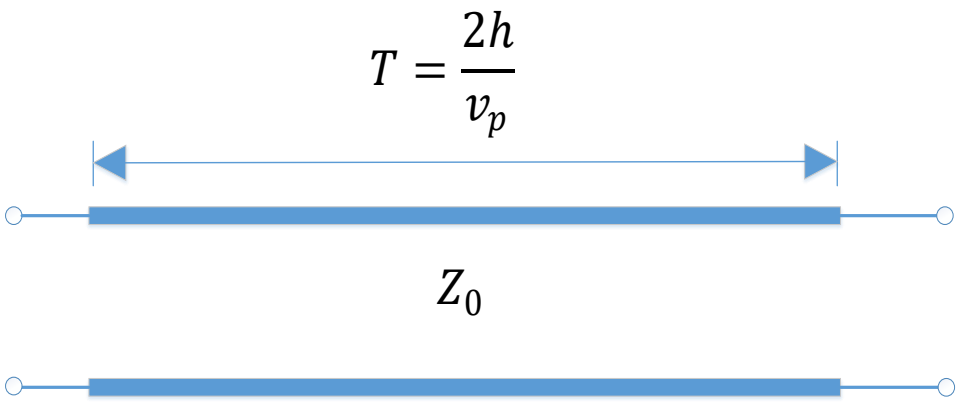


Figure 2-3: Transmission Line Capacitor Model

The transmission line model of the capacitor is completely characterised by two parameters. Firstly, the propagation delay (T) of the transmission line and secondly the characteristic impedance of the transmission line (Z_0). The propagation delay in [21] is taken as the round-trip delay for a wave to propagate across the length of the transmission line and then back again. This propagation delay definition is consistent with the TLM Stub model as will be seen in Chapter 3.4.3. The propagation delay is given by

$$T = 2hl\sqrt{\mu_o C_v} \tag{2.4}$$

The characteristic impedance of the capacitor is given by equation (2.3). For a given capacitor, C_{pu} can be modified to accurately encompass the various physical and dimensional aspects such as dielectric materials and plate thickness in terms of a per-unit volume capacitance (C_v).

$$Z_0 = \sqrt{\frac{L_{pu}}{C_{pu}}} = \sqrt{\frac{\mu_o l/w}{C_v wl}} = \frac{1}{w}\sqrt{\frac{\mu_0}{C_v}} \tag{2.5}$$

Ultimately making use of equations (2.2)-(2.5) the capacitance of the MLC capacitor can be determined. The capacitance is given by the following equation

$$C = \frac{T}{2Z_0} \tag{2.6}$$

2.4.2 Integrated structures

In recent times there has been a concerted effort to increase the power density of power electronic converters as pointed out in Chapter 2.2. A principle avenue to achieving increases in power densities is the physical integration of reactive components essentially forming an integrated electromagnetic structure. The integration of reactive components increases power densities in the converter because reactive components occupy a significant portion of real estate on the PCB board of power electronic converters. Subsequent integration of these reactive components into singular structures saves space and removes interconnect distances. In so doing this enables more components to be housed in closer spatial proximity to one another.

In attempting to represent the physically integrated structure with lumped element equivalent models, some limitations are encountered. A principle limitation of the lumped element representation of an integrated LC Resonant structure is that it is a modelling technique that is based solely on empirical measurement data of the frequency response of the integrated LC Resonant structure in question. Analysis of the frequency response reveals a fundamental zero along with two additional resonant frequencies. In efforts to represent these experimental observations a lumped element model that is comprised of four distinct L and C elements is adopted [20]. The fact that the developed model is not steeped in any sound theoretical basis and arises solely as a consequence of experimental/empirical observations in attempts to replicate the observed behaviour makes it unsuitable for modelling fundamental energy manipulation interactions [20]. In addition, no further insight into the complex electromagnetic environment of the integrated structure can be obtained with this type of modelling.

Understanding these challenges and limitations of modelling integrated LC structures with lumped element models, a modelling approach which views the integrated LC structure as a distributed model is adopted. If the integrated LC structure is to be used as a resonant structure i.e. LC Resonant tank then a $\lambda/4$ transmission line represents the most fundamental means of solving the modelling problem (Figure 2-4). The use of $\lambda/4$ transmission lines as resonant structures is not a new concept and is used extensively in microwave technology. However, the operational frequency of conventional microstrip resonators (GHz regions) as well as its unsuitability for power transmission mean that it cannot (in this form) act as a suitable replacement model [20]. Understanding this led to the development of more practical planar structures which operate at frequencies of $1MHz$ and lower which are closer to the achievable switching frequencies found in contemporary semiconductor devices [20]. In [20], it is shown that cascading two separate transmission line sections may result in a resonant frequency that is lower than the individual resonant frequencies of the individual transmission line sections.

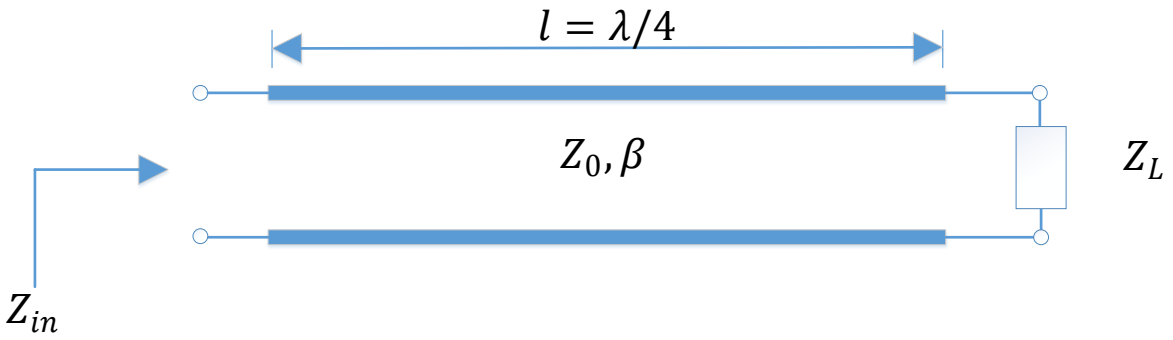


Figure 2-4: General $\lambda/4$ Transmission Line terminated by load Z_L (Adapted from [20])

The transmission line parameters Z_{in}, Z_0 and β specified in Figure 2-4 are given by equations (2.7) to (2.9).

$$Z_{in} = \frac{Z_0(Z_L + jZ_0 \tan(\beta l))}{Z_0 + jZ_L \tan(\beta l)} \tag{2.7}$$

$$\beta = \frac{2\pi}{\lambda} = 2\pi f_0 \sqrt{\epsilon_0 \epsilon_r \mu_o \mu_r} \tag{2.8}$$

$$Z_0 = \frac{377\sqrt{\mu_r}}{\sqrt{\epsilon_{eff}}} \left[\frac{w}{h} + 1.4 + 0.7ln\left(\frac{w}{h} + 1.4\right)\right]^{-1} \tag{2.9}$$

The characteristic impedance given by equation (2.9) was determined experimentally and is shown to be consistent with the characteristic impedance given for microstrip transmission lines. The effective permittivity (ϵ_{eff}) is given by the following equation

$$\epsilon_{eff} = \frac{\epsilon_r + 1}{2} + \frac{\epsilon_r - 1}{2} \left[1 + 12\frac{h}{w}\right]^{-\frac{1}{2}} \tag{2.10}$$

Now that the relevant transmission line parameters in the generic $\lambda/4$ transmission line illustrated in Figure 2-4 have been defined, the role of these parameters in forming parallel or series tuned resonant circuits can be discussed.

Dependent on the load Z_L, the $\lambda/4$ transmission line can be tuned to represent either a parallel or series tuned circuit. For a $Z_L = 0$ the input impedance Z_{in} will be seen as an open-circuit i.e. $Z_{in} = \infty$ and thus the $\lambda/4$ transmission line effectively represents a parallel tuned circuit. Alternatively, for a $Z_L = \infty$ (i.e. open circuit) the input impedance seen will be that of a short-circuit i.e. $Z_{in} = 0$ in this configuration the $\lambda/4$ transmission line will effectively represent a series tuned circuit [20].

Utilising these facts if the short-circuit $\lambda/4$ transmission line (i.e. parallel tuned circuit) is broken up into two distinct regions or sections that have a difference in material composition. At the point where the two TL sections meet, an interface or discontinuity will be created because of the difference in the characteristic impedances of the transmission lines. Each TL section will have its own characteristic impedance (Z_{0_1} and Z_{0_2} respectively), length (l_1 and l_2) as well as material composition ($\epsilon_{r_1}; \mu_{0_1}$ and $\epsilon_{r_2}; \mu_{0_2}$).

The characteristic impedances of the two sections Z_{0_1} and Z_{0_2} can be effectively manipulated by changing the physical dimensions of the TL segments in the different sections.

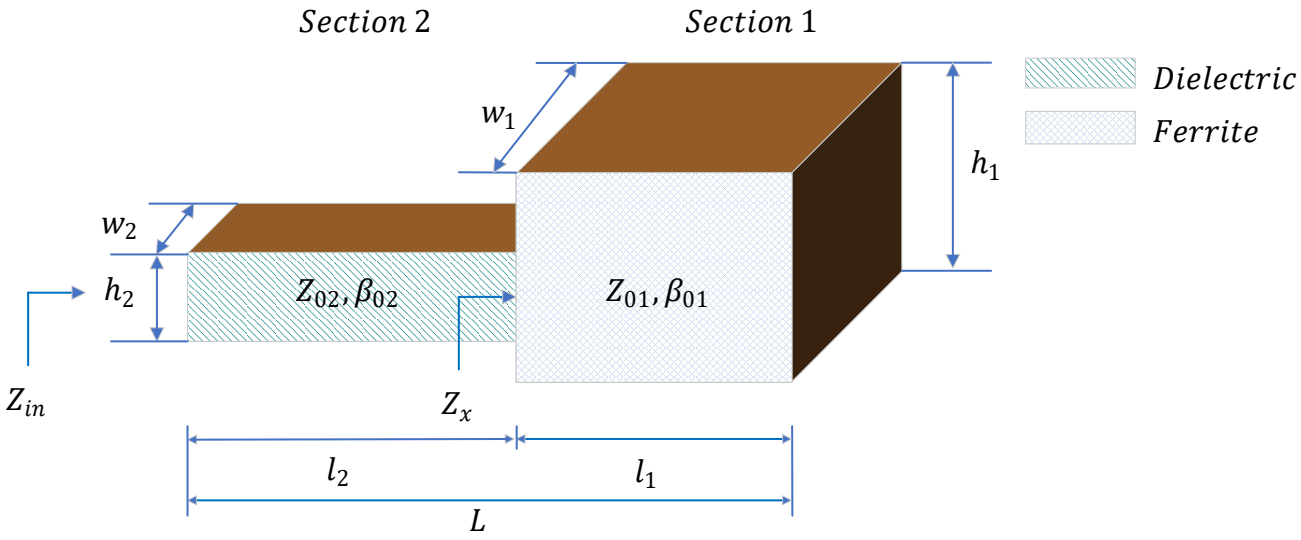


Figure 2-5: Parallel Planar LC Resonant Structure (Adapted from [20])

In order to form the LC Resonant structure given in Figure 2-5 the termination load (Z_L in Figure 2-4) in section 1 needs to be short-circuited (i.e. $Z_L = 0$) in a Ferrite medium ($\mu_{r_1} \gg 1; \epsilon_{r_1} = 1$). This results in a very large characteristic impedance being formed. The large characteristic impedance along with the high permeability μ_{0_1} essentially renders the TL segment in this section as an inductor. Conversely in section 2 the TL segment needs to be open-circuited (i.e. $Z_L = \infty$) in a dielectric medium ($\mu_{r_1} = 1; \epsilon_{r_1} \gg 1$). This results in a very low characteristic impedance being established. The low characteristic impedance in conjunction with the high permittivity ϵ_{r_1} renders the TL segment a capacitor. The input impedance of the complete LC structure can be calculated by using equation (2.12) and substituting the input impedance Z_x for Z_0 [20].

Since Z_x is given by:

$$Z_x = jZ_0 tan\beta_1 l_1 \tag{2.11}$$

The total input impedance of the parallel LC Resonant structure is given by

$$Z_{in} = \frac{Z_{0_2}[Z_x + jZ_{0_2} tan\beta_2 l_2]}{Z_{0_2} + jZ_x tan\beta_2 l_2} \tag{2.12}$$

The lengths l_1 and l_2 of the respective sections are given by the expressions in equations (2.13) and (2.14).

$$l_1 = \frac{1}{\beta_1} sin^{-1} \sqrt{\left[\frac{\zeta\beta_1 - \beta_2}{\beta_2(\zeta^2 - 1)}\right]} \tag{2.13}$$

$$l_2 = \frac{1}{\beta_2} sin^{-1} \sqrt{\left[\frac{\zeta\beta_2 - \beta_1}{\beta_1(\zeta^2 - 1)}\right]} \tag{2.14}$$

Where ζ is the ratio of characteristic impedances in the two sections given by:

$$\zeta = \frac{Z_{0_1}}{Z_{0_2}} \tag{2.15}$$

It should be noted that it is also possible to represent the TL section lengths l_1 and l_2 in terms of propagation delays. In order to do this, the lengths l_1 and l_2 merely need to be divided by the propagation velocity v_p (material dependent) of the respective section.

The propagation velocity v_p is given by

$$v_p = \frac{1}{\sqrt{\mu\epsilon}} \tag{2.16}$$

The propagation delay is given by the following equation:

$$\tau = \frac{l}{v_p} \tag{2.17}$$

The lengths given by equations (2.13) and (2.14) can be used along with the input impedance and characteristic impedances to form the basis of the TLM models that will be seen in Chapter 3.4. The cascaded transmission line representation of the parallel resonant LC structure is depicted in Figure 2-6.

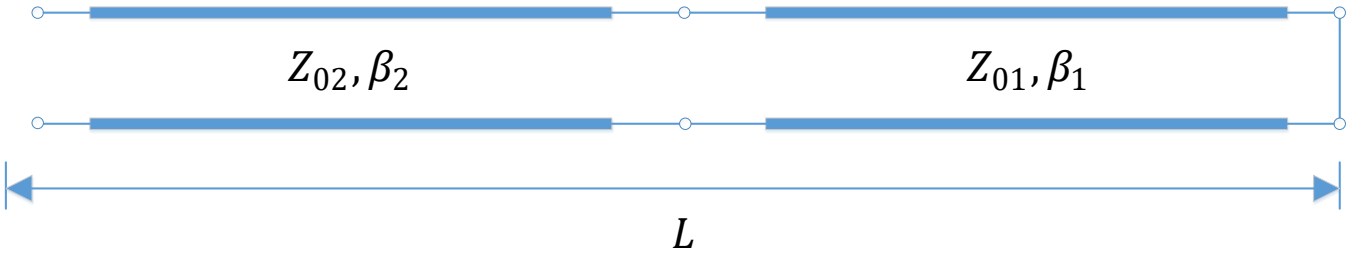


Figure 2-6: Transmission Line Model of Parallel LC Resonant Structure (Adapted from [20])

2.5 Electromagnetic Energy Flow

The study of electromagnetic energy propagation now more than ever is of critical importance in order to obtain increased insight into the internal structure of power modules. The study of electromagnetic energy flow and propagation is imperative for understanding the nuances of energy manipulations in reactive components. In [22] a summary of three principle methods for modelling electromagnetic energy flow and propagation are presented. The first method details the use of voltages and currents along with various network abstractions to model energy manipulations. The limitations and shortcomings of using this method to analyse and characterise energy manipulations has already been detailed in Chapter 2.3 (*Twin Capacitor* paradox) and will thus not be considered.

The second modelling paradigm makes use of electromagnetic wave propagation, which is represented by the energy flux density vector also known as the Poynting vector ($\mathcal{S} = \vec{E} \times \vec{H}$) [23].This describes the manner in which energy disseminates by examining the rate of energy storage and dissipation in a particular volume. The third modelling paradigm makes use of charge-potentials and is essentially a reformation of the Poynting vector based on Maxwell's concepts of "*electric fluid*" and "*electrokinetic momentum*".

In [22] various illustrative examples that detail the flow of electromagnetic energy are presented. The illustrative energy flow example that is of particular interest is one concerning an AC source connected to reactive components (either a capacitor or inductor). A working hypothesis at the time (20th century) was thought to be that if energy was transferred from an AC source (alternator) and connected to a reactive element, a portion of the energy would be lost to the heating of the conductor or transport material, whilst the remaining energy (electric or magnetic) would be stored within the electric and magnetic fields surrounding the particular reactive component. It was thought that this process was completely reversible until antithetical research in [24] disproved this hypothesis. Utilising a combination of reasoning based on the theoretical framework of Maxwell's displacement current (amendment to Ampère's law) proved that some energy must be lost to the AC source (alternator internal resistance etc.) and some of the energy must be radiated outwards. If the radiation of energy out of the system is allowed there will exist a net energy differential before and after the energy conversion processes have taken place in the reactive component. In such a scenario some of the nuances in the energy conversion and manipulation processes may be obfuscated by this loss of energy.

In order to remedy this, we consider the system as an ideal closed system where no effective means of dissipation or radiation of energy can occur. Since no dissipative elements are present in the system the would-be radiated energy has no "*escape path*" and is effectively confined or trapped by the system. Consequently, the role of this confined or trapped energy in the energy conversion and energy manipulation processes can now be assessed by various energy flow and propagation methods.

2.5.1 Energy Flux Density Vector

Mapping energy flow and propagation using the Poynting vector is advantageous because it enables energy conversion in a converter and hence reactive components to be traced to specific localized areas [7]. In addition, expressions for the maximum electromagnetic flux density and storage capabilities of reactive components can be ascertained. The electromagnetic energy flow and propagation by the use of the Poynting vector is best illustrated by its application to the following scenario(s). Consider a power line/transmission line (pair of parallel conductors) connected to a multilayer planar capacitor.

In [13], it is shown that the electromagnetic flux is confined to the space between the conductors. The conductors in this instance act as pseudo wave-guides that confine the flux. If the geometry of the planar capacitor is such that it can be represented by a singular pair or multiple conductor pairs all in parallel, essentially the capacitor can be represented by a transmission line segment. The transmission line representation of the capacitor is completely characterised by a specified length (or propagation delay) and characteristic impedance. The transmission line representation of the capacitor is advantageous because propagation effects/attributes of TEM propagating waves are readily examinable, and hence energy flow and propagation can be examined. Another principle benefit of this representation is that subsequent field quantities such as $\vec{E}$ (electric) and $\vec{H}$ (magnetic) fields can be determined whilst higher-level network abstractions like voltages and currents can also be ascertained. The point where the original power line/transmission line meets the capacitor ensures that an interface or discontinuity is effectively formed. The manner in which the confined energy flux of the power line interacts with the planar capacitor at the interface or discontinuity effectively represents energy conversion and transfer into the capacitor.

Dependent on the propagation delay (length) and characteristic impedance of the original power line/transmission line and the newly formed transmission line segment representing the capacitor, the TEM propagating waves and hence the energy flux may be subjected to internal reflections before the capacitor is fully charged. However, if a large discrepancy in the characteristic impedances of the power line and the TL segment representing the capacitor exists then multiple internal reflections and transmission effects will occur at the interface or discontinuity. The implications of this means that more discretised steps in the energy flux density will be seen as the capacitor charges up to its maximum energy flux density [4].

Considering that the interconnection of a capacitor and inductor can be represented by a parallel LC planar resonant structure (as seen in Figure 2-5), transmission line segments can be used to represent the capacitor and inductor in this planar LC Resonant tank configuration [20]. The transmission line representation here again enables the effects of energy propagation and energy flux to be examined. However, a principle difference in this scenario when compared to the connection of a power line and a planar capacitor is that at the interface or discontinuity between the capacitor and inductor an appreciably large difference in characteristic impedances will always occur. This large discrepancy in characteristic impedances at the interface stems from the manner in which the characteristic impedances in capacitors and inductors are defined in their respective TL representations.

A capacitor is characterised by a TL segment that has a finite length and low characteristic impedance. The capacitance is given by the ratio of the TL segment length/propagation delay and the characteristic impedance, whilst the associated inductance is given by the product of the TL propagation delay/length and characteristic impedance. In observing these relationships, it is readily apparent that in order to suppress the associated inductance of the TL segment a short propagation delay/length as well as a low characteristic impedance is required [25].

Alternatively, an inductor can be characterised by a TL segment that has a finite length and high characteristic impedance. In order to ensure the inductive portion of the TL segment is maximised whilst the capacitive portion of the TL is suppressed an appreciably large characteristic impedance with a short propagation delay/length is required. In TL segments that are predominantly capacitive or inductive the associated inductance (permeability) and capacitance (permittivity) respectively no matter how minutiae can never actually be equal to zero [25].

An associated inductance or capacitance of zero is consistent with ideal lumped element representations of a capacitor or inductor.

However, from an electromagnetic perspective this is problematic. As this tacitly implies that either the propagation delay/length or characteristic impedance of the TL segment are equal to zero in the case of a capacitor. Similarly, the tacit implication of a propagation delay/length that is equal to zero with an infinite characteristic impedance in the case of an inductor. Either of these eventualities will render the TL segment incapable of sustaining TEM wave propagation (which results in a propagation speed that violates the speed of light) which ultimately means no energy can be extracted from or deposited into either the capacitor or inductor. Now that the TL representation of the capacitor and inductor in the planar LC Resonant tank have been established, the effects due to electromagnetic flow and propagation of the energy flux can be explored.

In [4] and [13] energy propagation and flow in resonant and flyback converters are presented. The representations of the energy propagation graphically depict the flow of energy flux into and out of reactive components essentially speaking to the energy manipulation processes between electric and magnetic energies. These explanations presented are strictly qualitative in nature and in the case of [4] conducted under quasi-static conditions. These findings facilitate and present a more intuitive picture of energy flow and propagation in reactive components and converters. While useful, the next step or evolution in trying to understand more about the internal electromagnetic environment of power modules and reactive components calls for more rigorous qualitative and quantitative descriptions of these energy manipulation processes. A potential avenue to achieving this is by the principle examination of the effect that multiple internal reflections and transmissions that take place at the interfaces or discontinuities have on energy propagation, conversion and flux in reactive components, and thus providing an excellent opportunity for expanding the knowledge base of energy manipulations in reactive components.

2.5.2 Charge Potentials

In [26] Poynting's theorem is reformulated in terms of charge-potentials. The reformulation of the Poynting vector using charge potentials is advantageous for two principal reasons. The first principle benefit is that it simplifies the quantitative analysis and description of electromagnetic power transfer in circuits. The second benefit is that it is closely related to circuit theory and is an acceptable method of analysis in power frequency applications.

The rationale behind the reformulation of the Poynting vector stems from the fact that both the curl ($\nabla \times \mathcal{S}$) and divergence ($\nabla \cdot \mathcal{S}$) of the Poynting vector are not uniquely defined. Leveraging this fact leads to many different energy density and flow vectors [26], [27]. Traditionally the divergence of the Poynting vector is chosen in such a fashion that it conforms to the well-known electric and magnetic energy densities $\frac{1}{2}E \cdot D$ and $\frac{1}{2}H \cdot B$ respectively. However, another equally valid solution to the divergence of the Poynting vector can be obtained by the application of Maxwell's interpretation of *electrokinetic momentum*. Using this fact, the stored magnetic energy can now be expressed as $\frac{1}{2}J \cdot A$ where J is the current density and A the magnetic vector potential. The stored electric energy is expressed as $\frac{1}{2}\rho\Phi$ where ρ is the charge density and Φ is the *electrokinetic potential*. These modifications essentially transform the description of energy densities from field constructs to that of charge-potential constructs. Ultimately using these charge-potential representations or constructs allows the traditional energy flow vector $(\mathcal{S}_f = \vec{E} \times \vec{H})$ based on field theory to be reformulated. The new charge-potential equivalent expression is given by $\mathcal{S}_c = J\phi$.

Experimental evidence by way of the Aharonov-Bohm effect provides credence to the adaptation of charge-potential vectors [28]. The principal difference between charge-potentials and the field-vectors is in the perception of how electromagnetic energy is stored.

Carpenter here drastically and perhaps rather radically challenges the concepts of field theory and provides an alternative modelling paradigm for electromagnetic phenomena. His approaches provide an antithetical view of conductors as more than just passive waveguides as viewed in classical electromagnetic wave propagation theory. In this approach the energy flow and transfer does not take place in the free space around conductors but is rather done by the charge carriers themselves.

A major deterrent to the wide spread adaptation of the charge-potential energy flow vector ($\mathcal{S}_c$) representation is that it is incapable of describing/modelling the transfer of energy in open spaces i.e. the radiation of energies in free space. The more conventional field energy flow vector ($\mathcal{S}_f$) readily provides an explanation for electromagnetic propagation and energy flow in open regions and free space. In order to circumvent the inadequacies of the charge-potential representation it is necessary to develop a hybrid-modelling paradigm in which both field and charge-potentials quantities are utilised, the development of which is detailed in [29]. While this solves the limitation presented initially by the charge-potential representation it is at the cost of increased modelling complexity.

2.5.3 Discussion

In classical electromagnetic literature and theory, it is widely acknowledged that the Poynting vector is capable of accurately describing energy flow and densities in a given surface or region. The Poynting vector however is not unique. Sir J.J. Thomson illustrated this by exploiting the condition that an arbitrary vector could be added provided that the curl of that arbitrary vector is zero (i.e. $P = \nabla \times Q \rightarrow \iint \nabla Q . ds = 0$) [30]. Similarly, research by Slepian in [27] later proved that various other vectors could be used to describe the energy density vector paralleling the work done by Sir J.J Thomson in [30]**.**

Sumpner in [29] postulated that the Poynting vector does not accurately encapsulate all the nuances of energy flow and propagation. Sumpner proposed that perhaps actual energy flow and propagation could be better represented by the propagation of various wave fronts. In viewing the electromagnetic propagation as wave fronts (plane waves in this work) transmission line theory can be readily used to analyse the various energy manipulations in reactive components. The use of transmission line theorems in modelling reactive components is not a new concept as evidenced in the works of [18], [19],[31] and Chapter 2.4 speaks to this. However, what is new is the use of transmission line theory to model energy manipulation interactions that take place in reactive components.

Sumpner argues the fact that when an electromagnetic flux stream interacts at an interface, discontinuity or a boundary with a separate electromagnetic flux stream the interaction generally necessitates that the flux streams are superposed into a singular flux stream. This rationale does not account for the potential fissioning or splitting of the electromagnetic flux stream at the interface or discontinuity of two contacting materials or components. If the reactive components are modelled as TL segments, the effects of varying the propagation delay/length as well as the characteristic impedance will result in multiple internal reflections and transmissions taking place at the interface or discontinuity.

The principle examination of the ramifications of these potential transmission and reflection events i.e. potential fissioning or splitting of the electromagnetic flux streams has the potential to provide increased knowledge and insight into fundamental energy flow, propagation and conversion i.e. energy manipulation processes in reactive components.

2.6 Conclusion

Upon evaluation of the literature in this chapter it is evident that the prevalence of component integration in contemporary power electronic converters is ushering in an era of discrete power modules and integrated electromagnetic processors. This is done in attempts to increase power densities. The ever-increasing power densities mean that components are operating in closer spatial proximity and greater emphasis on the internal electromagnetic structure or environment of current and future power electronic converters is required. In light of this, a paradigm shift focusing on further exploration of fundamental energy conversion, propagation and transfer (i.e. energy manipulation) interactions in reactive components is required. A research opportunity or avenue therefore exists in the exploration of the fundamental energy manipulation interactions in reactive components in order to lay the necessary foundational work for a potential paradigm shift.

From the analysis of electromagnetic energy flow and propagation, it has been identified that the concept of ideal lumped element capacitors and inductors are not possible from an electromagnetic perspective. Further still the use of these lumped elements in modelling fundamental energy manipulations interactions in reactive components has glaring limitations. This is exemplified by the *Twin Capacitor* paradox where analysis using lumped elements and conventional circuit theory renders the system as an energy paradox. Therefore, more fundamental electromagnetic energy modelling paradigms are necessary to further examine the energy manipulation processes in these reactive components.

In order to address these limitations transmission line theory is selected to model the reactive components. Transmission line theory is selected to model the reactive components due to its flexibility in being able to model fundamental electromagnetic concepts such as wave propagation and energy fluxes whilst still being able to interface with higher-level abstractions such as voltages and currents.

Application of transmission line modelling reveals that energy stored or built up in reactive components takes place at the point where the reactive component meets an energy-ferrying device such as a power line, effectively forming an interface or discontinuity. Observation of the energy flux at this point indicates that the energy flux is built up in discretised step intervals.

The discretised nature in which the energy flux builds up is indicative of multiple transmission and reflection effects taking place between the power line and the reactive component until a specified or steady state energy flux density is reached. What is not evident in literature however is in the event that a principle difference in lengths between the two TL segments representing the reactive component and the power line exist what effects will this have on the build-up of energy flux. It is hypothesised that this will cause an effective splitting or fissioning of the propagating TEM waves culminating in additional transmission and reflection effects at an interface or discontinuity.

3 SYSTEM MODELLING

3.1 Overview

The principle aim of this chapter is to provide increased qualitative understanding of the energy manipulation processes in the *Twin Capacitor* and LC Resonant tank topologies. Before this is done an overview of various modelling paradigms in electromagnetics are presented and the applicability of each is briefly discussed. This is followed by a brief overview of fundamental transmission line theory necessary for understanding the TLM method as it pertains to reactive components. The following section details the derivation of TLM Stub and Link-Line models for reactive components. This is subsequently followed by the principle examination of the limitations of current modelling in describing energy manipulation processes in the *Twin Capacitor* and LC Resonant tank topologies. In order to address these limitations, the *Twin Capacitor* and LC Resonant tank topologies are modelled with 1-D TLM Link-Line equivalent models. A potential solution to the *Twin Capacitor* paradox is established providing the necessary affirmation that transmission line modelling does in fact reveal nuances in energy manipulation processes that are not visible with conventional lumped element modelling. The LC Resonant tank is examined next, and whilst this does not present an energy paradox in the traditional sense what is noted is that the mere process of initiating an energy manipulation event between the capacitor and inductor effectively results in sinusoidally bounded pulsating energy being stored in the associated self-inductance and self-capacitance of the capacitor and inductor respectively. Principle conclusions arising are that this bounded pulsating energy essentially facilitates the energy flow into and out of the capacitor and inductor. The preliminary work done in this chapter lays the necessary foundational framework for the results that follow in Chapter 6. In this chapter the propagation delays i.e. lengths of both TL segments are equal. A consequence of this means minimal *Fragmentation* occurs in the system. This is done in efforts to simplify the analysis as what is desired at this stage is a purely qualitative understanding of the fundamental energy manipulation processes with a more detailed quantitative analysis approach due to increased *Fragmentation* in the system following in Chapter 6.

3.2 Electromagnetic Modelling Hierarchy

In electrical engineering and a larger extent electromagnetics, a hierarchy of modelling structures exists. This modelling structure is analogous to Maslow's hierarchy of needs but pertains specifically to the modelling of electrical phenomena. Right at the base of the pyramid we have our foundational phase which are Maxwell's Equations and all accompanying ***Field theory***. At the pinnacle of the hierarchical pyramid are Kirchhoff's laws which are a subset of ***Network theory***. The link between the two levels right in the middle of the hierarchical pyramid is ***Transmission line theory*** [25]. The modelling level in the hierarchical structure selected depends largely on the level of complexity required to solve a specific problem. Common sense would dictate you do not use a sledge hammer to crack a nut and the same is true when it comes to selecting the modelling level in the hierarchy. Network theory is applicable and more than sufficient at lower frequencies. Frequency in this context is with reference to the electrical size of the circuit. At a particular frequency of interest, if the various components (interconnects, capacitors, inductors etc.) electrical size are very much larger than a wavelength, we can use Network theorems such as Kirchhoff's laws quite confidently.

However, if the circuit is electrically large in any singular dimension (limited to any one dimension) then the actual propagation of the various signals can be better represented by the use of a combination of forward and reverse travelling waves. In this instance, transmission line theory becomes more apt. Lastly if the circuit is electrically large in more than just one dimension (i.e. all three dimensions) then the problem should ideally be tackled using Maxwell's equations (Field Theory) [25].

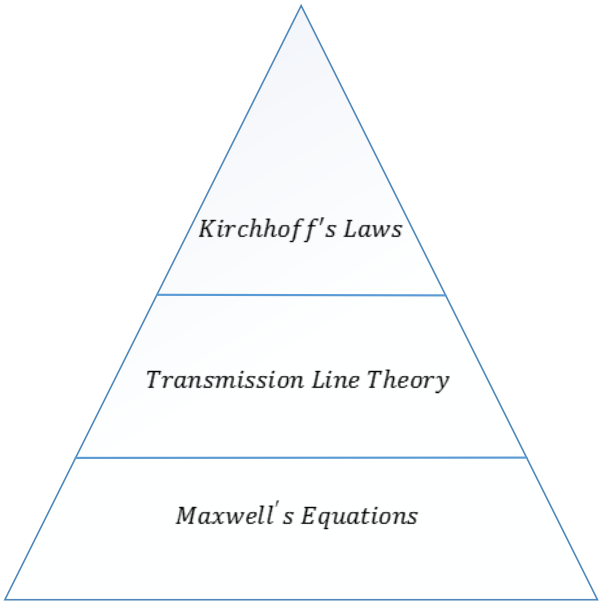


Figure 3-1: Electromagnetic Modelling Hierarchy

3.3 Transmission Line Theory Fundamentals

Central to the Transmission Line Matrix or Transmission Line Modelling method (TLM) is fundamental transmission line theory. Thus, this section provides a brief overview of critical aspects of transmission line theory such as the solution to the Telegrapher's equations. This is necessary as this governs all temporal and spatial interactions between propagating waveforms necessary for determining voltages and currents on the transmission line. These temporal and spatial interactions between propagating waveforms form the necessary foundational basis for the incident and reflected pulses in the 1-D TLM modelling of reactive components as outlined in Chapter 3.4.

3.3.1 Preliminaries

The following preliminaries or assumptions are applicable when deriving the reactive components' distributed parameter and 1-D TLM Link-Line equivalent models:

- Completely lossless TL segments for the Link-Line equivalent model are used.
- The *Twin Capacitor* and LC Resonant networks will be completely devoid of damping i.e. no resistive or dissipative elements are present i.e. $R = 0, G = 0$
- The TL segments are comprised of homogeneous mediums with a velocity factor of unity i.e. $VF = 1$
- All generated waveforms on the TL segments exhibit TEM propagation.
- Spatial discretisation takes place in the same singular dimension of assumed current flow.

3.3.2 Transmission Line Equations

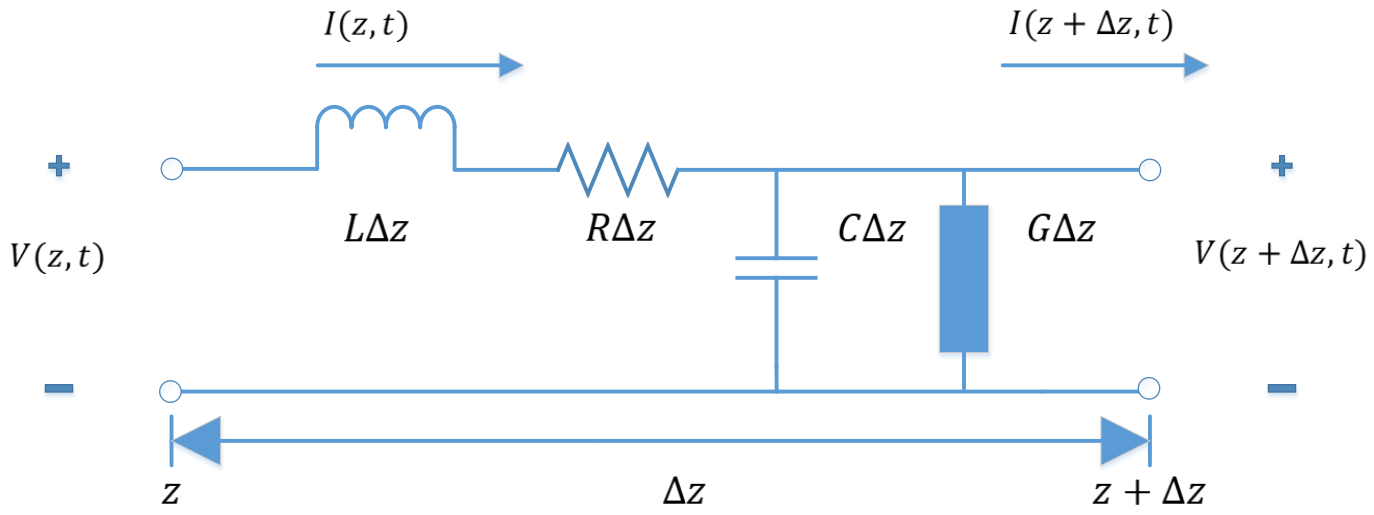


Figure 3-2: Per-Unit Length Distributed Parameter Segment

Analysing the single distributed parameter segment in Figure 3-2 gives rise to the well-known Telegraphers equations. From the solution of the Telegraphers equations the transmission line equations are established. The transmission line equations completely characterise the temporal and spatial interactions of the propagating waveforms on the transmission line. The derivation of the transmission line equations involves the discretization of the distributed segment. This discretization of the distributed parameter segment is in terms of segment length Δz.As a direct result the segment parameter, inductance, capacitance, resistance and conductance are all per-unit length quantities (L, R, C and G respectively). The total value of a specified parameter can be obtained by taking the product of the per-unit quantity and the segment length. For example, the total capacitance for a given segment is $C\Delta z$. As per the preliminaries in section 3.3.1 R and G are both zero, but are included in Figure 3-2 for completeness.

Applying KVL and KCL to the distributed segment gives rise to (3.1a) and (3.1b).

$$V(z+\Delta z,t) - V(z,t) = -L\Delta z \frac{\partial I(z,t)}{\partial t} \tag{3.1a}$$

$$I(z+\Delta z,t) - I(z,t) = -C\Delta z \frac{\partial V(z+\Delta z,t)}{\partial t} \tag{3.1b}$$

In order for this distributed segment to precisely represent a transmission line, the segment length Δz needs to be electrically small. To ensure this for all frequencies the limiting case of an infinitesimally small segment length i.e. $\Delta z \to 0$ is applied [32].

Dividing (3.1a) and (3.1b) by Δz gives rise to

$$\frac{V(z+\Delta z,t) - V(z,t)}{\Delta z} = -L \frac{\partial I(z,t)}{\partial t} \tag{3.2a}$$

$$\frac{I(z+\Delta z,t)-I(z,t)}{\Delta z}=-C\frac{\partial V(z+\Delta z,t)}{\partial t} \tag{3.2b}$$

Applying the limiting condition of an infinitesimally small segmentation length to (3.2a) and (3.2b) gives

$$\lim_{\Delta z\to 0}\frac{V(z+\Delta z,t)-V(z,t)}{\Delta z}=-L\frac{\partial I(z,t)}{\partial t} \tag{3.3a}$$

$$\lim_{\Delta z\to 0}\frac{I(z+\Delta z,t)-I(z,t)}{\Delta z}=-C\frac{\partial V(z+\Delta z,t)}{\partial t} \tag{3.3b}$$

The LHS of equations (3.3a) and (3.3b) are the definition of differentiation by first principles. Using this fact equation (3.3a) and (3.3b) are differentiated to give the transmission line equations

$$\frac{\partial V(z,t)}{\partial z}=-L\frac{\partial I(z,t)}{\partial t} \tag{3.4a}$$

$$\frac{\partial I(z,t)}{\partial z}=-C\frac{\partial V(z,t)}{\partial t} \tag{3.4b}$$

It is worth noting that L and C in equations (3.4a) and (3.4b) are per-unit length quantities. In order to avoid confusion with the total inductance and capacitance values. The per-unit inductance and capacitance quantities are therefore expressed as L_{pu} and C_{pu}. Equations (3.4a) and (3.4b) are thus expressed as

$$\frac{\partial V(z,t)}{\partial z}=-L_{pu}\frac{\partial I(z,t)}{\partial t} \tag{3.5a}$$

$$\frac{\partial I(z,t)}{\partial z}=-C_{pu}\frac{\partial V(z,t)}{\partial t} \tag{3.5b}$$

The general solution to the transmission line equations ((3.5a) and (3.5b)) gives the following

$$V(z,t)=V^{+}f\left(t-\frac{z}{v_p}\right)+V^{-}g\left(t+\frac{z}{v_p}\right) \tag{3.6a}$$

$$I(z,t)=\frac{1}{Z_0}\left[V^{+}f\left(t-\frac{z}{v_p}\right)-V^{-}g\left(t+\frac{z}{v_p}\right)\right] \tag{3.6b}$$

Where Z_0 is the characteristic impedance of the line given by

$$Z_0=\sqrt{\frac{L}{C}} \tag{3.7}$$

The coefficients V^{+} and V^{-} as well as the functions f and g are determined by the initial conditions and boundary conditions on the transmission line. The functions f and g can be completely arbitrary provided they are propagating functions [33]. The function f represents a propagating wave travelling from left to right on the line.

Conversely, the function g represents a propagating wave travelling from right to left on the line. The interaction of these propagating travelling waveforms completely characterises the voltage and current on the transmission line.

3.4 TLM Simulation of Reactive Components

3.4.1 History of TLM Modelling

The TLM method is a temporal and spatial discretisation simulation method designed for the modelling and analysis of electromagnetic phenomena. It is predominantly used as a time-domain simulation method however it has found application in certain frequency domain contexts. The governing principle of the TLM method is based on Huygen's principle of propagation applied to a series of interconnecting transmission lines in a singular dimension (1-D) or applied in a gridded 2-D or 3-D mesh [34]. The mesh of transmission lines effectively discretises the $\vec{E}$ (electric) and $\vec{H}$ (magnetic) fields in space and time, and thus enabling the propagation effects of the electromagnetic phenomena to be effectively studied. Johns starting in 1971 showed that the principles of TLM modelling could be extended to not only solve field problems but lumped element electrical networks as well [35]. This is not surprising considering that lumped element models governed by Kirchoff's circuital laws are a subset of network theory which is essentially a generalisation of transmission line theory as seen in Figure 3-1. Johns continuing his research in 1977 again demonstrated the viability of the TLM discretised models by the simulation of a 7 element Cebyschev filter [36]. Since then numerous authors such as Christopoulos and Hui have extended the application of the TLM modelling technique to analyse SMPS,AC-Drives and various other multi-stage power electronic systems [35], [37]–[39].

3.4.2 TLM Modelling Technique

The application of TLM modelling applied to lumped element networks involves obtaining discrete models for the given system. These discrete models are obtained by replacing the lumped element components in the network with various transmission line segments. In TLM modelling the transmission line segments can either be that of a TLM Stub or TLM Link-Line. Irrespective of the TLM implementation method chosen to model the reactive components, (be it Stub or Link-Line) central to both representations are two prerequisite parameters. These required parameters are the propagation delay (length) and the characteristic impedance. These parameters can be obtained by observing either the geometry of the reactive component for simple geometries or by experimental measurement and observation as seen in [40]. The specific geometry chosen to physically realise the reactive components is inconsequential provided that the propagation delay and characteristic impedance can be determined. The exact geometrical nature becomes important if one wishes to simulate electromagnetically radiating structures such as Horn Antennas and other electromagnetic cavities. In the modelling of reactive components in this work a 1-D TLM model is deemed sufficient. This is because the reactive components are not radiating structures and so the additional granularity afforded in using a 3-D TLM representation will not be explored at this stage. Further credence to the adaptation of the 1-D TLM model is provided by its use in the works of [18], [35], [38], [41] where its application is seen in modelling power electronic converters as well as AC drives. A tacit implication in using the 1-D TLM method is that the presumed current flow and wave propagation in the reactive components predominantly occurs in a singular dimension. Consequently, this means that the spatial discretisation of the reactive components takes place in this singular dimension as well.

Before a detailed implementation on the TLM Stub and Link-Line models is given, a brief discussion of the differences between the TLM and state-space model representations to solving circuit networks are briefly discussed. In the state-space representation a discretised system model is obtained from a continuous system model in order to determine the system states i.e. voltages and currents in the network. In order to solve for the system states various numerical integration techniques are required. The application of these numerical integration techniques adds another layer of discretisation which has the potential to introduce numerical errors as well as stability concerns if the system can be characterised as a stiff network. The TLM modelling approach also obtains a discrete model, however this is based on the modelled physical system [35]. In the TLM technique the voltages and currents are treated as discrete incident and reflected propagating pulses that interact on the transmission line at various time intervals or time-steps, in what can essentially be thought of as time discretised versions of (3.6a) and (3.6b). This feature allows the TLM method to obtain an exact solution to the discrete model without employing numerical integration techniques by merely just examining the interactions between incident and reflected propagating pulses at port interfaces and discontinuities.

3.4.3 Stub Model

In representing the discrete reactive components as TLM Stub models it is possible to emphasise certain properties of the TL segment whilst minimising others. By changing the characteristic impedance and the termination end of the TL segment a capacitor or inductor can be modelled. The basic simulation operation is as follows. An initial incident pulse that is determined from the initial conditions of the circuit or network is launched from the port and propagates down the TLM Stub. The incident pulses in each TLM Stub will take exactly τ seconds or one complete time-step or iteration ($\Delta\tau$ or $k\tau$) until it is incident back at the port [39]. After precisely $\tau/2$ seconds the initial incident pulse contacts the termination end of the Stub. Dependent on whether the termination of the TL Stub is open-circuited (Capacitive Stub) or short-circuited (Inductive Stub) the incident pulse polarity may or may not be inverted. Once back at the initial port this reflected pulse may interact with additional pulses and then subsequently becomes the new incident pulse for the next iteration or time-step in the simulation.

3.4.3.1 Capacitor TLM Stub

The TLM representation of a Capacitive Stub segment is such that it is open circuited at the termination end with a round trip transit-time of τ. This effectively means that the one-way propagation delay down the line is given by $\tau/2$ [39]. This is reminiscent of the propagation delay for the MLC capacitor geometry given by equation (2.4).

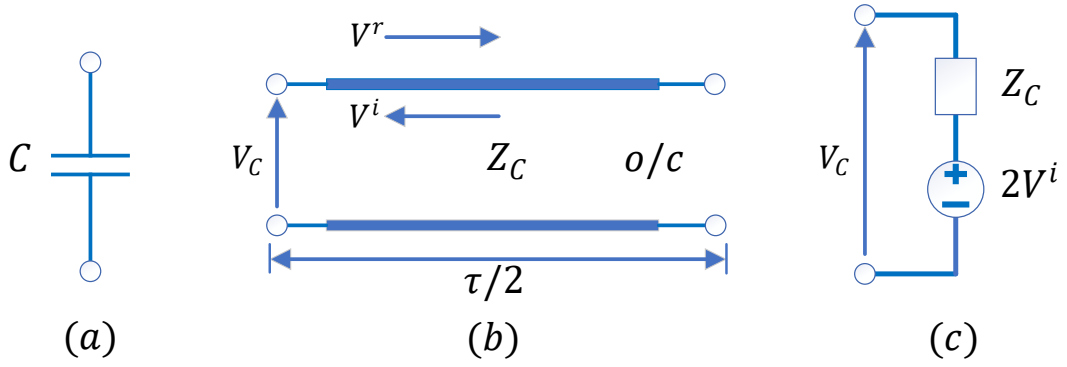


Figure 3-3: Capacitor Models a) Lumped Element b) TLM Stub c) Thevenin Equivalent Circuit

Examining the transmission line Stub model depicted in Figure 3-3b where τ is the round-trip propagation delay of the Stub and Z_C is the characteristic impedance with the associated self-inductance being given by L_e, the expressions for the port voltage (V_C) and current (I_C) can be calculated [25].

The characteristic impedance Z_C of the Capacitive TLM Stub segment is given by

$$Z_C = \frac{\tau/2}{C} = \frac{\tau}{2C} \tag{3.8}$$

The associated self-inductance L_e of the Capacitive TLM Stub is given by:

$$L_e = \frac{\tau}{2} Z_c = \frac{(\tau)^2}{4C} \tag{3.9}$$

The port voltage V_C across the Capacitive Stub is given by

$$V_C = V^i + V^r \tag{3.10}$$

Generalising the port voltage V_C in equation (3.10) for the k^{th} iteration gives the following

$${}_kV_C = {}_kV^r + {}_kV^i \tag{3.11}$$

Alternatively, if the Thevenin equivalent of the TLM Stub is used (Figure 3-3c) the port voltage V_C for the k^{th} iteration is given by

$${}_kV_C = {}_kI_C Z_C + 2\,{}_kV^i \tag{3.12}$$

The current I_C entering or leaving the port is as per equation (3.6b), generalised for the k^{th} time-step or iteration is given by

$${}_k I_C = \frac{1}{Z_C}\left[{}_k V^r - {}_k V^i\right] \tag{3.13}$$

Given that the termination of the capacitive TL Stub is open-circuited, the relationship between the reflected and incident voltage generalised for the $(k+1)^{th}$ iteration is given by

$${}_{k+1}V^i = {}_kV^r \tag{3.14}$$

Combining equations (3.13) and (3.14) ultimately gives the port current I_C generalised for the $(k+1)^{th}$ iteration

$${}_{k+1} I_C = \frac{1}{Z_C}\,{}_{k+1}V_C - \frac{2}{Z_C}\,{}_kV^r \tag{3.15}$$

Simplification of equation (3.15) by way of the expression for the current given in equation (3.13) yields the following

$${}_{k+1} I_C = \frac{1}{Z_C}\,{}_{k+1}V_C - \left(\frac{1}{Z_C}\,{}_kV_C + {}_kI_C\right) \tag{3.16}$$

If Z_C is substituted into equation (3.16) it gives the identical expression to the solution produced by the trapezoidal numerical integration method of a discrete model capacitor as seen in [42],[43]. The trapezoidal numerical integration algorithm is a popular means of solving for transient currents and voltages in reactive components in a simulated environment.

This is evident by its prevalence in various popular circuit simulators such as SPICE, MultiSim, Falstadt and EMPT [43]. The advantage of the TLM method is that it is capable of reaching the correct answer without employing numerical integration techniques explicit or implicit. This means that the solutions that the TLM method produces are always unconditionally stable and the TLM method is incapable of introducing instabilities into other portions of the network [35].

3.4.3.2 Inductor TLM Stub

Similarly, the TLM Stub representation of an inductor is given by emphasising the inductive aspects of the transmission line whilst minimising the capacitive aspects. This is achieved by a TL segment with a high characteristic impedance, short propagation delay and short-circuit termination. The TLM Stub representation of an inductor is effectively the dual of the Capacitive Stub representation. The principle difference in the Inductive Stub representation is that unlike the Capacitive Stub it is terminated by a short-circuit instead of an open-circuit [25].

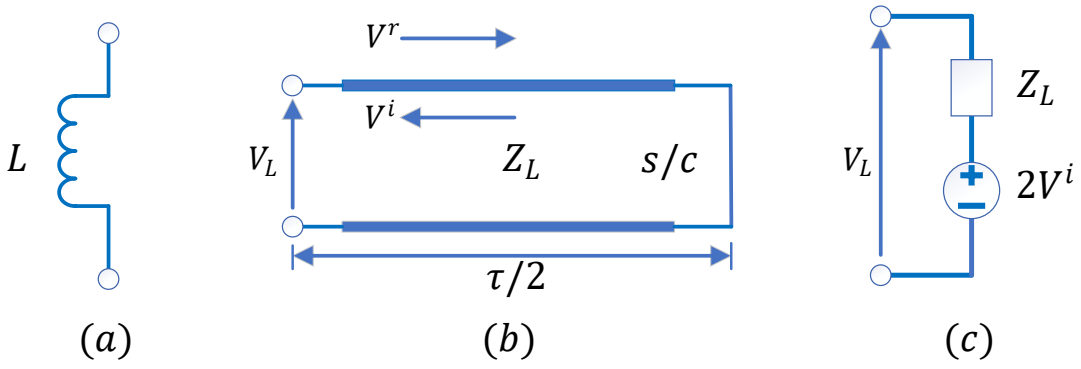


Figure 3-4: Inductor Models a) Lumped Element b) TLM Stub c) Thevenin Equivalent Circuit

Observing the inductive transmission line Stub model given in Figure 3-4b where τ is the round-trip propagation delay and Z_L is the characteristic impedance. The expressions for the port voltage and current (V_L and I_L respectively) can be determined. However, expressions for the characteristic impedance Z_L and self-capacitance C_e are first given.

The characteristic impedance Z_L of the Inductive TLM Stub is given by the following equation.

$$Z_L = \frac{2L}{\tau} \tag{3.17}$$

The associated self-capacitance C_e of the Inductive TLM Stub is given by

$$C_e = \frac{(\tau)^2}{4L} \tag{3.18}$$

The port voltage V_L across the Inductive Stub is given by

$$V_L = V^i + V^r \tag{3.19}$$

Similar to the generalisation for the port voltage (V_C) of the capacitive stub ((3.11)), the generalised inductor port voltage V_L for the k^{th} iteration is given by

$${}_kV_L = {}_kV^r + {}_kV^i \tag{3.20}$$

Using the Thevenin equivalent of the Inductive TLM Stub seen in Figure 3-4c an alternative expression for the port voltage V_L for the k^{th} iteration is given by

$${}_kV_L = {}_kI_LZ_L + 2\,{}_kV^i \tag{3.21}$$

Generalising the port current I_L for the k^{th} iteration or time-step is similar to equation (3.15), however since the termination in the Inductive Stub is short-circuited, the relationship between the reflected and incident voltage is always inverted.

Generalising this relationship for the $(k+1)^{th}$ iteration gives rise to the following

$${}_{k+1}V^i = -\,{}_kV^r \tag{3.22}$$

Since the Inductive Stub is essentially the dual of the Capacitive Stub, this means that the generalised expression for the $(k+1)^{th}$ iteration for the respective port currents will be almost identical. The difference is that the coefficient of the ${}_kV^r$ term is inverted as per equation (3.22).

The generalised port current I_L for the $(k+1)^{th}$ iteration is therefore ultimately expressed as

$${}_{k+1}I_L = \frac{1}{Z_L}\,{}_{k+1}V_L + \frac{2}{Z_L}\,{}_kV^r \tag{3.23}$$

Simplification of equation (3.23) gives an alternative expression of the generalised port current I_L as seen in equation (3.24).

$${}_{k+1}I_L = \frac{1}{Z_L}\,{}_{k+1}V_L + \frac{1}{Z_L}\,{}_kV_L + {}_kI_L \tag{3.24}$$

Equation (3.24) is identical to the solution produced by trapezoidal numerical integration of the discrete inductor model seen in [43],[44].

It is worth noting that a simplifying assumption made by most TLM simulations is that model synchronism is enforced. Model synchronism ensures that the propagation delays(lengths) of the respective TLM segments (Stub or Link-Line) for all the reactive components being modelled in the network are identical [25]. This effectively means that the incident and reflective pulses contact their respective terminals simultaneously in a predictable and consistent manner in every simulation iteration. This means that complex recombination effects can be neglected and only the pulses immediately to the left or right of each TL segment discontinuity or node are considered [25]. In this configuration the next incident pulse for a successive or proceeding time step or iteration is only ever given by the interaction of the same travelling pulses in a consistent manner.

This essentially represents the simplest case of *Fragmentation* generation where the lengths of the TL segments are identical. In such a case minimal *Fragmentation* will occur. In Chapter 4 various cases/instances where the propagation delays of the TL segments are not ideally matched are explored and various *Fragmentation* generation cases are identified.

3.4.4 Link-Line Model

The TLM Link-Line equivalent models of either capacitors or inductors are TL line segments that are open at both ends [25]. The ends of the TL segments represent the nodes or the terminals of the TL segment. The ports or nodes (terminals) of a Link-Line model can connect to either a load or successive Link-Line or Stub models effectively forming cascaded or linked TL chains. The true power of this Linked-Line representation is that a complex circuit can be broken up into various smaller sub-circuits with the various sub-circuits being decoupled from each other. This decoupled nature can now be leveraged to effectively simulate the sub-circuits in isolation. An additional benefit is that Link-Line modelling can isolate non-linear elements from the rest of the linear elements in a network. For example, a network containing *N* non-linear elements and hence equations can be solved in terms of *N* individual and isolated non-linear equations instead of *N* coupled linear and non-linear equations as in the hybrid formulation of the state-space equations. An additional benefit of the decoupled nature afforded by TLM Link-Line models is that various parallel computing algorithms to further increase computational speed and efficiency can be utilised as seen in [45].

In order to successfully implement the TLM Link-Line model much like the TLM Stub model the characteristic impedance and propagation delay are requisite parameters. However, where the TLM Link-Line model differs from the TLM Stub model is that the TLM Stub models are generalised one-port devices that can be used as direct replacements for reactive components with limited or non-existent linking capabilities. The Link-Line models however are two-port models that not only can be used to represent reactive components but can also be used as fundamental building blocks/units for linking multi-stage circuit models. In [39] the decoupling capabilities of TLM Link-Lines are highlighted by the simulation of various multi-stage power converters.

In developing the TLM Link-Line models the geometry used as a case study is the parallel LC Resonant tank as seen in Figure 2-5. However as stated prior, other geometrical representation may be used for the reactive components, and so the forthcoming derivations are generic and not dependent on the geometry.

3.4.4.1 Inductor TLM Link-Line

Figure 3-5 illustrates the Link-Line equivalent model of a series inductor L.The propagation delay of the TL segment is given by τ whilst the characteristic impedance of the line is given by Z_L. If the parallel planar LC Resonant geometry is assumed, equation (2.9) can be used to calculate Z_L.

The characteristic impedance Z_L of the inductive Link-Line in terms of the inductance and self-capacitance is given by

$$Z_L = \sqrt{\frac{L}{C_e}} \tag{3.25}$$

An inductive Link-Line TL segment exhibits a characteristic impedance that is appreciably large. In the limiting case where the propagation delay or time step is infinitesimally small the TL segment approximates an ideal inductor $Z_B \to \infty$.

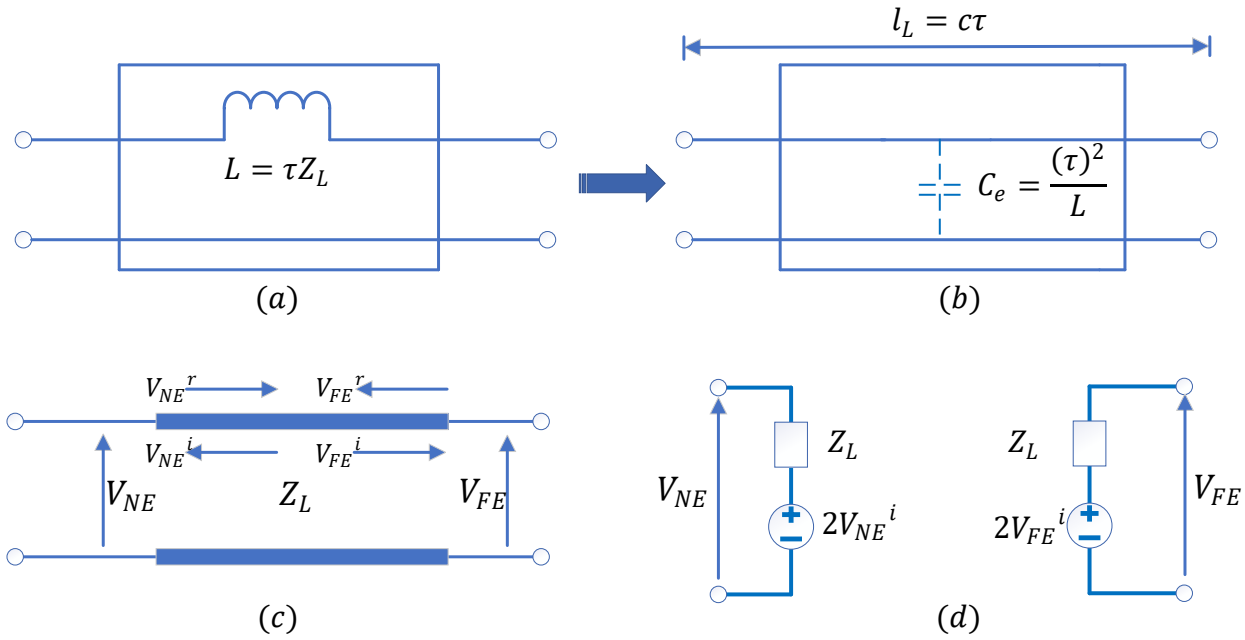


Figure 3-5: Series Inductor Models a) Lumped Element b) Self-Capacitance c) Link-Line d) Thevenin Equivalent

This ideal inductor however is not electromagnetically realisable as explained in Chapter 2.5. A detailed derivation of equations (3.26) to (3.28) are presented in [25] and for brevity will briefly be restated here.

The series inductance L in terms of the TL segment parameters is given by

$$L = \tau Z_L. \tag{3.26}$$

The self-capacitance C_e is represented by the shunt capacitor between line segments in Figure 3-5b and is given by the following:

$$C_e = \frac{(\tau)^2}{L} \equiv \frac{\tau}{Z_L} \tag{3.27}$$

The propagation velocity v_p of the pulses on the inductive Link-Line TL segment is given by

$$v_p = \frac{l_L}{\sqrt{LC_e}} \equiv c. \tag{3.28}$$

Where c represents the speed of light. The propagation velocity exhibits an ideal velocity factor as per the assumptions stated in Chapter 1.4. Now that the prerequisite transmission line parameters given in equations (3.26) to (3.28) have been defined the port and current voltages in the Link-Line model can be determined. The generalised current expression at the Near-End (*NE)* terminals I_{NE} (i.e. the left most port terminals of the Link-Line) for the k^{th} iteration or time-step is given by

$$_kI_{NE} = \frac{1}{Z_L}\left[\,_kV_{NE}{}^r - \,_kV_{NE}{}^i\,\right] \tag{3.29}$$

Observing Figure 3-5c (Link-Line model) and Figure 3-5d (Thevenin equivalent model) the port voltages at the *NE* terminals V_{NE} generalised for the k^{th} iteration or time-step are given by

$$ {}_kV_{NE} = {}_kV_{NE}{}^r + {}_kV_{NE}{}^i \quad (3.30a)$$

$$ {}_kV_{NE} = {}_kI_{NE}Z_L + 2_kV_{NE}{}^i \quad (3.30b)$$

The generalised current expression at I_{FE} at the Far-End (*FE)* terminals (i.e. the right-most port terminals on the Link-Line) for the k^{th} iteration or time-step is given by

$$ {}_kI_{FE} = \frac{1}{Z_L}\left[{}_kV_{FE}{}^r - {}_kV_{FE}{}^i \right] \quad (3.31)$$

Similarly, expressions for the port voltage V_{FE} at the *FE* terminals for the Link-Line and Thevenin equivalent models generalised for the k^{th} iteration or time-step are given by

$$ {}_kV_{FE} = {}_kV_{NE}{}^r + {}_kV_{NE}{}^i \quad (3.32a)$$

$$ {}_kV_{FE} = {}_kI_{FE}Z_L + 2_kV_{FE}{}^i \quad (3.32b)$$

Looking at Figure 3-5c it appears that the *NE* and *FE* Link-Line terminals are connected together and hence should always produce identical voltage and current expressions. However, subject to the boundary conditions or terminations at the *NE* and *FE* terminals the developed voltages and currents may differ.

The consequence of various boundary conditions at the *NE* and *FE* terminals can be expressed in terms of the reflection coefficients Γ_{NE} and Γ_{FE} at the *NE* and *FE* terminals respectively. The reflection coefficients Γ_{NE} and Γ_{FE} are given by (3.33) and (3.34) where Z_{NE} and Z_{FE} are the equivalent impedances seen at the *NE* and *FE* terminals.

$$ \Gamma_{NE} = \frac{Z_L - Z_{NE}}{Z_L + Z_{NE}} \quad (3.33)$$

$$ \Gamma_{FE} = \frac{Z_L - Z_{FE}}{Z_L + Z_{NE}} \quad (3.34)$$

Using equations (3.33) and (3.34) the relationship between the incident and reflected pulses at the *NE* and *FE* terminals for the generalised $(k+1)^{th}$ iteration or time-step can be calculated. The generalised incident pulse voltages at the *NE* and *FE* terminals are given by equation (3.35) and equation (3.36).

$$ {}_{k+1}V_{NE}{}^i = \Gamma_{FE}{}_kV_{FE}{}^r \quad (3.35)$$

$$ {}_{k+1}V_{FE}{}^i = \Gamma_{NE}{}_kV_{NE}{}^r \quad (3.36)$$

The voltage and current expressions for the *NE* and *FE* port terminals generalised for the $(k+1)^{th}$ iteration or time-step are ultimately as follows

$$ {}_{k+1}\,V_{NE} = {}_{k+1}V_{NE}{}^r + \Gamma_{FE}{}_kV_{FE}{}^r \quad (3.37)$$

$$ {}_{k+1}\,V_{FE} = {}_{k+1}V_{FE}{}^r + \Gamma_{NE}{}_kV_{NE}{}^r \quad (3.38)$$

$$ {}_{k+1}I_{NE} = \frac{1}{Z_L}\left[{}_{k+1}V_{NE}{}^{r} - \left(\Gamma_{FE_k} V_{FE}{}^{r} \right) \right] \tag{3.39} $$

$$ {}_{k+1}I_{FE} = \frac{1}{Z_L}\left[{}_{k+1}V_{FE}{}^{r} - \left(\Gamma_{NE_k} V_{NE}{}^{r} \right) \right] \tag{3.40} $$

3.4.4.2 Capacitor TLM Link-Line

Figure 3-6a and Figure 3-6b depicts the Link-Line equivalent model of a shunt capacitor C and its accompanying self-inductance L_e.The characteristic impedance is given by Z_C and the propagation delay down the TL segment is τ. If the geometry assumed for the capacitor is that of the parallel planar LC Resonant structure, equation (2.9) can be used to determine the characteristic impedance Z_C and equation (2.17) can be used to determine the propagation delay τ.

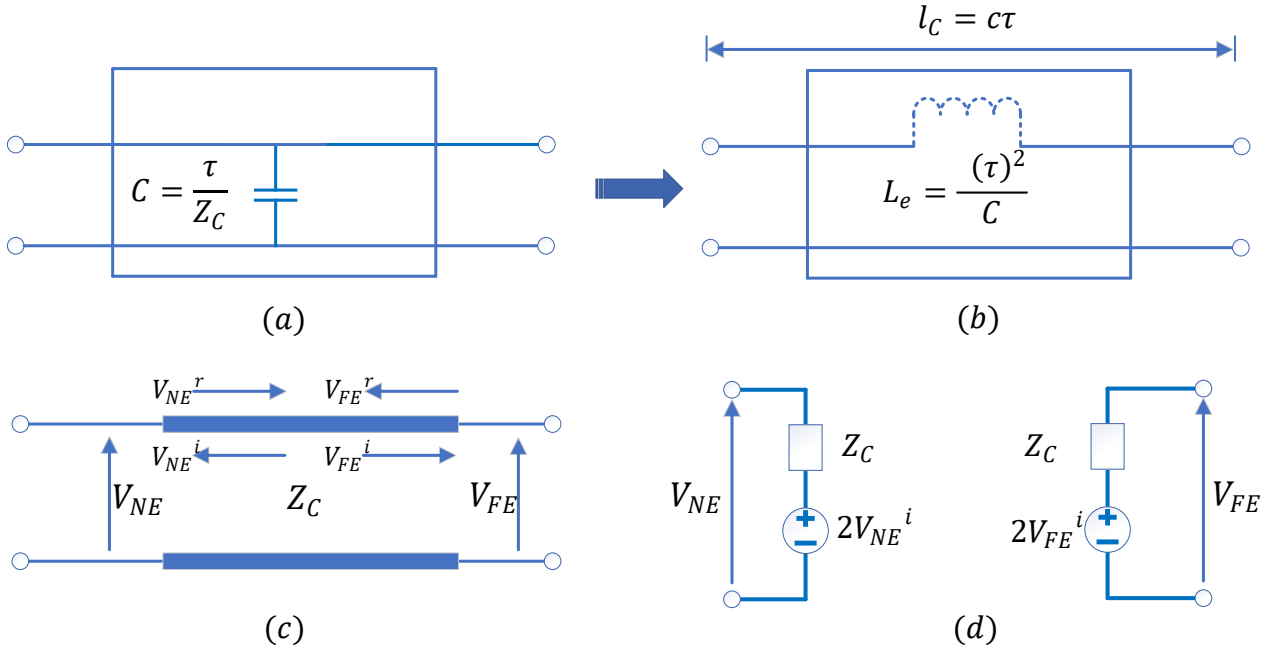


Figure 3-6: Shunt Capacitor Models a) Lumped Element b) Self-Inductance c) Link-Line d) Thevenin Equivalent

Alternatively, the characteristic impedance Z_C of the Capacitive Link-Line in terms of the self-inductance and the capacitance is given by the following

$$ Z_C = \sqrt{\frac{L_e}{C}} \tag{3.41} $$

A Capacitive Link-Line exhibits a low characteristic impedance. In the limiting case where the propagation delay or time-step is infinitesimally small, the TL segment approximates an ideal capacitor $Z_C \to 0$. As seen in Chapter 2.5 this is not realisable from an electromagnetic perspective. Similarly, the propagation velocity v_p is identical to equation (3.28) with L_e,C and l_C replacing L,C_e and l_L respectively.

The shunt capacitance in terms of TL segment parameters is given by

$$C = \frac{\tau}{Z_C} \tag{3.42}$$

The self-inductance is given by the following expression:

$$L_e = \frac{(\tau)^2}{C} \equiv \tau Z_C \tag{3.43}$$

The generalised voltage expressions (equation (3.30a) and (3.32a) as well as equations (3.35)-(3.38)) for the *NE* and *FE* terminals in the Capacitive and Inductive Link-Line model representation are identical, and thus will not be restated for brevity. The generalised current expressions for the Capacitive Link-Line model can be calculated using equations (3.39)-(3.40) by merely just interchanging Z_L with Z_C. Similarly, by interchanging Z_L with Z_C in equations (3.30b) and (3.32b) using the Thevenin equivalent model the generalised voltage expressions at the *NE* and *FE* terminals can be calculated.

3.4.5 Decoupling Systems Using TLM Link-Lines

TLM Link-Line models of series inductors and shunt capacitors can be used to effectively decouple systems from one another. The manner in which this decoupling is achieved is illustrated by two generic systems *A* and *B* as seen in Figure 3-7 [39]. Considering system *A* in Figure 3-7a, irrespective of the termination at the *FE* terminals (system *B's* terminals) of the Link-Line, the characteristic impedance seen (looking from the right hand side) will be Z_0. Similarly, for system *B* Figure 3-7a, irrespective of the termination at the *NE* terminals (system *A's* terminals) the characteristic impedance seen (looking from the left-hand side) will also be Z_0. From these observations it can be surmised that as far as systems *A* and *B* are concerned they are in essence connected to the Thevenin equivalent branches given at the *NE* and *FE* terminals as illustrated in Figure 3-7b [39].

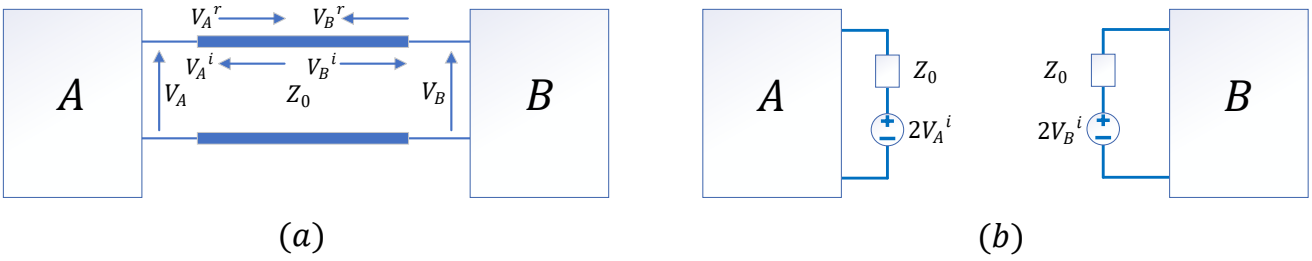


Figure 3-7: Decoupled Systems via a) Link-Line model b) Thevenin Equivalent model (Adapted from [39])

The Link-Line model depicted in Figure 3-7a is generic as evidenced by the characteristic impedance denoted Z_0. If $Z_0 = Z_C$ the Link-Line represents a shunt capacitor. However, if $Z_0 = Z_L$ the Link-Line represents a series inductor.

The port voltages and currents seen at both system *A's* and system *B's* terminals in both Link-line and Thevenin equivalent models can be calculated using equations (3.30b),(3.32b) and (3.37)-(3.40) where $V_{NE} \equiv V_A$ and $V_{FE} \equiv V_B$.

Considering system *A* for a moment, at each k^{th} simulation iteration or time-step the incident pulse ${}_kV_A{}^i$ (determined from initial conditions of the systems) contacts the arbitrary system *A*. The incident pulse is then reflected due to the interaction with system *A* and the reflected pulse ${}_kV_A{}^r$ is formed. This reflected pulse ${}_kV_A{}^r$ takes τ seconds or one iteration to propagate along the Link-Line and effectively become the incident pulse ${}_{k+1}V_B{}^i$ on system *B*'s terminals for the next k^{th} iteration or time-step [39].

Similarly, considering system *B* for the k^{th} iteration or time-step, the incident pulse ${}_kV_B{}^i$ is incident on system *B's* terminals. From this interaction ${}_kV_B{}^i$ is reflected and ${}_kV_B{}^r$ is formed. Again, it will take precisely τ seconds or one iteration for the reflected pulse to contact system *A's* terminals giving rise to ${}_{k+1}V_A{}^i$,which is the incident pulse for the next k^{th} iteration or time-step [39]. From these processes it can be surmised that the interactions of the linked systems (systems *A* and *B* respectively) are completely characterised by the reflected and incident pulses on the TLM Link-Line whilst simultaneously decoupling the two systems [39].

3.4.5.1 Switched Mode Power Supply

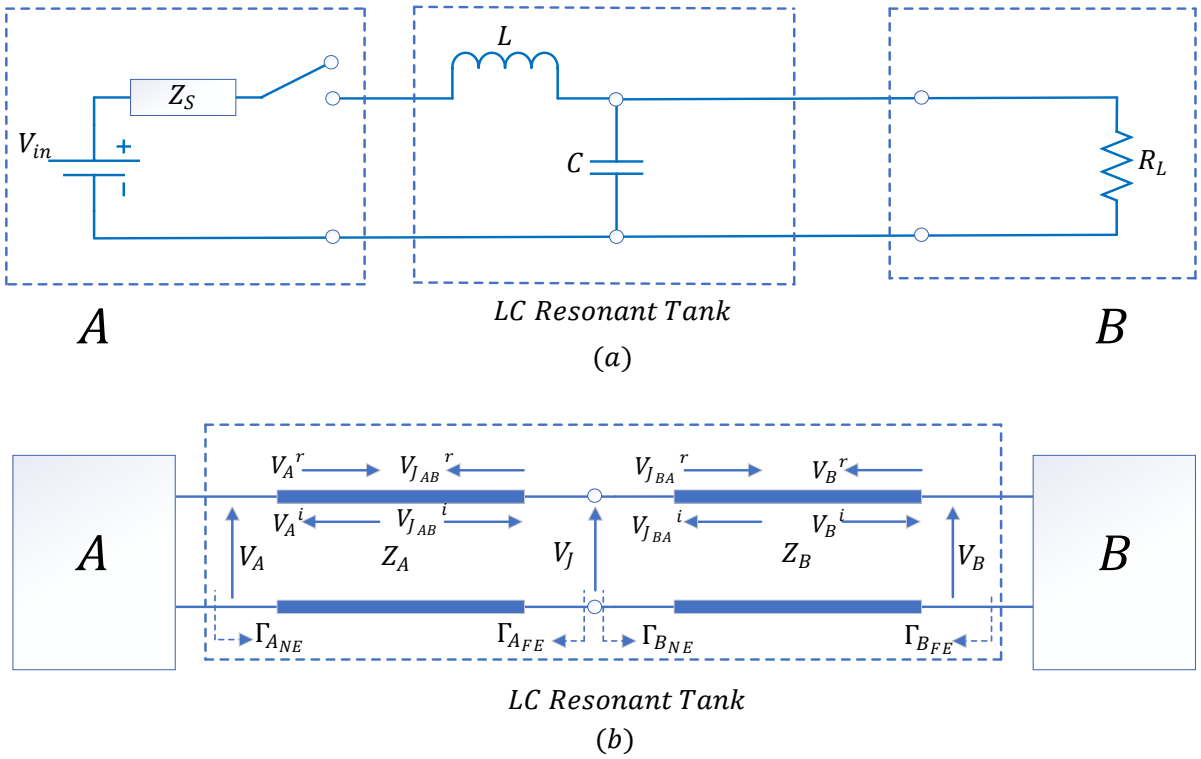


Figure 3-8: SMPS Converter System a) Coupled System b) Decoupled System

Figure 3-8 depicts a simple SMPS converter system. As seen in Figure 3-8a the input subsystem of the SMPS is given by system *A*. System *A* is comprised of a voltage source V_{in}, the impedance of the source Z_S and lastly an ideal switch. Similarly, the output subsystem is given by system *B*, contains only the output load resistor R_L. Systems *A* and *B* along with the cascaded TLM Link-Line segments (Line A and Line B) forming the LC Resonant tank effectively combine to form an ideal Buck-Converter SMPS.

In keeping in line with a principle aim of the research,studying the electric to magnetic energy manipulations (as explained in Chapter 1.2.2) requires the examination of the LC Resonant tank topology in isolation. The LC Resonant tank topology can be simulated in isolation, essentially decoupling it from system *A* and system *B* provided that the reactive components (L and C) are modelled with TLM Link-Line equivalent models [39].

The LC Resonant tank will be examined for one *Fragmentation initiation* event and in the presence of no loss. The consequences of the solitary switching or *Fragmentation initiation* event mean that only a single origin incident pulse (V_i) will be generated from system *A*. This is done in efforts to reduce complexity in the system due to multiple incident pulses being generated by system *A* due to multiple switching or *Fragmentation initiation* events. The results and insight gained from examining a solitary *Fragmentation initiation* event will form the necessary foundational framework for studying multiple switching or *Fragmentation initiation* events in future. Any results gained from examining the energy manipulations in the LC Resonant tank in isolation can later be integrated back into the SMPS depicted in Figure 3-8 or any other topology or application where an inductor and capacitor are interconnected, by merely just adjusting $\Gamma_{A_{NE}}$ and $\Gamma_{B_{FE}}$ in accordance with the boundary conditions established at the *NE* and *FE* port terminals of Line A and Line B respectively. The reflection coefficients $\Gamma_{A_{NE}}$ and $\Gamma_{B_{FE}}$ are defined as follows.

$$\Gamma_{A_{NE}} = \frac{Z_A - Z_S}{Z_A + Z_S} \tag{3.44}$$

$$\Gamma_{B_{FE}} = \frac{Z_B - R_L}{Z_B + R_L} \tag{3.45}$$

The generalised port voltages and currents for Line A i.e. the inductive line ($Z_A \equiv Z_L$) are given by equations (3.37) to (3.40) where $V_{NE} \equiv V_A; V_{FE} \equiv V_{JAB}$ and $\Gamma_{A_{FE}} \equiv \Gamma_{AB} = \frac{Z_B - Z_A}{Z_B + Z_A}$. Similarly, the generalised port voltages and currents for Line B i.e. the capacitive line ($Z_B = Z_C$) are again also given by equations (3.37) to (3.40) where $V_{FE} \equiv V_B; V_{NE} \equiv V_{JBA}$ and $\Gamma_{B_{NE}} \equiv \Gamma_{BA} = -\Gamma_{AB} = \frac{Z_A - Z_B}{Z_B + Z_A}$. The voltage at the junction or discontinuity V_J where Line A meets Line B is calculated from equation (3.46a) or equation (3.46b).

$$_kV_J = {}_kV_{JAB}{}^r + {}_kV_{JAB}{}^i \tag{3.46a}$$

$$_kV_J = {}_kV_{JBA}{}^r + {}_kV_{JBA}{}^i \tag{3.46b}$$

3.4.5.2 Switched Capacitor Converter

Figure 3-9 depicts a simple a SCC. Similar to the SMPS the input (system *A*), *Twin Capacitor* topology and output (system *B*) subsystems can all be decoupled from one another if C_A and C_B are modelled with Link-Line equivalent models. In decoupling the three subsystems the fundamental electric to electric energy manipulation interactions can be examined.

Since the energy manipulations between C_A and C_B being considered are due to a solitary *Fragmentation initiation* event the continuous switching of the capacitors is not modelled. Even though the results obtained in this research are due to the *Twin Capacitor* topology in isolation, they can readily be integrated into the SCC or any other topology where the direct interconnection of two capacitors occurs.

This can be achieved by altering $\Gamma_{A_{NE}}$ and $\Gamma_{B_{FE}}$ to reflect the changes in boundary conditions caused by arbitrary systems connecting to the *NE* and *FE* terminals of Line A and B respectively. Thus, effectively altering the incident and reflected pulses on Line A and Line B which are used to calculate the new voltages and currents in the system.

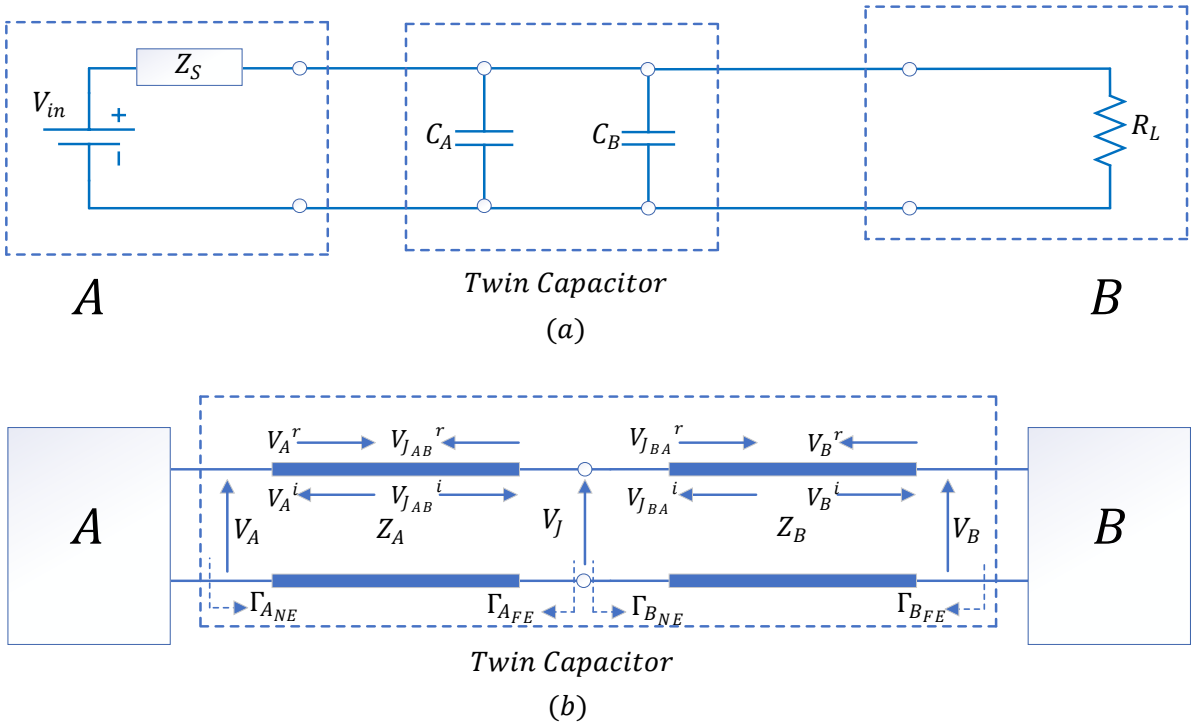


Figure 3-9: Switched Capacitor Converter System a) Coupled System b) Decoupled System

Similar to the SMPS case the port voltages and currents for both Line A (C_A i.e. $Z_A = Z_{C_A}$) and Line B (C_B i.e. $Z_B = Z_{C_B}$) can be calculated from equations (3.37) to (3.40) by interchanging $V_{NE} \equiv V_A; V_{FE} \equiv V_{JAB}$ and $\Gamma_{A_{FE}} \equiv \Gamma_{AB}$ for C_A and $V_{FE} \equiv V_B; V_{NE} \equiv V_{JBA}$ and $\Gamma_{B_{NE}} \equiv \Gamma_{BA} = -\Gamma_{AB}$ for C_B.

The traditional TLM modelling of lumped element networks is concerned with assessing the temporal nature of the voltages and currents at the TL port terminals after various time-steps or iterations. In only examining the voltages and currents at the ports exclusively, the spatial-discretisation aspects of the TL segments are left unexplored. Exploring the spatial voltage and current interactions is necessary because unlike what is assumed by conventional circuit theory the instantaneous voltage and current may not be uniform at every point on the TL segments i.e. reactive elements. The temporal and spatial nature of the propagating voltage and current waveforms are explored in the proceeding section, in the *Twin Capacitor* and LC Resonant tank topologies. This is necessary in order to examine the total energy stored on the TL segments and hence examine the qualitative nature of the energy manipulation processes in reactive components.

3.5 Limitations of Current Modelling

Circuit theory although a very useful method of analysing a plethora of topologies and configurations. However, is limiting when it comes to modelling energy manipulations and interactions in reactive components. A distributed parameter or TL Link-Line model reveals nuances and insight into these processes that is absent from circuit theory. This is exemplified in two scenarios. The first scenario is the case of the classical *Twin Capacitor* energy paradox. This exemplifies the energy manipulations of electric to electric energies that take place between two capacitive energy stores. The second scenario is the ubiquitous LC Resonant tank where electrical and magnetic energies oscillate in SHM in the absence of damping. This exemplifies the energy manipulations of electric to magnetic energies and vice versa between capacitive and inductive energy stores.

3.5.1 Twin Capacitor Paradox

The *Twin Capacitor* paradox as first detailed in Chapter 2.4 exemplifies the fundamental electric to electric energy manipulations between in capacitive energy stores. This section explores the paradox in more detail and quantifies how much "*Missing Energy"* occurs in the system for arbitrary capacitances values of C_A and C_B. The analysis that follows will be focused on the energies in both capacitors before and after the system has reached equilibrium. In so doing the development towards a potential explanation for the "*Missing Energy"* or *perceived* energy loss in the system will be carried out [16]. This ultimately facilitates increased insight into the nuances of the energy manipulation processes that typify the transfer and conversion of electrical energy between capacitive energy stores.

The *Twin Capacitor* paradox involves the transfer of electrical energy from an initially charged capacitor C_A to a discharged capacitor C_B. The conductors joining C_A to C_B are ideal (i.e. $R = 0$) and hence the system is completely lossless. The energy interactions in the system are considered paradoxical because even though the system is completely lossless a *perceived* energy loss is observed. This *perceived* energy loss is commonly referred to as *"Missing Energy"* [16]. This occurs when the initially charged capacitor exchanges energy with the discharged capacitor.

Assuming C_A is initially charged to a rated voltage V_0. The electric energy stored in C_A denoted U_{EA} effectively represents the initial energy in the system U_0.

The initially stored system energy U_0 is given by

$$U_0 = U_{EA} = \frac{1}{2} C_A {V_0}^2 \tag{3.47}$$

Once C_A is connected to the discharged capacitor C_B,intuitively we expect the system to reach equilibrium when the associated voltages across both C_A and C_B are half the initial or charge voltage i.e. $\frac{V_0}{2}$. At this point we expect to have zero current flowing in the system. If $C_A = C_B$ and the voltage is distributed evenly amongst both capacitors we expect that the energy in the system will be distributed evenly amongst both capacitors U_{EA} and U_{EB} respectively. It is expected that summing the associated energies of the two capacitors will equate to the initial system energy i.e. $U_0 = U_{EA} + U_{EB}$.

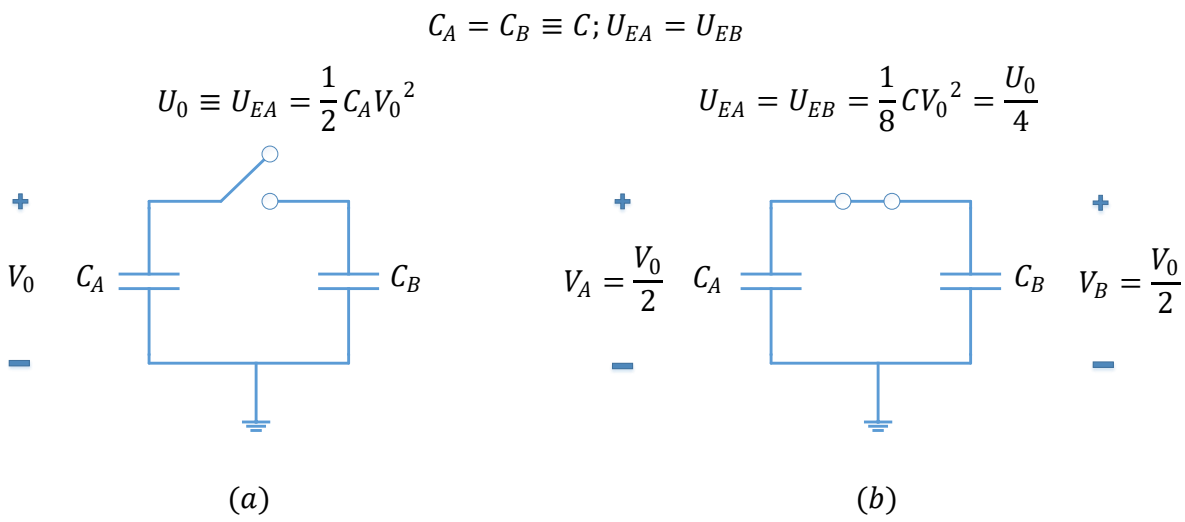


Figure 3-10: Twin Capacitor Paradox a) Initial Charged State b) Equilibrium State

However, this is not the case as the energy stored by each capacitor is a quarter of the initial system energy as illustrated in Figure 3-10. Upon summing the electrical energies in both capacitors, it appears as though the system has lost energy.

$$U_{EA} + U_{EB} = 2\left(\frac{1}{8} C {V_0}^2\right) = \frac{1}{4} C {V_0}^2 = \frac{U_0}{2} \neq U_0$$

The *perceived* energy loss experienced by the system is exactly half the initial system energy i.e. $\frac{U_0}{2}$. The *"Missing Energy"* that the system experiences for an arbitrary selection of C_A and C_B is quantified by equation (3.48) [16].

$$\Delta U = \frac{U_0 C_B}{C_A + C_B} \tag{3.48}$$

The *"Missing Energy"* in the system highlights the deficiencies of conventional circuit theory in modelling energy manipulation processes. In a lossless system there can be no dissipation or loss of energy i.e. energy must remain constant for all time. It is thus necessary to use an alternative modelling paradigm to solve the paradox. If C_A and C_B are both represented with their Link-Line equivalent models a solution to the energy paradox is found. The *Twin Capacitor* paradox will be explored in the classical case where $C_A = C_B$. Consequently, this means the Link-Line equivalent models are identical and all corresponding TL parameters are equal. A repercussion of both Link-Line TL segments having identical lengths i.e. $l_A = l_B$ means that minimal *Fragmentation* takes place on the respective lines. This is done in efforts to simplify the interactions between propagating waves on the respective TL segments. The effects of varying propagation delays (lengths) leads to various *Fragmentation* generation cases that are detailed in Chapter 4.

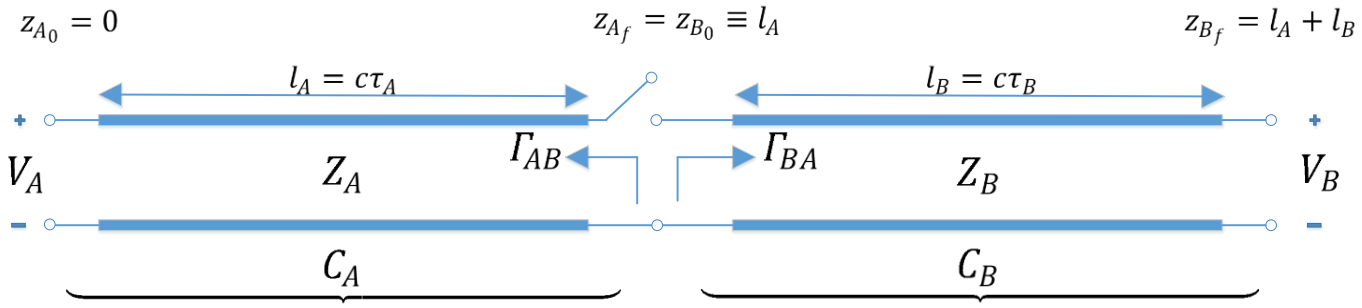


Figure 3-11: Twin Capacitor Link-Line Equivalent Model (Switch Open)

The cascaded Link-Line equivalent model of the *Twin Capacitor* topology is depicted in Figure 3-11. The specified dimensions l_A and l_B effectively represent the height dimension if the MLC geometry for the capacitors is to be assumed as seen in Figure 2-2. The height dimension is thus the dimension which will be spatially discretised. Line A is initially charged by an external DC source (not shown) to the rated voltage V_0. The open-circuit boundary conditions established at z_{A_0}(Line A's Near-End terminals) and z_{A_f}(Line A's Far-End terminals) ensure that the incident and reflected coefficients V^+ and V^- given in (3.6a) are equal. Consequently, this produces a static (steady state) voltage on Line A ($v_A(z,t)$) that is equal to the charge voltage. The voltage present everywhere in space on Line A before closing the junction switch at $t = 0^-$ is as follows

$$v_A(z,t) = V^+ u\left(t - \frac{z}{v_p}\right) + V^- u\left(t + \frac{z}{v_p}\right) = V_0$$

Where $V^+ = V^- = \frac{V_0}{2}$

The junction switch at z_{A_f} is then subsequently closed at $t = 0^+$ (Figure 3-12) and this gives rise to Reverse and Forward propagating waveforms. The Reverse propagating waveform travels exclusively on Line A, whilst the Forward propagating waveform propagates exclusively on Line B.

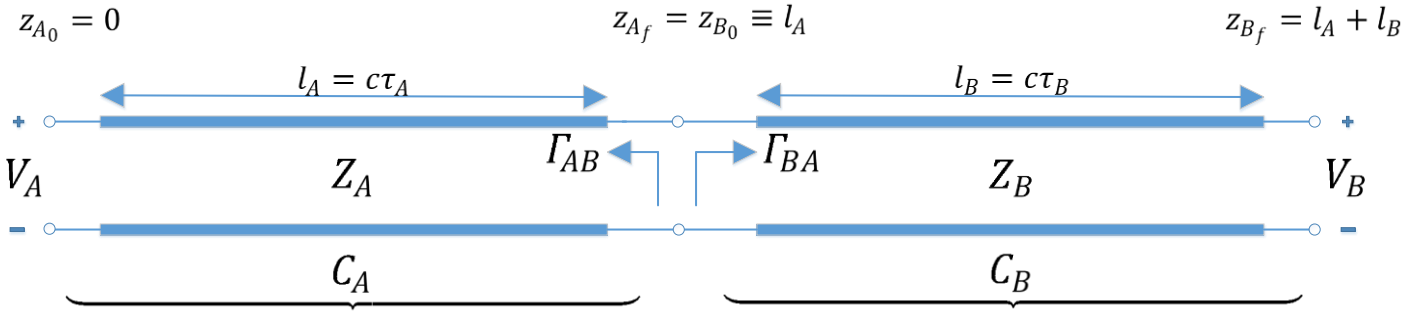


Figure 3-12: Twin Capacitor Link-Line Model (Switch Closed)

The voltage present on Line A $v_A(z,t)$ due to the Reverse propagating wave is

$$v_A(z,t) = {V_R}^+ u\left(t - \frac{z}{v_p}\right) + {V_R}^- u\left(t + \frac{z}{v_p}\right) \tag{3.49}$$

Where $z_{A_0} \leq z \leq z_{A_f}$

Similarly, the current present on Line A $i_A(z,t)$ is

$$i_A(z,t) = \frac{1}{Z_0}\left[{V_R}^{+}u\left(t - \frac{z}{v_p}\right) - {V_R}^{-}u\left(t + \frac{z}{v_p}\right)\right] \tag{3.50}$$

Where $z_{A_0} \leq z \leq z_{A_f}$

The voltage on Line B $v_B(z,t)$ due to the Forward propagating wave is

$$v_B(z,t) = {V_F}^{+}u\left(t - \frac{z}{v_p}\right) + {V_F}^{-}u\left(t + \frac{z}{v_p}\right) \tag{3.51}$$

Where $z_{B_0} \leq z \leq z_{B_f}$

The current on Line B $i_B(z,t)$ is given by

$$i_B(z,t) = \frac{1}{Z_0}\left[{V_F}^{+}u\left(t - \frac{z}{v_p}\right) - {V_F}^{-}u\left(t + \frac{z}{v_p}\right)\right] \tag{3.52}$$

Where $z_{B_0} \leq z \leq z_{B_f}$

At the instant the switch is closed at $t = 0^+$ the boundary conditions at z_{A_f} change. The once open-circuit termination of z_{A_f} is replaced with the characteristic impedance Z_B of the discharged Line B. This change in boundary conditions will alter the reflected wave coefficient ${V_R}^{-}$. This is due to the change in the reflection coefficient Γ_{AB}. The reflection coefficient Γ_{AB} is given by

$$\Gamma_{AB} = \frac{Z_B - Z_A}{Z_A + Z_B} \tag{3.53}$$

Since $C_A = C_B$ and the characteristic impedances of both lines are matched ($Z_A = Z_B$). The reflection coefficient $\Gamma_{AB} = 0$. This means that at $t = 0^+$ ${V_R}^{-}$changes. The new value of ${V_R}^{-}$ at $t = 0^+$ is

$${V_R}^{-} = {V_R}^{+}\Gamma_{AB} \tag{3.54}$$

Applying (3.54) gives a reflected wave coefficient of zero i.e. ${V_R}^{-} = 0$. As the reflected wave propagates from z_{Af} to z_{A_0} a reduction in the voltage on Line A will be seen. When the boundary terminal at z_{A_0} is reached the voltage on Line A will be equal to half the initial charge voltage i.e. $|v_A(z,t)| = \frac{V_0}{2}$. In addition, the current on the Line A is $|i_A(z,t)| = I_0 \equiv \frac{V_0}{2Z_A}$. The open-circuit boundary conditions at z_{A_0} ensure that ${V_R}^{+} = {V_R}^{-}$. Therefore, as the incident wave propagates from z_{A_0} back to z_{A_f}, the propagating voltage and current waveforms collapse. As a direct result both $v_A(z,t)$ and $i_A(z,t)$ tend to zero.

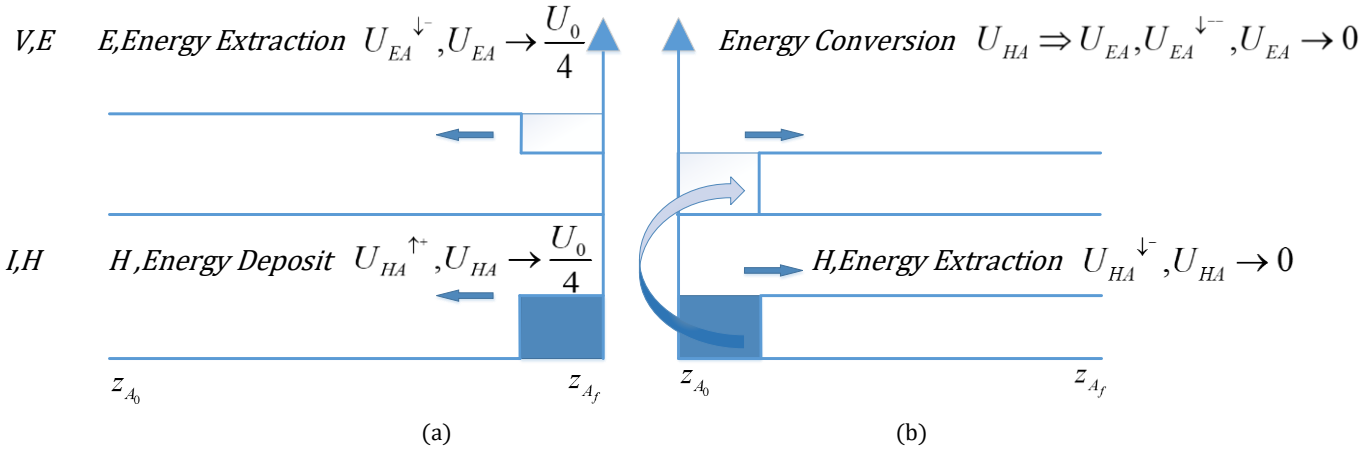


Figure 3-13: Energy Interactions on C_A Wave Propagation Towards a) z_{A0} b) z_{A_f}

The implications of the changing ${V_R}^+$ and ${V_R}^-$ have on the energy interactions on Line A (i.e. C_A) are depicted in Figure 3-13. The reduced voltage as the Reverse propagating wave propagates from z_{A_f} to z_{A_0} (Figure 3-13a) manifests as an extraction of electric energy on Line A. In order for a propagating wave to be sustained on Line A both electric and magnetic energies must be present. As electric energy is extracted from Line A the accompanying propagating current waveform ensures magnetic energy is deposited on Line A. This magnetic energy is stored in the self-inductor L_{eA}. As the propagating waveforms move from z_{A_f} to z_{A_0} (Figure 3-13a) the electric energy reduces to a quarter of the initial system energy $U_{EA} \rightarrow \frac{U_0}{4}$, whist the magnetic energy increases to a quarter of the initial system energy $U_{HA} \rightarrow \frac{U_0}{4}$.

As the propagating waveforms encounter the boundary at z_{A_0} the open-circuit boundary conditions facilitate a collapse in the voltage and current waveforms. The open-circuit boundary conditions give rise to a new incident voltage coefficient ${V_R}^+$ that is equal to the reflected voltage coefficient ${V_R}^-$(Reflection coefficient at z_{A_0} is 1). Consequently, both $v_A(z,t)$ and $i_A(z,t)$ will tend to zero i.e. $|v_A(z,t)| \rightarrow 0$ and $|i_A(z,t)| \rightarrow 0$.The implications this has on the energy interactions on Line A or C_A are that both electric and magnetic energies on the line are reduced to zero ($U_{EA} \rightarrow 0, U_{HA} \rightarrow 0$). Already from this result, we are seeing a divergence from results predicted by conventional circuit theory. Circuit theory predicts that C_A will discharge into C_B until C_A and C_B share an equal amount of charge and hence energy. Analysing the paradox with propagating waveforms is already showing at this stage that there is at least an instant in time ($t = 2\tau_A$) where the electric energy present in C_A is zero. This ultimately means that the electric energy (U_{EA}) present in C_A fully transfers to C_B i.e. $U_{EA} \rightarrow 0$ whilst $U_{EB} \rightarrow U_0$ (Figure 3-14b).

At $t = 0^+$ the Forward propagating wave will propagate from z_{B_0} to z_{B_f} as the junction switch is closed. The amplitude of the incident voltage coefficient ${V_F}^+$ is due to the transmission of the incident voltage coefficient ${V_R}^+$ on Line A at the same time. The incident voltage coefficient ${V_F}^+$is

$$ {V_F}^+ = \frac{2Z_B}{Z_A + Z_B} {V_R}^+ \equiv \mathcal{T}_{AB} {V_R}^+ \tag{3.55} $$

Where $\mathcal{T}_{AB}$ is the voltage transmission coefficient from Line A to Line B. Using (3.55) the incident voltage coefficient at $t = 0^+$ is ${V_F}^+ = \frac{V_0}{2} = {V_R}^+$.

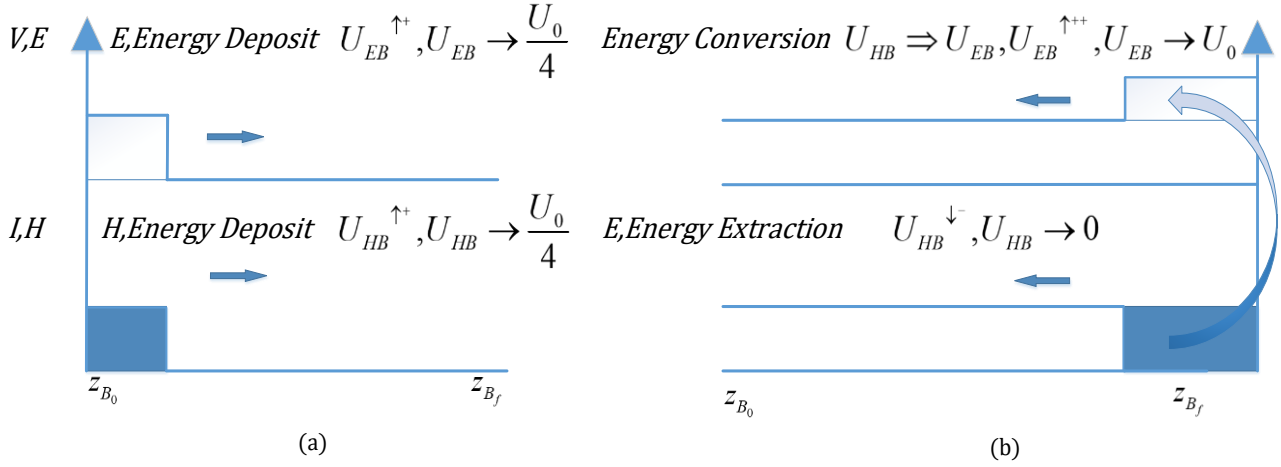


Figure 3-14: Energy Interactions on C_B Wave Propagation Towards a) z_{A0} b) z_{A_f}

The implications the propagating Forward traveling waves have on the energy interactions on Line B (C_B) are depicted in Figure 3-14. An increase in electrical (U_{EB}) as well as magnetic (U_{HB}) energies are seen as the propagating waveforms travel from z_{B_0} (Line B's Near-End Terminals) to z_{B_f}(Line B's Far-End Terminals) as seen in Figure 3-14a. The electric and magnetic energies are stored in C_B and L_{eB} respectively. The energies U_{EB} and U_{HB} increase to a quarter of the initial system energy by the time the propagating waveforms contact the boundary at z_{B_f} ($t = \tau_B$). The open circuit boundary condition at z_{B_f} necessitates that the reflected and incident voltage coefficients are equal i.e. $V_F^- = V_F^+$(reflection coefficient at z_{B_f} is 1). As the propagating waveforms travel from z_{B_f} back to z_{B_0} the line voltage $|v_B(z,t)| \to V_0$ whilst the current $|i_B(z,t)| \to 0$ as evidenced by (3.51) and (3.52) respectively. Once the propagating waveforms contact the boundary z_{B_0} at $t = 2\tau_B$, the entirety of the magnetic energy U_{HB} stored in L_{eB} will be converted into electric energy U_{EB} stored in C_B (Figure 3-14b). Incidentally, the capacitor C_B now contains the entirety of the initial system energy U_0 that was once contained in C_A i.e. $U_{EB} = U_0$. This effectively means that the capacitor C_A is in a *fully discharged* state and contains zero associated electric and magnetic energies. Upon observation of Figure 3-13b we can see that this is indeed the case.

Table 3.1: Time intervals for energy interaction states in C_A and C_B

Time Intervals	C_A	L_{eA}	C_B	L_{eB}
$(4n-4)\tau \le t \le (4n-3)\tau, n \in \mathbb{Z}$	$U_{EA} \to \frac{U_0}{4}$	$U_{HA} \to \frac{U_0}{4}$	$U_{EB} \to \frac{U_0}{4}$	$U_{HB} \to \frac{U_0}{4}$
$(4n-3)\tau \le t \le (4n-2)\tau, n \in \mathbb{Z}$	$U_{EA} \to 0$	$U_{HA} \to 0$	$U_{EB} \to U_0$	$U_{HB} \to 0$
$(4n-2)\tau \le t \le (4n-1)\tau, n \in \mathbb{Z}$	$U_{EA} \to \frac{U_0}{4}$	$U_{HA} \to \frac{U_0}{4}$	$U_{EB} \to \frac{U_0}{4}$	$U_{HB} \to \frac{U_0}{4}$
$(4n-1)\tau \le t \le (4n)\tau, n \in \mathbb{Z}$	$U_{EA} \to U_0$	$U_{HA} \to 0$	$U_{EB} \to 0$	$U_{HB} \to 0$

Upon observation of the energy interaction states in Table 3.1 it is readily apparent that the total system energy predicted by circuit theory is wrong. Circuit theory predicts that the total energy present in the circuit once equilibrium is reached is the sum of the electric energies present in both capacitors i.e. $U_0 = U_{EA} + U_{EB}$.

This expression leads one to believe that a *perceived* energy loss exists in the system. The fact that only the electric energies (U_{EA} and U_{EB}) in both capacitors are considered leads to the notion of *"Missing Energy"* in the system. The electric and magnetic energies stored on Line A and Line B are as follows

$$U_{EA}(z,t) = \frac{1}{2}C_A v_A(z,t)^2 \tag{3.56}$$

$$U_{EB}(z,t) = \frac{1}{2}C_B v_B(z,t)^2 \tag{3.57}$$

$$U_{HA}(z,t) = \frac{1}{2}L_{eA} i_A(z,t)^2 \tag{3.58}$$

$$U_{HB}(z,t) = \frac{1}{2}L_{eB} i_B(z,t)^2 \tag{3.59}$$

If the magnetic energies stored in L_{eA} and L_{eB} are observed the "*Missing Energy"* in the system can be accounted for. The total system energy needs to be modified to account for the magnetic energies stored in L_{eA} and L_{eB}.The total system energy U_0 incorporating both U_{HA} and U_{HB} is given by

$$U_0 = U_{EA} + U_{EB} + U_{HA} + U_{HB} \tag{3.60}$$

From the energies presented in Table 3.1 and using (3.60) it is readily apparent that there is no violation of energy conservation in the system. At every single time instance or interval, for the energy interactions in C_A and C_B energy is conserved. The shortcoming of circuit theory in modelling these energy interactions is in its *perceived* equilibrium state. The use of the phrase equilibrium state to describe when both capacitors share an equal amount of charge is a misnomer. This state merely describes the *partially charged* state, and is one of the three states C_A and C_B may occupy. Circuit theory predicts that after some finite amount of time both capacitors C_A and C_B have the same potential and as a result no current flows between the capacitors once charged. It is assumed that both C_A and C_B exhibit constant steady state voltages whilst the circulating current is equal to zero. As is shown in the voltage and current progressions in Figure 3-15a and Figure 3-15b respectively this is in fact erroneous. The voltage and current values predicted by circuit theory are the time average values of the voltage and current progressions on Line A and Line B (equations (3.69) to (3.72)).

In the equilibrium state only the electrical energies U_{EA} and U_{EB} are considered and this quite rightly sums to half the initial system energy i.e. $U_{EA} + U_{EB} = \frac{U_0}{2}$. However, in assuming C_A and C_B are ideal capacitors no allowance is made for any magnetic energy storage. This incorrect assumption implies that $U_{HA} = U_{HB} = 0\ \forall t$ .Analysing the circuit with Link-Line equivalent models clearly shows this is not the case. The system never reaches a state of equilibrium. In actuality C_A and C_B experience three distinct states. These are the *fully charged, partially charged* and *fully discharged* states. At any instant in time C_A and C_B may occupy anyone of these states or be transitioning from one state to another. It must be noted however that the *fully charged* state is mutually exclusive in reverence to C_A and C_B.

The *fully charged* state can only be occupied by either C_A or C_B at a particular time instant. This is due to the fact that if C_A is in the *fully charged* state C_B must be in the *fully discharged* state and vice versa.

From equations (3.49) to (3.52) it is readily apparent that the voltages and currents produced on Line A and Line B are multivariable space-time functions. A one-to-one mapping of these functions is obtained if one of the variables is held constant whilst the other is free to vary. Restriction of the functions in this manner effectively discretizes the voltage and current functions. In time discretization, the evolution or progression in time of the voltage and current waveforms at a specified or fixed point on the transmission line is given. In spatial discretization the evolution or progression of the voltages and currents in space, at a specific time instance are given.

The voltage and current progressions used in the analysis of the *Twin Capacitor* and LC Resonant tank topologies are spatially averaged time progressions. This involves looking at how the spatial averages in the voltages and currents vary w.r.t. time. The spatially averaged voltage and current progressions will simply be called progressions for brevity from this point forth.

The voltage progressions on Line A and Line B are

$$V_A(t) = \frac{1}{l_A}\int_0^{l_A} v_A(z,t)dz \tag{3.61}$$

$$V_B(t) = \frac{1}{l_B}\int_0^{l_B} v_B(z,t)dz \tag{3.62}$$

The current progressions on Line A and Line B are

$$I_A(t) = \frac{1}{l_A}\int_0^{l_A} i_A(z,t)\,dz \tag{3.63}$$

$$I_B(t) = \frac{1}{l_B}\int_0^{l_B} i_B(z,t)\,dz \tag{3.64}$$

The resulting electric and magnetic energy progressions on Line A and Line B are

$$U_{EA}(t) = \frac{1}{l_A}\int_0^{l_A} U_{EA}(z,t)dt \tag{3.65}$$

$$U_{EB}(t) = \frac{1}{l_B}\int_0^{l_B} U_{EB}(z,t)dt \tag{3.66}$$

$$U_{HA}(t) = \frac{1}{l_A}\int_0^{l_A} U_{HA}(z,t)dt \tag{3.67}$$

$$U_{HB}(t) = \frac{1}{l_B}\int_0^{l_B} U_{HB}(z,t)dt \tag{3.68}$$

The time averages of the progressions are taken over one complete charge discharge cycle. Since $\tau_A = \tau_B \equiv \tau$ a full charge discharge cycle is comprised of two round-trips on either Line A or Line B. The time taken for two complete round-trips on either Line A or Line B is four times the one-way propagation delay down Line A or Line B i.e. $T = 4\tau$

Equations (3.69) to (3.72) give the time averaged voltage and current progressions on the respective lines.

$$\overline{V_A(t)} = \frac{1}{T}\int_0^T V_A(t)dt = \frac{1}{4\tau}\int_0^{4\tau} V_A(t)dt \tag{3.69}$$

$$\overline{V_B(t)} = \frac{1}{T}\int_0^T V_B(t)dt = \frac{1}{4\tau}\int_0^{4\tau} V_B(t)dt \tag{3.70}$$

$$\overline{I_A(t)} = \frac{1}{T}\int_0^T I_A(t)dt = \frac{1}{4\tau}\int_0^{4\tau} I_A(t)dt \tag{3.71}$$

$$\overline{I_B(t)} = \frac{1}{T}\int_0^T I_B(t)dt = \frac{1}{4\tau}\int_0^{4\tau} I_B(t)dt \tag{3.72}$$

The linear voltage and current progressions for both TL segments that map to the energy interactions in Table 3.1 for C_A and C_B are depicted in Figure 3-15 and Figure 3-16.

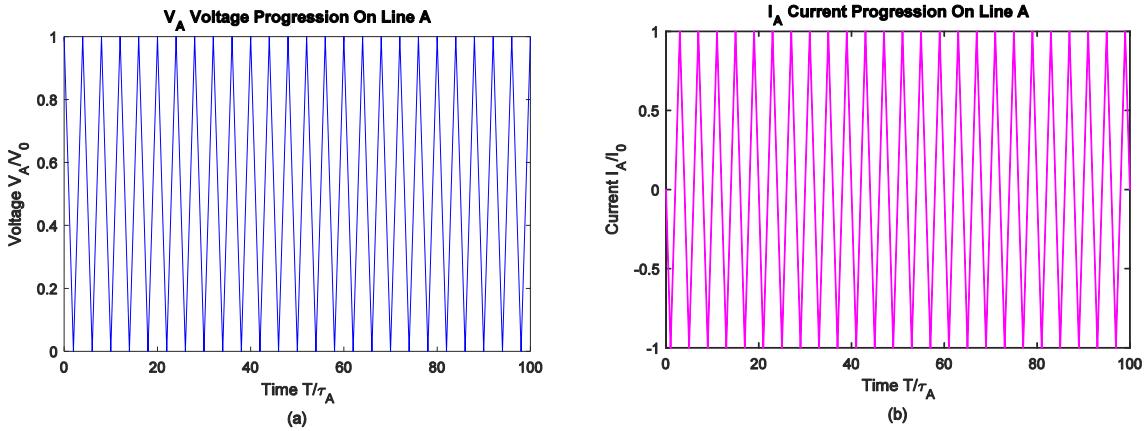


Figure 3-15: Line A (C_A) Voltage and Current Progressions a) Voltage b) Current

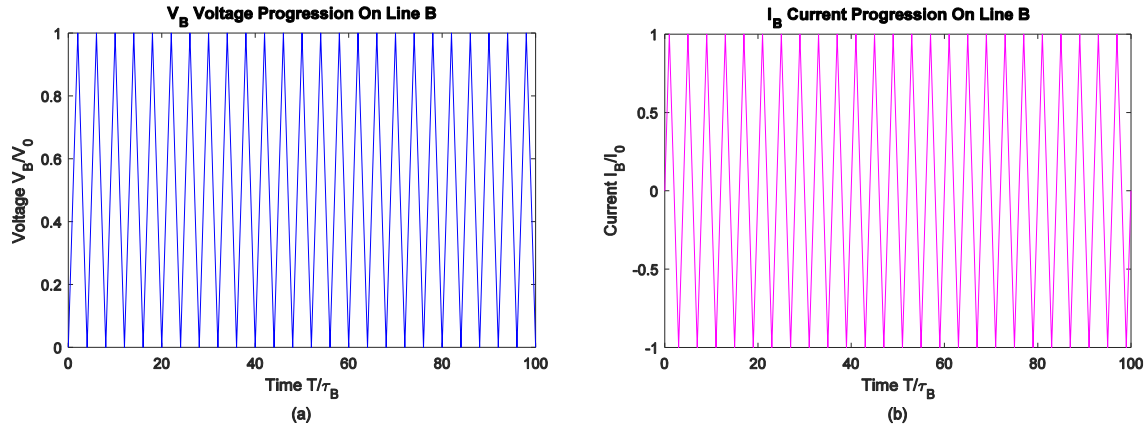


Figure 3-16: Line B (C_B) Voltage and Current Progressions a) Voltage b) Current

The voltage and current progressions ($V_A(t)$ and $I_A(t)$ respectively) in Figure 3-15 and Figure 3-16 are normalised w.r.t the respective propagation delays τ_A and τ_B as well as the respective peak amplitudes V_0 and I_0. This is necessary to preserve the qualitative nature of the examined energy conversion problem. As this ensures that, any arbitrary selection of the set parameters ($V_0, I_0, C_A,$ and C_B.) do not affect the consistency of the generated waveforms. The only restriction imposed is that the propagation delays of both TL segments are matched i.e. $\tau_A = \tau_B$. This ensures that the voltage and current progressions increase in a linear fashion and explicit analytical expressions for all progressions can be found. Analytical expressions for $V_A(t)$,$V_B(t)$, $I_A(t)$ and $I_B(t)$ are given by equations (3.73) to (3.76). Chapter 4 expounds more on the topic of *Fragmentation* generation, which speaks to cases where the propagation delays of the respective lines are not necessarily equal.

$$V_A(t) = \begin{cases} \left[\frac{V_0}{2\tau_A}\right](t-(4n-4)\tau_A) & ;(4n-4)\tau_A \le t \le (4n-2)\tau_A \\ \left[\frac{-V_0}{2\tau_A}\right](t-(4n)\tau_A) & ;(4n-2)\tau_A \le t \le (4n)\tau_A \\ n \in \mathbb{Z} \end{cases} \tag{3.73}$$

$$V_B(t) = \begin{cases} \left[\frac{V_0}{2\tau_B}\right](t-(4n-4)\tau_B) & ;(4n-4)\tau_B \le t \le (4n-2)\tau_B \\ \left[\frac{-V_0}{2\tau_B}\right](t-(4n)\tau_B) & ;(4n-2)\tau_B \le t \le (4n)\tau_B \\ n \in \mathbb{Z} \end{cases} \tag{3.74}$$

$$I_A(t) = \begin{cases} \left[\frac{-I_0}{\tau_A}\right](t-(4n-4)\tau_A) & ;(4n-4)\tau_A \le t \le (4n-3)\tau_A \\ \left[\frac{I_0}{\tau_A}\right](t-(4n-2)\tau_A) & ;(4n-3)\tau_A \le t \le (4n-1)\tau_A \\ \left[\frac{-I_0}{\tau_A}\right](t-(4n)\tau_A) & ;(4n-1)\tau_A \le t \le (4n)\tau_A \\ n \in \mathbb{Z} \end{cases} \tag{3.75}$$

$$I_B(t) = \begin{cases} \left[\frac{I_0}{\tau_B}\right](t-(4n-4)\tau_B) & ;(4n-4)\tau_B \le t \le (4n-3)\tau_B \\ \left[\frac{-I_0}{\tau_A}\right](t-(4n-2)\tau_B) & ;(4n-3)\tau_B \le t \le (4n-1)\tau_B \\ \left[\frac{I_0}{\tau_B}\right](t-(4n)\tau_B) & ;(4n-1)\tau_B \le t \le (4n)\tau_B \\ n \in \mathbb{Z} \end{cases} \tag{3.76}$$

Further analysis of Figure 3-15 and Figure 3-16 reveals that conventional circuit theory and the Link-Line equivalent model produce contrasting results. Conventional circuit theory predicts constant DC voltage and current waveforms once the equilibrium state is reached in C_A and C_B. However, the Link-Line equivalent model gives rise to time varying voltage and current progressions that are never constant w.r.t. time. If, however the time averaged progressions ($\overline{V_A(t)}, \overline{V_B(t)}, \overline{I_A(t)}$ and $\overline{I_B(t)}$) are juxtaposed with the expected results from circuit theory, good congruency of the results is observed.

This stems from the fact that the DC component by its very definition represents the time average component of a time varying waveform. So, in obtaining the time averaged progressions for the voltages and currents on the respective lines good congruency should be seen with the predicted DC waveforms from circuit theory.

The main point or crux of the paradox centers on the notion of zero current flow in the *Twin Capacitor* topology in the equilibrium state. Whilst the time averaged current progressions $\overline{I_A(t)}$ and $\overline{I_B(t)}$ are zero, however the instantaneous currents vary from I_0 to $-I_0$. These current progressions essentially represent pure AC waveforms (Figure 3-15b and Figure 3-16b). As is widely known for any pure AC waveform the average or DC component will always be zero. So ultimately the notion of zero current flow in this faux equilibrium state arises from the fact that circuit theory takes the DC or time average of the current progressions ($\overline{I_A(t)}$ and $\overline{I_B(t)}$) and assumes that this average is also indicative of the instantaneous current on the line.

The preconceived notion of this zero current leads to the conventional wisdom that capacitors C_A and C_B and hence the *Twin Capacitor* topology reaches and maintains an equilibrium state with no circulating current. However, the oscillating current progressions speaks to the contrary. The oscillating $I_A(t)$ and $I_B(t)$ essentially mean C_A and C_B are consistently charging and discharging each other. This effectively means that the electric and magnetic energies present on both Line A and Line B are always in perpetual oscillation. Consequently, if the initial system energy in totality is seen in either C_A or C_B , it can be said C_A or C_B is in the *fully charged* state. In the transitioning states when C_A and C_B are neither *fully charged* nor *fully discharged* they are said to be in the *partially charged* state. In this state, both C_A and C_B each contain a quarter of the system energy whilst the associated self- inductors L_{eA} and L_{eB} each contain a quarter of the initial system energy (as seen in the Table 3.1).

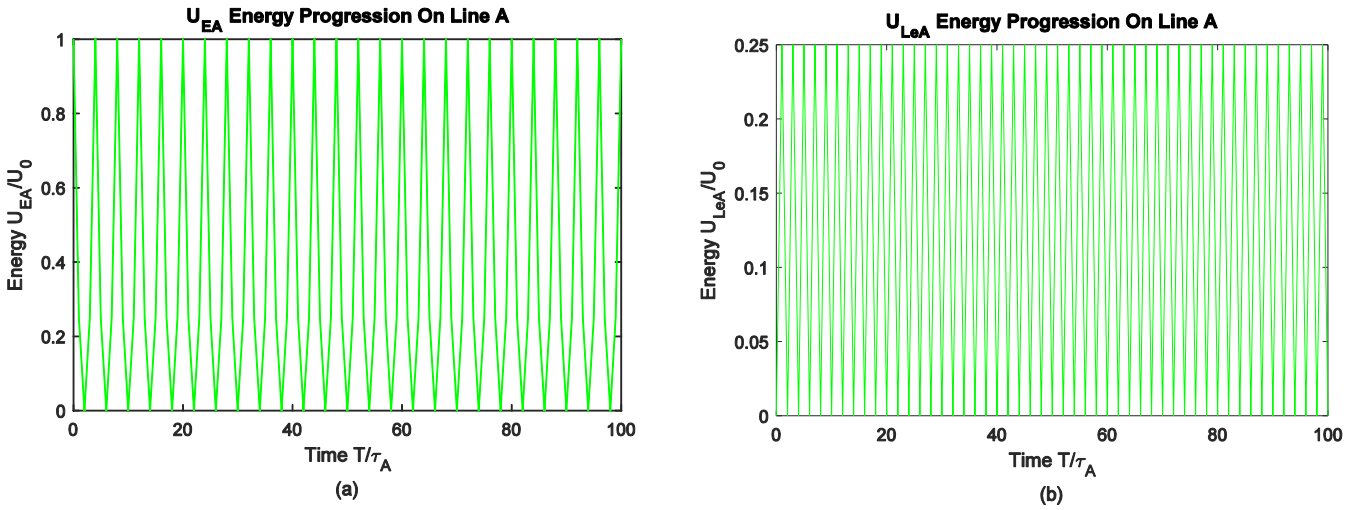


Figure 3-17:Line A (C_A) Energy Progressions a) U_{EA} b) U_{LeA}

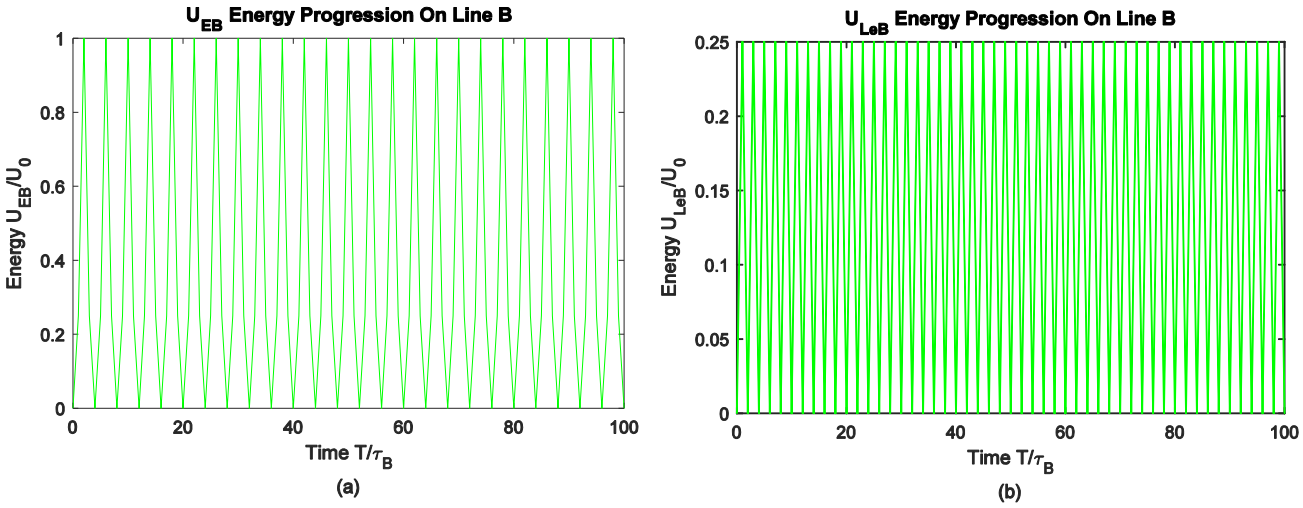


Figure 3-18: Line B (C_B) Energy Progressions a) U_{EB} b) U_{LeB}

The energy progression for C_A and C_B are displayed in Figure 3-17 and Figure 3-18 respectively. These graphs have been normalised w.r.t their respective propagation delays as well as the initial system energy U_0. Upon further observation of the electrical energy progressions U_{EA} and U_{EB} it is readily seen that the energy oscillates between U_0 and zero during the interval $4n-4 \leq t \leq 4n, n \in \mathbb{Z}$. Whilst the magnetic energies oscillate between a quarter of the initial system energy $\frac{U_0}{4}$ and zero. This occurs during the time interval $2n-2 \leq t \leq 2n, n \in \mathbb{Z}$.

3.5.1.1 Summary

Synthesising the results seen in the voltage, current and energy progressions in Figure 3-15-Figure 3-18 some pertinent facts and conclusions are drawn. Firstly, whenever electric energy (U_{EA} or U_{EB}) is deposited on either line it is always accompanied by the deposit of magnetic energies (U_{HA} or U_{HB}) on the respective lines. When energy conversion takes place at the z_{A_0} and z_{B_f} boundary terminals the associated magnetic energies collapse and are converted into electric energies. Dependent on the instant in time the magnetic to electric energy conversion processes occur, this will either facilitate an increase or decrease in the respective line voltage. Consequently, if the line voltage is increased this is accompanied by an increase in electrical energy on the line, ultimately culminating in the totality of the system energy being stored on that line. Conversely, if the line voltage is reduced this effectively means that the electric energy on the line is being extracted. This will persist until such a time that the line is completely devoid of all associated electric energy. From these processes we can conclude that the often neglected associated self-inductors (L_{eA} and L_{eB}) provide an integral role in facilitating any and all energy manipulation processes within the *Twin Capacitor* topology when represented with Link-Line equivalent models.

3.5.2 LC Resonator Tank

Analysing the natural response of the LC Resonant tank provides insight into the fundamental energy manipulations between electric and magnetic energies. A capacitor C_r is charged to an arbitrary voltage V_0 after which it is connected to an inductor L_r. Conventional circuit theory quite rightly predicts that there will be an oscillation of electric and magnetic energies in SHM. In the presence of no damping, this persists *ad infinitum*.

What however is not readily apparent from conventional circuit theory, is how energy of different forms converts from one form to another. In the LC Resonant tank, it is widely known that electrical energy is converted into magnetic energy and vice versa. However, conventional modelling obfuscates the actual process of conversion. From this conventional modelling approach, we intuitively understand that a decrease in one energy accompanies a corresponding increase in the other. This speaks to the sinusoidal and co-sinusoidal variations in voltages and currents, and hence energies predicted in a LC Resonant tank by conventional circuit theory.

3.5.2.1 Energy Interactions Capacitor

In Figure 3-19 the cascaded Link-Line equivalent model of a LC Resonant tank is depicted. If the planar geometry for the LC Resonant structure given in Figure 2-5 is assumed, the length dimensions l_1 and l_2 correspond to the l_A and l_B lengths given in Figure 3-19 and Figure 3-20 and thus, spatial discretisation is taken along these dimensions. The capacitive line denoted as Line A, is initially charged to a rated voltage V_0.

When the switch is open ($t = 0^-$), no terminations exist at positions z_{A_0} and z_{A_f}, and hence open-circuit boundary conditions are established. The boundary conditions established at these terminals ensure that a static DC voltage V_0 is present on Line A. Consequently, $V^+ = V^- = \frac{V_0}{2}$ and the line voltage is given as per (3.6a). As a direct result, all associated system energy U_0 on Line A will be purely electric in nature i.e. $U_{EA} = U_0$.

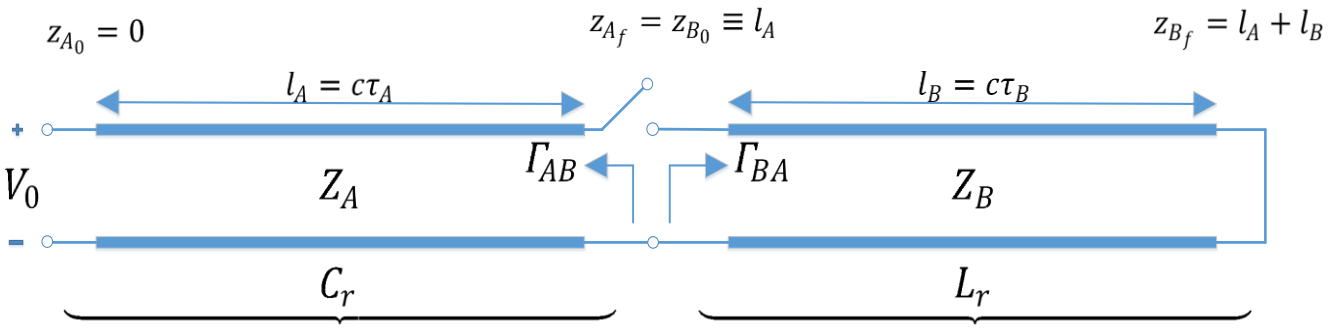


Figure 3-19: Resonator Tank Link-Line Equivalent Model (Switch Open)

The energy manipulation processes begin in earnest when the junction switch at position z_{A_f} is closed. Figure 3-20 depicts this scenario. As predicted by conventional circuit theory the SHM waveforms $v(t)$ and $i(t)$ are established in the resonant tank. The expressions for the voltage and current are as follows:

$$v(t) = V_0 \cos(\omega_0 t)$$

$$i(t) = I_0 \sin(\omega_0 t)$$

Examining the energy manipulation processes from the viewpoint of propagating waveforms on transmission lines reveals additional insight and nuances in the electric to magnetic energy manipulation processes in the LC Resonant tank.

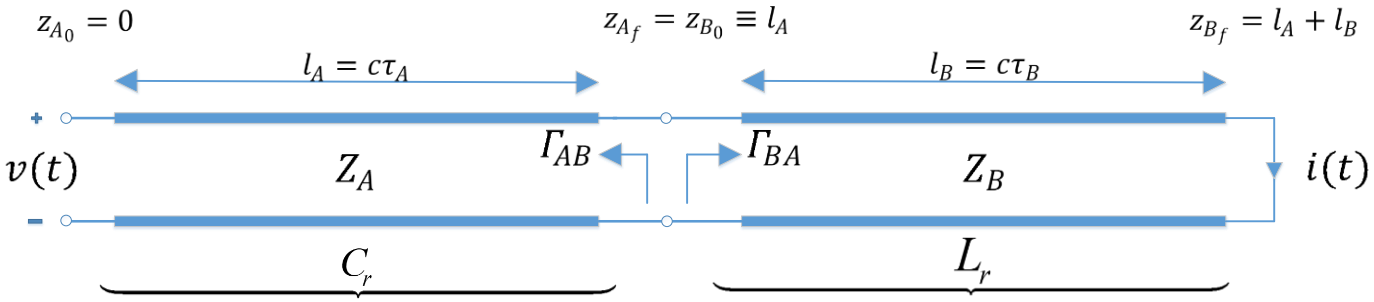


Figure 3-20: Resonator Tank Link-Line Equivalent Model (Switch Closed)

At the instant the junction switch is closed ($t = 0^+$) Reverse and Forward propagating travelling waveforms are spawned. The Reverse propagating waveform travels towards z_{A_0} on Line A (Figure 3-21a), whilst the Forward travelling waveform travels towards z_{B_f} on Line B. Equations (3.49) to (3.52) again govern the interactions between the incident and reflected voltage coefficients. As the junction switch is closed at z_{A_f} the characteristic impedance of Line B (Z_B) becomes the new termination at the z_{A_f} terminals. This change in termination brings about a change in the reflection coefficient Γ_{AB}. By equation (3.53) $\Gamma_{AB} \to 1$. The reflection coefficient at the junction $\Gamma_{AB} \to 1$ because of the vast differences in the characteristic impedances of Line A and Line B. Since Line A represents a capacitor (C_r) and Line B an inductor (L_r) the relationship between the characteristic impedances is such that $Z_A \ll Z_B$. In the limiting case of when ideal capacitors and inductors are used $\Gamma_{AB} = 1$. However, in this case Line B appears as an open circuit to Line A and thus no energy will be transmitted to Line B.

This reason provides further credence as to why ideal capacitors and inductors cannot facilitate energy transfer and conversion. Finite characteristic impedances for Z_A and Z_B must be selected that do not result in a $\Gamma_{AB} = 1$. For the purposes of the qualitative exploration of the electric to magnetic energy conversion problem $Z_B = 10000Z_A$. The new V_R^- is given by application of (3.54). The new reflected voltage coefficient $V_R^- \cong 0.999V_R^+ = 0.4995V_0$. As V_R^- propagates from z_{A_f} to z_{A_0} this leads to a reduction in line voltage $v_A(z,t)$. This is indicative of energy extraction or removal from the initially charged Line A.

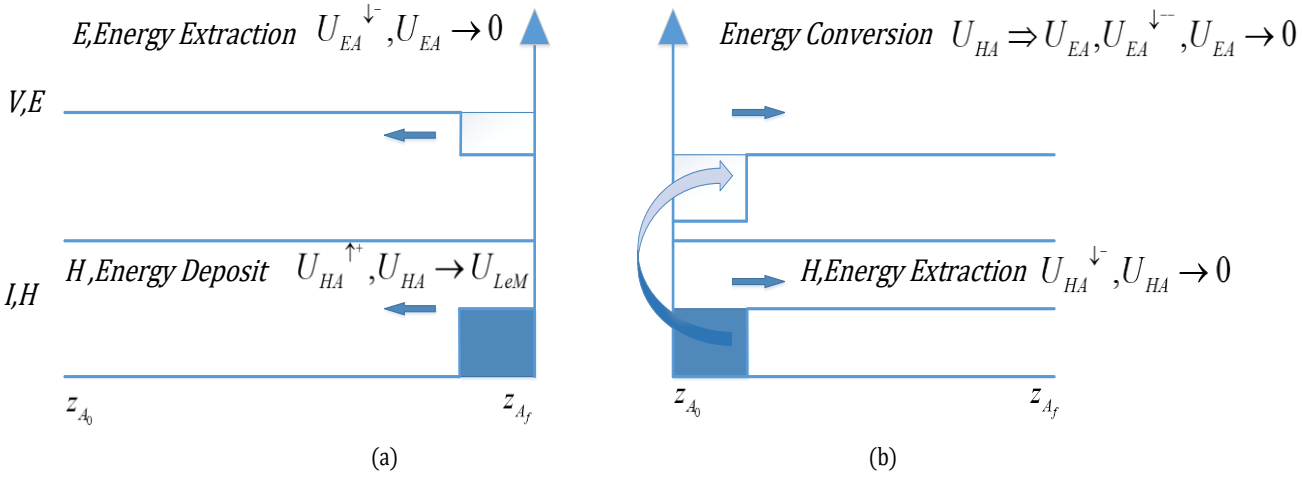


Figure 3-21: Electromagnetic Energy Interactions on C_r, Wave Propagation Towards (a) z_{A_0} (b) z_{A_f}.

In Figure 3-21a it is readily seen that the Reverse travelling voltage and current waveforms propagate from z_{A_f} to z_{A_0}. An accompanying decrease in the electrical energy (U_{EA}) on Line A occurs because of the reduction in $v_A(z,t)$ brought about by V_R^-. In addition, the negative current amplitude on the line facilitates an increase in the magnetic energy stored on Line A. In order to sustain a propagating travelling waveform on Line A, both electric and magnetic energies must be present in the propagating waveform. As seen in the *Twin Capacitor* scenario. The magnetic energy will always be stored in the self-inductor L_{eA} on Line A. As a direct consequence, electromagnetically speaking an ideal capacitor cannot exists. An ideal capacitor contains zero self-inductance i.e. $L_{eA} = 0$. The implications of having zero inductance means that the permeability μ of the TL segment is also zero. Substituting these values into equation (2.16) result in a velocity of propagation v_p that is faster than the speed of light. As is well documented in classical physics no transportation of information or energy in a medium can move faster than the speed of light [46]. This ultimately means that a finite self-inductance L_{eA} must always be present on Line A i.e. $L_{eA} \neq 0$.

In Figure 3-21b the Reverse propagating travelling waveform reaches the terminal at z_{A_0}. At this instant in time ($t = \tau_A$) the open-circuit boundary conditions at z_{A_0} necessitate an energy conversion. The energy conversion that takes place is one from magnetic to electric energy i.e. $U_{HA} \rightarrow U_{EA}$. The open-circuit boundary condition imposes the collapse of the current waveform present on Line A. As a direct consequence, the associated magnetic energy stored in the self-inductor L_{eA} must convert to electrical energy. This manifests as an effective doubling in voltage of the propagating waveform, whilst the current waveform reduces to zero. The energy interaction processes in Figure 3-21a and Figure 3-21b persist until the electric energy in C_r is at minimum value i.e. $U_{EA} \cong 0$. This occurs when the voltage on Line A reaches zero i.e. $v_A(z,t) \cong 0$ (Figure 3-22a) at time instance $t = \frac{T_0}{4}$. A precursor to this is the current on Line A reaching a minimum value $i_A(z,t) = -I_0$ as evidenced in Figure 3-22b at time instance $t = \frac{T_0}{4} - \tau_A$.

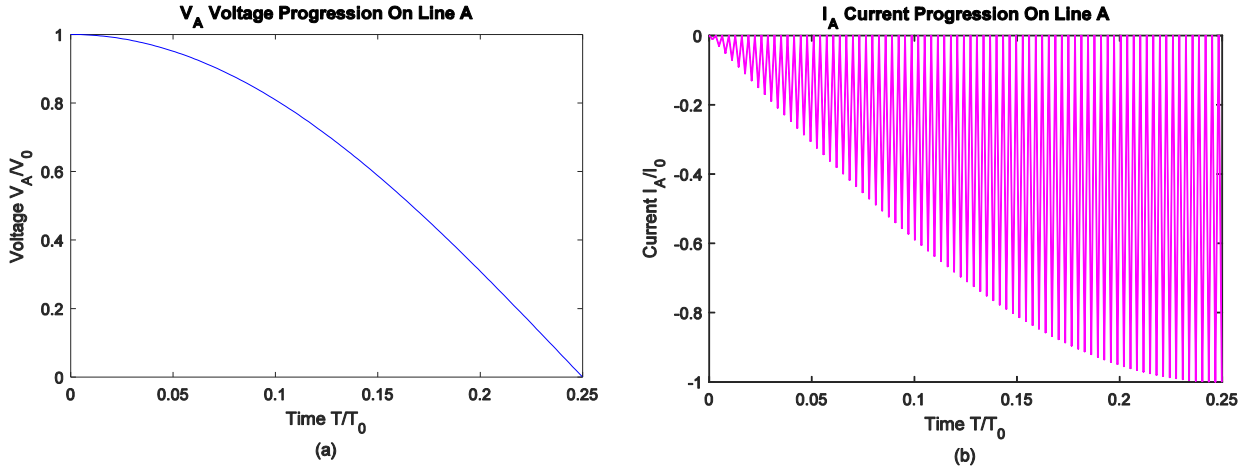


Figure 3-22: Line A (C_r) Voltage and Current Progressions (a) Voltage ($V_A \rightarrow 0$) (b) Current ($I_A \rightarrow -I_0$)

Similarly, the voltage and current progressions in Figure 3-22 are calculated using (3.61) and (3.63). The voltage and current progressions ($V_A(t)$ and $I_A(t)$ respectively) are normalised w.r.t the period of oscillation T_0 and the respective peak amplitudes V_0 and I_0. This in turn ensures that an arbitrary selection of set parameters (V_0, I_0, C_r, L_r and ω_0.) do not affect the consistency of the generated waveforms and the generated results are truly generic in nature. The only restriction imposed is that the propagation delays of both TL segments have matched propagation delays i.e. $\tau_A = \tau_B$.

This ensures that both Line A and Line B contain only a solitary propagating travelling waveform. Further observation of Figure 3-22 shows that conventional circuit theory and the Link-Line equivalent models show great congruency when predicting the voltage progression on Line A. Both models rightly predict the cosine progression of the voltage in C_r (Line A) clearly illustrated in Figure 3-22a. The differences however occur when looking at the current progression on Line A. Conventional circuit theory predicts that the current in the circuit will vary in a purely sinusoidal manner. This is true, however only for the current progression $I_B(t)$ on Line B as seen in Figure 3-25b. The actual current progression on Line A is that of a pulsating triangular wave that is bounded by a sinusoidal envelope. The sinusoidal envelope seen in Figure 3-22b is the negative reciprocal of the sinusoidal current progression seen on Line B i.e. $I_A(t) = -I_B(t)$. The prediction of which is not given by conventional circuit theory. The analytical expression for the current progression $I_A(t)$ during conversion from electric to magnetic energies is as follows:

$$I_A(t) = \begin{cases} \left[-\dfrac{I_0 \sin(\omega_0(2n-1)\tau_A)}{\tau_A}\right](t-(2n-2)\tau_A) \quad ; (2n-2)\tau_A \le t \le (2n-1)\tau_A \\ \left[\dfrac{I_0 \sin(\omega_0(2n-1)\tau_A)}{\tau_A}\right](t-(2n)\tau_A) \quad ; (2n-1)\tau_A \le t \le (2n)\tau_A \\ \left[T_0(n-1), \dfrac{(4n-3)T_0}{4}\right] = \left\{t \in \mathbb{R} \middle| T_0(n-1) \le t \le \dfrac{(4n-3)T_0}{4}\right\} \\ n \in \mathbb{Z} \end{cases} \tag{3.77}$$

The current progression on Line A lends itself to a piecewise representation. This is necessary in order to better encapsulate the energy deposit and extraction processes seen in Figure 3-21a and Figure 3-21b. During time intervals, $(2n-2)\tau_A \le t \le (2n-1)\tau_A$ a propagating current waveform exists on Line A i.e. $I_A(t) \neq 0$. As $t \to \frac{(4n-3)T_0}{4}$ the current progression $I_A(t)$ becomes increasingly negative with each successive propagation from z_{A_f} to z_{A_0}.This persists until the current progression is approximately equal to the negative peak amplitude i.e. $I_A(t) \cong -I_0$. As a consequence, the magnetic energy deposited in L_{eA}, and hence the magnetic energy progression on Line A reaches a maximum $U_{LeA_{Max}}$. The expression for the maximum magnetic energy $U_{LeA_{Max}}$ stored on Line A is given by

$$U_{HA} \equiv U_{LeA_{Max}} = \frac{1}{2} L_{eA}(-I_0)^2 \tag{3.78}$$

Conversely, during time intervals $(2n-1)\tau_A \le t \le (2n)\tau_A$ the propagating current waveform travels from z_{A_0} to z_{A_f}. The interaction at the boundary z_{A_0}ensures that the current progression completely collapses i.e. $I_A(t) = 0$ by the time the propagating waveform reaches z_{A_f} $(t = 2n\tau_A)$. This effectively means the entirety of the magnetic energy that was previously stored in the self-inductor is converted to electrical energy. The implications of collapsing the current waveform mean that the propagating voltage waveform becomes increasingly more negative. In so doing the voltage progression $V_A(t) \to 0$ as well as the electrical energy progression $U_{EA}(t) \to 0$.

The accompanying energy progressions for the electric $U_{EA}(z,t)$ and magnetic $U_{HA}(z,t)$ energies are depicted in Figure 3-23a and Figure 3-23b. Similar to the *Twin Capacitor* case $U_{EA}(z,t)$ and $U_{HA}(z,t)$ are governed by equations (3.56) and (3.58) respectively. Both energy progressions are normalised w.r.t T_0 and their respective peak energy magnitudes U_0 and $U_{LeA_{Max}}$.

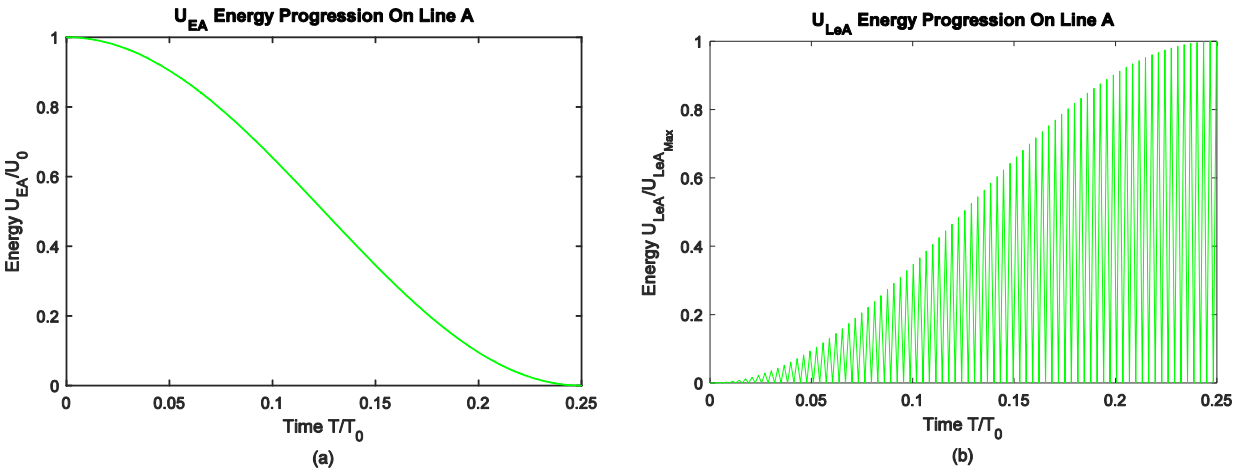


Figure 3-23: Normalized Energy Progressions Line A (a) U_{EA} (b) U_{LeA}

3.5.2.2 Energy Interactions Inductor

At the instant the switch is closed ($t = 0^+$) the Forward travelling propagating waveforms travel towards z_{B_f}. The incident voltage coefficient $V_F{}^+$ is given by the transmission of the incident voltage coefficient $V_R{}^-$ from Line A to Line B. Applying (3.55) the incident voltage coefficient $V_F{}^+ = 0.9995V_R{}^+ = 0.9995V_0$ since $\mathcal{T}_{AB} = 1.999$. Therefore, the Forward propagating waveforms exhibit positive voltage and current amplitudes.

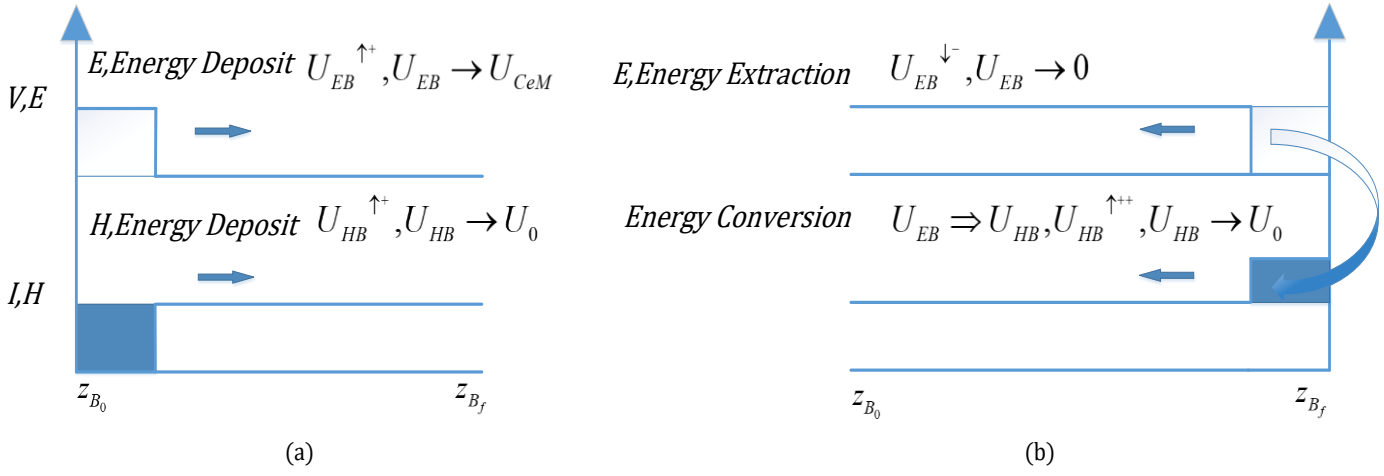


Figure 3-24 Electromagnetic Energy Interactions on L_r, Wave Propagation Towards (a) z_{B_f} (b) z_{B_0}

This is indicative of the deposit of both electric and magnetic energies onto Line B. As a result, all the initial electric energy present in the system will be converted to magnetic energy stored in L_r i.e. $U_{HB} \to U_0$.

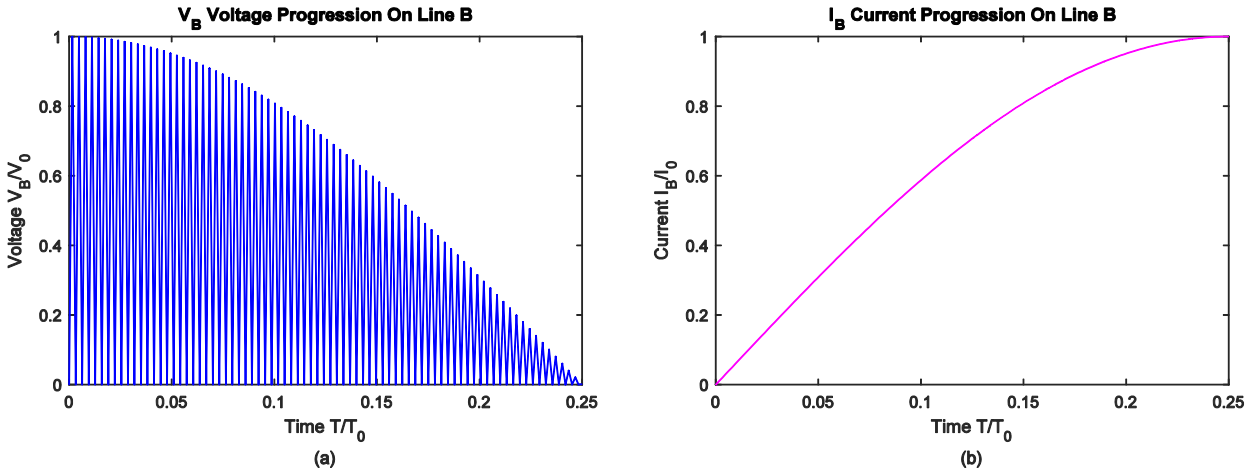


Figure 3-25: Line B Voltage and Current Progressions (a) Voltage ($V_B \to 0$) (b) Current ($I_B \to I_0$)

For reasons given in Chapter 3.5.2.1 a perfectly ideal inductor that has zero self-capacitance is not electromagnetically realisable. This means that L_r will always have a finite self-capacitance C_{eB} associated with it. As a direct consequence electric energy will always be stored in the self-capacitance C_{eB} during wave propagation from z_{B_0} to z_{B_f}. At the instance the propagating waveform contacts z_{B_f} short circuit boundary conditions are enforced. This necessitates the collapse of the propagating voltage waveform. As a result the voltage progression $V_B(t)$ on Line B goes to zero during propagation from z_{B_f} to z_{B_0}. An implication of this is that the amplitude of the propagating current waveform doubles. This is seen as a increase in the current progression $I_B(t)$. Additional implications are that all stored electrical energy ($U_{EB} \equiv U_{CeB}$) is converted to magnetic energy i.e. $U_{EB} \to U_{HB}$. This manifests as an increase in the effective stored magnetic energy U_{HB} in L_r. As seen in the magnetic energy progression $U_{HB}(t)$ given in Figure 3-26a.

Similar to the energy interactions for the capacitor. Good congruency between conventional circuit theory and the Link-Line equivalent models is observed. This is evident when studying $I_B(t)$ depicted in Figure 3-25b. Both circuit theory and the Link-Line equivalent model predict a sinusoidal current progression. However, a divergence is evident in $V_B(t)$.Circuit theory quite rightly predicts a cosinusoidal envelope for $V_B(t)$ as illustrated in Figure 3-25a. However application of the Link-Line model shows that $V_B(t)$ does not follow a continuous cosine progression. The voltage progression is actually better represented by a pulsating triangular waveform. The analytical expression for the voltage progression $V_B(t)$ is expressed as follows

$$V_B(t) = \begin{cases} \left[\frac{V_0 \cos(\omega_0(2n-1)\tau_B)}{\tau_B}\right](t-(2n-2)\tau_B) & ;(2n-2)\tau_B \le t \le (2n-1)\tau_B \\ \left[-\frac{V_0 \cos(\omega_0(2n-1)\tau_B)}{\tau_B}\right](t-(2n)\tau_B) & ;(2n-1)\tau_B \le t \le (2n)\tau_B \\ \left[T_0(n-1), \frac{(4n-3)T_0}{4}\right] = \left\{t \in \mathbb{R} \middle| T_0(n-1) \le t \le \frac{(4n-3)T_0}{4}\right\} & \\ n \in \mathbb{Z} & \end{cases} \quad (3.79)$$

Again a peicewise representation for the voltage progression $V_B(t)$ on Line B is used. The time intervals $(2n-2)\tau_B \le t \le (2n-1)\tau_B$ and $(2n-1)\tau_B \le t \le (2n)\tau_B$ represent the electric energy deposit (Figure 3-24a) and extraction (Figure 3-24b) respectively.

During the time interval $(2n-2)\tau_B \leq t \leq (2n-1)\tau_B$ with every successive propagation from z_{B_0} to z_{B_f}. The amplitude of the propagating voltage waveform reduces. The implications of this are that the electric energy deposited on Line B is reduced with successive propagation cycles. During the first propagation interval i.e. $0 \leq t \leq \tau_B$ the maximum amount of electric energy $U_{CeB_{Max}}$ is stored in C_{eB}. The maximum electric energy stored is

$$U_{EB} \equiv U_{CeB_{Max}} = \frac{1}{2} C_{eB} (V_0)^2 \tag{3.80}$$

After the Forward propagating waveform contacts the boundary at z_{B_f}. The short-circuit boundary conditions necessitate that the propagating voltage waveform collapses. This facillitates the extraction of electrical energy previously stored in C_{eB}. This electric energy is subsequently converted to magnetic energy $U_{EB} \rightarrow U_{HB}$. The energy deposit and extraction processes are responsible for producing the pulsating triangular waveforms observed in the voltage as well as the electric energy progressions. As seen in Figure 3-25a and Figure 3-26b respectively.

Once the magnitude of the voltage progression on Line B is at a minimum i.e. $V_B(t) \cong 0$. The energy conversion process is essentially complete. This occurs at time instances of $t = \frac{(4n-3)T_0}{4}$. At this point no electric energy is deposited in the self-capacitance C_{eB} and hence zero electric energy is present on Line B.

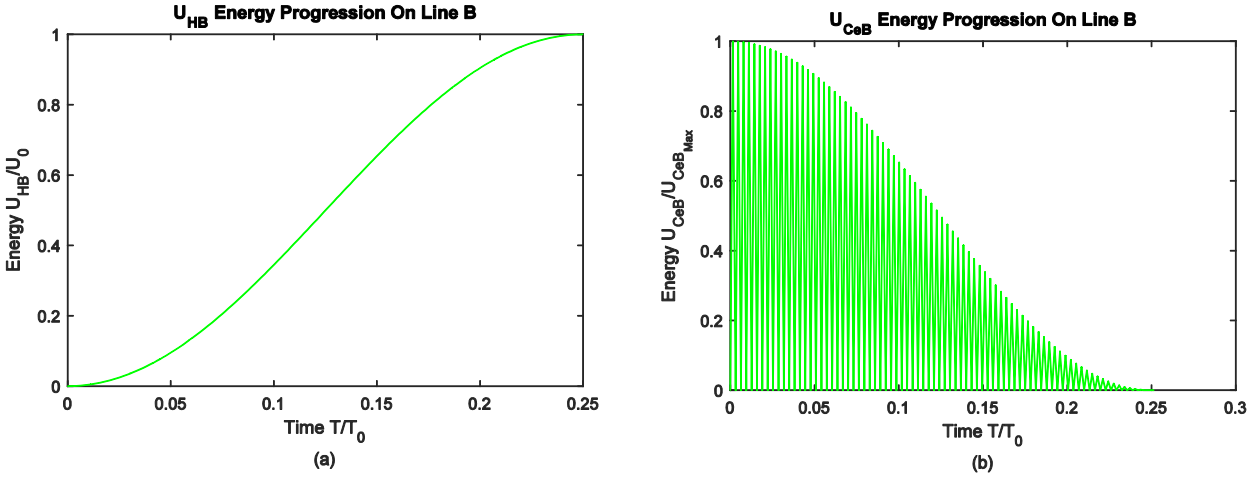


Figure 3-26: Normalized Energy Progressions Line B (a) U_{HB} (b) U_{CeB}

3.5.2.3 Summary

From the various results presented in Figure 3-22 to Figure 3-26 some principle conclusions about the electric to magnetic energy manipulation processes can be drawn. Firstly, considering the energy interactions that take place in the capacitor. During the energy extraction a cosinusoidal decline in the voltage progression is seen whilst a sinusoidally bounded pulsating triangular current progression is also seen. The pulsating nature of the current progression speaks to the fact that current and hence magnetic energy is being stored and discharged in the self-inductance of the capacitor in order to facilitate the energy conversion process from electric to magnetic energy.

The peaks in magnetic energy coincide with time instances where the propagating waves are incident at z_{A_f} whilst the nadir of the spikes occur at time instances when the propagating waveforms are incident at z_{A_0}.

Now considering the energy interactions in the inductor the following conclusions can be made. The sinusoidal rise in current predicted by circuit theory is seen. However, it is accompanied by a pulsating sinusoidally bounded voltage progression. The pulsating nature of the voltage progression is indicative of electrical energy storage and discharge in the self-capacitance of the inductor at instances when electrical energy is converted to magnetic energy. The subsequent peaks in electrical energy occur at instances when the propagating waveforms are incident at z_{B_f} whilst the nadir of the spikes occur at instances where the propagating waveforms are incident at z_{B_0}.

3.6 Conclusion

Transmission line models for the reactive components are derived and implemented in terms of 1-D TLM Link-Line models. It is shown that the reactive components can be completely characterised by the Link-Line TL model provided the propagation delay and characteristic impedance are determined. The 1-D TLM discretises the reactive component in a singular dimension of assumed current flow and propagation. A key benefit in using Link-Line models is the ability to decouple large multi-stage circuits. This decoupling allows for specific portions or subsystems like the *Twin Capacitor* topology and LC Resonant tank found in SCC and SMPS respectively, to be simulated and analysed in isolation. Limitations in modelling energy manipulation processes are assessed in the *Twin Capacitor* and the LC Resonant tank topologies. Modelling the energy manipulation processes with 1-D TLM Link-Line equivalents reveals nuances in the electric to electric and electric to magnetic energy manipulation processes that are not visible with conventional circuit theory. An alternative solution to the *Twin Capacitor* paradox is identified. The solution involves examining voltage and current progressions on the respective transmission lines at various instances in time and the *"Missing Energy"* is found to be stored in the self-inductance of the capacitors. Analysis of the LC Resonant tank reveals a plethora of energy storage and extraction events take place in the self-inductance and self-capacitance of the respective lines. The voltage and current waveform progressions seen in the capacitor and inductor respectively are predicted by conventional circuit theory. However, accompanying these predicted progressions are pulsating sinusoidally bounded current and voltage waveforms in the capacitor and inductor respectively. These pulsating voltage and current progressions give rise to pulsating electric and magnetic energies. The significance of this is that the pulsating magnetic and electric energy must be stored at least momentarily in the self-inductance and self-capacitance of the capacitor and inductor respectively. This is necessary in order to facilitate the electric to magnetic energy manipulation processes in the LC Resonant tank.

4 FRAGMENTATION

4.1 Overview

This chapter explores the concept of *Fragmentation* and how it pertains to two cascaded transmission lines. The concept of *Fragmentation* is established to explain the splitting or fissioning of propagating waves and hence energy flux that takes place at the junction or discontinuity in the event the propagation delays of the respective TL segments are mismatched. This chapter is structured as follows: Firstly, formal definitions pertaining to *Fragmentation* are presented. This is then followed by the identification of fundamental *Fragmentation* generation cases which describe the manner in which new propagating waves or fragments are formed. The three fundamental *Fragmentation* generation cases found are: Finite Fragment Generation Non-Integer Matched Delays (FFGNIMD) Finite Fragment Generation Integer Multiple Delays (FFGIMD); Finite Fragment Generation Matched Delays (FFGMD) and lastly, a special case of FFGNIMD called Infinite Irrational Fragment Generation (IIFG) is also identified. Proceeding this is the development of a generic algorithm that is capable of describing the various interactions that take place on the respective TL segments for the various *Fragmentation* generation cases. The characterisation of the various *Fragmentation* generation cases is a prerequisite in order to quantitatively explore the effects that the interaction of various propagating waves in the system caused by *Fragmentation* have on the energy manipulation processes which are integral to answering the research question.

4.2 Formal Definitions

4.2.1 Fragmentation

For the purposes of this research, it is necessary to formally define *Fragmentation* as follows:

Fragmentation – *The effective splitting or fissioning that occurs when an incident propagating travelling waveform makes contact or reaches a discontinuity between two adjoining cascaded transmission lines at an instant in time when no other propagating waveform is contacting the discontinuity. In this event the incident propagating waveform will fission into two new propagating waveforms in the forward and reverse directions respectively.*

The *Fragmentation* process can be better visualized via a transmission line bounce diagram depicted in Figure 4-1.

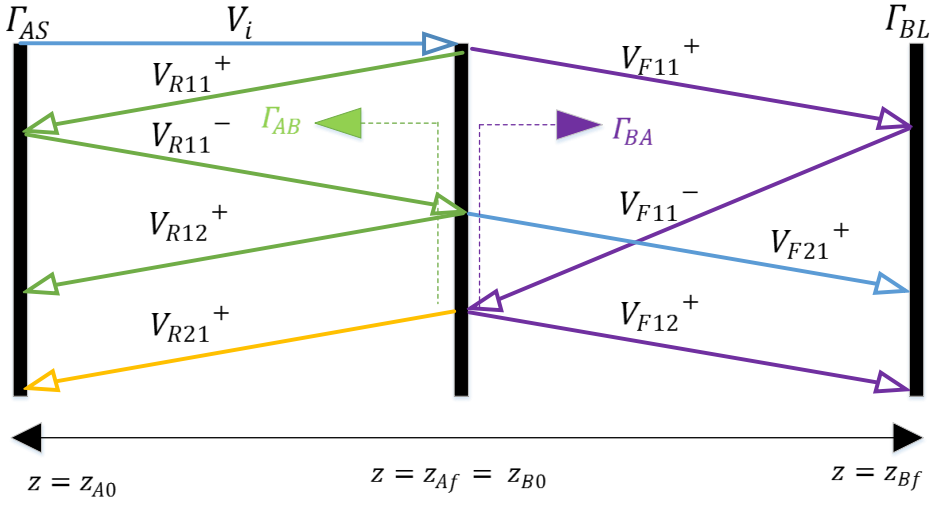


Figure 4-1: Fragmentation Bounce Diagram

4.2.2 Propagating Waveform Characteristics

In Figure 4-1 the initial incident propagating wave denoted by V_i is incident on the discontinuity or junction node of the two adjoining transmission lines, Line A and Line B respectively. Since at the instant V_i arrives at the junction node there are no other propagating travelling waveforms so as a result V_i effectively fissions into two new propagating waveforms. These new propagating waveforms now travelling in the Reverse and Forward directions (w.r.t V_i) are denoted by ${V_{R11}}^+$ and ${V_{F11}}^+$ respectively. The first subscript either "*R*" or "*F*" is indicative of the **Propagation direction** of the travelling waveform. The second subscript represents the **Fragment Number**, this is indicative of how many *Fragmentation* events have taken place prior to the propagating waveform's origin. The last subscript is the **Cycle Number**, this represents how many internal bounce cycles the propagating waveform has completed on its respective line. An internal bounce cycle is defined as one complete round trip starting an ending at the junction node or discontinuity. Lastly the superscript "+" or "−" are indicative of whether the propagating waveform is travelling away from ("+") or towards ("−") the junction or discontinuity. For a Reverse propagating waveform the forward travelling direction ("+") is from right to left and conversely for the Forward propagating waveform the forward travelling direction is from left to right. For both respective propagating waveforms the reverse travelling direction ("−") is the reciprocal of the forward direction and is always towards the junction node or discontinuity.

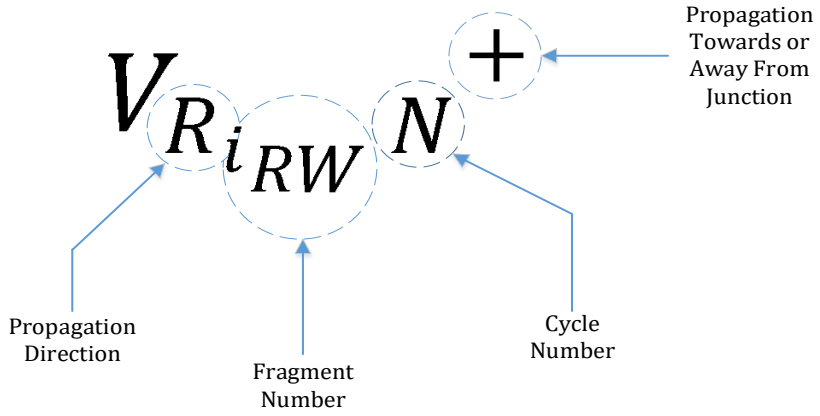


Figure 4-2: Propagating Waveform Characteristics

4.2.3 Fragmentation Ratio

The *Fragmentation Ratio* is representative of the total amount of fragments (i.e. propagating waves) that will ultimately be present on Line A when compared to the total amount of fragments that will be present on Line B. The *Fragmentation Ratio* is now formally derived.

The ratio of the propagation delay of Line A (τ_A) to that of Line B (τ_B) is

$$\tau_A : \tau_B$$

In order to account for cases where the propagation delays of both Line A and B are not necessarily integers but rather rational numbers it makes sense to express the propagation delays of Line A and Line B as fractions, and hence the propagation delays of the respective lines are defined as follows:

$$\tau_A \equiv \frac{\tau_{AN}}{\tau_{AD}} \text{ and } \tau_B \equiv \frac{\tau_{BN}}{\tau_{BD}}$$

Where τ_{AN},τ_{BN} and τ_{AD},τ_{BD} are the numerators and denominators of the propagation delays for Line A and Line B respectively. If τ_A and τ_B are treated as rational numbers then the ratio of the propagation delays can be better expressed as the following product:

$$\tau_{AN}\tau_{BD}:\tau_{BN}\tau_{AD}$$

In order to ascertain the exact number of generated fragments on both Line A and B the products $\tau_{AN}\tau_{BD}$ and $\tau_{BN}\tau_{AD}$ are divided by the Highest Common Denominator (HCD) between them. The ratio of the propagation delays between Line A and Line B is now in its simplest form and hence represents the *Fragmentation Ratio*. The *Fragmentation Ratio* is thus defined as:

$$\frac{\tau_{AN}\tau_{BD}}{HCD}:\frac{\tau_{BN}\tau_{AD}}{HCD}$$

$$F_{RA} \equiv \frac{\tau_{AN}\tau_{BD}}{HCD}, F_{RB} \equiv \frac{\tau_{BN}\tau_{AD}}{HCD}$$

$$F_{RA}:F_{RB} \tag{4.1}$$

F_{RA} and F_{RB} represent the total number of generated fragments or propagating waves on Line A and Line B respectively, and thus F_{RA},$F_{RB} \in \mathbb{Z}$.

4.3 Fragment Generation

The qualitative energy manipulation results presented in Chapter 3 are predicated on the fact that minimal *Fragmentation* occurs on the respective transmission lines. Minimal *Fragmentation* refers to the fact that after the initial *Fragmentation Initiation* or switching event, only singular Reverse and Forward propagating waves are created on Line A and B respectively. Under these conditions, qualitative insight into the electric to electric and electric to magnetic energy manipulation processes are obtained. However, whilst useful these results are constrained by the condition of minimal *Fragmentation* in the system. The implications of which mean that the various recombination and transmission effects experienced at the junction or discontinuity always occur in a consistent and predictable manner. Additionally, the recombination and transmission effects never result in the creation of new propagating waves or fragments. Consequently, the energy flux is always superposed into singular flux streams of the respective propagating waves and never fissions or splits.

This is consistent with the physical conceptions eluded to by Poynting in [47] where the tacit implication formed is that these energy flux streams (by way of the propagating waves) when superposed always form singular energy flux stream systems. However, if the propagation delays of the TL segments are mismatched in anyway, the once consistent manner in which the Reverse and Forward propagating waves (i.e. energy flux streams) experience recombination and transmission effects at the junction or material interface will be disrupted, and hence lead to *Fragmentation* generation events.

The ramifications of these *Fragmentation* generation events mean that the once singular flux streams of the Reverse and Forward propagating waves will fission or split at the junction or discontinuity. In so doing giving rise to new Reverse and Forward propagating waves and hence multiple energy flux streams are now present in the system.

The presence of multiple propagating waves means that the respective line voltages, currents and hence energies are not governed by solitary Reverse and Forward propagating waves as seen in the minimal *Fragmentation* case, but are now governed by the interaction or interference (constructive and destructive) of multiple propagating waves or fragments.

Before a more quantitative description of the energy manipulation processes by way of *Energy Conversion Efficacy* and noise implications takes place (as will be seen later in Chapter 6) it is prudent to characterise the *Fragmentation* generation processes that arise due to arbitrary selection of propagation delays on the TL segments. Effective characterisation is necessary to establish a relationship that is capable of predicting the total number of fragments on the respective TL segments. As seen in Chapter 4.2.3 the nature of this relationship is represented by the *Fragmentation Ratio*. The *Fragmentation Ratio* along with various recombination and transmission effects essentially characterise the *Fragmentation* generation process i.e. the effective splitting or fissioning of the propagating waves and hence the energy flux. This characterisation speaks to the potential effects that may take place due to multiple reflection, recombination and transmissions of the propagating waves or fragments at the junction or discontinuity. Understanding the implications these multiple reflection and transmission effects have on the system energies, and hence the energy manipulation processes is vital to answering the research question presented in Chapter 1.3.

4.3.1 Fragmentation Generation Case Hierarchy

Figure 4-3 illustrates the hierarchy of the fundamental *Fragmentation* generation cases. At the base or foundation of the hierarchical structure is the FFGNIMD *Fragmentation* generation case. This is the most generic *Fragmentation* generation case and from it the FFGIMD and FFGMD *Fragmentation* generation cases are derived. What makes the FFGNIMD case the most generic *Fragmentation* generation case is that no restrictions are imposed on the propagation delays of the transmission line segments (Line A and Line B). The propagation delays of both TL segments are free to be either integer, rational or irrational numbers. If the pairing of propagation delays on the TL segments is such that one propagation delay is a rational number whilst the other propagation delay is an irrational number, this results in the special case of IIFG *Fragmentation* generation. As a consequence of no restrictions being imposed on the propagation delays, the *Fragmentation Ratio* is free to exhibit a non-integer multiple relationship.

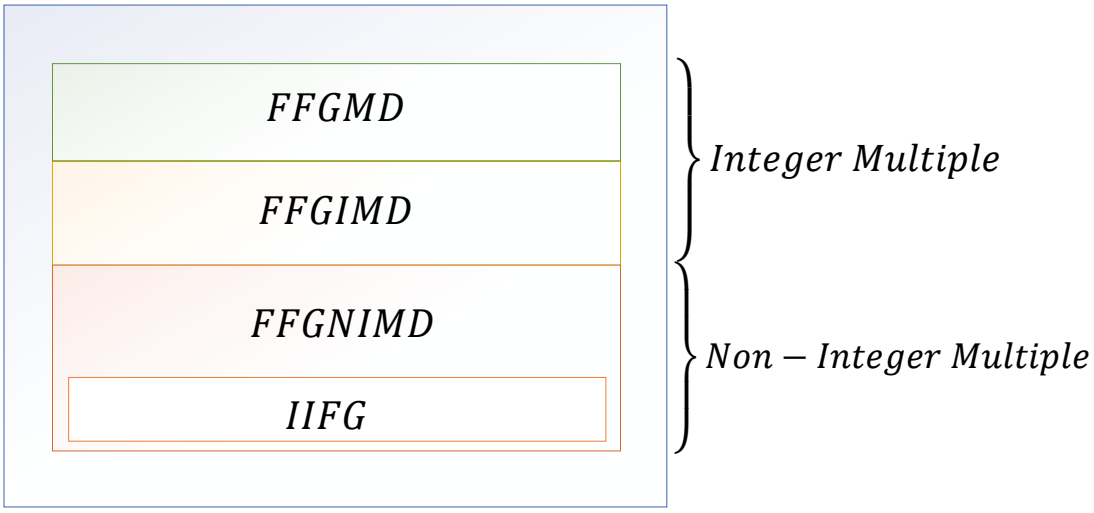


Figure 4-3: Fragmentation Generation Case Hierarchy

If the FFGNIMD *Fragmentation* generation case is generalised somewhat by necessitating that the *Fragmentation Ratio* exhibit an integer multiple relationship, the *Fragmentation* generation case established is FFGIMD. The FFGIMD represents the intermediary level in the *Fragmentation* generation hierarchical structure (as seen in Figure 4-3) where some flexibility in terms of propagation delays is allowed with one principle restriction. In FFGIMD the propagation delays of both TL segment are free to be either integer or rational numbers but are generally restricted from being irrational numbers. However, in the special case where the propagation delay of one TL segment is an irrational number, the propagation delay of the other TL segment must equal the product of the same irrational number and any arbitrary integer. This is necessary in order to ensure that the integer multiple relationship of the *Fragmentation Ratio* is not violated.

The final *Fragmentation* generation case FFGMD is a generalisation of the FFGIMD case. Like the FFGIMD case from which the FFGMD *Fragmentation* generation case is derived, the *Fragmentation Ratio* must maintain an integer multiple relationship. The FFGMD case is the highest level in the *Fragmentation* generation hierarchical structure, and as a consequence is subject to the greatest number of restrictions on the propagation delays of the TL segments. In FFGMD it is necessary that the propagation delays of both TL segments are completely identical. Consequently, this results in a one-to-one *Fragmentation Ratio.* The FFGMD *Fragmentation* generation case typifies the relationship between propagation delays found in conventional 1-D TLM simulation of reactive components that enforce model synchronism [25].

4.3.2 Fragmentation Generation Algorithm

Central to the development of the *Fragmentation* generation cases is the study and observation of how propagating waveforms interact on cascaded transmission line bounce diagrams (Figure 4-7-Figure 4-9). In order to efficiently characterise the various *Fragmentation* generation cases a standardised procedure or algorithm is necessary. In order to keep the algorithm as generic as possible it is prudent to develop it by considering the interactions that take place in the FFGNIMD *Fragmentation* generation case. This is done because all other *Fragmentation* generation cases can be derived from the FFGNIMD case. This means if the algorithm is capable of accurately characterising the FFGINMD case, it will be capable of characterising all the other *Fragmentation* generation cases. The principle rationale in the development of the algorithm lays in studying when the origin Reverse ($i_{RW} = 1$) and Forward ($i_{FW} = 1$) waves experience *Fragmentation* generation events i.e. Fragment Creation as well as the arithmetic sequence formed by the Recombination & Transmission Effects of the origin and various child waves or fragments at the junction or discontinuity.

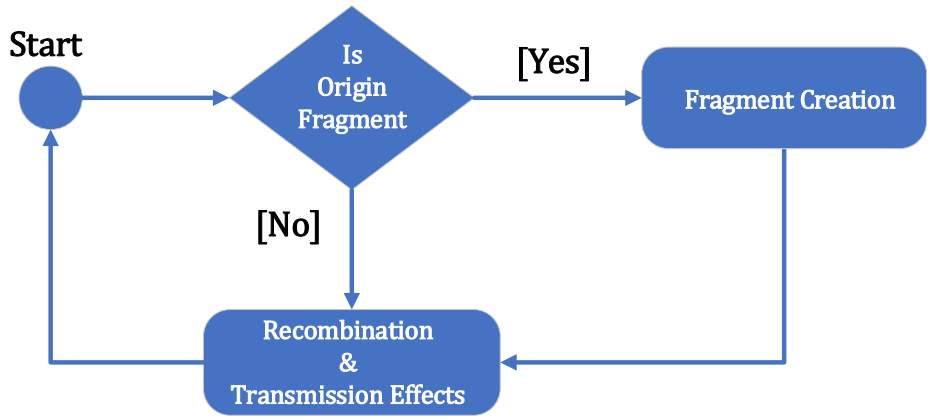


Figure 4-4:High Level Algorithm for Establishing Fragmentation Generation Cases

Figure 4-4 depicts a high-level representation of the algorithm developed in order to establish the level of *Fragmentation* and hence the *Fragmentation* generation case that the cascaded transmission line setup may be subjected to. At the start of the algorithm the *Fragmentation Ratio* is determined. The *Fragmentation Ratio* establishes how many fragments or waves will ultimately propagate on the TL segments. Consequently, this establishes the required internal bounce cycles (N_{FRA} and N_{FRB}) of the origin Reverse and Forward propagating waves or fragments that need to elapse before the Fragment Creation process completes.

The next step in the algorithm is to determine whether or not the propagating wave or fragment approaching the junction or discontinuity is either the origin Reverse or Forward fragment. This is necessary because (as will be seen later) only the origin Reverse and Forward fragments actually participate in the creation of new Reverse and Forward propagating waves or fragments.

A common step in the algorithm for origin and child fragments alike is to determine the various Recombination & Transmission Effects that the origin and child waves or fragments are subjected to at the junction or discontinuity. The manner in which the origin and various child fragments interact at the junction or discontinuity forms a cyclical arithmetic progression that repeats after a specified number of cycles given by the *Fragmentation Ratio*. The consequence of the various Recombination & Transmission Effects is used to determine the state of the fragments for successive internal bounce cycles on the respective TL segments. After the Recombination & Transmission Effects for all fragments have been processed the algorithm returns to the first step and all the steps are repeated for the next internal bounce cycle.

4.3.2.1 Fragment Creation

A more detailed version of the Fragment Creation process shown in Figure 4-4 is presented in Figure 4-5. If the fragment approaching the junction or discontinuity is either the origin Reverse or Forward fragment i.e. V_{R1N} and V_{F1N} it is then evaluated by the Fragment Creation process of the algorithm. The Fragment Creation process has two main aspects. The first being, establishing whether or not N_{FRA} and N_{FRB} cycles have elapsed on the origin Reverse and Forward propagating waves or fragments. The second aspect deals with the creation of new Reverse and Forward propagating waves or child fragments.

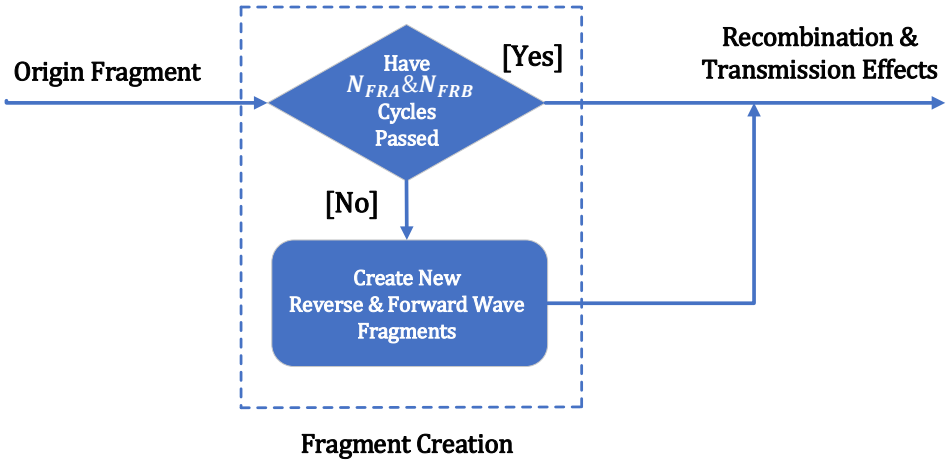


Figure 4-5:Algorithm Determining Fragment Creation At The Junction Or Discontinuity

4.3.2.1.1 Determining N_{FRA} and N_{FRB} cycles

Observing Figure 4-7 it can be seen that only after N_{FRA} and N_{FRB} cycles have elapsed, the origin Reverse and Forward fragments meet at the junction or discontinuity. Considering the origin Reverse propagating wave or fragment first, N_{FRA} represents the number of internal bounce cycles that must elapse before the origin Reverse propagating wave or fragment meets the origin Forward fragment at the junction. Similarly, N_{FRB} speaks to the number of internal bounce cycles that must elapse before the origin Forward propagating wave or fragment comes into contact with the origin Reverse fragment at the junction or discontinuity.

The requisite number of cycles N_{FRA} and N_{FRB} are given by the following expressions:

$$N_{FRA} = F_{RB} \tag{4.2}$$

$$N_{FRB} = F_{RA} \tag{4.3}$$

Where F_{RA} and F_{RB} are obtained from the *Fragmentation Ratio* as per (4.1). After N_{FRA} and N_{FRB} cycles have elapsed no new Reverse and Forward propagating waves or fragments may be created. The origin and generated child fragments will now only experience Recombination & Transmission Effects.

4.3.2.1.2 Create New Reverse & Forward Wave Fragments

Before the generalisation of the newly created Reverse and Forward propagating waves or child fragments takes place, it is necessary to establish the origin Reverse and Forward propagating waves or fragments travelling in both the forward and reverse directions for N_{FRA} and N_{FRB} cycles respectively.

The origin Reverse propagating waveform's 1st internal bounce cycle travelling in the forward direction is given by:

$$V_{R11}{}^{+} = V_i \Gamma_{AB} \leftrightarrow N = 1 \tag{4.4a}$$

If Line A is pre-charged with a specified static voltage V_0:

$$V_{R11}{}^{+} = -V_0 \left[\frac{Z_A}{Z_A + Z_B}\right] \leftrightarrow N = 1 \tag{4.4b}$$

The origin Reverse propagating waveform's 1st internal bounce cycle travelling in the reverse direction is given by:

$$V_{R11}{}^{-} = V_{11}{}^{+} \Gamma_{AS} \leftrightarrow N = 1$$

Thereafter all successive internal bounce cycles of the origin Reverse propagating wave or fragment travelling in the forward direction can be derived. The internal bounce cycles up to and including the N_{FRA} cycle in the forward direction are given by

$$V_{R1N}{}^{+} = V_{R1(N-1)}{}^{-} \Gamma_{AB} \text{ , } 2 \leq N \leq N_{FRA} \text{ where } N \in \mathbb{Z} \tag{4.5}$$

Since there is no other Link-Line segment present at z_{A0} (Line A's Near-End terminals) the generalised expression for the N^{th} internal bounce cycle for the origin Reverse propagating wave or fragment travelling in the reverse direction is given by

$$V_{R1N}{}^{-} = V_{R1N}{}^{+} \Gamma_{AS} \ \ \forall N \tag{4.6}$$

Now considering the origin Forward propagating waveform, the 1st internal bounce cycle travelling in the forward direction is given by:

$$V_{F11}{}^{+} = V_i(1 + \Gamma_{AB}) \leftrightarrow N = 1 \tag{4.7a}$$

Alternatively, If Line A is pre-charged with a specified static voltage V_0 and Line B is initially discharged:

$$V_{F11}{}^{+} = V_0\left[\frac{Z_B}{Z_A + Z_B}\right] \leftrightarrow N = 1 \tag{4.7b}$$

The origin Forward propagating waveform's 1st internal bounce cycle travelling in the reverse direction is given by:

$$V_{F11}{}^{-} = V_{F11}{}^{+}\Gamma_{BL} \leftrightarrow N = 1$$

The generalised expression for the origin Forward propagating wave or fragment travelling in the forward direction for the first N_{FRB} cycles is as follows:

$$V_{F1N}{}^{+} = V_{F1(N-1)}{}^{-}\Gamma_{BA}\ , 2 \le N \le N_{FRB} \text{ where } N \in \mathbb{Z} \tag{4.8}$$

Considering at z_{Bf} (Line B's Far-End terminals) no other Link-Line segments are present, the generalised expression for the origin Forward propagating wave or fragment for the N^{th} internal bounce cycle travelling in the reverse direction is given by

$$V_{F1N}{}^{-} = V_{F1N}{}^{+}\Gamma_{BL}\ \ \forall\, N \tag{4.9}$$

Studying Figure 4-7 it can readily be seen that when the internal bounce cycle of the origin fragments is not equal to N_{FRA}(i.e.F_{RB}) and N_{FRB}(i.e.F_{RA}) respectively. New Reverse and Forward propagating waves or child fragments will be created. New Reverse propagating waves or child fragments are created as a direct consequence of the *Fragmentation* that occurs when the origin Forward propagating wave contacts the junction or discontinuity before N_{FRB} cycles have elapsed. Observing Figure 4-7 a relationship between the Fragment Number (i_{RW}) of the newly created Reverse propagating wave child fragments and the specific internal bounce cycle (N_{FW}) of the origin Forward propagating wave is seen. This relationship is expressed as follows:

$$i_{RW} = \begin{cases} 2, & N_{FW} = 1 \\ 3, & N_{FW} = 2 \\ 4, & N_{FW} = 3 \\ \vdots & \vdots \\ F_{RA}, & N_{FW} = F_{RA} - 1 \end{cases}$$

$$i_{RW} = N_{FW} + 1, 1 \le N_{FW} \le F_{RA} - 1$$

From examining this relationship, the 1st internal bounce cycle for all newly created Reverse propagating waves or child fragments travelling in the forward direction is as follows:

$$V_{Ri_{RW}1}{}^{+} = (1 + \Gamma_{BA})V_{F1N_{FW}}{}^{-}\ , 1 \le N_{FW} \le F_{RA} - 1 \tag{4.10}$$

The creation of New Forward propagating waves or child fragments is the dual of the creation of New Reverse propagating waves or child fragments. A relationship between the Fragment Number (i_{FW}) of the newly created Forward propagating waves or child fragments and the specific internal bounce cycle (N_{RW}) of the origin Reverse propagating wave or fragment leads to the generalised expressions for the 1st internal bounce cycle travelling in the forward direction. The established relationship between i_{FW} and N_{RW} is as follows:

$$i_{FW} = \begin{cases} 2, & N_{RW} = 1 \\ 3, & N_{RW} = 2 \\ 4, & N_{RW} = 3 \\ \vdots & \vdots \\ F_{RB}, & N_{RW} = F_{RB} - 1 \end{cases}$$

$$i_{FW} = N_{RW} + 1, 1 \leq N_{RW} \leq F_{RB} - 1$$

The 1st internal bounce cycle in the forward direction for these newly created Forward propagating waves or child fragments are a direct result of the transmission of the origin Reverse propagating waveform through the junction or discontinuity. This can be expressed as follows:

$$V_{Fi_{FW}1}{}^{+} = (1 + \Gamma_{AB})V_{R1N_{RW}}{}^{-}, 1 \leq N_{RW} \leq F_{RB} - 1 \qquad (4.11)$$

4.3.2.2 Recombination & Transmission Effects

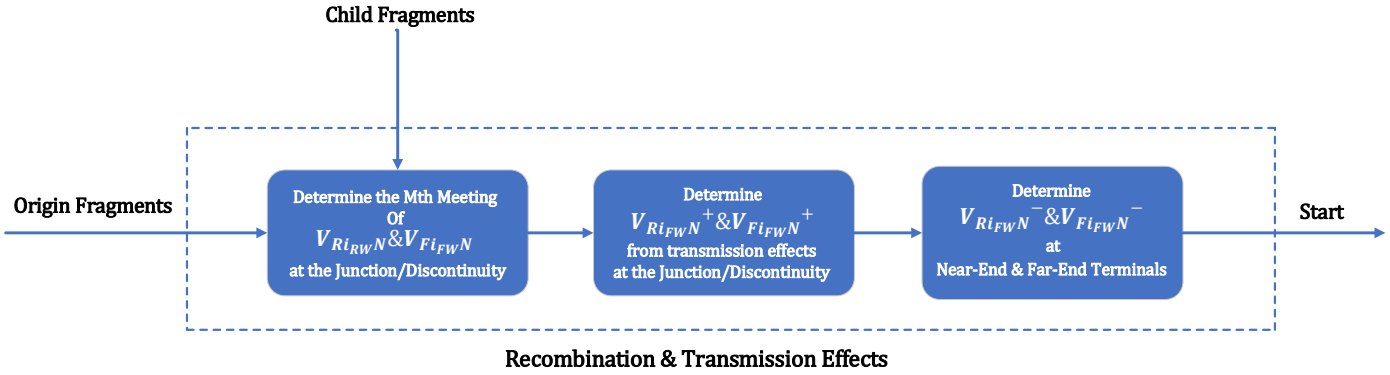


Figure 4-6:Algorithm Detailing Recombination Effects At The Junction Or Discontinuity

Figure 4-6 illustrates a detailed view of the various aspects involved in the Recombination & Transmission Effects of the origin and child fragments. The first step in the algorithm is to determine the M^{th} meeting between specific Reverse and Forward propagating waveforms at the junction or discontinuity. The identification of the M^{th} meeting between fragments is essentially the core or foundation of the recombination effects that take place at the junction or discontinuity. Once the M^{th} meeting has been identified information such as the specific internal bounce cycles and fragment numbers necessary for generalising the Reverse and Forward propagating waves or fragments in the forward and reverse directions can be determined.

4.3.2.2.1 M^{th} Meeting Of $V_{Ri_{RW}N}$ & $V_{Fi_{FW}N}$

Observing Figure 4-7 it can be seen that there is a sort of cyclical progression or sequence to the manner in which the Reverse and Forward propagating waveforms interact at the junction or discontinuity after the Fragment Creation process completes i.e. N_{FRA} and N_{FRB} cycles on the origin Reverse and Forward waves have elapsed..

Considering the case of a ***specific*** Reverse propagating wave or fragment interacting with the various Forward propagating waves or fragments at the junction or discontinuity, the following observations are noted. The manner in which these interactions between fragments takes place at the junction or discontinuity forms a unique arithmetic progression or sequence. The Fragment Number (i_{FW}) of the various Forward propagating waves or fragments that the specific Reverse propagating wave or fragment contacts or meets at the junction or discontinuity is given by:

$$i_{FW} = (N \bmod F_{RB}) + 1 \text{ where } N \geq 1;\ N, i_{FW} \text{ and } F_{RB} \in \mathbb{Z} \tag{4.12}$$

Where:

- i_{FW} – Fragment Number of the Forward propagating waves
- F_{RB} – Total number of Forward propagating waves as per the *Fragmentation Ratio*
- N – Represents the current internal bounce cycle of the specific Reverse propagating wave or fragment.

A specific Reverse propagating waveform will come into contact with the various Forward propagating waveforms or fragments in chronological order of Fragment Number. This happens until contact is made at the junction or discontinuity with the last Forward propagating waveform that was created during the Fragment Creation process. At this instant in time the arithmetic sequence is completed and effectively resets. The specific Reverse propagating waveform will again meet or come into contact with all the various Forward propagating waveforms or fragments at the junction or discontinuity for a second time. This process of completing and resetting the arithmetic sequence will continue *ad infinitum*(indefinitely), and hence the M^{th} meeting between a specific Reverse propagating wave and the various Forward propagating waves or fragments forms a necessary component to characterising the arithmetic sequence.

The developed arithmetic sequence besides being a function of the M^{th} meeting between a specific Reverse propagating wave and the various Forward propagating waves or fragments is also dependent on the Fragment Numbers of the Reverse and Forward propagating waves (i_{RW} and i_{FW} respectively) as well as the total number of Fragments created on Line B (F_{RB})

The arithmetic sequence is thus given by:

$$N = F_{RB}\left(M - 1 + 0^{i_{RW}-1}\right) + (i_{FW} - 1) \tag{4.13}$$

Rearranging and solving for the M^{th} meeting yields:

$$M = \frac{N + F_{RB}(1 - 0^{i_{RW}-1}) - (i_{FW} - 1)}{F_{RB}} \tag{4.14}$$

The internal bounce cycle N_{FW} of the various Forward propagating waves or fragments that will come into contact with a specific Reverse propagating wave or fragment is given by:

$$N_{FW} = F_{RA}\left(M - 1 + 0^{i_{RW}-1}\right) + (i_{RW} - 1) \tag{4.15}$$

The manner in which a ***specific*** Forward propagating wave interacts with various Reverse propagating waves or fragments at the junction or discontinuity, is essentially the dual or the mirror of the case described for a ***specific*** Reverse propagating wave interacting with various Forward propagating waves or fragments at the junction or discontinuity as explained prior. In light of this for brevity the exact process of how the arithmetic sequence forming the M^{th} meeting of the specific Forward propagating wave or fragment with various Reverse propagating waves or fragments will not be restated. However, the necessary equations in order to determine the M^{th} meeting and the internal bounce cycle N_{RW} are presented in equations (4.16)-(4.19).

The Fragment Number (i_{RW}) for the various Reverse propagating waves or fragments that may come into contact with the specific Forward propagating waveform is given by the following:

$$i_{RW} = (N \bmod F_{RA}) + 1 \text{ where } N \geq 1;\ N, i_{RW} \text{ and } F_{RA} \in \mathbb{Z} \tag{4.16}$$

Similarly, where:

- i_{RW} – Fragment Number of the Reverse propagating waves
- F_{RA} – Total number of Reverse propagating waves as per the *Fragmentation Ratio*
- N – Represents the current internal bounce cycle of the specific Forward propagating wave or fragment.

The arithmetic sequence is thus given by:

$$N = F_{RA}\left(M - 1 + 0^{i_{FW}-1}\right) + (i_{RW} - 1) \tag{4.17}$$

The M^{th} meeting at the junction or discontinuity between the specific Forward propagating wave or fragment and various Reverse propagating waves or fragments is as follows:

$$M = \frac{N + F_{RA}(1 - 0^{i_{FW}-1}) - (i_{RW} - 1)}{F_{RA}} \tag{4.18}$$

The internal bounce cycle N_{RW} of the various contacting Reverse propagating waves or fragments can now be expressed as:

$$N_{RW} = F_{RB}\left(M - 1 + 0^{i_{FW}-1}\right) + (i_{FW} - 1) \tag{4.19}$$

4.3.2.2.2 Generalised Expressions For $V_{Ri_{RW}N}{}^{+}$ & $V_{Fi_{FW}N}{}^{+}$

Prior to the Fragment Creation process being completed the generalised expression for the origin Reverse propagating wave or fragment travelling in the forward direction is given by (4.5). However, after the Fragment Creation process is complete ($N > F_{RB}$) the expression for the N^{th} internal bounce cycle in the forward direction making use of equation (4.15) is given by the following:

$$V_{R1N}{}^{+} = V_{R1(N-1)}{}^{-}\Gamma_{AB} + (1 + \Gamma_{BA})V_{i_{FW}(N_{FW})}{}^{-}\ N > F_{RB} \tag{4.20}$$

For all created or child Reverse propagating waves or fragments (i.e. $F_{RA} \geq i_{RW} \geq 2$) the 1st internal bounce cycle in the forward direction is given by equation (4.10). Thereafter for all subsequent internal bounce cycles travelling in the forward direction, the generalised expression for the N^{th} internal bounce cycle is given by

$$V_{Ri_{RW}N}{}^{+} = V_{Ri_{RW}(N-1)}{}^{-}\Gamma_{AB} + (1 + \Gamma_{BA})V_{Fi_{FW}(N_{FW})}{}^{-}\ N \geq 2 \tag{4.21}$$

Considering the origin Forward propagating wave or fragment prior to the completion of the Fragment Creation process, equation (4.8) governs the internal bounce cycles in the forward direction. Thereafter equation (4.22) gives the generalised expression for the N^{th} internal bounce cycle in the forward direction

$$V_{F1N}{}^{+} = V_{F1(N-1)}{}^{-}\Gamma_{BA} + (1+\Gamma_{AB})V_{Ri_{RW}(N_{RW})}{}^{-}\ N \geq F_{RA} \tag{4.22}$$

For all created or child Forward propagating waves or fragments (i.e. $F_{RB} \geq i_{FW} \geq 2$) the 1st internal bounce cycle in the forward direction is given by (4.11) whereas for any subsequent internal bounce cycles thereafter are governed by equation (4.23)

$$V_{Fi_{FW}N}{}^{+} = V_{Fi_{FW}(N-1)}{}^{-}\Gamma_{BA} + (1+\Gamma_{AB})V_{Ri_{RW}(N_{RW})}{}^{-} \tag{4.23}$$

4.3.2.2.3 Generalised Expressions For $V_{Ri_{RW}N}{}^{-}$ & $V_{Fi_{FW}N}{}^{-}$

For all Reverse propagating waves or fragments travelling in the reverse direction the generalised expression for the N^{th} internal bounce cycle is expressed as:

$$V_{Ri_{RW}N}{}^{-} = V_{Ri_{RW}N}{}^{+}(\Gamma_{AS})\ \ \forall\ N \tag{4.24}$$

Similarly, for all Forward propagating waveforms travelling in the reverse direction the generalised N^{th} internal bounce cycle can be expressed as:

$$V_{Fi_{FW}N}{}^{-} = V_{Fi_{FW}N}{}^{+}(\Gamma_{BL})\ \ \forall\ N \tag{4.25}$$

4.3.3 Finite Fragment Generation Non-Integer Multiple Delays

Finite Fragmentation Generation Non-Integer Multiple Delays (FFGNIMD) is the most generic of the *Fragmentation* generation cases as seen in the Fragmentation hierarchy in Figure 4-3. For FFGNIMD fragment generation the propagation delays of Line A and Line B are subject to minimal restrictions. The only principle requirements are that the propagation delays are rational numbers i.e. $\tau_A, \tau_B \in \mathbb{Q}$ and are not integer multiples of one another i.e. $\tau_B \neq k\tau_A$ or $\tau_A \neq k\tau_B$ where $k \in \mathbb{Z}$. The implications of this leads to the most generic *Fragmentation Ratio* of F_{RA}: F_{RB} being established. The interactions of the various Reverse and Forward propagating waves in the FFGNIMD process is illustrated in Figure 4-7. In FFGNIMD multiple Reverse and Forward propagating waveforms will be present on both Line A and B after the Fragment Creation process (as seen in Chapter 4.3.2.1) has been completed. The N^{th} internal bounce cycle expressions for the origin Reverse and Forward propagating waveforms are presented first, and then followed by the expressions for the various created Reverse and Forward propagating waves or child fragments.

4.3.3.1 Origin Propagating Waves

Since the algorithm presented in Chapter 4.3.2 is derived primarily by examining the most generic *Fragmentation* generation case (FFGNIMD) the expressions that characterise the interactions for the origin Reverse and Forward propagating waves in both the forward and reverse directions are given by equations (4.4),(4.7),(4.20),(4.22) ,(4.24) and (4.25)

4.3.3.1.1 Reverse Propagating Wave

The 1st internal bounce cycle for the origin Reverse propagating waveform ($N = 1$) in the forward direction are given by equations (4.4a) and (4.4b). Thereafter during the Fragment Creation process the N^{th} internal bounce cycle in the forward direction is given by (4.5). After the Fragment Creation process equation (4.20) is used to represent the N^{th} internal bounce cycle in the forward direction. The generalised expression for the origin Reverse propagating wave traveling in the reverse direction before and after the Fragment Creation process is given by equation (4.6).

4.3.3.1.2 Forward Propagating Wave

For the origin Forward propagating wave, the 1st internal bounce cycle ($N = 1$) in the forward direction are given by equations (4.7a) and (4.7b) respectively. After the 1st internal bounce cycle but during the Fragment Creation process, the generalised expression for the N^{th} internal bounce cycle travelling in the forward direction is given by equation (4.8). After the Fragment Creation process completes the N^{th} internal bounce cycle expression in the forward direction is now given by equation (4.22). The generalised N^{th} internal bounce cycle expression for the Forward propagating wave travelling in the reverse direction during and after the Fragment Creation process is given by equation (4.9).

4.3.3.2 Created Reverse and Forward Propagating Waves (Child Fragments)

For all newly created or child fragments ($i_{RW}, i_{FW} \geq 2$) of the origin Reverse and Forward propagating waves, the generalised expressions for the internal bounce cycles in the forward and reverse directions are subject to a plethora of Recombination & Transmission Effects that take place at the junction or discontinuity. The generalised expression for all the created Reverse propagating waves in the forward and reverse directions are given by equations (4.10),(4.21) and (4.24). Similarly, for the created Forward propagating waves the generalised expressions for the internal bounce cycles in the forward and reverse direction are given by equations (4.11), (4.23) and (4.25).

4.3.3.2.1 Reverse Propagating Waves

All newly created Reverse propagating waves on Line A occur due to the transmission effect of the origin Forward propagating wave or fragment during the Fragment Creation process. This can readily be seen by examining the 1st internal bounce cycle travelling in the forward direction of all the child Reverse propagating waves which is given by equation (4.10). Thereafter the generalised expression for all child Reverse propagating waves or fragments in the reverse and forward directions are given by equation (4.21) and (4.24) respectively.

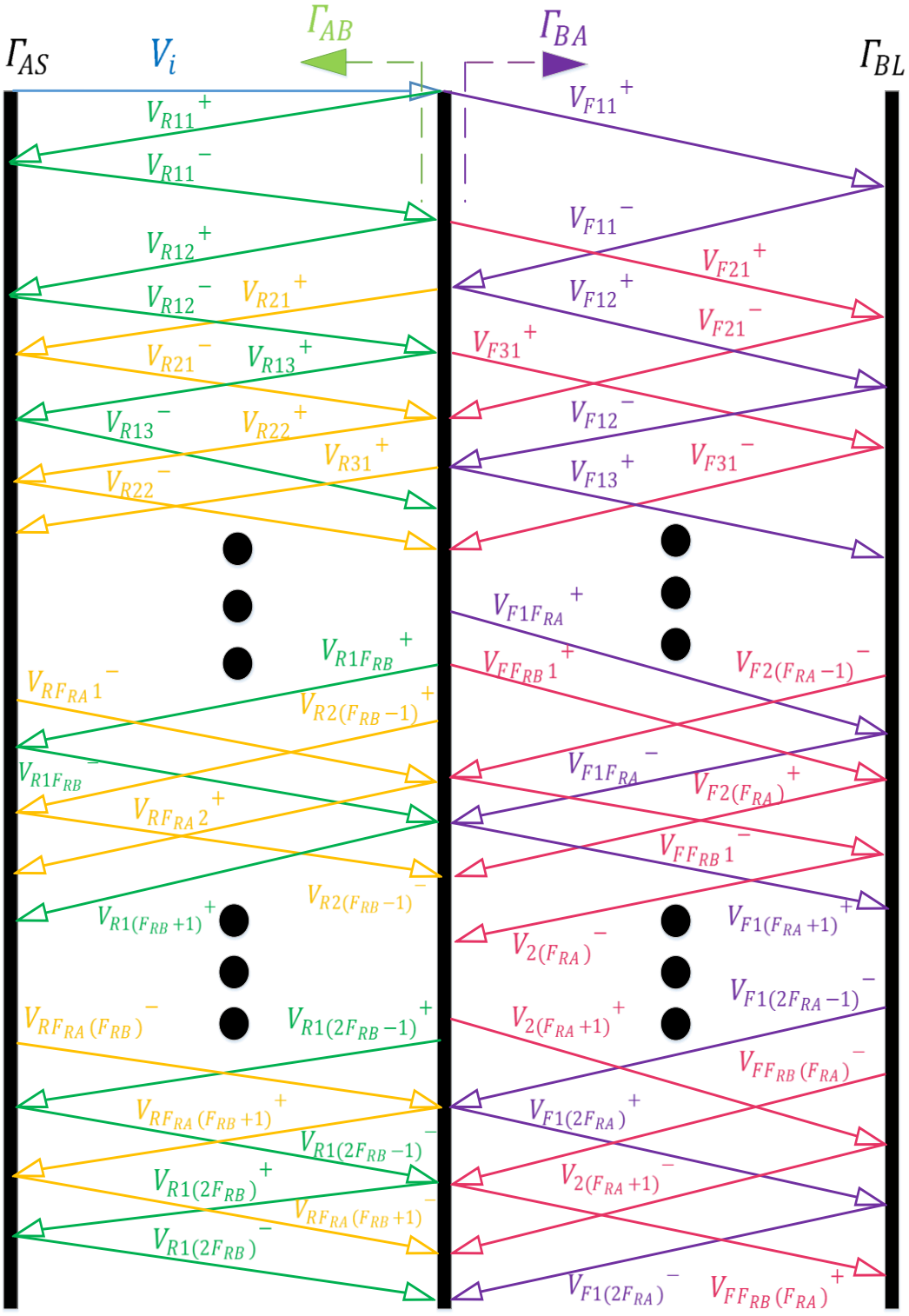


Figure 4-7: Finite Fragment Generation F_{RA}: F_{RB} (FFGNIMD)

4.3.3.2.2 Forward Propagating Waves

For all the newly created child or Forward propagating fragments on Line B originate from a partial transmission of the origin Reverse propagating wave or fragment at the junction or discontinuity that occurs during the Fragment Creation process. Equation (4.11) speaks to this fact, as the influence of the origin Reverse fragment can be seen in the 1st internal bounce cycle of all child fragments travelling in the forward direction. Equations (4.23) and equation (4.25) govern all the subsequent internal bounce cycles thereafter travelling in the forward and reverse directions respectively.

4.3.4 Infinite Irrational Fragment Generation

Infinite Irrational Fragment Generation (IIFG) is a special case of the FFGNIMD *Fragmentation* generation case. In the IIFG *Fragmentation* generation case the Fragment Creation process is never completed, hence an infinite number of propagating waves or fragments are created. In order to achieve a IIFG *Fragmentation* generation case the propagation delays of Line A and Line B cannot be integer multiples of one another i.e. $\tau_B \neq k\tau_A$ or $\tau_A \neq k\tau_B$ where $k \in \mathbb{Z}$ additionally either τ_A or τ_B cannot be a rational number i.e. $\tau_A \notin \mathbb{Q}$ or $\tau_B \notin \mathbb{Q}$ .This ultimately ensures that a non-integer multiple *Fragmentation Ratio* is established like in the FFGNIMD *Fragmentation* generation case. In all finite *Fragmentation* generation cases (FFGMD, FFGIMD and FFGNIMD) the *Fragmentation Ratio* predicts the exact number of fragments that will propagate on the respective TL segments once the Fragment Creation process is completed. However, in IIFG the Fragment Creation process never completes and so the *Fragmentation Ratio* merely predicts the rate at which fragments are created on the respective transmission lines. This is because the actual number of generated fragments will tend to infinity i.e. $F_{RA}, F_{RB} \to \infty$.

4.3.4.1 Origin Propagating Waves

Similarly, as with the FFGNIMD case the 1st internal bounce cycle for the origin ($i_{RW}, i_{FW} = 1$) Reverse and Forward propagating waves or fragments in the forward and reverse directions are given by equations (4.4a),(4.4b),(4.6) and (4.7a),(4.7b),(4.9) respectively. However, a principle difference in the IIFG *Fragmentation* generation case is that the Fragment Creation process never completes. The implications of this mean that aside from an infinite number of fragments or propagating waveforms being created. The origin Reverse and Forward propagating waves or fragments will never interact, and hence will experience no Recombination & Transmission Effects at the junction or discontinuity. This means the generalised expressions for the N^{th} internal bounce cycles for the Reverse and Forward propagating waves or fragments in the forward directions need to be revised.

4.3.4.1.1 Reverse Propagating Wave

Since in IIFG the Fragment Creation process never completes the generalised expression for the N^{th} internal bounce cycle in the forward direction is determined by modifying equation (4.5) to indicate its validity for all internal bounce cycles after the 1st internal bounce cycle. The new generalised N^{th} internal bounce cycle expression for the origin Reverse propagating wave or fragment in the forward direction is given by:

$$V_{R1N}{}^{+} = V_{R1(N-1)}{}^{-}\Gamma_{AB} \; N \geq 2 \text{ where } N \in \mathbb{Z} \tag{4.26}$$

The generalised expression in the reverse direction is given by equation (4.6).

4.3.4.1.2 Forward Propagating Wave

Similar to the origin Reverse propagating wave on account of the Fragment Creation process never completing the expression for the N^{th} internal bounce cycle in the forward direction requires modification. Since the origin Forward propagating waveform will never interact with another Reverse propagating wave or fragment at the junction or discontinuity, the generalized expressions in both the forward and reverse directions are governed solely by the reflection coefficients Γ_{BA} and Γ_{BL}. The new generalized expression for the N^{th} internal bounce cycle in the forward direction is given by:

$$V_{F1N}{}^{+} = V_{F1(N-1)}{}^{-}\Gamma_{BA}\ , N \geq 2 \text{ where } N \in \mathbb{Z} \tag{4.27}$$

The generalised expression in the reverse direction is again given by equation (4.9).

4.3.4.2 Created Reverse and Forward Propagating Waves (Child Fragments)

For all newly created Reverse and Forward propagating waves the 1st internal bounce cycle in the forward directions are still governed by equations (4.10) and (4.11) respectively. However, for subsequent internal bounce cycles unlike the origin Reverse and Forward propagating waves or fragments they will be subject to Recombination & Transmission Effects at the junction or discontinuity. The principle difference in the Recombination & Transmission Effects in the IIFG *Fragmentation* generation case when compared to the FFGNIMD case occurs in the arithmetic sequence, and hence the expression for the M^{th} meeting. As a consequence of the Fragment Creation process never completing the arithmetic sequence for a ***specific*** Reverse or Forward propagating wave or fragment interacting with various Reverse or Forward propagating waves or fragments at the junction or discontinuity never resets. Consequently, this means that a ***specific*** Reverse or Forward propagating wave or fragment will only ever meet or interact once the with another Reverse or Forward propagating wave or fragment at the junction or discontinuity. This means that the expression for the M^{th} meeting will always evaluate to unity (i.e. $M = 1$) and as a result, a new expression for the N^{th} internal bounce cycle in the forward direction must be determined.

4.3.4.2.1 Reverse Propagating Waves

Utilising the fact that the M^{th} meeting between propagating waves or fragments given by equation (4.14) always evaluates to unity. The expression for the internal bounce cycle (N_{FW}) of the contacting Forward propagating wave or fragment at the junction or discontinuity is simplified to produce the following:

$$N_{FW} = i_{RW} - 1 \tag{4.28}$$

The expression for the N^{th} internal bounce cycle of a specific Reverse propagating wave or fragment in the forward direction is given by modifying equation (4.21) by substituting (4.28) for the N_{FW} term.

4.3.4.2.2 Forward Propagating Waves

Since the interaction of a specific Forward propagating wave or fragment at the junction or discontinuity is the dual or mirror of the case given for the Reverse propagating waves in Chapter 4.3.4.2.1.

In light of this the expression for the internal bounce cycle (N_{RW}) of the contacting Reverse propagating wave or fragment at the junction or discontinuity is given by the following:

$$N_{RW} = i_{FW} - 1 \tag{4.29}$$

The expression for the N^{th} internal bounce cycle of a specific Forward propagating wave travelling in the forward direction is given by modifying equation (4.21) by substituting (4.29) for the N_{RW} term.

4.3.5 Finite Fragment Generation Integer Multiple Delays

For the case of Finite Fragment Generation Integer Multiple Delays (FFGIMD) the propagation delays of Line A and Line B are integer multiples of one another i.e. $\tau_B = k\tau_A$ or $\tau_A = k\tau_B$ where $k \in \mathbb{Z}$. If $k = 1$ the FFGIMD degenerates to FFGMD because the propagation delays of Line A and Line B will be identical and hence the *Fragmentation Ratio* is 1: 1. If the propagation delays of Line A and B are related by integer multiples other than one i.e. $k \geq 2$ we will truly have a case of FFGIMD. Dependent on the relationship of the propagation delays on the two lines, two different *Fragmentation Ratios* can be realized.

If $\tau_B > \tau_A$ the following *Fragmentation Ratio* is applicable:

$$1{:}\,k \text{ where } F_{RA} = 1 \text{ and } F_{RB} = k$$

Conversely if $\tau_A > \tau_B$ the *Fragmentation Ratio* established will be:

$$k{:}\,1 \text{ where } F_{RA} = k \text{ and } F_{RB} = 1$$

For the instance of $\tau_B = k\tau_A$ with $\tau_B > \tau_A$ the *Fragmentation Ratio* $1{:}\,k$ depicted in Figure 4-8 FFGIMD can be generalized to determine the N^{th} internal bounce cycles for both the origin Reverse propagating wave on Line A and the several Forward propagating waves on Line B.
In this case $F_{RA} = 1$ which is indicative of only a solitary Reverse propagating wave present on Line A, (the origin Reverse propagating wave) whilst various Forward propagating waves or fragments can be seen on Line B as a result of the Fragment Creation process. The number of generated Forward propagating waveforms is equal to F_{RB}. Where $F_{RB} = k \leftrightarrow \tau_B = k\tau_A$.

4.3.5.1 Origin Propagating Waves

Considering that the case of FFGIMD being explored is for a *Fragmentation Ratio* $1{:}\,k$ where $k \in \mathbb{Z}$. The 1st internal bounce cycle for the origin ($i_{RW}, i_{FW} = 1$) Reverse and Forward propagating waves or fragments in the forward and reverse directions are given by equations (4.4a),(4.4b),(4.6) and (4.7a),(4.7b),(4.9) respectively. Since the only propagating wave or fragment on Line A is the origin Reverse wave, the generalised expression for the N^{th} internal bounce cycle for the Reverse and Forward waves in the forward directions are given by simplified expressions of (4.13)-(4.15),(4.17)-(4.19), (4.20),(4.22) and (4.23) whilst in the reverse directions the generalised expressions are still given by (4.24) and (4.25).

4.3.5.1.1 Reverse Propagating Wave

The generalised internal bounce cycle expressions in the forward direction are given by equations (4.4a) and (4.4b) for the 1st internal bounce cycle and equation (4.5) during the Fragment Creation process. Once the Fragment Creation process is complete a simplified expression of equations (4.13)-(4.15) can be derived. This is because only the origin propagating wave exists on Line A. These simplified expressions arise principally due to the simplifications in the expressions for the arithmetic sequence, the M^{th} meeting and the internal bounce cycle N_{FW} of the interacting Forward propagating wave. By setting $i_{RW} = 1$ equations (4.13)-(4.15) reduce to equations (4.30)-(4.32).

The simplified arithmetic sequence is as follows:

$$N = F_{RB}(M) + (i_{FW} - 1)\, N \geq F_{RB} \tag{4.30}$$

The simplified expression for the M^{th} meeting is given by the following expression:

$$M = \frac{N - (i_{FW} - 1)}{F_{RB}}\ M \geq 1 \tag{4.31}$$

The simplified expression for the internal bounce cycle N_{FW} of the contacting Forward propagating wave or fragment is given by:

$$N_{FW} = F_{RA}(M) \tag{4.32}$$

Equation (4.32) can now be substituted into equation (4.20) to determine the expression for the N^{th} internal bounce cycle in the forward direction.

4.3.5.1.2 Forward Propagating Wave

The implications of the 1: *k Fragmentation Ratio* mean that the origin Forward propagating wave or fragment does not participate in the Fragment Creation process and so no new Reverse propagating waves or fragments are created. The expression for the 1st internal bounce cycle in the forward and reverse directions are given by equations (4.7a),(4.7b),(4.9) respectively. As a consequence of only one Reverse propagating wave being present on Line A the origin Forward propagating wave will experience Recombination & Transmission Effects at the junction or discontinuity solely due to the origin Reverse propagating wave. This is reflected in the simplification of equations (4.17)-(4.19).The simplified expressions are given by equations (4.33) to (4.35).

Since the Fragment Numbers of the origin Reverse and Forward propagating wave are both equal to one i.e. $i_{RW} = i_{FW} = 1$,the arithmetic sequence can be simplified to the following expression:

$$N = F_{RA}(M)\ N \geq F_{RA} \tag{4.33}$$

The simplified expression for the M^{th} meeting between the origin Reverse and Forward propagating waves at the junction or discontinuity is given by:

$$M = \frac{F_{RA}}{N}, M \geq 1 \tag{4.34}$$

The current internal bounce cycle of the origin Reverse propagating waveform denoted N_{RW} is given by:

$$N_{RW} = F_{RB}(M) \tag{4.35}$$

Equation (4.35) is then substituted into (4.22) to ascertain the generalised expression for the N^{th} internal bounce cycle in the forward direction

4.3.5.2 Created Reverse and Forward Propagating Waves (Child Fragments)

For a $1:k$ *Fragmentation Ratio* there are no newly created or child Reverse propagating wave or fragments. This is a direct consequence of the origin Forward propagating wave not participating in the Fragment Creation process. However, for a $k:1$ *Fragmentation Ratio* the dual or mirror of this case would be seen with only a solitary Forward propagating wave on Line B with numerous created or child Reverse propagating waves on Line A. For the newly created or child Forward propagating waves the Recombination & Transmission Effects experienced at the junction are greatly simplified. This is principally due to the fact the only propagating waveform that the various Forward propagating waveforms can interact with at the junction or discontinuity is the origin Reverse propagating waveform. This again leads to the simplification of equations (4.17)-(4.19).

4.3.5.2.1 Reverse Propagating Waves

Since the *Fragmentation Ratio* being considered is $1:k$ this means that there are no propagating waves on Line A apart from the origin propagating wave. That being said if the *Fragmentation Ratio* is changed to $k:1$ this will result in numerous newly created or child Reverse propagating waves effectively forming the dual or mirror of the situation being considered for a $1:k$ *Fragmentation Ratio*.

4.3.5.2.2 Forward propagating waves

For the numerous newly created or child Forward propagating waves the 1st internal bounce cycle in the forward direction is still given by equation (4.11). For all subsequent internal bounce cycles the Recombination & Transmission Effects due to the solitary Reverse propagating wave on Line A need to be considered. As stated prior the implications of a sole Reverse propagating wave leads to simplified expressions for equations (4.17)-(4.18). However, since in this instance the Fragment Number is not equal to unity, equations (4.33)-(4.35) are not directly applicable. Simplified expressions are obtained by again setting $i_{RW} = 1$ but allowing i_{FW} to vary i.e. $F_{RB} \geq i_{FW} \geq 1$. The new simplified expressions are given by equations (4.36) and (4.37).

As prior stated since $F_{RA} = 1$, $i_{RW} = 1 \; \forall i_{FW}$ the simplified arithmetic sequence is given by:

$$N = F_{RA}(M - 1) \tag{4.36}$$

The simplified M^{th} expression is given by:

$$M = \frac{N + F_{RA}}{F_{RA}}, M \geq 1 \tag{4.37}$$

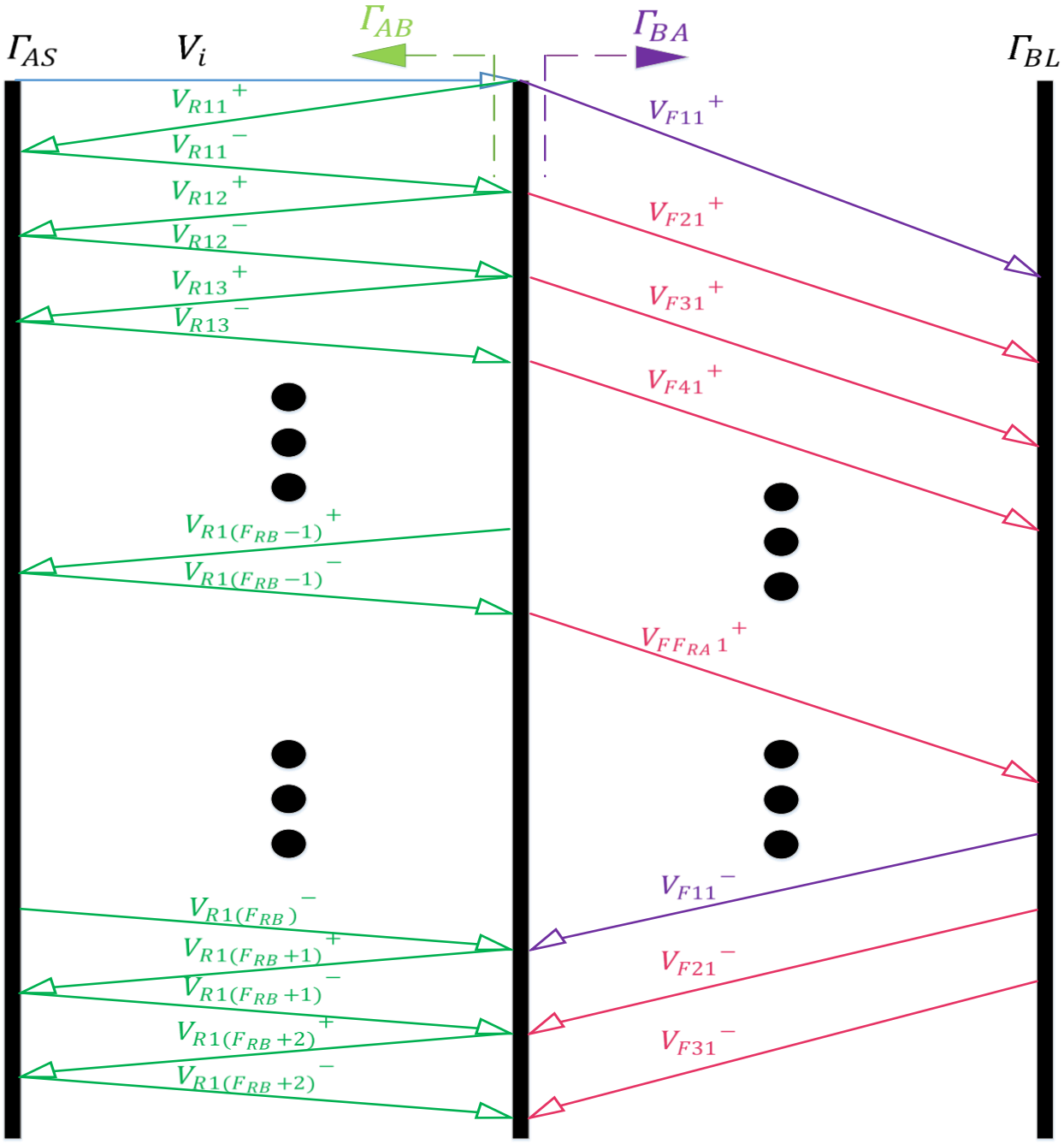


Figure 4-8: Finite Fragment Generation $1:k$ *(FFGIMD)*

The simplified expression given by equation (4.37) can then be substituted into equation (4.15) which is then ultimately substituted into equation (4.23) to give the generalised expression for the N^{th} internal bounce cycle in the forward direction.

4.3.6 Finite Fragment Generation Matched Delays

The Finite Fragment Generation Matched Delays (FFGMD) is the *Fragmentation* generation case with the most stringent restrictions on the propagation delays of the TL segments. The propagation delays of Line A and Line B are required to be completely identical i.e. $\tau_A = \tau_B$. The identical propagation delays facilitate a *Fragmentation Ratio* of $1:1$, where $F_{RA} \equiv F_{RB} = 1$. This means that other than the origin Reverse and Forward propagating waves that arise from the first *Fragmentation* initiation event as a direct consequence of V_i contacting the junction or discontinuity. No additional Reverse and Forward propagating waveforms are created. The interactions between the origin Reverse and Forward propagating waveforms are illustrated in Figure 4-9.

4.3.6.1 Origin Propagating Waves

In the FFGMD *Fragmentation* generation case there is no period of Fragment Creation and so apart form the 1st internal bounce cycle, all successive internal bounce cycles are subject to Recombination & Transmission Effects. The expressions for the 1st internal bounce cycle for the Reverse and Forward propagating waves in the forward and reverse directions are given by equations (4.4a),(4.4b),(4.6) and (4.7a),(4.7b),(4.9) respectively. For all internal bounce cycles thereafter travelling in the forward and reverse directions are governed by equations (4.20) ,(4.24) and (4.22),(4.25) .

4.3.6.1.1 Reverse Propagating Wave

As a consequence of the identical propagation delays imposed by the FFGMD *Fragmentation* generation case the Recombination & Transmission Effects imposed on the origin Reverse propagating wave ensures that it exclusively interacts with the origin Forward propagating wave for every internal bounce cycle except the 1st. The N^{th} internal bounce cycle expressions are thus given by equations (4.20) and (4.24).

4.3.6.1.2 Forward Propagating Wave

Similar to the case of the origin Reverse propagating wave the restrictions on the propagation delays ensure that the origin Reverse and Forward propagating waves interact or meet one another for every internal bounce cycle except the first. Equations (4.22) and (4.25) give the generalised expressions for the N^{th} internal bounce cycle in both the forward and reverse directions.

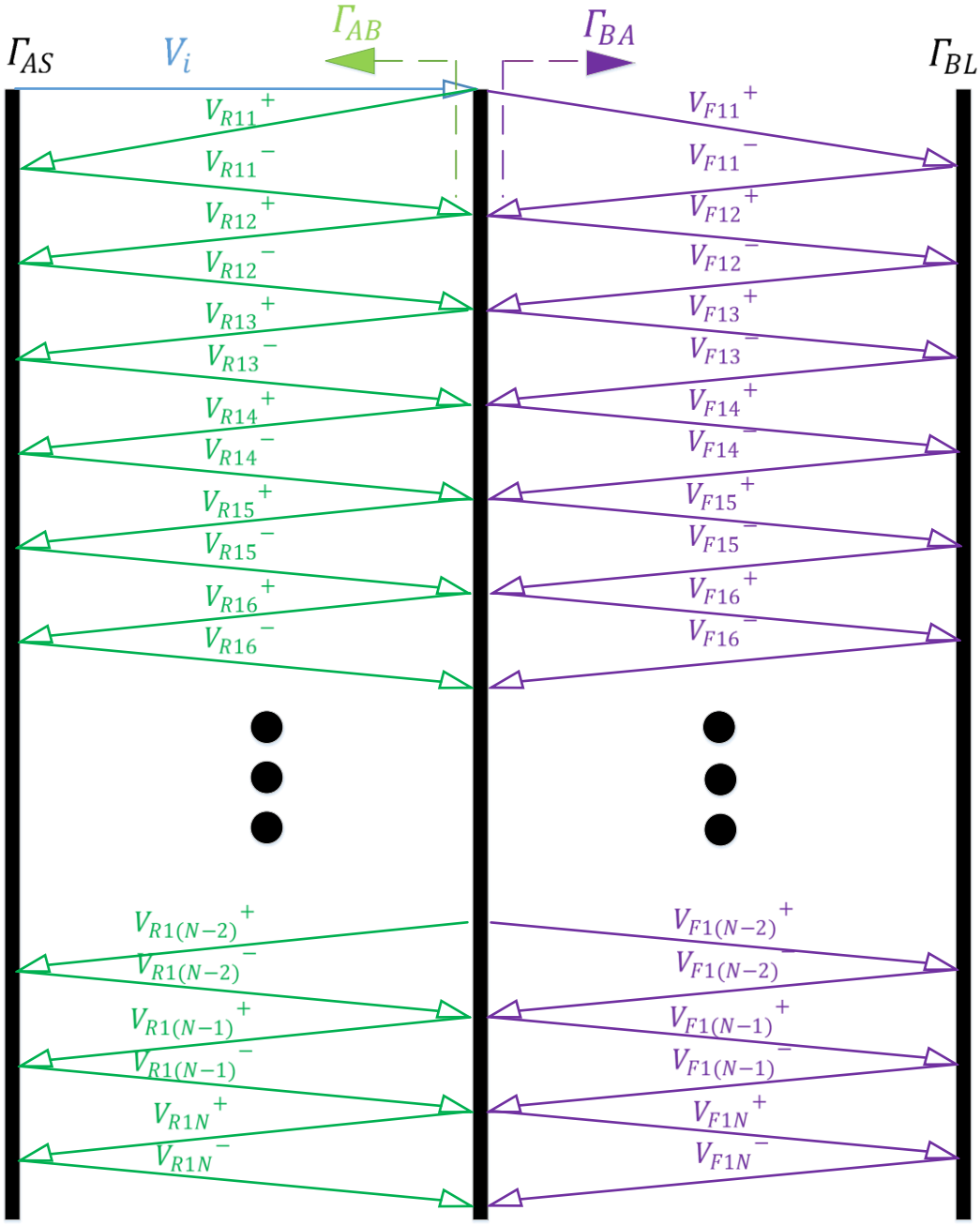


Figure 4-9: Finite Fragment Generation 1: 1 *(FFGMD)*

4.4 Conclusion

In this chapter the concept of *Fragmentation* is introduced and three principal *Fragmentation* generation cases FFGNIMD, FFGIMD and FFGMD are identified. An additional *Fragmentation* generation case IIFG is also identified as a special or unique case of the FFGNIMD *Fragmentation* generation case. *Fragmentation* at its core represents the effective splitting or fissioning of a propagating waveform at a junction or discontinuity of two cascaded TL segments. A generalized algorithm based on the FFGNIMD *Fragmentation* case is presented in order to completely characterize the various *Fragmentation* generation cases. The application of the algorithm leads to generalized expressions for the N^{th} internal bounce cycles for all propagating waves or fragments in the various *Fragmentation* generation cases.

Dependent on the propagation delays of the TL segments a *Fragmentation Ratio* is established. The classification of the *Fragmentation* generation cases is governed by the *Fragmentation Ratio*. The *Fragmentation Ratio* speaks directly to the number of propagating waves or fragments that will be present on the respective transmission lines. As the number of fragments or propagating waves are increased on the TL segments the frequency of reflection and recombination effects at the junction is increased. The manner in which these reflection and transmission effects interact at the junction or discontinuity is of vital importance because the nature of this interaction at the junction or boundary extremities ultimately affects the line voltages,currents and energies and hence the energy manipulation processes.

5 FRAGMENTATION SIMULATOR REALISATION

5.1 Overview

This chapter provides a high-level description of an approach to implementing and realising the *Fragmentation* generation process outlined in Chapter 4. The implementation algorithm is broken down into three areas namely Pre-Processing, Processing and Post-Processing. Presentation of the algorithm is achieved using activity diagrams and various code listings where appropriate. Key abstractions in modelling the Forward and Reverse propagating waves lend themselves to implementation in a programming language that supports OOP.

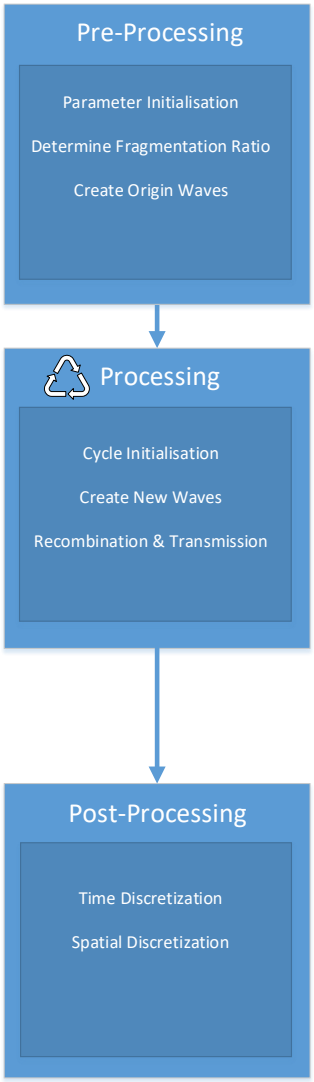


Figure 5-1: Fragmentation Generation Algorithm

5.2 Pre-Processing

All functions and activities in the pre-processing block pertain to establishing the initial conditions before the algorithm effectively starts. In pre-processing, the main activities lay in the creation and initialisation of the simulation variables. After the initialisation of the critical simulation parameters, the creation of the origin Reverse and Forward propagating waves follows. Lastly based on the propagation delays of the respective lines the *Fragmentation* ratio and whether or not the *Fragmentation* generation process completes can be ascertained.

5.2.1 Parameter Initialisation

In order for the simulator to run effectively, the following key parameters need to be initialised. These parameters essentially establish the simulation environment of the cascaded TL segments. The pertinent simulation parameters during initialisation are as follows:

- $T_D -$ Desired simulation time $[ns]$
- $V_0 -$ Initial charge/Source voltage $[V]$
- $\tau_A -$ Propagation delay on Line A $[ns]$
- $\tau_B -$ Propagation delay on Line B $[ns]$
- $Z_A -$ Characteristic impedance of Line A $[\Omega]$
- $Z_B -$ Characteristic impedance of Line B $[\Omega]$
- $Z_{SA} -$ Impedance at z_{A_0} terminals $[\Omega]$
- $Z_{BL} -$ Impedance at z_{B_f} terminals $[\Omega]$
- $\Gamma_{AB} -$ Reflection coefficient from Line A to Line B
- $\Gamma_{BA} -$ Reflection coefficient from Line B to Line A
- $\Gamma_{AS} -$ Reflection coefficient at z_{A_0} terminals
- $\Gamma_{BL} -$ Reflection coefficient at z_{B_f} terminals

These key simulation parameters should ideally be contained in a centralised data structure or container. This should be done in order to ensure that various other functions and subroutines in the program are able to gain access to these parameters when required.

The user is free to arbitrarily assign any value to the initial parameters however, special care must be taken when selecting Z_A and Z_B. The differences in the characteristic impedances of Line A and Line B denoted ΔZ must not exceed $1 \times 10^8 \Omega$ i.e. $\Delta Z = |Z_A - Z_B| < 1 \times 10^8 \Omega$. This is necessary to ensure that $\Gamma_{AB} < 1$ because if $\Gamma_{AB} = 1$ the terminal at z_{Af} essentially represents an open-circuit and as a result no energy will be transferred to the adjoining Line B.

In order to establish the initial conditions necessary to simulate the *Twin Capacitor* topology the magnitudes of the characteristic impedances of both lines must be relatively similar. In essence ΔZ is appreciably small. A secondary condition requires that the impedance at Line B's end terminals needs to be infinite i.e. $Z_{BL} = \infty$. This is necessary to ensure $\Gamma_{BL} = 1$ which establishes open-circuit boundary conditions at z_{B_f}.

Alternatively, the conditions necessary to simulate the LC resonant tank rely on two principle conditions. The first condition is that the difference in characteristic impedances of Line A and Line B must be appreciably large. In essence ΔZ is appreciably large. The second condition is that $Z_{BL} = 0$ in order to establish a $\Gamma_{BL} = -1$ which facilitates the short-circuit boundary conditions at z_{B_f}. Listing 1 depicts a possible implementation of the initial parameter initialisation for the simulator.

```
//   PARAMETER INITIALISATION
Function ParameterInitialisation(V0,TD,TA,TB,ZA,ZB,ZSA,ZLB)
    V_0 = V0;// Charge Voltage [V]
    T_D = TD;// Desired Simulation Time [ns]
    T_A = TA;// Propagation Delay Line A [ns]
    T_B = TB;// Propagation Delay Line B [ns]
    Z_A = ZA;// Characteristic Impedance Line A [Ohms]
    Z_B = ZB;// Characteristic Impedance Line B [Ohms]
    Z_SA = ZSA;// Impedance @ z_A_0 terminal [Ohms]
    Z_LB = ZLB;// Impedance @ z_B_f terminal [Ohms]
    Refl_Coeff_AB = (Z_B-Z_A)/(Z_A+Z_B);// Refl Coeff @ z_A_f
    Refl_Coeff_BA = -Refl_Coeff_AB;// Refl Coeff @ z_B_0
    Refl_Coeff_Line_A_End = (Z_SA-Z_A)/(Z_SA+Z_B);// Refl Coeff @ z_A_0
    Refl_Coeff_Line_B_End = (Z_LB-Z_B)/(Z_LB+Z_B);// Refl Coeff @ z_B_f
End
```

Listing 1: Parameter Initialisation

5.2.2 Determine Fragmentation Ratio

After the initialisation of the key simulation parameters, the *Fragmentation* ratio must be determined. The *Fragmentation* ratio is determined as per (4.1). The procedure required to determine the *Fragmentation* ratio is given by the activity diagram in Figure 5-2.

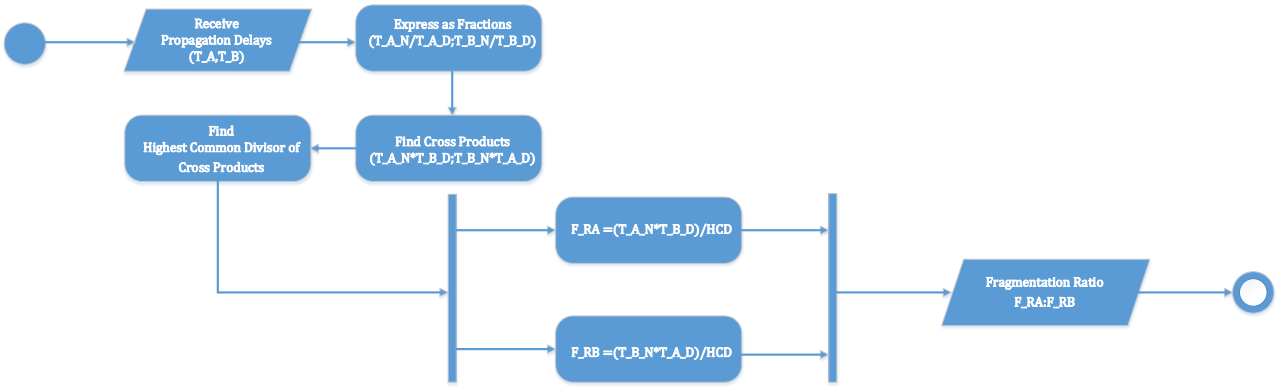


Figure 5-2: Determine Fragmentation Ratio (F_{RA}: F_{RB})

The propagation delays τ_A and τ_B are fetched after a function call is made to the parameter initialisation routine seen in Listing 1. The propagation delays are then expressed as fractions and then subsequently cross-multiplied to form two distinct products. The distinct cross products will eventually represent the total number of generated fragments on their respective lines once divided by the greatest common divisor. At this point the *Fragmentation* ratio (F_{RA}: F_{RB}) given by (4.1) has been successfully determined. This can now be used to process whether or not the *Fragmentation* process completes within the desired simulation time (T_D). It is of utmost importance to establish whether the *Fragmentation* process completes because this has implications on the number of new fragments created.

If the *Fragmentation* process does not complete, the origin Reverse and Forward waves will not create the total number of fragments given by the *Fragmentation* ratio $F_{RA}: F_{RB}$. The simulation parameters involved in ascertaining whether the *Fragmentation* generation process completes are as follows:

- $First\ Meeting\ Time\ (FMT)$ – The instant in time the 1st meeting of the origin Reverse and Forward waves takes place.
- $Fragmentation\ Generation\ Completes (FGC)$ –The *Fragmentation* generation process complete within the desired simulation time (T_D).

Dependent on the *Fragmentation* generation type (FFGMD, FFGIMD, FFGNIMD etc.) the rate at which fragments are created differs. The activity diagram in Figure 5-3 shows the procedure necessary to ascertain whether the *Fragmentation* process completes.

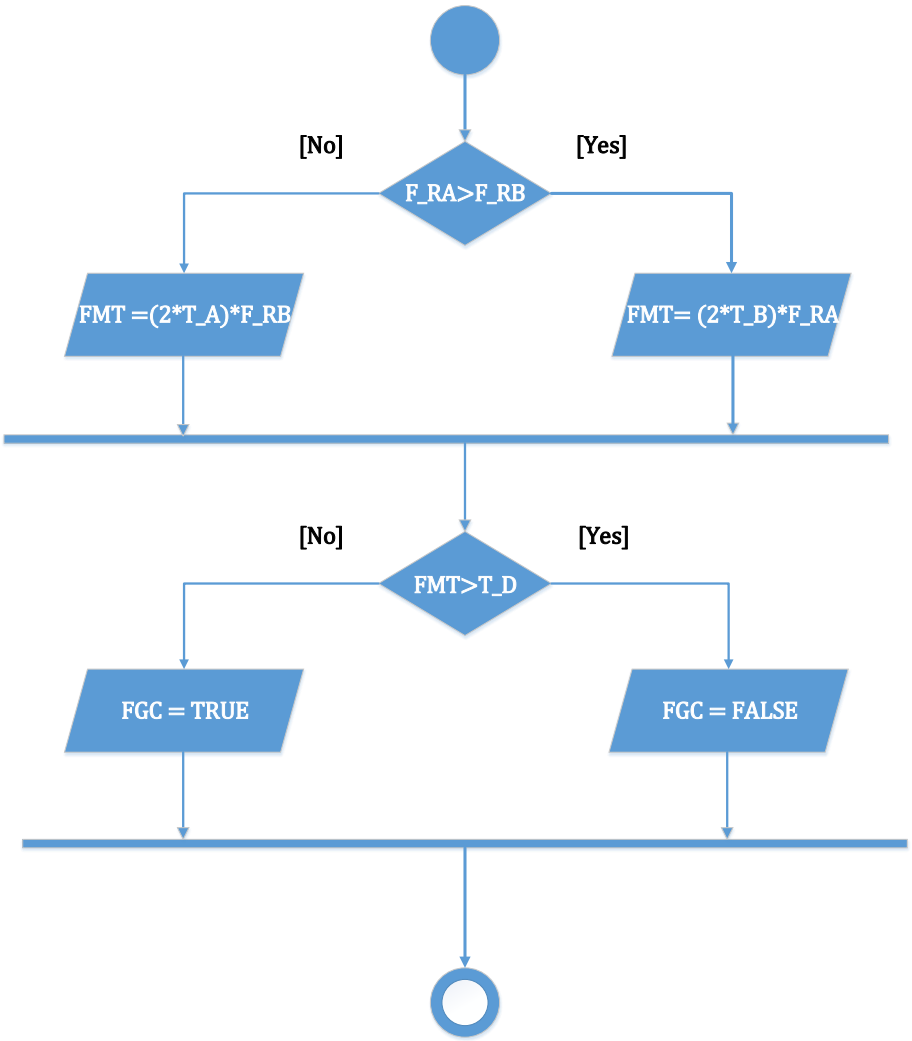


Figure 5-3: State Of Fragment Generation Process

5.2.3 Create Origin Waves

The simulation starts at the instant $t = 0^+$ when the junction switch at z_{A_f} closes. This produces the origin Reverse and Forward propagating travelling waves. Dependent on the *Fragmentation* ratio these origin waves may spawn additional fragments. The behaviour of individual Reverse and Forward waves are best encapsulated by data structures comprised of the following fields:

- $Parent\ Wave$ – The wave fragment number responsible for creating the current fragment.
- $Storage\ Container (RW\ \&\ FW)$ – Storage containers for all generated fragments
- $Time\ Initial\ Start\ (TIS)$ – The initial start time when the fragment is created
- $Internal\ Bounce\ Cycle\ (IBC)$ – Currently completed internal bounce cycles
- $Cycle\ Start\ Time\ (CST)$ – The time the current internal bounce cycle starts
- $Cycle\ End\ Time\ (CET)$ – The time the current internal bounce cycle ends
- $Fragment\ Number\ (FN)$ – Fragment Number $i_{RW}\ or\ i_{FW}$
- $Time\ Incident\ Line\ End\ (TILE)$ – The time the fragment will contact the terminal ends at z_{A_0}(Reverse waves) or z_{B_f}(Forward waves).
- $Voltage\ Incident\ Line\ End\ (VILE)$ – Voltage incident on the terminal ends ${V_{Ri_{RW}}}^{+} or\ {V_{Fi_{FW}}}^{+}$
- $Time\ Incident\ Junction\ (TIJ)$ – The time the fragment will contact the junction at z_{A_f}(Reverse waves) or z_{B_0}(Forward waves)
- $Voltage\ Incident\ Junction\ (VIJ)$ –Voltage that is incident on the junction ${V_{Ri_{RW}}}^{-} or\ {V_{Fi_{RW}}}^{-}$
- $Update$ – Is the fragment allowed to update to a new internal bounce cycle

```
//                      CREATE ORIGIN REVERSE WAVE
Function CreateOriginReverseWave(Ref RW)
        Declare Struct OG_RW; // Initialise Origin Reverse Wave In A Data Container Of
Structures
        OG_RW.Parent_Wave = NaN; ;// Origin Reverse Wave Has No Parent Wave
        OG_RW.TIS = 0;// Initial Start Time Of Wave
        OG_RW.IBC = 1;
        OG_RW.CIBC(1).CST = 0;// Current Inernal Bounce Cycle Start Time
        OG_RW.CIBC(1).TILE = OG_RW.CIBC(1).CST + T_A;// Time Incident @ z_A_0
        OG_RW.CIBC(1).TIJ = OG_RW.CIBC(1).TILE + T_A;// Time Incident @ z_A_f
        OG_RW.CIBC.CET = OG_RW.CIBC.TIJ;// Cycle End Time
        if (is_Line_Initially_Charged == true) then
            OG_RW.CIBC(1).VILE = -V_0*(Z_A/(Z_A+Z_B));// V_R11_+
        else
            OG_RW.CIBC(1).VILE = V_0*Refl_Coeff_AB;// V_R11_+
        end
        OG_RW.CIBC(1).VIJ = OG_RW.CIBC(1).VILE*Refl_Coeff_Line_A_End;// V_R11_-
        OG_RW.CIBC(1).Update = 1;// Update == 1 Yes Update == 0 No
        RW[1]= OG_RW;// Place Origin Reverse Wave In Data Container For All Reverse Waves
"RW"
end
```

Listing 2: Create Origin Reverse Wave

```
//                      CREATE ORIGIN FORWARD WAVE
Function CreateOriginForwardWave(Ref FW)
        Declare Struct OG_FW; // Initialise Origin Forward Wave In A Data Container
        OG_FW.Parent_Wave = NaN; // Origin Forward Wave Has No Parent Wave
        OG_FW.IBC = 1;
        if (is_Line_Initially_Charged == true) then
            OG_FW.TIS = 0; // Time Initial Start
            OG_FW.CIBC(1).CST = 0; // Current Internal Bounce Cycle Start Time
            OG_FW.CIBC(1).VILE = (V_0/2)*(1+Refl_Coeff_AB); // V_F11_+
        else
            OG_FW.CIBC(1).TIS = T_A; // Time Initial Start
            OG_FW.CIBC(1).CST = T_A; // Cycle Start Time
            OG_FW.CIBC(1).VILE = V_0*(Z_A/(Z_A+Z_SA)); // V_F11_+
        end
        OG_FW.CIBC(1).TILE = CST + T_B; // Time Incident @ z_B_f
        OG_FW.CIBC(1).TIJ = TILE + T_B; // Time Incident @ z_B_0
        OG_FW.CIBC(1).CET = TIJ; // Cycle End Time
        OG_FW.CIBC(1).VIJ = OG_FW.CIBC(1).VILE*Refl_Coeff_Line_B_End; // V_F11_-
        OG_FW.CIBC(1).Update = 1; // Update == 1 Yes Update == 0 No
        FW[1] = OG_FW // Place Origin Reverse Wave In Data Container For All Forward Waves
"FW"
end
```

Listing 3: Create Origin Forward Wave

Listing 2 and Listing 3 provide detailed implementation code for creating the origin Reverse and Forward waves respectively. The origin waves data fields are populated and then subsequently stored in the pre-allocated storage containers *RW* and *FW*. At this point all preliminary pre-processing activities are completed and the main processing and interaction of the various fragments may begin.

5.3 Processing

The processing block pertains to all activities and functions that provide the majority of the computation throughout the simulators main programming loop. The main programming cycle effectively loops through all currently created fragments (Reverse and Forward waves) and proceeds to initialise their current internal bounce cycles. After this, new waves or fragments are subsequently created. However, this is subject to the *Fragmentation* ratio and whether or not the *Fragmentation* process completes within the simulation time. Following this the internal bounce cycle of all current fragments are updated to account for the various transmission and recombination effects that take place at the junction or discontinuity. A fragment is only allowed to be updated to a new cycle if there is still time to complete a round-trip on the respective transmission line within the allocated simulation time. A high-level overview of the important activities taking place in the main processing loop are depicted in Figure 5-4. The main processing loop persists until no fragments can be updated to a new cycle. At this point the simulation is effectively complete and all fragments are ready for post-processing.

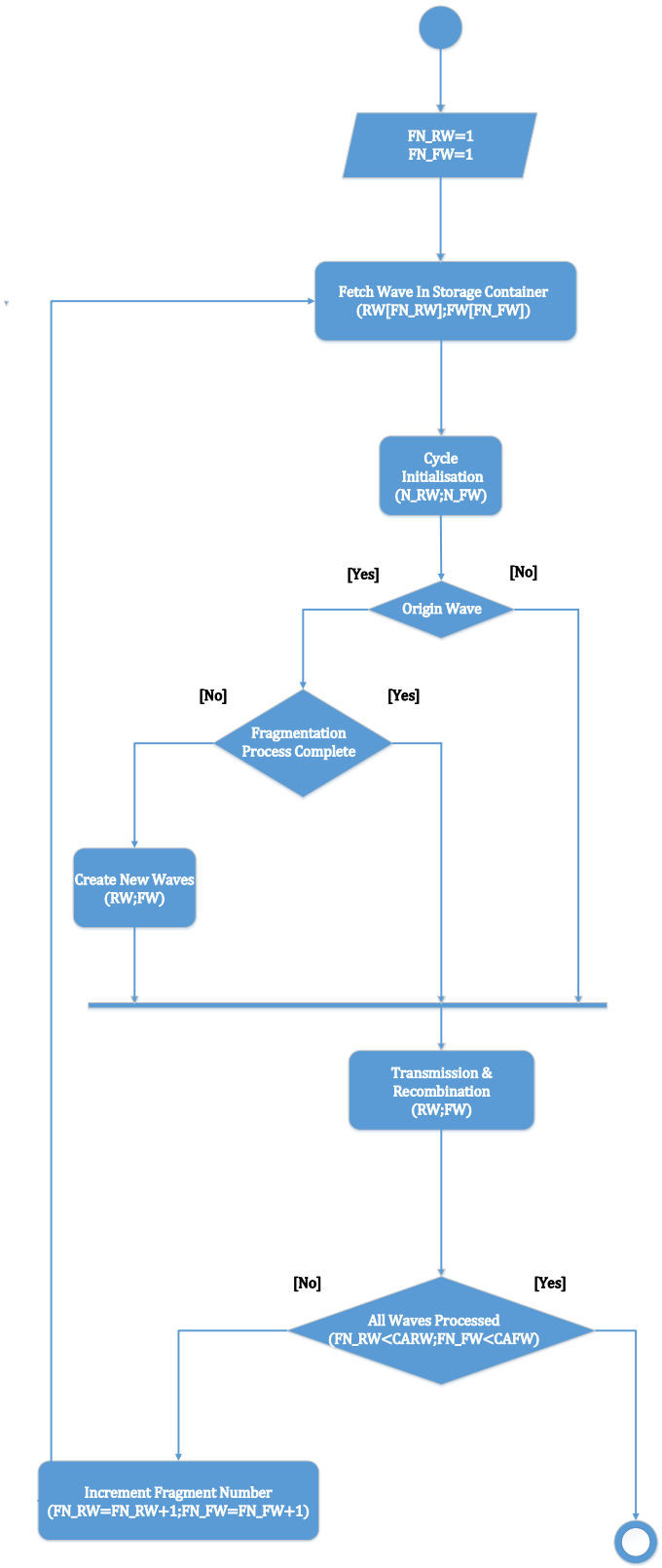


Figure 5-4: Processing Activities Overview

5.3.1 Cycle Initialisation

The cycle initialisation activity responsibilities are to ensure that data fields of a specific fragments current internal bounce cycle are initialised. This is done by establishing whether a specific fragment is allowed to update to a new internal bounce cycle. If this is the case the internal bounce cycle data fields are identical to the fields used in the creation of the origin waves seen in Chapter 5.2.3. The only new additions are the following:

- $Voltage\ Transmitted\ Through\ Junction(VTJ)$ – Representative of the voltage that is transmitted from Line A to Line B or vice versa
- $Voltage\ Reflected\ at\ Junction\ (VRJ)$ – The reflected voltage at the junction terminals at positions z_{A_f} or z_{B_0}.

Listing 4 and Listing 5 presents the N^{th} cycle initialisation procedure for all Reverse and Forward wave fragments. Only cycles after the first internal bounce cycle require initialisation. This is due to the fact that upon creation of a new fragment the first internal bounce cycle ($CIBC(1)$) is always initialised as is seen in Listing 6. In order to initialise subsequent internal bounce cycles all the currently active propagating fragments on Line A and Line B are fetched from their pre-allocated storage containers RW and FW respectively. The data fields for every fragment are populated as per the data fields presented in Chapter 5.2.3.However two new data fields (VTI and VRJ) are also subsequently populated. The data field VTJ represents the voltage transmitted through the junction from a particular fragment before recombination effects have occurred. After factoring in the various recombination and transmission effects that may occur at the junction or discontinuity this data field will be updated if required. The VRJ data field simply represents the reflected voltage at the junction or discontinuity. Similar to the VTJ data field recombination and transmission effects may affect the voltage ultimately reflected from the junction. After the cycle initialisation process is completed the next activity in the processing loop is the creation of new fragments.

```
//                      REVERSE WAVES Nth CYCLE INITIALISATION
Function ReverseWaveCycleInitialisation(Ref FN_FW,FN_RW)
N_RW=RW[FN_RW].IBC;
if(N_RW>1 && RW[FN_RW].CIBC(N_RW).Update==true)then
 RW_Fragment = RW[FN_RW].CIBC(N_RW);
 RW_Fragment.CST = RW[FN_RW].CIBC(N_RW-1).CET;
 RW_Fragment.TILE = RW_Fragment.CST + T_A;
 RW_Fragment.TIJ = RW_Fragment.TILE + T_A;
 RW_Fragment.CET = RW_Fragment.TIJ;
 RW_Fragment.VILE = RW[FN_RW].CIBC(N_RW-1).VRJ;
 RW_Fragment.VIJ = RW_Fragment.VILE*(Refl_Coeff_Line_A_End);
 RW_Fragment.VRJ = RW_Fragment.VIJ*(Refl_Coeff_Line_AB);
 RW_Fragment.VTJ = RW_Fragment.VIJ*(1+Refl_Coeff_Line_AB);
end
```

Listing 4: Reverse Waves N^{th} Cycle Initialisation

```
//                      FORWARD WAVE Nth CYCLE INITIALISATION
Function ForwardWaveCycleInitialisation(Ref FN_FW,FN_RW)
N_FW=FW[FN_FW].IBC;
if(N_FW>1 && FW[FN_FW].CIBC(N_FW).Update==true)then
 FW_Fragment = FW[FN_FW].CIBC(N_FW);
 FW_Fragment.CST=FW[FN_FW].CIBC(N_FW-1).CET;
 FW_Fragment.TILE=FW_Fragment.CST + T_B;
 FW_Fragment.TIJ=FW_Fragment.TILE + T_B;
 FW_Fragment.CET=FW_Fragment.TIJ;
 FW_Fragment.VILE=FW[FN_FW].CIBC(N_FW-1).VRJ;
 FW_Fragment.VIJ=FW_Fragment.VILE*(Refl_Coeff_Line_B_End);
 FW_Fragment.VRJ=FW_Fragment.VIJ*(Refl_Coeff_Line_BA);
 FW_Fragment.VTJ=FW_Fragment.VIJ*(1+Refl_Coeff_Line_BA);
end
```

Listing 5: Forward Waves N^{th} Cycle Initialisation

5.3.2 Create New Waves

The create new waves activity is only ever accessed or called by the origin Reverse and Forward propagating waves. This is because the origin fragments are solely responsible for the creation of all fragments in the system as seen in Chapter 4. If the *Fragmentation* process does not complete this activity will be called every time an origin fragment is incident on the junction or discontinuity. Dependent on the simulation duration not all the specified fragments as per the *Fragmentation* ratio may be created. In order to keep track of the total amount of fragments that may be present on Line A and Line B at any instance in time, the following data fields are introduced

- $Currently\ Active\ Reverse\ Waves(CARW)$ – This represents the total amount of Reverse waves present on Line A at a given instant in time.
- $Currently\ Active\ Forward\ Waves(CAFW)$ – This represents the total amount of Forward waves present on Line B at a given instant in time.
- $Voltage\ Reflected\ at\ Junction(VRJ)$ – This represents the voltage reflected at the junction terminal (z_{A_f} and z_{B_f})
- $Voltage\ Transmitted\ Through\ Junction\ (VTJ)$ – This speaks to the voltage transmitted through the junction terminal. This can either be from Line A to Line B as is the case with Reverse waves. Alternatively, this can also be from Line B to Line A as is the case with Forward waves.

The subsequent creation of new fragments persists until the number of currently active fragments is equal to the quantity specified by the *Fragmentation* ratio i.e. $CARW = F_{RA}$ and $CAFW = F_{RB}$. If the *Fragmentation* process does not complete and the *Fragmentation* generation type is something other than FFGMD then currently active waves in the system will not be equal to F_{RA} and F_{RB} and as a consequence the create new waves activity will be called at every instance an origin wave is incident on the junction or discontinuity. Once a new fragment has been fully initialised the CET data field is evaluated against T_D. If the newly created fragment is incapable of completing a round-trip on its respective transmission line it is not allowed to update to a new cycle. A possible implementation of the create new waves activity is given in Listing 6. After the subsequent creation of new waves all currently active fragments are passed to the recombination and transmission activity.

```
//                      CREATE NEW FORWARD WAVES
Function CreateNewForwardWaves(Ref FN_RW)
if(FN_RW==1)then
   N_RW = RW[FN_RW].IBC;
   RW_Fragment = RW[FN_RW].CIBC(N_RW);
   if(N_RW<F_RB)then
      if(RW_Fragment.CET<T_D)then
        CAFW=CAFW+1;
        FW[CAFW].Parent_Wave=FN_RW;
        FW[CAFW].IBC = 1;
        FW[CAFW].TIS = RW_Fragment.CET;
        FW[CAFW].CIBC(1).CST = FW[CAFW].TIS;
        FW[CAFW].CIBC(1).TILE = FW[CAFW].CIBC(1).TCS + T_B;
        FW[CAFW].CIBC(1).TIJ = FW[CAFW].CIBC(1).TILE + T_B;
        FW[CAFW].CIBC(1).CET = FW[CAFW].CIBC(1).TIJ;
        FW[CAFW].CIBC(1).VILE = RW_Fragment.VTJ;
        FW[CAFW].CIBC(1).VIJ = FW[CAFW].CIBC(1).VILE*(Refl_Coeff_Line_B_End);
        FW[CAFW].CIBC(1).VRJ = FW[CAFW].CIBC(1).VIJ*(Refl_Coeff_BA);
       if(FW[CAFW].CIBC(1).CET<T_D)then
        FW[CAFW].CIBC(1).Update = True;
        else
        FW[CAFW].CIBC(1).Update = False;
      end
   end
end
//                      CREATE NEW REVERSE WAVES
Function CreateNewReverseWaves(Ref FN_FW)
if(FN_FW==1)then
   N_FW = FW[FN_FW].IBC;
   FW_Fragment = FW[FN_FW].CIBC(N_FW);
   if(N_FW<F_RA)then
       if(FW_Fragment.CET<T_D)then
         CARW=CARW+1;
         RW[CARW].Parent_Wave=FN_FW;
         RW[CARW].IBC = 1;
         RW[CARW].TIS = FW_Fragment.CET;
         RW[CARW].CIBC(1).CST = RW[CARW].TIS;
         RW[CARW].CIBC(1).TILE = RW[CARW].CIBC(1).CST + T_A;
         RW[CARW].CIBC(1).TIJ = RW[CARW].CIBC(1).TILE + T_A;
         RW[CARW].CIBC(1).CET = RW[CARW].CIBC(1).TIJ;
         RW[CARW].CIBC(1).VILE = FW_Fragment.VTJ;
         RW[CARW].CIBC(1).VIJ = RW[CARW].CIBC(1).VILE*(Refl_Coeff_Line_A_End);
         RW[CARW].CIBC(1).VRJ = RW[CARW].CIBC(1).VIJ*(Refl_Coeff_AB);
        if(RW[CARW].CIBC(1).CET<T_D)then
         RW[CARW].CIBC(1).Update = True;
         else
         RW[CARW].CIBC(1).Update = False;
      end
   end
end
```

Listing 6: Create New Waves

5.3.3 Recombination and Transmission

The recombination and transmission activity is primarily responsible for handling the interactions between the Forward and Reverse waves at the junction or discontinuity. This is similar to the connection phase that happens in the traditional TLM algorithm seen in [18]. After the *Fragmentation* generation process is complete every Reverse and Forward fragment will come into contact with a corresponding Forward or Reverse fragment whenever it is incident on the junction or discontinuity. This process is well documented in Chapter 4 and effectively represents the N^{th} internal bounce cycles travelling in the forward directions ${V_{Ri_{RW}N}}^{+}$ and ${V_{Fi_{FW}N}}^{+}$ respectively. Irrespective of the *Fragmentation* generation type, the rationale in finding the N^{th} internal bounce cycle travelling in the forward direction will always consist of four primary processes. The first process is concerned with identifying the fragment number (i_{RW} or i_{FW}) of the contacting fragment at the junction. Once this has been ascertained the M^{th} meeting of these particular fragments at the junction can be determined. Subsequently following this the internal bounce cycle (N_{RW} or N_{FW}) of the contacting wave is established. Consequently the N^{th} internal bounce cycle in the forward direction can now be determined. This is achieved by adding the initially reflected voltage to the voltage transmitted through the junction as a result of the contacting wave. In so doing, the VRJ data field is updated to account for the newly transmitted voltage from the corresponding fragment on the opposing side of the junction or discontinuity. Listing 7 and Listing 8 present a possible implementation of the recombination and transmission activities. After the recombination and transmission activity is completed the main processing loop returns to the N^{th} cycle initialisation to process a new internal bounce cycle.

```
//                      RECOMBINATION AND TRANSMISSION
 // REVERSE WAVE TRANSMISSION AND RECOMBINATION
Function TransmissionAndRecombination(Ref FN_RW,FN_FW)
 N_RW = RW[FN_RW].IBC; //Reverse Wave Internal Bounce Cycle
 FN_FW=0; //Contacting Forward Wave Fragment Number
 N_FW=0; //Contacting Forward Wave Internal Bounce Cycle
 FN_FW=mod(N_RW,F_RB)+1; //Determine Contacting Fragment Number
 M=(N_RW-(FN_FW-FN_RW))/F_RB; //Compute Mth Junction Meeting
 N_FW = F_RA*M; //Determine Contacting Fragment Number
 RW_Fragment=RW[FN_RW].CIBC(N_RW);
 FW_Fragment=FW[FN_RW].CIBC(N_FW);
 RW_Fragment.VRJ = RW_Fragment.VRJ + FW_Fragmen.VTJ;
 if(RW_Fragment.CET<T_D)then
  RW_Fragment.Update=True;
  RW[FN_RW].IBC=N_RW+1;
  RW[FN_RW].CIBC(N_RW+1).Update=True;
 else
  RW_Fragment.Update=False;
 end
end
```

Listing 7: Transmission and Recombination Effects at Junction (Part I)

```
//                      TRANSMISSION AND RECOMBINATION (CONT'D)
// FORWARD WAVE TRANSMISSION AND RECOMBINATION
Function TransmissionAndRecombination(Ref FN_RW,FN_FW)
 N_FW=FW[FN_FW].IBC;
 FN_RW=0;//Contacting Reverse Wave Fragment Number
 N_RW=0;//Contacting Reverse Wave Internal Bounce Cycle
 FN_RW=mod(N_FW,F_RA)+1;//Determine Contacting Fragment Number
 M = (N_FW-(FN_FW-FN_RW))/(F_RA);//Compute Mth Junction Meeting
 N_RW = F_RB*M;//Determine Contacting Fragment Number
 FW_Fragment=FW[FN_FW].CIBC(N_FW);
 RW_Fragment=RW[FN_RW].CIBC(N_RW);
 FW_Fragment.VRJ=FW_Fragment.VRJ+RW_Fragment.VTJ;
 if(FW_Fragment.CET<T_D)then
  FW_Fragment.Update = True;
  FW[FN_FW].IBC = FW[FN_FW].IBC+1;
  FW[FN_FW].CIBC(N_FW+1).Update=True;
 else
  FW_Fragment.Update = False;
 end
end
```

Listing 8: Transmission and Recombination Effects at Junction (Part II)

5.4 Post Processing

Once the main simulation loop has completed and all currently active Reverse and Forward wave internal bounce cycles have been examined thoroughly against the desired simulation time. The simulation process is essentially over and the information obtained from the various fragments requires representation in a meaningful way. The post-processing block is principally concerned with displaying the results of the main processing block in one of two representations. In the time discretisation representation the voltages and currents are displayed at specific discrete points and a progression in time is observed. In spatial discretisation the entirety of the voltages and currents in space are displayed for a fixed instant in time. Both the time and spatial discretisation representation make use of the same data produced by the main processing loop. The principle difference is in how both representation display the results.

5.4.1 Time Discretisation

The time discretisation activity is comprised of three main processes. The first process involves populating point structs at specific points of interest. The voltages and currents are then computed at these points and their progression in time is tracked. The second process ensures that all the point structs are sorted w.r.t the incident time of the various fragments that are incident at the specific point/node of interest. This is necessary to ensure that an accurate progression in chronological order of time is maintained. Consequently, this ensures the contribution of specific fragments and internal bounce cycles are computed at the right time instances. The third and final processes involves recursively adding the individual entries of each point struct to one another to produce the final voltage and current time progressions. Possible implementation code for the time discretisation process is given in Listing 9 and Listing 10.

```
//                      TIME DISCRETIZATION
// 1.) Populate Structs
// Examine All Reverse Waves
Function TimeDiscretization(Ref CARW,CAFW)
for FN_RW = 1 to CARW
    TIBC = RW[FN_RW].IBC;
    for N_RW = 1 to TIBC
        RW_Fragment = RW[FN_RW].CIBC(N_RW);
        // Position @ z_A_0
        z_A_0.Time = RW_Fragment.TILE
        z_A_0.Voltage = RW_Fragment.VILE(1+Refl_Coeff_Line_A_End);
        z_A_0.Current = (RW_Fragment.VILE(1-Refl_Coeff_Line_A_End))/Z_A;
        Struct_z_A_0.Push(z_A_0);
        // Position @ z_A_f = z_Junction
        z_A_f.Time = RW_Fragment.TIJ;
        z_A_f.Voltage = RW_Fragment.VIJ + RW_Fragment.VRJ;
        z_A_f.Current = (RW_Fragment.VIJ - RW_Fragment.VRJ)/Z_A;
        Struct_z_J_AB.Push(z_A_f);
    end
end
// Examine All Forward Waves
for FN_FW = 1 to CAFW
    TIBC = FW[FN_FW].IBC;
    for N_FW = 1 to TIBC
        FW_Fragment = FW[FN_FW].CIBC(N_FW);
        // Position @ z_B_f
        z_B_f.Time = FW_Fragment.TILE;
        z_B_f.Voltage = FW_Fragment.VILE(1+Refl_Coeff_Line_B_End);
        z_B_f.Current = (FW_Fragment.VILE(1-Refl_Coeff_Line_B_End))/Z_B;
        Struct_z_B_f.Push(z_B_f);
        // Position @ z_B_0 = z_Junction
        if(mod(F_RA,F_RB)!=0||mod(F_RB,F_RA)!=0)then
            z_B_0.Time = FW_Fragment.TIJ;
            z_B_0.Voltage = FW_Fragment.VIJ+FW_Fragment.VRJ;
            z_B_0.Current = (FW_Fragment.VRJ-FW_Fragment.VIJ)/(Z_B);
            Struct_z_J_AB.Push(z_A_f);
        end
    end
end
//-------------------------------------------------------------------------
// 2.) Sort Structs In Ascending Order w.r.t. Time
SortAscending(Ref Struct_z_A_0,Struct_z_J_AB,Struct_z_B_f);
//-------------------------------------------------------------------------
```

Listing 9:Time Discretisation (Populating and Sorting Structs)

```
//                      TIME DISCRETISATION (CONT'D)
// 3.) Perform Recursive Addition
for X = 1 to size(Struct_z_A_0)
    if(X==1)then
        V_z_A_0(X).Voltage = Struct_z_A_0(X).Voltage;
        I_z_A_0(X).Current = Struct_z_A_0(X).Current;
    else
        V_z_A_0(X).Voltage = V_z_A_0(X-1).Voltage + Struct_z_A_0(X).Voltage;
        I_z_A_0(X).Current = V_z_A_0(X-1).Current + Struct_z_A_0(X).Current;
    end
    T_z_A_0(X).Time = Struct_z_A_0(X).Time;
end
for X = 1 to size(Struct_z_J_AB)
    if(X==1)then
        V_z_J_AB(X).Voltage = Struct_z_J_AB(X).Voltage;
        I_z_J_AB(X).Current = Struct_z_J_AB(X).Current;
    else
        V_z_J_AB(X).Voltage = V_z_J_AB(X-1).Voltage + Struct_z_J_AB(X).Voltage;
        I_z_J_AB(X).Current = I_z_J_AB(X-1).Current + Struct_z_J_AB(X).Current;
    end
    T_z_J_AB(X).Time = Struct_z_J_AB(X).Time;
end
for X = 1 to size(Struct_z_B_f)
    if(X==1)then
        V_z_B_f(X).Voltage = Struct_z_B_f(X).Voltage;
        I_z_B_f(X).Current = Struct_z_B_f(X).Current;
    else
        V_z_B_f(X).Voltage = V_z_B_f(X-1).Voltage + Struct_z_B_f(X).Voltage;
        I_z_B_f(X).Current = V_z_B_f(X-1).Current + Struct_z_B_f(X).Current;
    end
    T_z_B_f(X).Time = Struct_z_B_f(X).Time;
end
```

Listing 10: Time Discretisation (Recursive Addition of Structs)

5.4.2 Spatial Discretisation

The spatial discretisation activity comprises three principle processes. The first process involves effectively discretising the TL segments length into smaller linearly spaced segments. Special care should be taken when selecting the segmentation length as this has implications on processing time. As a generally accepted rule of thumb a segmentation length that is ten times smaller than the smallest wavelength of interest (i.e. $\frac{\lambda}{10}$) is typically chosen [18]. The second process involves populating position structs in order to ascertain the individual contribution of each fragment to the overall line voltage and current on a specific TL segment. The last process involves recursively adding the contributions of the individual fragments to ultimately obtain the final line voltages and currents. Superposition can be used in this manner because no strict emphasis is placed on the chronological order in which the contributions of the individual fragments are processed. Listing 11 and Listing 12 depict a possible implementation of the spatial discretisation activity.

```
//                      SPATIAL DISCRETIZATION
//1). Compute Preliminary Line Voltages and Currents
function SpatialDiscretisation(Ref CARW,CAFW,Seg_Number)
l_A = c*T_A;
l_B = c*T_B;
delta_Seg = l_A/Seg_Number;
I_A_Calc=0;I_B_Calc=0;V_B_Calc=0;
V_Line_A;I_Line_A;
z_A = LinSpace(Seg_Number,l_A); //Create Linearly Spaced Position Vector
z_B = LinSpace(Seg_Number,l_B); //Create Linearly Spaced Position Vector
if(is_Line_Initially_Charged==true)then
   V_A_Calc = V_0;
else
    V_A_Calc = 0;
end
//                Line A
for FN_RW = 1 to CARW
    TIBC = RW[FN_RW].IBC;
    for N_RW = 1 to TIBC;
      RW_Fragment = RW[FN_RW].CIBC(N_RW);
      if(RW_Fragment.CET<T_D)then
        V_A_Calc = V_A_Calc + RW_Fragment.VILE*(1+Refl_Coeff_Line_A_End);
        I_A_Calc = I_A_Calc + (RW_Fragment.VILE*(1-Refl_Coeff_Line_A_End))/Z_A;
       else //RW_Fragment.CET>=T_D
           if(RW_Fragment.CST<T_D)then
               if(RW_Fragment.TILE<=T_D)then // RW_(-) -------->
                   V_A_Calc = V_A_Calc + RW_Fragment.VILE;
                   I_A_Calc = I_A_Calc + (RW_Fragment.VILE)/Z_A;
                   tau = T_D - RW_Fragment.TILE;
                   V_A_F = RW_Fragment.VIJ*heaviside(-z_A+c*tau);
                   V_A_Net = V_A_Calc*heaviside(z_A)+V_A_F;
                   I_A_Net = I_A_Clac*heaviside(z_A)-(V_A_F)/Z_A;
                   V_Line_A.push(V_A_Net);
                   I_Line_A.push(I_A_Net);
               else // RW_(+) <---------
                   tau = T_D - RW_Fragment.CST;
                   V_A_R = RW_Fragment.VILE*heaviside(z_A-c*tau);
                   I_A_R = V_A_R/Z_A;
                   V_A_Net = V_A_Calc*heaviside(z_A)+V_A_R;
                   I_A_Net = I_A_Calc*heaviside(z_A)+I_A_R;
                   V_Line_A.push(V_A_Net);
                   I_Line_A.push(I_A_Net);
               end
           end
       end
    end
    V_A_Calc = 0;I_A_Calc=0;
end
```

Listing 11: Spatial Discretisation (Preliminary Voltages and Currents)

```
//             SPATIAL DISCRETIZATION (CONT'D)
//                    Line B
for FN_FW = 1 to CAFW
    TIBC = FW[FN_FW].IBC;
    for N_FW = 1 to TIBC;
      FW_Fragment = FW[FN_FW].CIBC(N_FW);
      if(FW_Fragment.CET<T_D)then
        V_B_Calc = V_B_Calc + FW_Fragment.VILE*(1+Refl_Coeff_Line_B_End);
        I_B_Calc = I_B_Calc + (FW_Fragment.VILE*(1-Refl_Coeff_Line_B_End))/Z_B;
       else //FW_Fragment.CET>=T_D
           if(FW_Fragment.CST<T_D)then
               if(FW_Fragment.TILE<=T_D)then //FW_(-) <--------
                   V_B_Calc = V_B_Calc + FW_Fragment.VILE;
                   I_B_Calc = I_B_Calc + (FW_Fragment.VILE)/Z_B;
                   tau = T_D - FW_Fragment.TILE;
                   V_B_F = FW_Fragment.VIJ*heaviside(-z_B+c*tau);
                   V_B_Net = V_B_Calc*heaviside(z_B)+V_B_F;
                   I_B_Net = I_B_Clac*heaviside(z_B)-(V_B_F)/Z_B;
                   V_Line_B.push(V_B_Net);
                   I_Line_B.push(I_B_Net);
               else//FW_(+) --------->
                   tau = T_D - FW_Fragment.CST;
                   V_B_R = FW_Fragment.VILE*heaviside(z_B-c*tau);
                   I_B_R = V_B_R/Z_B;
                   V_B_Net = V_B_Calc*heaviside(z_B)+V_B_R;
                   I_B_Net = I_B_Calc*heaviside(z_B)+I_B_R;
                   V_Line_B.push(V_B_Net);
                   I_Line_B.push(I_B_Net);
               end
           end
       end
    end
    V_B_Calc = 0;I_B_Calc=0;
end
//2). Calculate Final Line Voltages and Currents
V_A = 0*heaviside(z_A);I_A=0*heaviside(z_A);
V_B = 0*heaviside(z_B);I_B=0*heaviside(z_B);
for X = 1 to size(V_Line_A)
    V_A = V_A + V_Line_A(X);
    I_A = I_A + I_Line_A(X);
end
for X = 1 to size(V_Line_B)
    V_B = V_B + V_Line_B(X);
    I_B = I_B + I_Line_B(X);
end
```

Listing 12: Spatial Discretisation (Final Line Voltages and Currents)

5.5 Conclusion

Presented in this chapter is a high-level breakdown of an algorithm necessary for practical realisation of the various *Fragmentation* generation processes in a simulated environment. The algorithm is comprised of three distinct sections namely pre-processing, processing and post-processing. The pre-processing section pertains to all forms of parameter initialisation whilst the processing section deals with the bulk of the computation and interactions that take place between the various fragments at terminals and the junction or discontinuity. The post-processing section takes the processed data and represents it in either a time or spatial discretisation representation. The manner in which the various fragments and ancillary data structures are modelled in the algorithm leans heavily towards implementation in a programming language that exhibits OOP capabilities.

6 ENERGY MANIPULATION

6.1 Overview

Utilizing the Link-Line transmission line model for reactive components the electric to electric and electric to magnetic energy manipulation processes are explored using two subsets. These subsets are classified by the dissimilarity or similarity of the characteristic impedances of two adjoining transmission lines in relation to one another. The first subset of similarity is explored by modelling both transmission lines as capacitors. This is best highlighted or demonstrated by exploring the classical case of the *Twin Capacitor Paradox*. An alternative solution to the paradox is found and the so called *"Missing Energy"* is fully contained within the associated magnetic fields of the associated self-inductors of both capacitors. This discovery further highlights the deficiency in modelling the capacitor using strictly network paradigms and lumped element models. Both subsets are evaluated and assessed under various different *Fragmentation Ratios* and the generated waveforms are compared against ideal reference waveforms. The second subset of dissimilarity is explored by modelling the two transmission lines as a capacitor and inductor respectively. The interconnection of a capacitor and inductor form a ubiquitous fundamental building block found in almost all power electronic converter topologies. In this subset the capacitor and inductor are connected in a LC Resonant tank configuration as this configuration represents the quintessential form of energy conversion between electric and magnetic field energies. The oscillation between electric and magnetic field energies represents a simple harmonic oscillation (SHO). The LC Resonant tank and hence the SHO will be evaluated under lossless no damping conditions at the fundamental resonant frequency under various *Fragmentation* generation techniques.

6.2 Similar Transmission Lines

The relative similarity or dissimilarity of the two adjoining transmission lines can be completely classified by observing the absolute difference in the characteristic impedances of the two adjoining transmission lines.

$$\Delta Z_{AB} = |Z_A - Z_B| \tag{6.1}$$

Two adjoining transmission lines are similar if the difference between the respective characteristic impedances ΔZ_{AB} is in the following range:

$$0\ \Omega \leq \Delta Z_{AB} \leq 1 \times 10^3\ \Omega$$

This simulation range was determined during numerous simulation iterations by examining TL segments of various characteristic impedances. It is found that if the differences in characteristic impedances exceeds the boundaries of this range, this results in reflection coefficients at the junction or discontinuity that approaches open-circuit conditions. In this event, the TL segment begins to better approximate an inductor instead of the desired capacitor. The effect of the various *Fragmentation* generation methods are applied to the *Twin Capacitor Paradox* and the role the self-inductances have on influencing ECE is interrogated and observations recorded. The *Fragmentation* generation methods that are explored are FFGMD and FFGIMD. Before the various *Fragmentation* generation methods can be applied to the *Twin Capacitor Paradox* it is necessary to formally define the *Energy Conversion Efficacy* metric.

Energy Conversion Efficacy is thus formally defined as:

Energy Conversion Efficacy *– A quantification metric that establishes the efficacy of a given energy manipulation process by assessing it according to two principal attributes. The first attribute establishes the maximum energy transferred from a primary energy store to a secondary energy store in the desired form. The second attribute explores how readily this transferred/converted energy in the secondary store can be transferred/reconverted back into the original form in the primary energy store essentially reconstituting the energy, hence establishing the reversibility of the given energy manipulation process.*

Expressing the two attributes of ECE in an analytical relationship or manner leads to the following formula

$$ECE = \frac{\left(U_{A_{Reconstituted}}(\%) + U_{B_{Desired}}(\%)\right)}{2} \tag{6.2}$$

Where $U_{A_{Reconstituted}}$ represents the maximum amount of energy that can be reconstituted back into the primary energy store in the original form. In the context of the *Twin Capacitor* topology, the energy initially present in C_A before the switch is closed at $t = 0^+$ is purely electric in nature i.e. U_{EA}. If the energy manipulation process supports perfect reconstitution, at some instant in time it should be possible to fully recapture all the energy in Line A and have it completely stored as electric energy just as before any energy manipulation has taken place. The second term $U_{B_{Desired}}$ represents the maximum amount of energy transferred or converted and stored in the secondary energy store from the primary energy store in the desired form. In the context of the *Twin Capacitor* topology $U_{B_{Desired}}$ represents the maximum electrical energy that is transferred from C_A to C_B.

The influence of the FFGMD and FFGIMD generation methods in the *Twin Capacitor* topology will be assessed in accordance with the ECE metric and the principle implications this imposes on energy in the system will be evaluated. The principle manipulations are classified as either ideal or non-ideal energy manipulation. The ideal and non-ideal energy manipulation cases are defined as follows

- *Ideal Energy Manipulation:* The entirety of the energy manipulation interactions that take place in the system are due to only the origin fragments. The implications of this manipulation on ECE will be assessed by varying C_B (secondary energy store) whilst maintaining a constant unity *Fragmentation Ratio* (FFGMD*)*
- *Non-Ideal Energy Manipulation:* The interactions that take place in the system are attributed to the interaction of various fragments on the respective TL segments and at the junction or discontinuity. The implications this poses on ECE is assessed by varying the *Fragmentation Ratio* (FFGIMD) whilst keeping the capacitance of C_B constant.

Both principle cases are examined by means of simulated examples and are explored using spatial discretisation of the l_A and l_B TL segment length dimensions. The Link-Line equivalent representation of the *Twin Capacitor* topology for which the simulation parameters in Table 6.1 map to are given in Figure 3-12 and Figure 3-13. The methodology or basis for which the various conjectures that characterize ECE pertaining to various *Fragmentation* generation techniques are ultimately steeped in simulated data and observations, and hence the simulation parameters for the examples presented are selected arbitrarily and are not application specific.

Table 6.1: Twin Capacitor FFGMD Simulation Parameters

$Parameter$	$Value$
U_0	$5000pJ$
V_0	$1V$
I_0	$500mA$
τ_A	$10ns$
τ_B	$10ns$
Z_A	$100m\Omega$
Z_B	$100m\Omega$
l_A	$3m$
l_B	$3m$
C_A	$100nF$
L_{eA}	$1nH$
C_B	$100nF$
L_{eB}	$1nH$
n_{seg}	10000

The results depicted in Table 3.1 give the energy interactions on the two TL segments when $C_A = C_B$ and the *Fragmentation Ratio* is unity ($F_{RA} = 1, F_{RB} = 1$). According to (3.48) the *"Missing Energy"* in this system should be equal to 50% ($\Delta U = 50\%$) provided $C_A = C_B$. Utilising the simulation parameters in Table 6.1 this is shown to be in fact erroneous. As the entirety of the system energy, U_0 can be accounted for at all times. The average values of the voltages and current should not be used when attempting to calculate system energy only in the exceptional case of dealing with purely DC waveforms. At the intervals or time instances given in Table 3.1 pure DC waveforms are generated on the TL segments at the boundaries of the time intervals. However, if the spatial line voltages are examined at time instances that are not integer multiples of the propagation delays (τ_A and τ_B) purely DC voltage and current waveforms will not be observed. It is therefore more rigorous to determine the system energy using spatial discretisation. In spatial discretisation the lengths of the TL segments (l_A and l_B) are subdivided into smaller segments of length Δz. In order to ascertain the electric $(U_{EA}(z,t), U_{EB}(z,t))$ and magnetic $(U_{HA}(z,t), U_{HB}(z,t))$ energies present on the respective lines in totality, the individual contributions of each segment need to be considered. In order to do this the segmentation length as well as the per-unit capacitance and inductance quantities on both lines (seen in Figure 3-12) are required. The segmentation length Δz as well as the per-unit capacitance and inductance quantities are given by the following:

$$\Delta z = \frac{l_{elec}}{n_{seg}} \tag{6.3}$$

$$C_{A_{pu}} = \frac{C_A}{l_A} \tag{6.4}$$

$$L_{eA_{pu}} = \frac{L_{eA}}{l_A} \tag{6.5}$$

$$C_{B_{pu}} = \frac{C_B}{l_B} \tag{6.6}$$

$$L_{eB_{pu}} = \frac{L_{eB}}{l_B} \tag{6.7}$$

For the simulated parameters given in Table 6.1 the segmentation length of an individual segment is given by the following:

$$\Delta z = \frac{l_{phys}}{n_{seg}} = \frac{3}{10000} \cong 300 \times 10^{-6} = 300\ \mu m$$

The per-unit capacitance and inductance quantities using equations (6.4)-(6.7) are as follows:

$$C_{A_{pu}} \cong 3.333\ nF/m$$

$$L_{eA_{pu}} \cong 333.333\ \mu H/m$$

$$C_{B_{pu}} \cong 3.333\ nF/m$$

$$L_{eB_{pu}} \cong 333.333\ \mu H/m$$

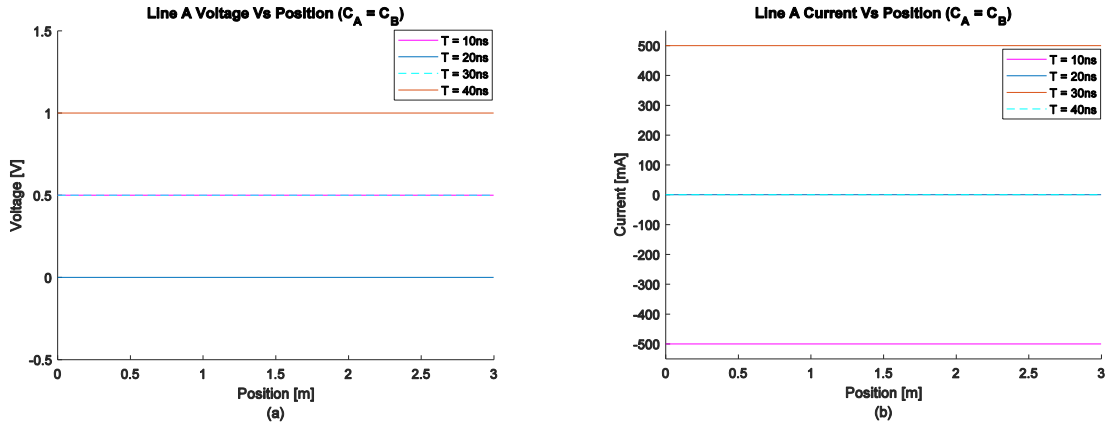


Figure 6-1: FFGMD Line A Distributions ($C_A = C_B$) a) Voltage b) Current

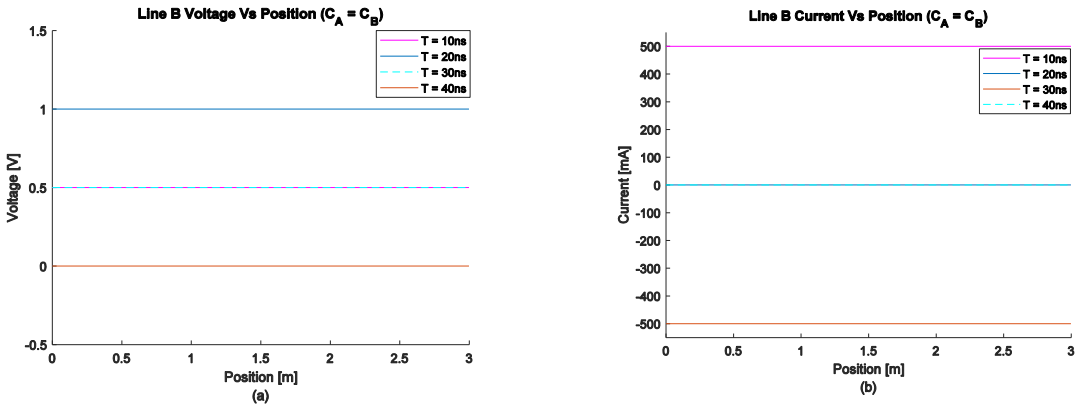


Figure 6-2: FFGMD Line B Distributions ($C_A = C_B$) a) Voltage b) Current

In the case of FFGMD generation it is permissible to use equations (3.49)-(3.52) to represent the voltage and current spatial distributions seen in Figure 6-1 and Figure 6-2.

If however, another *Fragmentation* generation method is used, the voltage and current distributions given in (3.49)-(3.52) need to be modified. This is because equations (3.49)-(3.52) operate on the implicit assumption of only one propagating waveform being present on Line A and Line B respectively. The modified instantaneous spatial distributions on Line A and Line B at a particular time instant t_0 for any *Fragmentation* generation method are as follows:

$$v_A(z,t_0) = v_{A_{initial}}(z) + \sum_{k=1}^{i_{RW}} {V_{RkN}}^{+} u\left(t_0 - \frac{z}{v_p}\right) + {V_{RkN}}^{-} u\left(t_0 + \frac{z}{v_p}\right) \tag{6.8}$$

$$i_A(z,t_0) = i_{A_{initial}}(z) + \sum_{k=1}^{i_{RW}} \frac{{V_{RkN}}^{+}}{Z_A} u\left(t_0 - \frac{z}{v_p}\right) - \frac{{V_{RkN}}^{-}}{Z_A} u\left(t_0 + \frac{z}{v_p}\right) \tag{6.9}$$

$$v_B(z,t_0) = v_{B_{initial}}(z) + \sum_{k=1}^{i_{FW}} {V_{FkN}}^{+} u\left(t_0 - \frac{z}{v_p}\right) + {V_{FkN}}^{-} u\left(t_0 + \frac{z}{v_p}\right) \tag{6.10}$$

$$i_B(z,t_0) = i_{B_{initial}}(z) + \sum_{k=1}^{i_{FW}} \frac{{V_{FkN}}^{+}}{Z_B} u\left(t_0 - \frac{z}{v_p}\right) - \frac{{V_{FkN}}^{-}}{Z_B} u\left(t_0 + \frac{z}{v_p}\right) \tag{6.11}$$

Where $v_{A_{initial}}(z)$,$i_{A_{initial}}(z)$, $v_{B_{initial}}(z)$ and $i_{B_{initial}}(z)$ represent any existing voltages and currents present on Line A and B before t_0. When utilizing FFGMD as the method of *Fragmentation* generation equations (6.8)-(6.11) can be simplified because only the origin Reverse and Forward propagating waveforms are created. The simplified expressions are

$$v_A(z,t_0) = {V_{R1N}}^{+} u\left(t_0 - \frac{z}{v_p}\right) + {V_{R1N}}^{-} u\left(t_0 + \frac{z}{v_p}\right) + v_{A_{initial}}(z) \tag{6.12}$$

$$i_A(z,t_0) = \frac{{V_{R1N}}^{+}}{Z_A} u\left(t_0 - \frac{z}{v_p}\right) - \frac{{V_{R1N}}^{-}}{Z_A} u\left(t_0 + \frac{z}{v_p}\right) + i_{A_{initial}}(z) \tag{6.13}$$

$$v_B(z,t_0) = {V_{F1N}}^{+} u\left(t_0 - \frac{z}{v_p}\right) + {V_{F1N}}^{-} u\left(t_0 + \frac{z}{v_p}\right) + v_{B_{initial}}(z) \tag{6.14}$$

$$i_B(z,t_0) = \frac{{V_{F1N}}^{+}}{Z_B} u\left(t_0 - \frac{z}{v_p}\right) - \frac{{V_{F1N}}^{-}}{Z_B} u\left(t_0 + \frac{z}{v_p}\right) + i_{B_{initial}}(z) \tag{6.15}$$

The area of the instantaneous line voltages and currents are determined by taking the Riemann sums of equations (6.12)-(6.15)

$$V_A(z,t_0) = S_{PV_A} = \sum_{m=1}^{n_{seg}} v_A(c_m,t_0)^2 \Delta z_m \tag{6.16}$$

$$I_A(z,t_0) = S_{PI_A} = \sum_{m=1}^{n_{seg}} i_A(c_m,t_0)^2 \Delta z_m \tag{6.17}$$

$$V_B(z,t_0) = S_{PV_B} = \sum_{m=1}^{n_{seg}} v_B(c_m,t_0)^2 \Delta z_m \tag{6.18}$$

$$I_B(z,t_0) = S_{PI_B} = \sum_{m=1}^{n_{seg}} i_B(c_m,t_0)^2 \Delta z_m \tag{6.19}$$

The expected error produced by the Riemann sum definite integral approximation should be minimal because the voltage and current functions are linear combinations of Heaviside unit step functions. These functions when combined in a linear fashion will exhibit an inherently rectangular shape. The segmentation length Δz is also selected to be sufficiently small in efforts to mitigate any potential approximation errors. The instantaneous electric and magnetic energies are given by the following expressions:

$$U_{E_AT}(z,t_0) = \frac{1}{2} C_{A_{pu}} V_A(z,t_0) \tag{6.20}$$

$$U_{H_AT}(z,t_0) = \frac{1}{2} L_{eA_{pu}} I_A(z,t_0) \tag{6.21}$$

$$U_{E_BT}(z,t_0) = \frac{1}{2} C_{B_{pu}} V_B(z,t_0) \tag{6.22}$$

$$U_{H_BT}(z,t_0) = \frac{1}{2} L_{eB_{pu}} I_B(z,t_0) \tag{6.23}$$

The instantaneous energies in totality for the spatial distributions present on Line A and B are ultimately given by:

$$\begin{aligned} U_{T_A}(z,t_0) &= U_{E_AT}(z,t_0) + U_{H_AT}(z,t_0) \\ &= \frac{1}{2}\left[C_{A_{pu}} V_A(z,t_0) + L_{eA_{pu}} I_A(z,t_0)\right] \end{aligned} \tag{6.24}$$

$$\begin{aligned} U_{T_B}(z,t_0) &= U_{E_BT}(z,t_0) + U_{H_BT}(z,t_0) \\ &= \frac{1}{2}\left[C_{B_{pu}} V_B(z,t_0) + L_{eB_{pu}} I_B(z,t_0)\right] \end{aligned} \tag{6.25}$$

Applying equations (6.20)-(6.25) to the voltage and current waveforms in Figure 6-1 and Figure 6-2 the electric and magnetic energies, and hence the system energy for the simulated parameters in Table 6.1 are calculated and the results tabulated in Table 6.2.

Table 6.2: Instantaneous Line Energies ($C_A = C_B$)

$Time\ Instance$	U_{EA}	U_{EA}/U_0	U_{EB}	U_{EB}/U_0	U_{HA}	U_{HA}/U_0	U_{HB}	U_{HB}/U_0
$10ns$	$1250pJ$	25%	$1250pJ$	25%	$1250pJ$	25%	$1250pJ$	25%
$20ns$	$0pJ$	0%	$5000pJ$	100%	$0pJ$	0%	$0pJ$	0%
$30ns$	$1250pJ$	25%	$1250pJ$	25%	$1250pJ$	25%	$1250pJ$	25%
$40ns$	$5000pJ$	100%	$0pJ$	0%	$0pJ$	0%	$0pJ$	0%

Upon observation of the results in Table 6.2 it is readily apparent that they show great congruency with the results predicted in Table 3.1. This illustrates that energy is indeed conserved at all instances in time and that the *"Missing Energy"* is not missing at all, but has rather just changed forms from electric to magnetic energy.

Now that expressions for the total instantaneous energies present on Line A and B at any given instant in time have been derived, the nuances of the energy manipulation processes in the *Twin Capacitor* topology can be explored using ECE and various *Fragmentation Ratios* in accordance with ideal and non-ideal energy manipulation cases.

6.2.1 Energy Implications

6.2.1.1 Ideal Energy Manipulation (FFGMD)

In order to establish the ECE of a particular setup in the *Twin Capacitor* topology it is necessary to examine the spatial energy distributions of both TL segments at specified time intervals. This will be illustrated by examining the energies present in the system as the capacitance of the secondary energy store is increased whilst a *Fragmentation Ratio* of unity is maintained. From equation (3.48) it can readily be seen that as $C_B \to \infty, \Delta U \to \infty$. This implies that as C_B increases, the totality of the energy in the system will be classified as *"Missing Energy"*. As shown earlier this *"Missing Energy"* is equal to the magnetic field energy stored in the self-inductors L_{eA} and L_{eB}.

When utilizing a *Fragmentation Ratio* of unity the maximum electrical energies $U_{EA_{Max}}$ and $U_{EB_{Max}}$ will occur at time instances that are integer multiples of the round-trip propagation delays of Line A and Line B i.e. $T = n(2\tau_A)$ and $T = n(2\tau_B)$. Conversely the maximum magnetic energies $U_{HA_{Max}}$ and $U_{HB_{Max}}$ on the respective TL segments occur at the time instances $T = (2n-1)\tau_A$ for Line A and $T = (2n-1)\tau_B$ for Line B. The maximum electrical energies ($U_{EA_{Max}}$ and $U_{EB_{Max}}$) coincide with the minimum magnetic energies ($U_{HA_{Min}}$ and $U_{HB_{Min}}$).Similarly, the maximum magnetic energies ($U_{HA_{Max}}$ and $U_{HB_{Max}}$) that occur in the system are however always accompanied by a finite or minimum amount of electrical energies ($U_{EA_{Min}}$ and $U_{EB_{Min}}$).

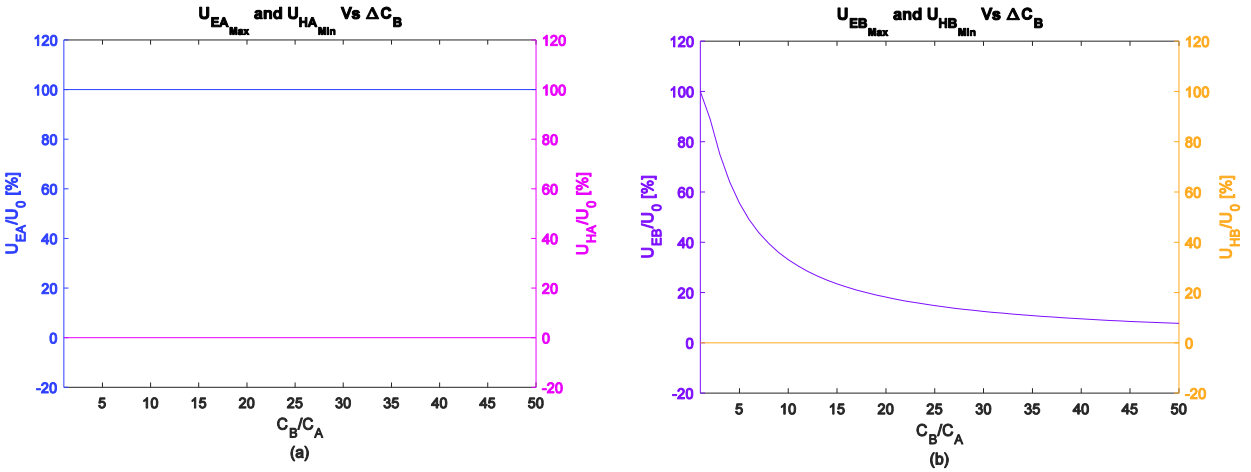


Figure 6-3: Max Electrical and Min Magnetic Line Energies Vs. Capacitance

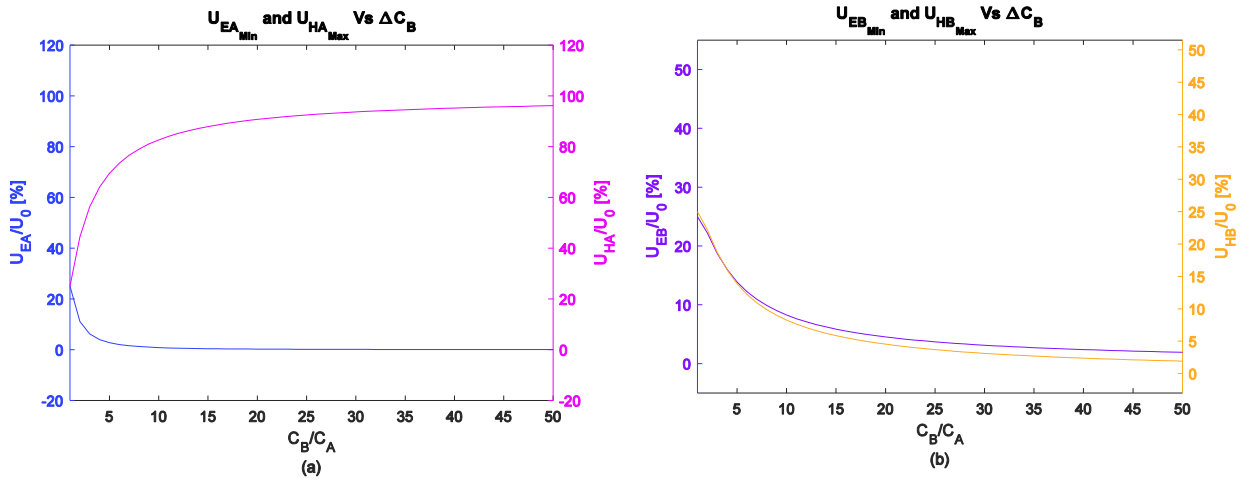


Figure 6-4: Min Electrical and Max Magnetic Line Energies Vs. Capacitance

Figure 6-3 and Figure 6-4 illustrate how the maximum and minimum electric and magnetic energies present on Line A and Line B vary with an increasing C_B. In order to increase C_B whilst maintaining a unity *Fragmentation Ratio* Z_B needs to be effectively lowered. The consequences of lowering Z_B results in a lower self-inductance L_{eB} as per equation (3.43). In Figure 6-3a it can readily be seen that $U_{EA_{Max}} = 100\%$ at all capacitance values of C_B. This result effectively illustrates that provided a *Fragmentation Ratio* of unity (FFGMD) is maintained the maximum electrical energy in the system can always be reconstituted back into C_A i.e. the primary energy store. The implications of this mean that the system is fully capable of returning to its initial state ($U_{EA} = U_0$) before the energy manipulation process is started i.e. before the junction switch is closed at time $t = 0^+$. Observing Figure 6-3b it is readily apparent that increasing C_B lowers the maximum amount of electrical energy that can be present and stored on Line B at any instant in time. This means that in the event that C_B becomes appreciably large i.e. $C_B \cong 40C_A$ according to (3.48) this should result in a $\approx 97.6\%$ reduction in $U_{EB_{Max}}$ whilst the *"Missing Energy"* in

the system increases by the same amount. This *"Missing Energy"* manifest as an exponential increase in the maximum magnetic energy $U_{HA_{Max}}$ as seen in Figure 6-4a. This can be attributed to the fact that an increase in C_B must be accompanied by a decrease in Z_B (in accordance with (3.42)) since the *Fragmentation Ratio* is constant which inherently implies that τ_B is constant. As $Z_B \to \infty$ the reflection coefficient at the junction $\Gamma_{AB} \to -1$. This effectively transforms the TL segment known as Line A into a pseudo resonator. Since the boundary conditions at z_{A_0} (Line A's Near-End Terminal) and $z_{A_f} = z_{B_0} \equiv z_J$ (junction or discontinuity) will now represent an open-circuit and short-circuit respectively. At this point oscillations between electric and magnetic energies will occur on Line A and no energy will be transferred to Line B causing both U_{EB} and U_{HB} to equal zero.

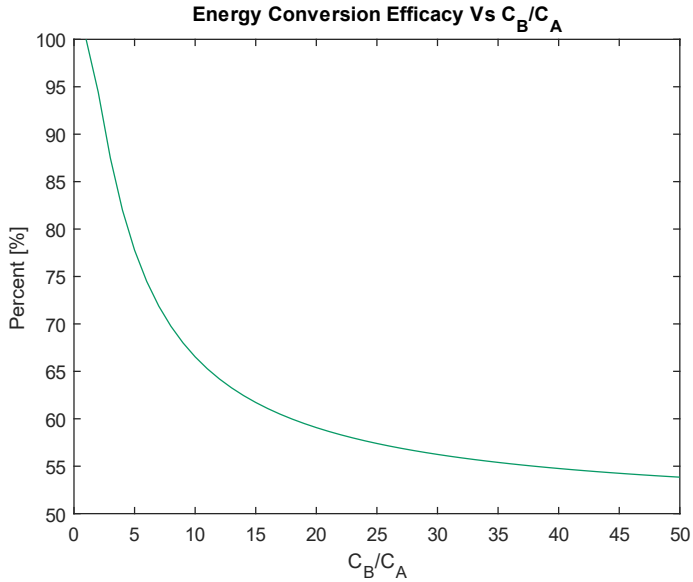


Figure 6-5: Energy Conversion Efficacy Vs. Capacitance

In Figure 6-5 the ECE of the system for the parameters given in Table 6.1 are illustrated. The ECE is determined by substituting $U_{EA_{Max}}$ and $U_{EB_{Max}}$ for $U_{A_{Reconstituted}}$ and $U_{B_{Desired}}$ respectively in equation (6.2). In a lossless system, it is a moot point to quantify performance in terms of conventional efficiency because input power will always equal output power in the absence of loss. It is therefore advantageous to examine the energy manipulations from the perspective of maximum energy transfer and energy reconstitution. The ECE metric as prior stated establishes how much energy can be transferred from a primary to a secondary store and once this energy is transferred how much of it appears in the desired form. In the *Twin Capacitor* context, any associated energy that appears as magnetic energy in the system represents energy in an undesirable form. The more the converted or transferred energy deviates from the desired form the lower the ECE of the energy manipulation process, and hence a reduction in ECE is seen. It is seen in Figure 6-5 that as the capacitance of C_B increases a reduction in ECE is observed. In the limiting case where $C_B \to \infty$,$U_{B_{Desired}} \equiv U_{EB_{Max}} \to 0\%$ which leads to $ECE \to 50\%$ (Since $U_{A_{Reconstituted}} = U_{EA_{Max}} = 100\% \forall C_B$)

Upon further observation of Figure 6-5 it is worth noting that there is a point at which peak or *Maximum Energy Conversion Efficacy* (Max ECE) in the system is achieved. In the context of the simulated example given by the parameters specified in Table 6.2 the maximum attainable ECE in the system is 100% i.e. $ECE = 100\%$. This occurs when the differences in characteristic impedances of the two TL segments is zero i.e. $\Delta Z_{AB} = 0$.

In this scenario since $\Gamma_{AB} = \Gamma_{BA} = 0$ there will be no reflected waves propagating towards either z_{A_0} (Line A's Near-End terminals) or z_{B_f} (Line B's Far-End terminals) on the respective TL segments after they are incident on the junction or discontinuity. Consequently, this means maximum transmission of the origin propagating waves through the junction or discontinuity always occurs. This fact coupled with a unity *Fragmentation Ratio* facilitates instances in time where the respective TL segments occupy both the *fully charged* and *discharged* states as evidenced in Figure 6-1 and Figure 6-2. In this scenario the energy manipulation processes that take place are idyllic. An idyllic energy manipulation process is one in which the primary energy store is capable of reconstituting the entirety of the initial system energy in the original form irrespective of changes in the capacity or magnitude of the secondary energy store. In the *Twin Capacitor* topology, whilst using FFGMD *Fragmentation* generation 100% of the energy transferred/converted to the secondary energy store can always be reconstituted back into the primary energy store.

6.2.1.2 Non-ideal Energy Manipulation (FFGIMD)

The ECE of the system will be examined by maintaining a constant capacitance of the secondary energy store whilst the *Fragmentation Ratio* is varied in accordance with FFGIMD. In order to maintain a constant C_B with a varying *Fragmentation Ratio* the propagation delay (τ_B) as well as the characteristic impedance (Z_B) need to be manipulated or adjusted by the same scalar integer factor k. This is necessary because the capacitance of the secondary energy store is governed by the ratio of the propagation delay to the characteristic impedance as seen in (3.42). Any alterations to the propagation delay τ_B by the given scalar factor need to be applied to the characteristic impedance Z_B in order to ensure the ratio remains unchanged by increases in propagation delay. As an implication of varying the *Fragmentation Ratio* the time instances in which the maximum electrical and magnetic energies occur on Line A and Line B will not be the same. It is necessary to iterate over various simulation runs in order to determine the exact instances the maximum and minimum electric and magnetic energies occur. In accordance with FFGIMD a principal requirement is that the propagation delays are related by integer multiples (i.e. $\tau_B = k\tau_A, k \in \mathbb{Z}$), it is therefore decided that the spatial discretisation iterations will be examined at intervals that are equal to the one-way propagation delay of the shortest TL segment (τ_A). In the given example Line A maintains its propagation delay whilst the propagation delay of Line B is varied. The maximum electrical energies for Line A and Line B for various *Fragmentation Ratios* are presented in Figure 6-6a and Figure 6-6b. In addition, the ECE is presented in Figure 6-7.

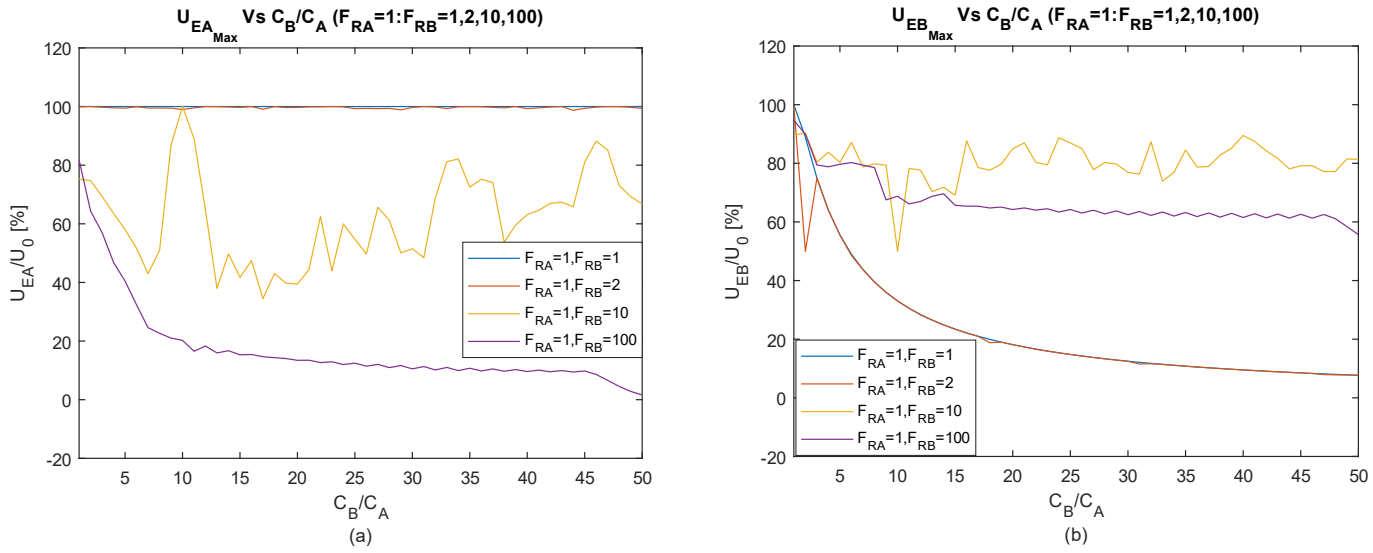


Figure 6-6: Maximum Electrical Energies vs. Changing Capacitance (FFGIMD) a) $U_{EA_{Max}}$ b) $U_{EB_{Max}}$

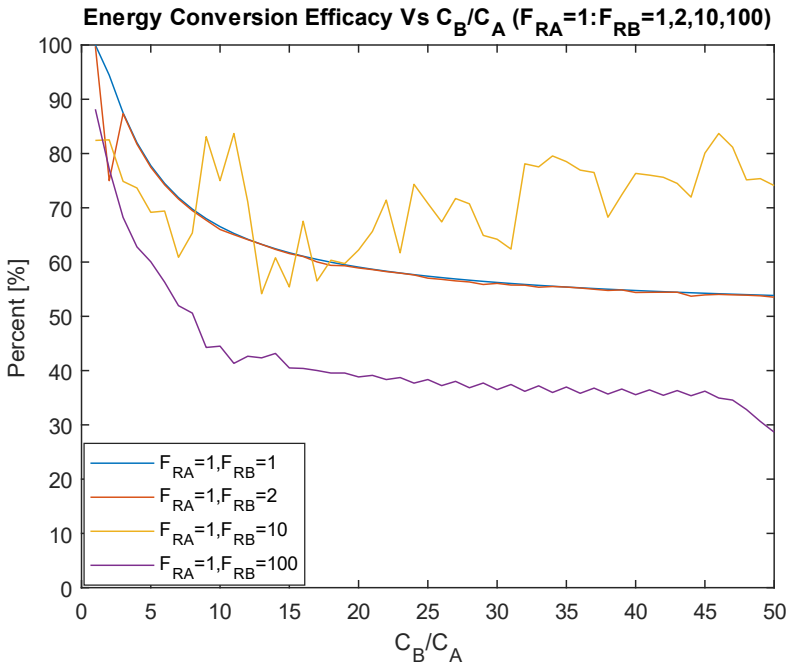


Figure 6-7: Energy Conversion Efficacy vs. Changing Capacitance (FFGIMD)

Upon analysis of Figure 6-6a it can be seen that near perfect energy reconstitution can be achieved for all capacitance values provided the *Fragmentation Ratio* is not greater than $1:2$. As the *Fragmentation Ratio* increases an accompanying decline in $U_{EA_{Max}}$ is experienced.

However, for the *Fragmentation Ratio* $1:10$ a sharp spike to 100% reconstituted energy is seen at $C_B \cong 10C_A$. This can be attributed to the fact that at $C_B \cong 10C_A$ with a propagation delay of $\tau_B = 10\tau_A$. This leads to identical characteristic impedances of the two lines i.e. $Z_B = Z_A$. As a direct consequence the reflection coefficients at the junction are equal to zero i.e. $\Gamma_{AB} = \Gamma_{BA} = 0$. As seen from the ideal energy manipulation case prior, if the difference in characteristic impedances ΔZ_{AB} is appreciably small then an appreciable amount of the system energy is capable of being reconstituted back into the primary energy store. Figure 6-6b illustrates the maximum electric energy stored in the secondary energy store at any given instant in time. From the plots it is readily apparent that as the *Fragmentation Ratio* increases $U_{EB_{Max}} \to 0$ for the majority of the *Fragmentation Ratios*. An outlying case or exception is seen for the case of a *Fragmentation Ratio* of $1:10$. For this *Fragmentation Ratio* an initial decline in the maximum electrical energy is observed but as $C_B \cong 10C_A$ an increase in $U_{EB_{Max}}$ is seen. After this point $U_{EB_{Max}}$ oscillates in and around 70%.

This can be attributed to the fact that at capacitances values close to $C_B \cong 10C_A$ the differences in characteristic impedances are still relatively low, and consequently a majority of the incident voltages from the various fragments are transmitted through the junction or discontinuity with minimal reflection effects. Figure 6-7 details the ECE for the various *Fragmentation Ratios* and in accordance with the trends in $U_{EA_{Max}}$ and $U_{EB_{Max}}$ for all *Fragmentation Ratios* that are not $1:10$ an exponential decrease in ECE is observed. However, the $1:10$ *Fragmentation Ratio* appears to plateau at an ECE of $\approx 70\%$.

6.2.2 Noise Implications

In order to explore the effect that various *Fragmentation Ratios* have on intrinsic noise or EMI generation the temporal progressions in voltage and current along the various TL segments needs to be examined. In order to achieve this, time discretisation is required. This representation examines the time evolution of the voltage and current waveforms at particular points. Theoretically any points on the two adjoining TL segments may be examined. However, considering Figure 3-11 and Figure 3-12 for brevity only z_{A_0} (Line A's Near-End terminals), z_{B_f} (Line B's Far-End terminals) and $z_J \equiv z_{A_f} = z_{B_0}$(the junction or discontinuity) are explored. In the context of the *Twin Capacitor* topology the boundary conditions present at z_{A_0} and z_{B_f} enforce open-circuits conditions. Consequently, the generated current waveforms $i_A(z_{A_0}, t)$ and $i_B(z_{B_f}, t)$ will always be equal to zero and hence will be omitted from the analysis. The current at the junction or discontinuity $i_A(z_J, t)$ will however be examined. The respective terminal voltages $v_A(z_{A_0}, t)$ and $v_B(z_{B_f}, t)$ as well as the voltage and current at the junction or discontinuity ($v(z_J, t)$ and $i(z_J, t)$ respectively) for the simulation parameters presented in Table 6.1 are given in Figure 6-8-Figure 6-11.

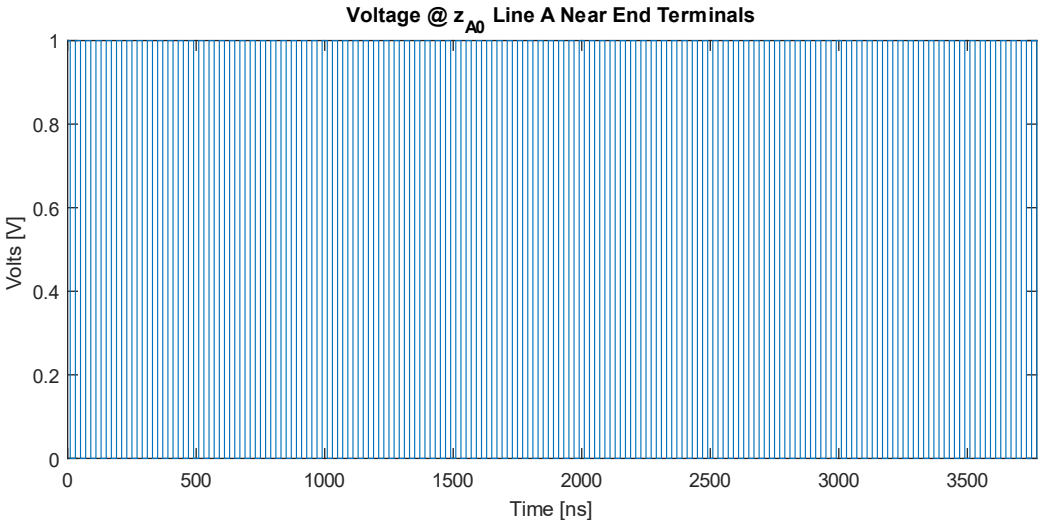


Figure 6-8: Line A Voltage at z_{A_0} terminals ($F_{RA} = 1, F_{RB} = 1$)

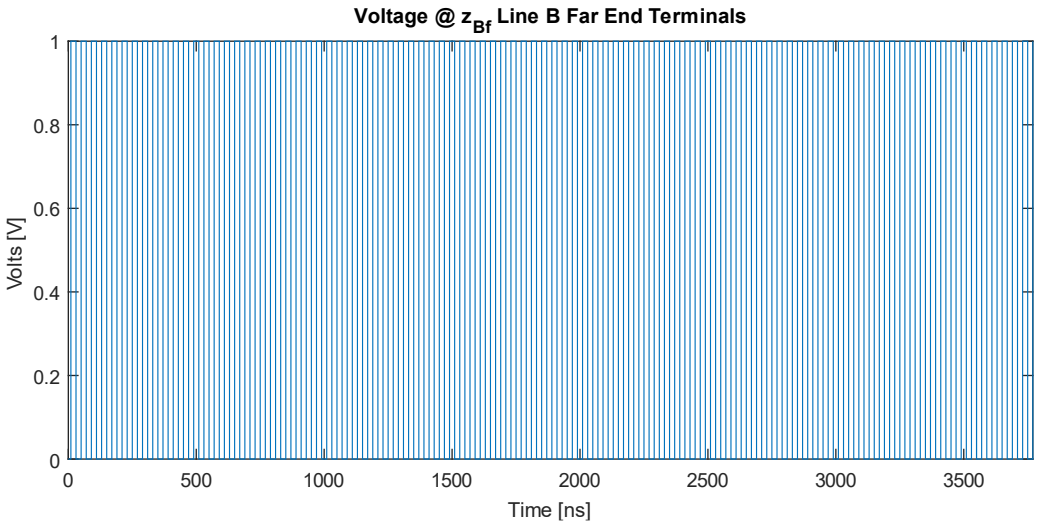


Figure 6-9: Line B Voltage at z_{B_f} terminals ($F_{RA} = 1, F_{RB} = 1$)

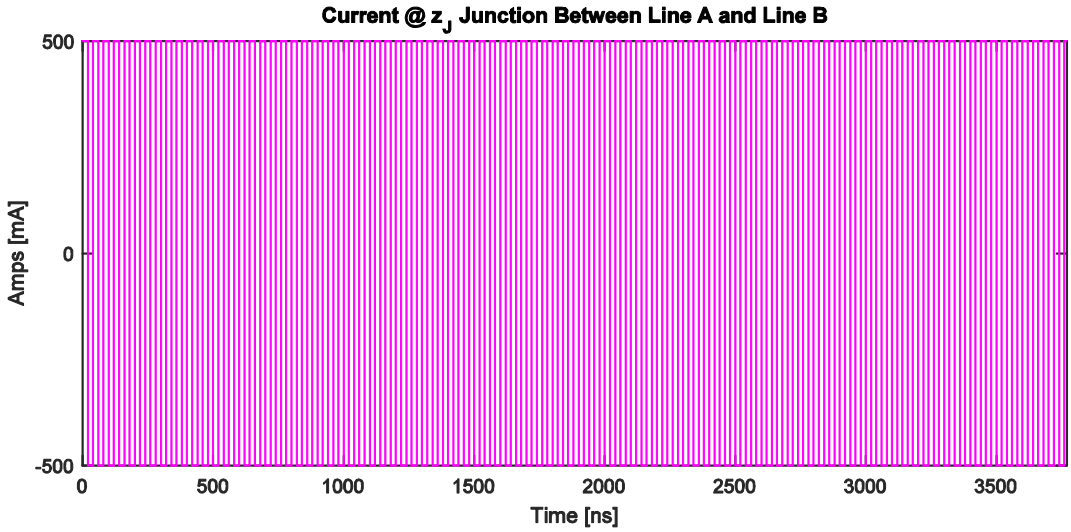


Figure 6-10: Current at z_J Junction terminal ($F_{RA} = 1, F_{RB} = 1$)

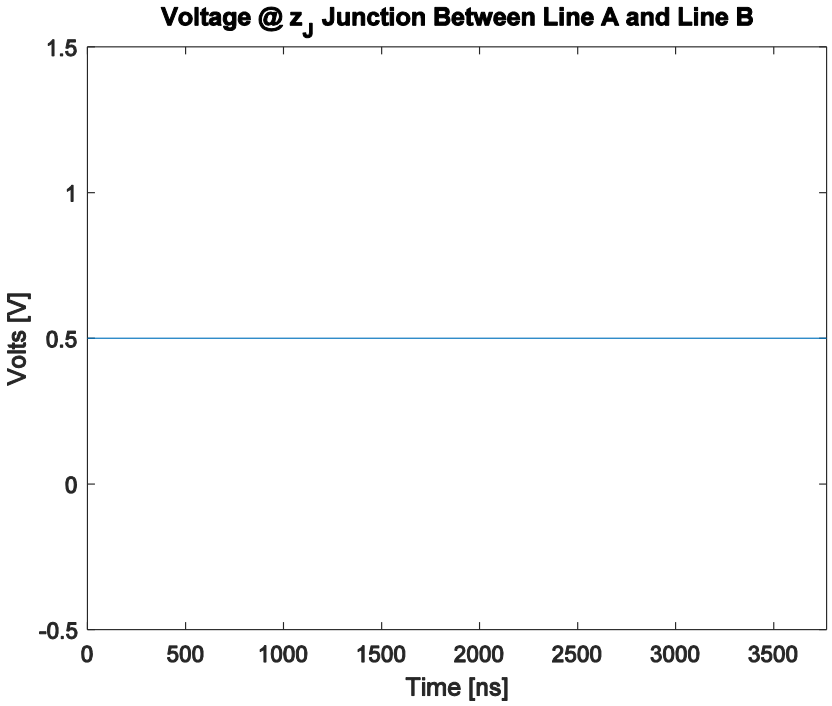


Figure 6-11: Voltage at z_J Junction Terminal ($F_{RA} = 1, F_{RB} = 1$)

Observing Figure 6-8 and Figure 6-9 it is readily seen that the generated voltages on Line A and Line B are bi-polar square waves with a DC offset equal to $\frac{V_0}{2}$. The period of the generated waves corresponds to exactly one round-trip on either Line A or Line B i.e. $T_0 = 2\tau_A \equiv 2\tau_B$. Further observations reveal that the square waves spend half the period at V_0 and the other half at 0. This essentially establishes a duty cycle of 50%. The time averages of the terminal voltages and the junction current waveforms are given by (3.69)-(3.72).

If the mean or time averages $\overline{v_A(z_{A_0}, t)}$ and $\overline{v(z_{B_f}, t)}$ are taken, the resultant or expected voltages are as follows

$$E[X] = \overline{V_A(t)} = \overline{V_B(t)} = \frac{V_0}{2}$$

This is the expected result predicted by conventional circuit theory and literature. Since the DC component by definition is inherently the time average of a given waveform this is not surprising. Upon observation of the current waveform in Figure 6-10 it can readily be seen that $i_A(z_J, t)$ is a purely AC waveform. The time average of $i_A(z_J, t)$ using (3.71) can be taken but it is well known for any purely AC waveform the DC component is zero. Using this fact leads to the notion of zero current flow during the *faux* equilibrium state when both capacitors are charged. If the energies in the system are calculated using the time averages $\overline{V_A(t)}, \overline{V_B(t)}$ and $\overline{I_J(t)}$ the perceived *"Missing Energy"* $\Delta U = 50\%$ will be observed.

The effect of various *Fragmentation Ratios* on the temporal progressions in voltage and current can be assessed by examining the variance of the waveforms produced by the time discretisation at the various points. If we consider any fluctuation or perturbation from the expected DC or average value as indicative of higher frequency components that give rise to generated noise in the waveform. If there are no perturbations or fluctuations in the voltage or current then we expect the deviation (variance) from the DC voltage (mean) to ideally be equal to zero. However, if the variance at z_{A_0} and z_{B_f} line terminals is not equal to zero then this is indicative of EMI generation. The variance for an arbitrary function, signal or process $f(x)$ is given by the following equation [33]

$$\begin{aligned} \sigma^2 &= Var(X) \\ &= E[(X - E[X])^2] \\ &= \int_{-\infty}^{\infty} (x - \overline{X})^2 f(x) dx \end{aligned} \tag{6.26}$$

Algebraically manipulating (6.26) the variance can be represented as

$$\begin{aligned} \sigma^2 &= \overline{X}^2 - (\overline{X})^2 \\ &= E[X^2] - (E[X])^2 \end{aligned} \tag{6.27}$$

The $\overline{X}^2$ and $\overline{X}$ terms in (6.27) represents the mean square value (which can be rearranged to find the root mean square) and the mean respectively. The mean square value of the function or process is given by

$$\begin{aligned} \overline{X^2} &= E[X^2] \\ &= \int_{-\infty}^{\infty} x^2 f(x) dx \end{aligned} \tag{6.28}$$

The mean square value can also be used as a measure of average power in the signal waveform. Since the context where the generated waveforms are produced is in a simulated environment the mean and variance equations are modified to account for this discretised nature. The discretised mean and variance equations are therefore given in (6.29) and (6.30).

$$\overline{X} = \frac{1}{N} \sum_{n=1}^{N} X[n] \tag{6.29}$$

$$\overline{X^2} = \frac{1}{N}\sum_{n=1}^{N}\left(x - \overline{X}\right)^2 x[n] \tag{6.30}$$

The generated noise in the *Twin Capacitor* system is assessed by calculating the variance using (6.30) for the generated waveforms in Figure 6-8-Figure 6-11 as well as additional waveforms generated due to changing *Fragmentation Ratios*. The full list of examined *Fragmentation Ratios* as well as other associated parameters are presented in Table 6.3. Application of (6.27) to the time discretised waveforms at the terminals and junction in Figure 6-12-Figure 6-15 produces the variance plots seen in Figure 6-16-Figure 6-18. For brevity only the time generated waveforms for $1:1,1:10,1:100$ *Fragmentation Ratios* are plotted.

Table 6.3: Twin Capacitor Variance Simulation Parameters

$C_B = C_A$								
$F_{RA}:F_{RB}$	k	$\tau_A[ns]$	$\tau_B[ns]$	$Le_A[nH]$	$Le_B[nH]$	$Z_A[\Omega]$	$Z_B[\Omega]$	ΔZ_{AB}
$1:1$	1	10	10	1	1	1	1	0
$1:2$	2	10	20	1	4	1	2	1
$1:10$	10	10	100	1	100	1	10	9
$1:50$	50	10	500	1	2500	1	50	49
$1:100$	100	10	1000	1	10000	1	100	99

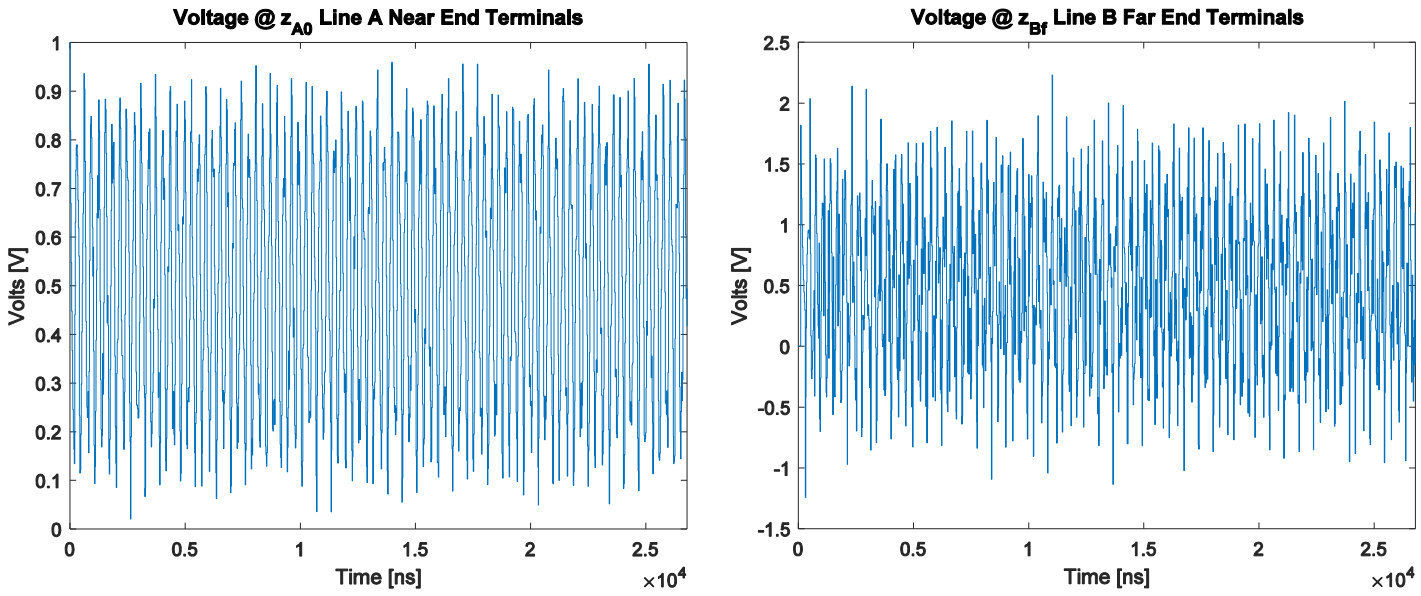


Figure 6-12: Terminal Voltages a) $v(z_{A_0}, t)$ b) $v(z_{B_f}, t)$ ($F_{RA} = 1, F_{RB} = 10$)

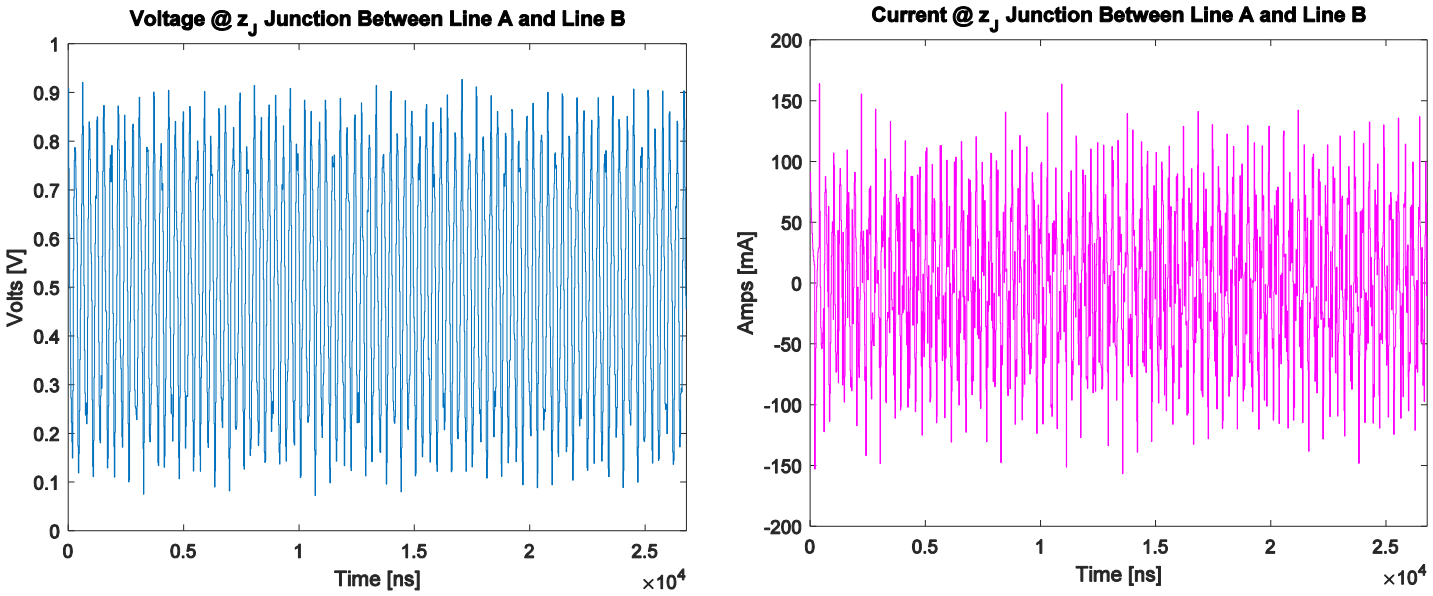


Figure 6-13: Junction Voltage and Current a) $v(z_J, t)$ b) $i(z_J, t)$ ($F_{RA} = 1, F_{RB} = 10$)

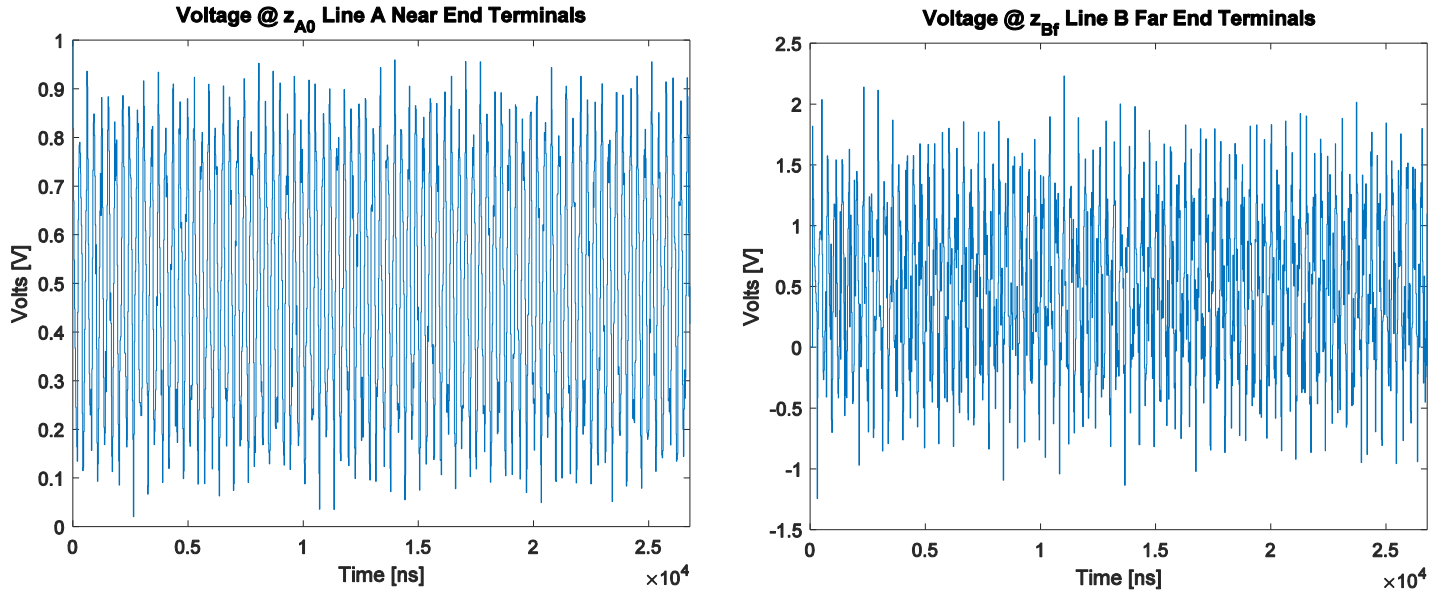


Figure 6-14: Terminal Voltages a) $v(z_{A_0}, t)$ b) $v(z_{B_f}, t)$ ($F_{RA} = 1, F_{RB} = 100$)

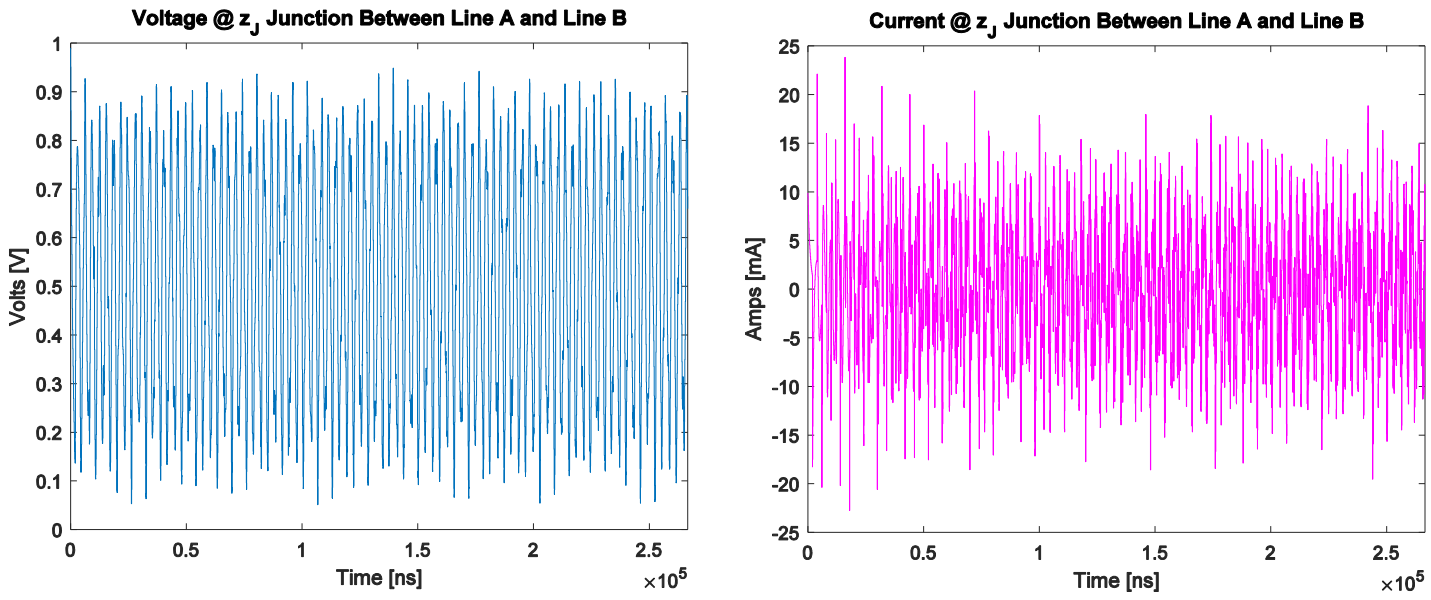


Figure 6-15: Junction Voltage and Current a) $v(z_J, t)$ b) $i(z_J, t)$ ($F_{RA} = 1, F_{RB} = 100$)

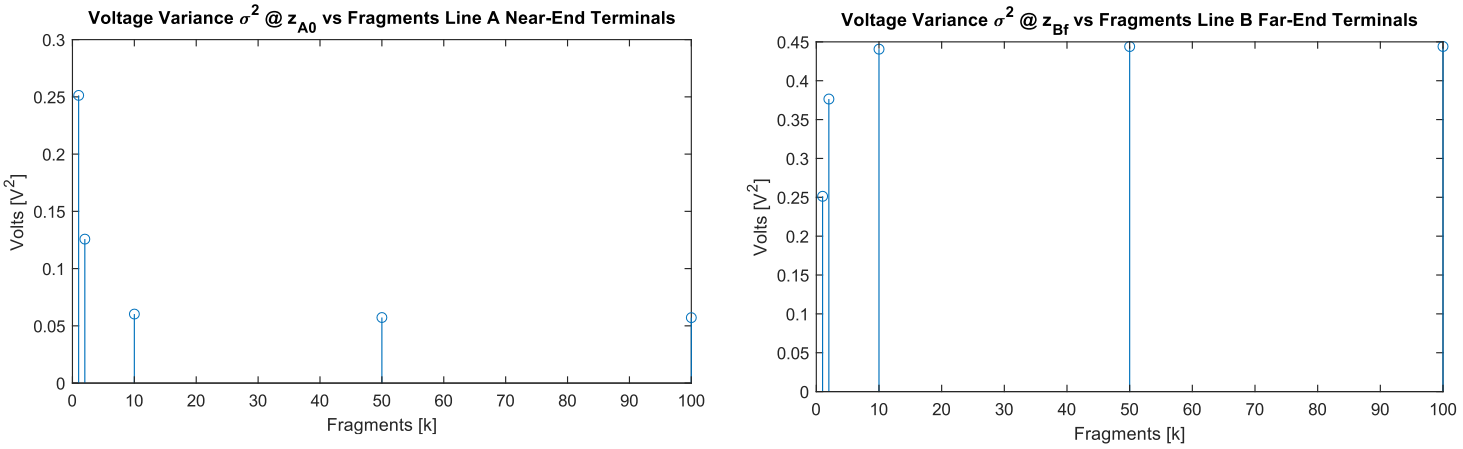


Figure 6-16: Terminal Voltage Variance a) $Var(v(z_{A_0}, t))$ b) $Var(v(z_{B_f}, t))$ ($F_{RA} = 1, F_{RB} = 1,2,10,50,100$)

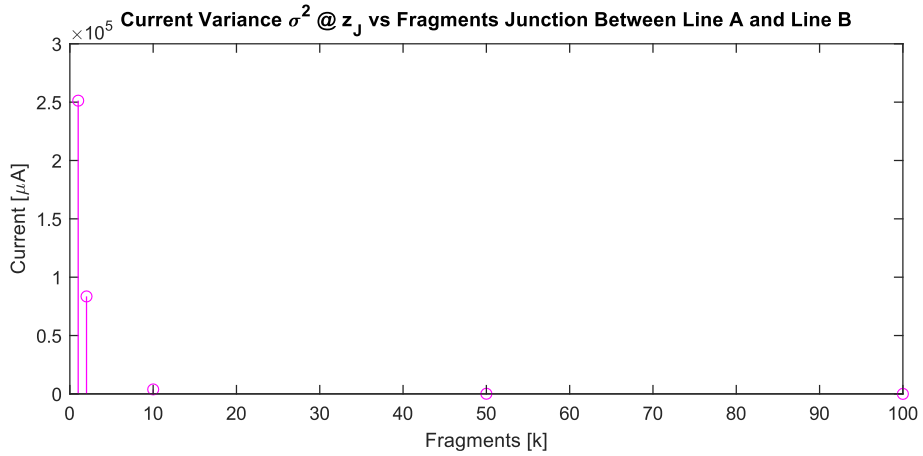


Figure 6-17: Junction Current Variance $Var(i(z_J,t))$ *(*$F_{RA}=1, F_{RB}=1,2,10,50,100$*)*

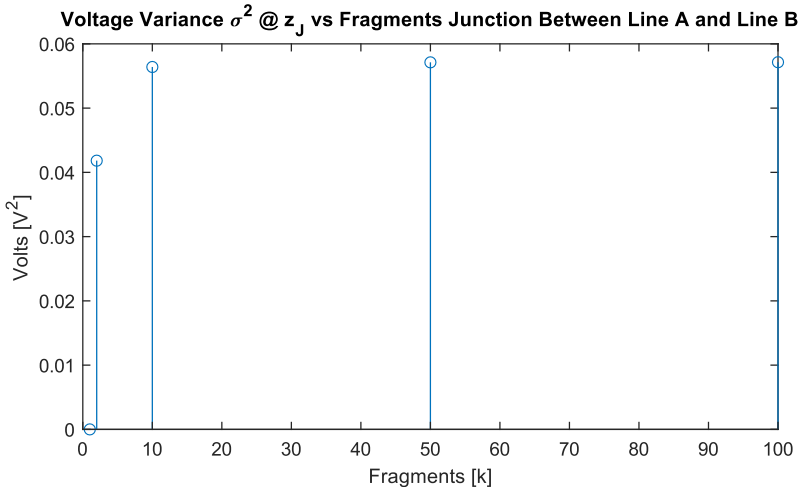


Figure 6-18: Junction Voltage Variance $Var(v(z_J,t))$ *(*$F_{RA}=1, F_{RB}=1,2,10,50,100$*)*

Analysing the variance plots in Figure 6-16-Figure 6-18 leads to the following observations. In Figure 6-16a the variance trend is downward as the number of fragments increase. A decline in variance is indicative of a decline in the generated noise or EMI seen at that position (z_{A_0}, z_{B_f} or z_J) or terminal point. After about 10 fragments (i.e. $k \geq 10$) have been generated in the system the variance at z_{A_0} remains constant. However, it is important to note that during the use of FFGIMD there is only a solitary origin fragment responsible for all the energy manipulation interactions that may take place at z_{A_0} or any other subsequent point on Line A. So interactions or changes in the voltage seen at positions only occur once as the origin Reverse wave either propagates towards z_{A_0} or towards z_{A_f}. This is contrasting to the variance in voltage seen at the terminals at the position z_{B_f}. As a direct consequence of k fragments propagating on Line B there is a greater opportunity for multiple interactions between fragments to take place as fragments travel towards z_{B_f} and z_{B_0}. From this observation, it can come as no surprise that the variance in voltage also increases with successive *Fragmentation* generation. The variance in the voltage however appears to reach a peak or plateau point after 10 fragments have been generated in the system. These results indicate that the noise produced by *Fragmentation* does not grow unbounded or in a directly proportional manner with increases in fragments, but rather appears to tend to some maximum threshold or plateau.

6.3 Dissimilar Transmission Lines

The two cascaded TL segments can be considered dissimilar if an appreciably large difference in characteristic impedances exists between the two lines. The extremities of the simulated range of what constitutes as appreciably large is found by running the *Fragmentation* simulator over various characteristic impedances. It is found that if the absolute difference in characteristic impedances of the two TL segments denoted $|\Delta Z_{AB}|$ can be classified as dissimilar provided $|\Delta Z_{AB}|$ adheres to the following dynamic range

$$1 \times 10^2\ \Omega \leq |\Delta Z_{AB}| \leq 1 \times 10^8\ \Omega$$

If $|\Delta Z_{AB}| \leq 1 \times 10^2\ \Omega$ the SHO and sinusoidal envelopes begin to degenerate to the square waveforms seen in the *Twin Capacitor Paradox*. Conversely if $|\Delta Z_{AB}| \geq 1 \times 10^8\ \Omega$ the reflection coefficient at the junction or discontinuity $\Gamma_{AB} \to 1$, which represents open-circuit boundary conditions, and thus no energy manipulation will take place from Line A to Line B.

The LC Resonant tank unlike the *Twin Capacitor Paradox* does not present an energy paradox and conventional network paradigms correctly predict the sinusoidal envelopes that govern the developed voltages and currents in SHO. It is shown in Chapter 3.5.2 however that this is indeed not the full story. Bounded by the predicted sinusoidal envelopes are pulsating triangular waveforms that peak at integer multiples of the one-way propagation delay down the respective TL segments. The rationale employed when analysing the cascaded TL setup was under minimal *Fragmentation* conditions i.e. the TL segments have identical propagation delays. Consequently, only the origin Reverse and Forward propagating waveforms existed on the TL segments. Since the characterisation of various *Fragmentation* cases established in Chapter 4, the cascaded transmission line setup seen in Figure 3-19 and Figure 3-20 is now revisited. The implications of the various *Fragmentation Ratios* on ECE as well as on EMI or generated noise can now be examined

Using the definition of ECE expressed in Chapter 6.2 but applying it to the context of the LC Resonant tank requires one principle change. The desired energy transferred to the secondary energy store in the *Twin Capacitor* topology was purely electric in nature i.e. $U_{B_{Desired}} = U_{EB_{Max}}$. However, since the secondary storage element in the LC Resonant tank is an inductor, it makes intuitive sense to redefine the desired converted and stored energy to be purely magnetic in nature i.e. $U_{B_{Desired}} = U_{HB_{Max}}$.

Similar to the case of the *Twin Capacitor Paradox* examined in Chapter 6.2 the effect of various *Fragmentation Ratios*, changing impedances and associated self-inductances and self-capacitances and their collective and individual effect on ideal and non-ideal energy manipulations will be interrogated using the ECE metric. In addition, the role *Fragmentation* plays in generating noise will be examined by analysing the temporal distributions in voltages and currents at the terminal and junction nodes. The definitions for ideal and non-ideal energy manipulations are the same as per the *Twin Capacitor* topology detailed in Chapter 6.2 with the only change being that an inductor instead of a capacitor now represents the secondary energy store. The LC Resonant tank is modelled in the simulated environment by the Link-Line equivalent representation given in Figure 3-19 and Figure 3-20.

6.3.1 Energy Implications

6.3.1.1 Ideal Energy Manipulation (FFGMD)

Before more sophisticated *Fragmentation* generation methods (such as FFGIMD) are employed, it is important to get a qualitative feel for how the electric to magnetic energy manipulation interactions in the LC Resonant tank take place at a base level. In order to achieve this a *Fragmentation Ratio* of unity ($F_{RA} = 1, F_{RB} = 1$) and hence the FFGMD *Fragmentation* generation method is assessed in the simulated environment. The simulation parameters for the example are presented in Table 6.4. The natural oscillating frequency f_0 corresponding to the angular frequency ω_0 are selected such that the electrical lengths of both Line A and B are very much greater than the physical lengths l_A and l_B. As a result, minimal phase delay effects will be experienced by the origin Reverse and Forward travelling propagating waveforms on Line A and Line B respectively. The electrical lengths for Line A and Line B are calculated as follows:

$$l_{elec} \equiv \lambda = \frac{c}{f_0} = \frac{2\pi(3 \times 10^8)}{318280\pi} \cong 1885\ m$$

As a general rule of thumb propagation effects need to be considered when the physical lengths of a TL segment at a particular operating frequency approaching a tenth of a wavelength or a tenth of the electrical length i.e. $l_{phys} \cong \frac{l_{elec}}{10}$. Since $l_A = l_B \equiv l_{phys} \ll \frac{l_{elec}}{10}$ minimal propagation delay effects will be experienced.

Table 6.4: LC Resonant FFGMD Simulation Parameters

$Parameter$	$Value$
U_0	$5000\ pJ$
V_0	$1\ V$
I_0	$10\ mA$
τ_A	$10\ ns$
τ_B	$10\ ns$
Z_A	1Ω
Z_B	$10\ k\Omega$
ΔZ_{AB}	$9.999\ k\Omega$
l_A	$3\ m$
l_B	$3\ m$
C_A	$10\ nF$
L_{eA}	$1\ nH$
L_B	$100\ \mu H$
C_{eB}	$1\ pF$
C_0	$1pF$
ω_0	$318280\pi\ rad/sec$
n_{seg}	10000

In order to examine the implications of *Fragmentation* on the system energy in the LC Resonant tank, the spatial distributions in voltage and current are required at specific time intervals. This spatial discretisation takes place along the l_A and l_B lengths in Figure 3-19 and Figure 3-20. Unlike the case of the *Twin Capacitor* topology the LC Resonant tank produces AC harmonic oscillatory waveforms. The time varying voltage and current waveforms established in the resonant tank are thus given by

$$V(t) = V_0\cos(\omega_0 t) \tag{6.31}$$

$$I(t) = I_0\sin(\omega_0 t) \tag{6.32}$$

Due to the harmonic nature of the voltages and currents, the time instances at which the spatial distributions will be taken will coincide with the respective voltage and current peaks. Maximum or peak voltage will be seen at time instances $T = nT_0, n \in \mathbb{Z}$, whereas maximums or peaks in current will be observed at time instances of $T = \frac{nT_0(2n-1)}{2}, n \in \mathbb{Z}$. This is readily apparent upon examination of the generated voltage and current waveforms in Figure 6-19 and Figure 6-20. In Figure 6-21 and Figure 6-23 the spatial distributions in voltage and current on Line A at $t = T_0$ are depicted. In accordance with the expected voltage waveform given by (6.31) it is expected that the entirety of the system energy will be electric in nature and hence confined solely to Line A. Upon observation of Figure 6-21 the instantaneous voltage present on Line A ***appears*** to be equal to V_0, however there is an infinitesimally small difference between V_0 and the voltage presently on Line A $|v_A(z, t_0)|$. The repercussions of this seemingly minutiae difference in voltages at a time $t = T_0$ means that not all of the electrical energy initially present in C_A before its connection to L_B has been reconstituted to C_A. From this observation, it is sufficient to conclude that even in the case of FFGMD an ECE of 100% in the LC Resonant tank is not realisable. The implications of this mean that there will always be a deficiency in the electrical energy stored in C_A at every time instance $T = nT_0, n \in \mathbb{Z}$ after the energy manipulation process is started. This so-called deficiency in electrical energy on Line A can be explained by noting the fact there is an instantaneous residual line current $i_B(z, t_0)$ present on Line B as seen in Figure 6-23.As a direct result of this residual current the instantaneous magnetic field energy on Line B will not be zero.

The magnitude of the magnetic field energy stored on Line B is appreciably smaller than the electric field energy found on Line A, however it is non-zero and will always be finite. In addition, upon observing the magnitude of the magnetic field energy present on Line B it becomes readily apparent that it is precisely equal to the magnitude of the deficiency in electrical energy seen on Line A.

The significance of this result means that the deficiency in electrical energy on Line A has actually changed forms and has in fact manifested as magnetic energy on Line B because of the residual current seen on Line B. This residual current can be thought of as a form of taxation on the electrical energy during the energy manipulation processes. As soon as the electrical energy is converted to magnetic energy and then back to electrical energy, even in a lossless and ideal environment the initial energy U_0 can never fully be reconstituted into the primary energy store C_A. The deficiency in electrical energy present on Line A can be quantified by calculating the percentage of energy stored on Line B due to the non-zero residual current present in the system. Using (6.23) the magnetic energy present on Line B as a function of the line position can be determined.

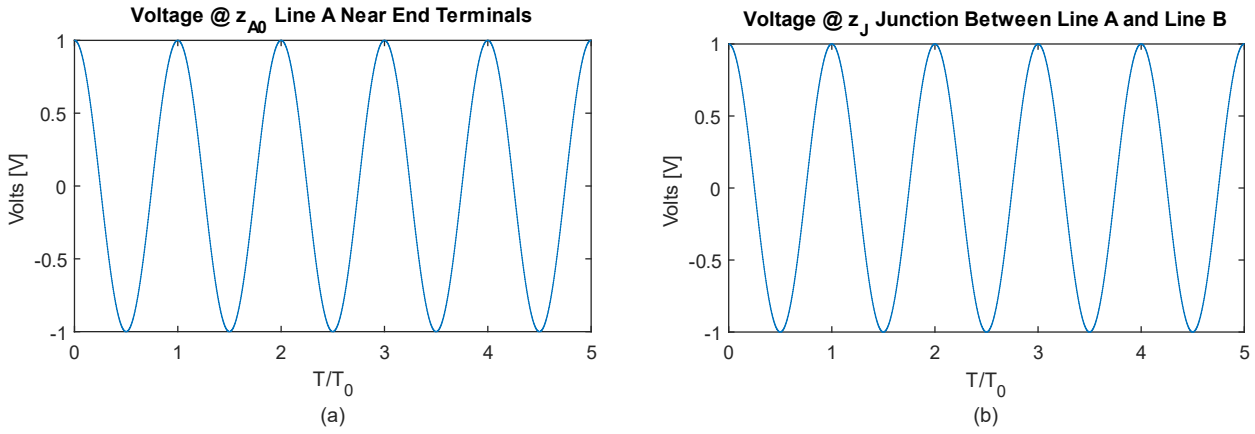


Figure 6-19: LC Resonator Terminal and Junction Voltages a) $v_A(z_{A_0}, t)$ b) $v_A(z_J, t)$

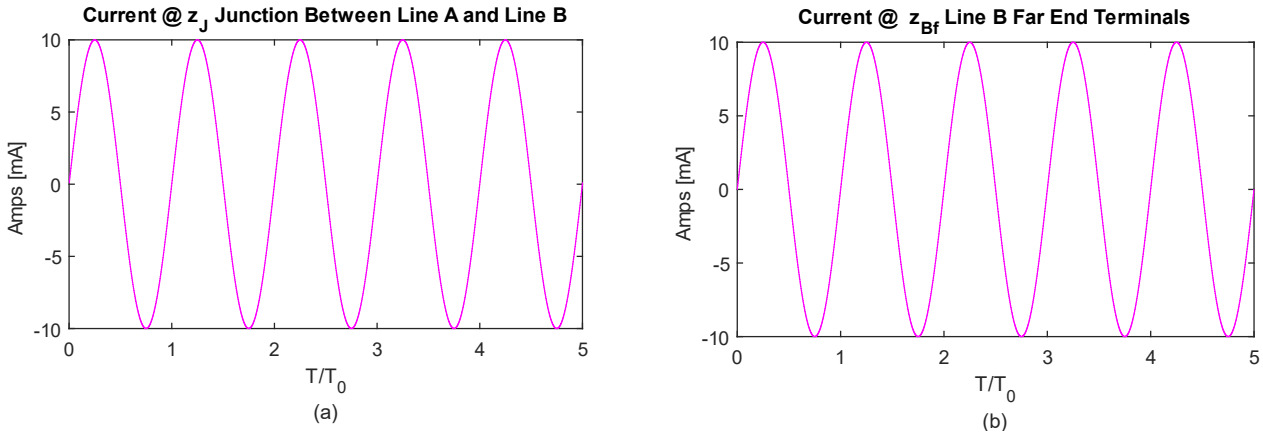


Figure 6-20: LC Resonator Junction and Terminal Currents a) $i_B(z_J, t)$ b) $i_B(z_{B_f}, t)$

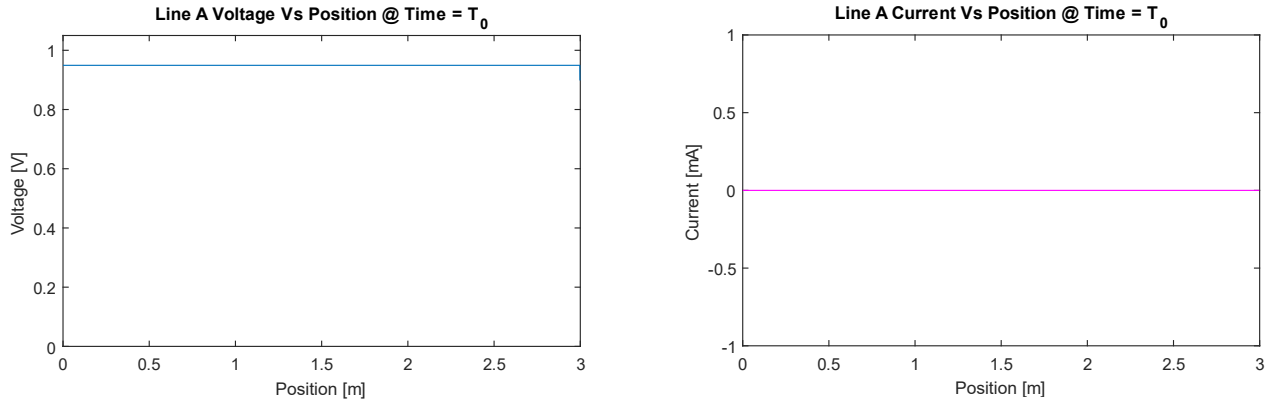


Figure 6-21: LC Resonator Line A Voltage and Current @ T_0 ($v_A(z, T_0)$, $i_A(z, T_0)$)

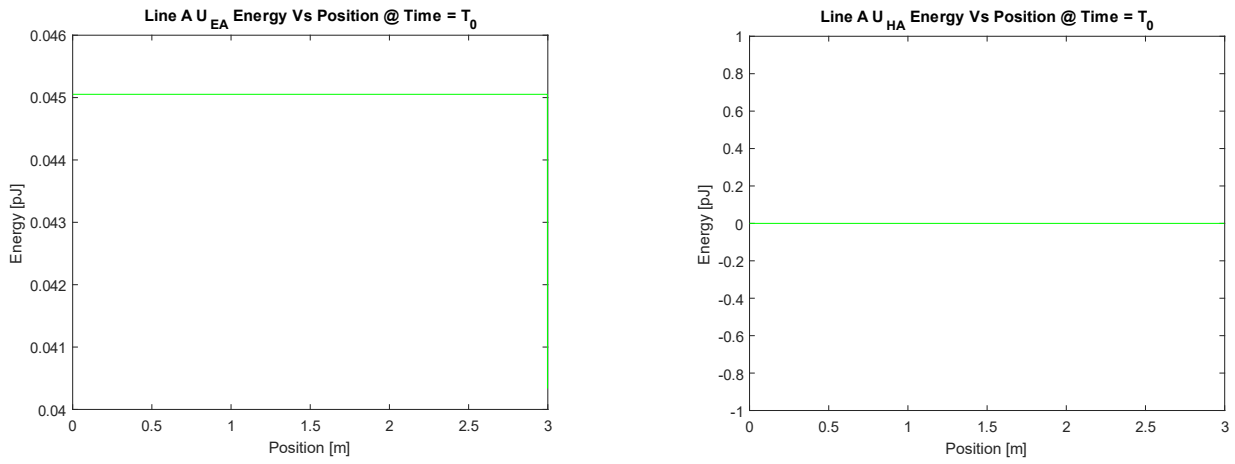


Figure 6-22: LC Resonator Line A Electric and Magnetic Energies @ T_0 ($U_{EA}(z,T_0)$, $U_{HA}(z,T_0)$)

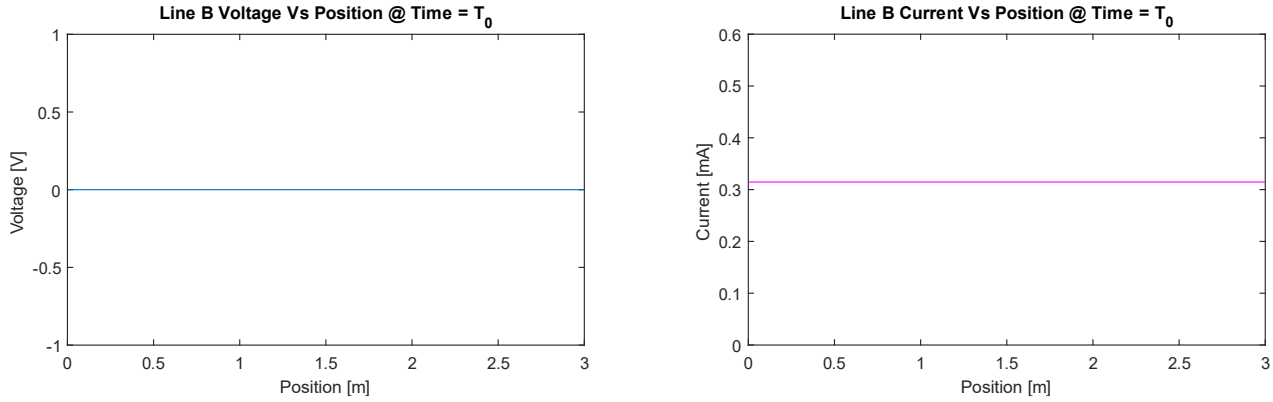


Figure 6-23: LC Resonator Line B Voltage and Current @ T_0 ($v_B(z,T_0)$, $i_B(z,T_0)$)

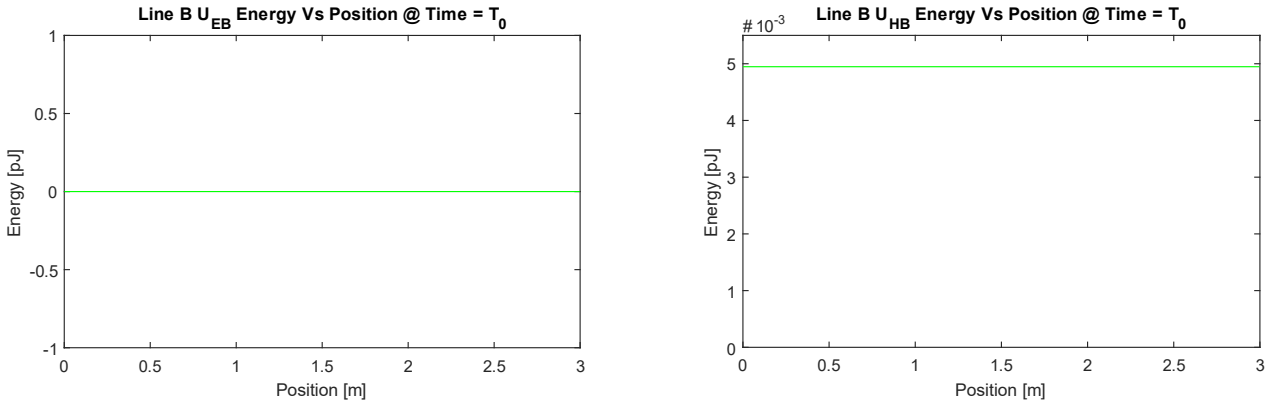


Figure 6-24: LC Resonator Line B Electric and Magnetic Energies @ T_0 ($U_{EB}(z,T_0)$, $U_{HB}(z,T_0)$)

The total magnetic field energy stored on Line B is found by multiplying $U_{H_BT}(z,t_0)$ by the total number of discretized segments n_{seg} on Line B.

$$U_{H_BT} = n_{seg}\left|U_{H_BT}(z,t_0)\right| \tag{6.33}$$

Using(6.33) the total magnetic energy on Line B is found to be $0.050\ pJ$.

$$U_{H_BT} = 10000 \times (0.5 \times 10^{-6}) \times 10^{-12} = 0.050\ pJ$$

Expressing U_{H_AT} as a percentage of the initial energy U_0 present in the system.

$$U_{H_BT}\ \% = \frac{U_{H_BT}}{U_0} = \left(\frac{0.050 \times 10^{-12}}{5000 \times 10^{-12}}\right) \times 100 = 0.001\%$$

Upon observation of the energy stored in Line B it can be readily concluded that the deficiency in electrical energy in this instance represents a truly minutiae amount of energy. As minutiae as this energy may be it is truly irrecoverable and will always be observed at integer multiples of the oscillation period T_0 i.e. $T = nT_0, n \in \mathbb{Z}$. Under minimal *Fragmentation* conditions (i.e. FFGMD is used) $F_{RA} = F_{RB}$. Subsequently what is seen is that the deficiency in electrical energy is a function of the self-capacitance (C_{eB}) stored on Line B, as well as the dissimilarity in characteristic impedances ΔZ_{AB} of the two TL segments. The magnitude of the residual current present on Line B at instances of T_0 is directly proportional to ΔZ_{AB}. In order for ΔZ_{AB} to change whilst maintaining a constant propagation delay the impedance of Line B must ultimately be lowered. In reducing Z_B a corresponding increase in C_{eB} will be observed. The ramifications of this increasing self-capacitance will be explored by examining the maximum electrical and magnetic energies as the self-capacitance is increased. Figure 6-25a and Figure 6-25b relates the current self-capacitance denoted C_{eB} to a reference self-capacitance C_0 detailed in Table 6.4.

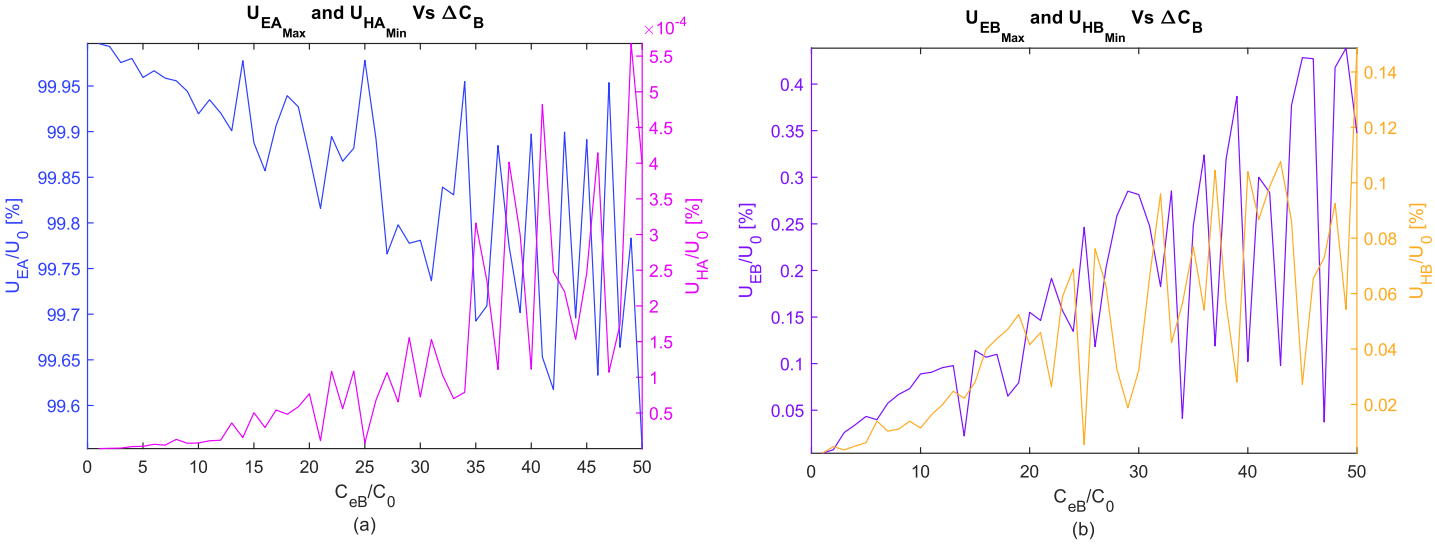


Figure 6-25: LC Resonator Max Electrical and Min Magnetic Line Energies Vs. Self-Capacitance

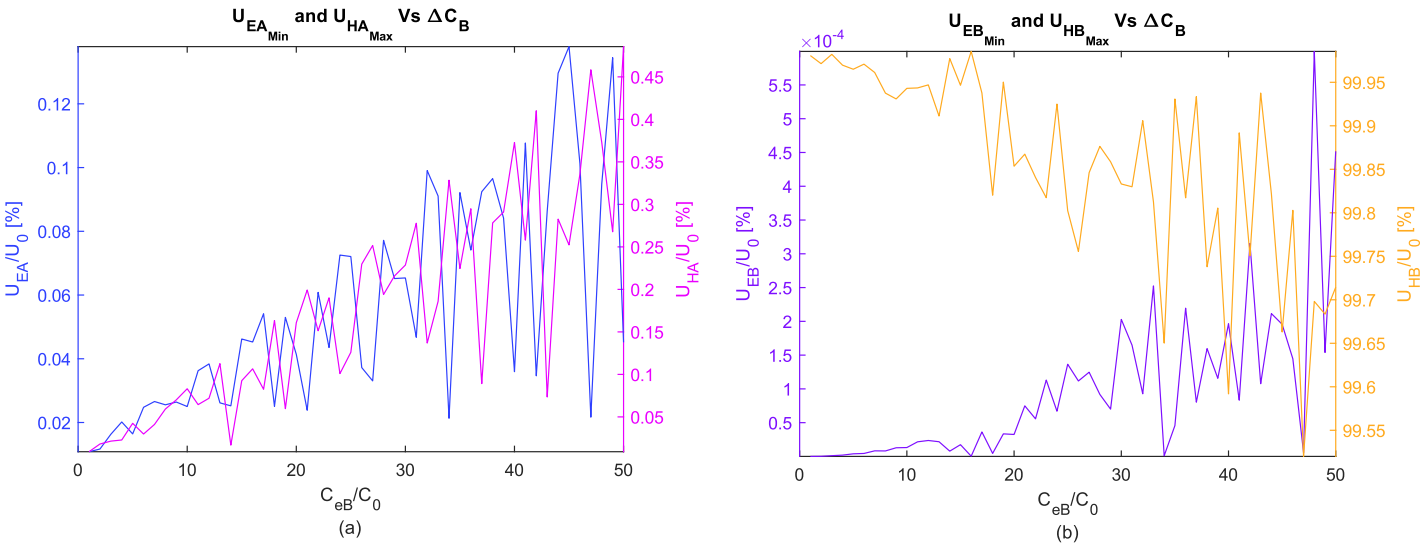


Figure 6-26: LC Resonator Min Electrical and Max Magnetic Line Energies Vs. Self-Capacitance

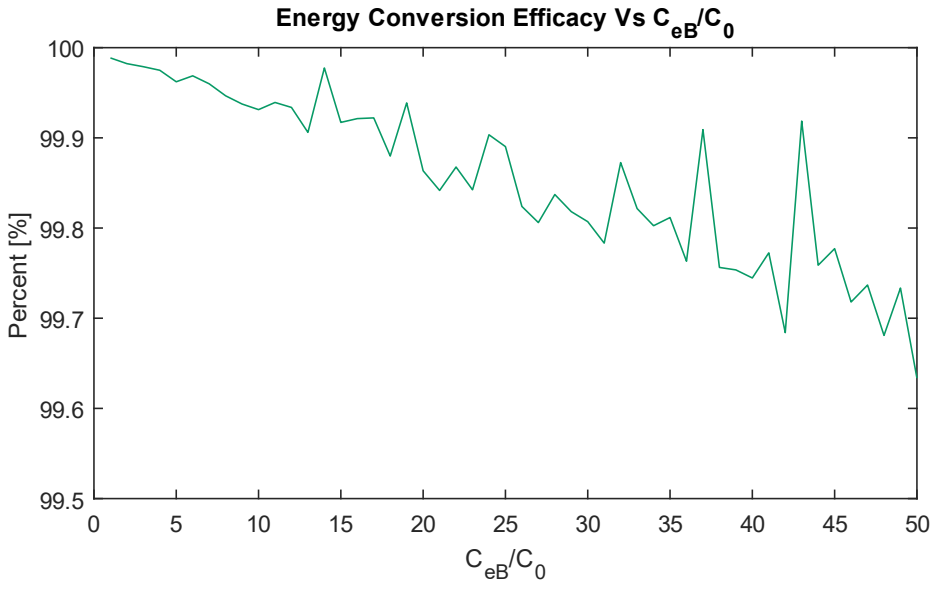


Figure 6-27: LC Resonator Energy Conversion Efficacy Vs. Self-Capacitance

Observation of the maximum electrical and magnetic energies in Figure 6-25-Figure 6-26 yields the following observations. The maximum electrical energy present in the capacitor ($U_{EA_{Max}}$) appears to remain quite resolute in spite of increases in the self-capacitance (C_{eB}) of the inductor L_B. At most a 0.3% drop in $U_{EA_{Max}}$ is seen across the entirety of the self- capacitance range. The minimum magnetic energy $U_{EA_{Min}}$ experiences subsequent increases in energy with an increasing C_{eB}. This occurs because of the reduction in Z_B required to increase C_{eB}, and as a consequence of the lower impedance higher current values will be noted on Line A.

These higher current values however do not lead to appreciable amounts of energy being stored on Line A because the associated self-inductance on Line A (L_{eA}) has a small magnitude. Nevertheless, the increase in line current facilitates an increase in the minimum magnetic energy $U_{HA_{Min}}$. Considering the maximum and minimum magnetic and electric energies on Line B, it is quite evident that appreciable changes in the self-inductance (more than an order of magnitude) have little effect on the maximum magnetic energy stored in the inductor L_B. Ultimately, observing the maximum ECE of the LC Resonant tank speaks to the robustness of the LC Resonant tank in handling energy manipulation interactions in spite of the increasing self-capacitance.

6.3.1.2 Non-Ideal Energy Manipulation (FFGIMD)

The implications of FFGIMD generation will be illustrated in the LC Resonant tank by examining the effects that various fragments have on ECE when the self-capacitance of the inductor is increased. From (3.26) it is seen that in order to keep L_B constant in spite of varying *Fragmentation Ratio* the characteristic impedance Z_B must be divided by the propagation delay on Line B i.e. $\frac{Z_B}{\tau_B}$. The implications of reducing Z_B whilst maintaining a constant *Fragmentation Ratio* means that the self-capacitance C_{eB} will be increased by the square of the propagation delay on the line i.e. $\Delta C_{eB} = C_{eB}(\tau_B)^2$. This result merely just restates the alternative formula for capacitance given in (3.27).Unlike the case of the *Twin Capacitor* topology the instances in which the maximum electric and magnetic energies occur will still happen at full and half integer multiples of the period T_0 ($T = nT_0$ and $T = \frac{2n-1}{2}T_0$ respectively). In the presented scenario Line A is the propagating waveform that gives rise to the k new Forward waves or fragments that are present on Line B. The maximum electrical and magnetic energies for the various *Fragmentation Ratios* are presented in Figure 6-28 and Figure 6-29 whilst the ECE is given in Figure 6-30.

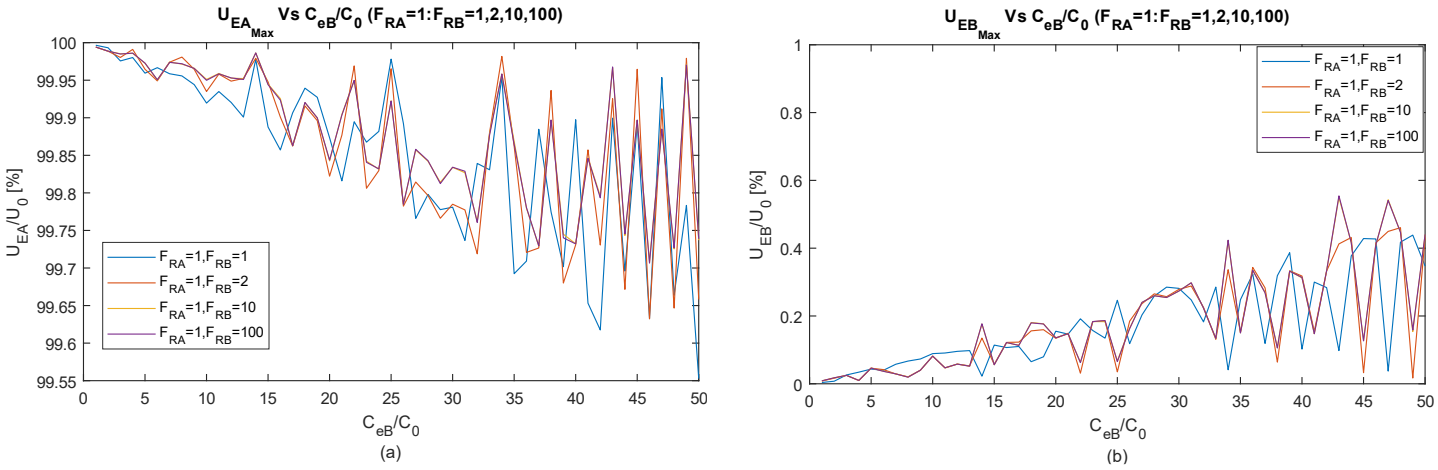


Figure 6-28: LC Resonator Max Electrical Energies vs. Self-Capacitance (FFGIMD) a) $U_{EA_{Max}}$ b) $U_{EB_{Max}}$

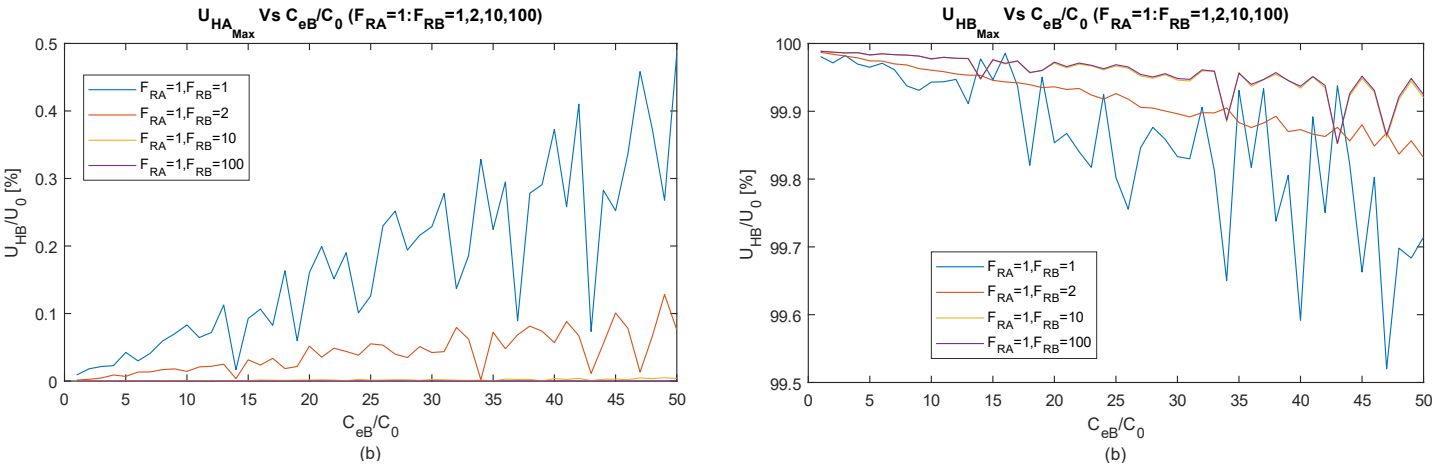


Figure 6-29: LC Resonator Max Magnetic Line Energies vs. Self-Capacitance (FFGIMD) a) $U_{HA_{MAX}}$ b)$U_{HB_{Max}}$

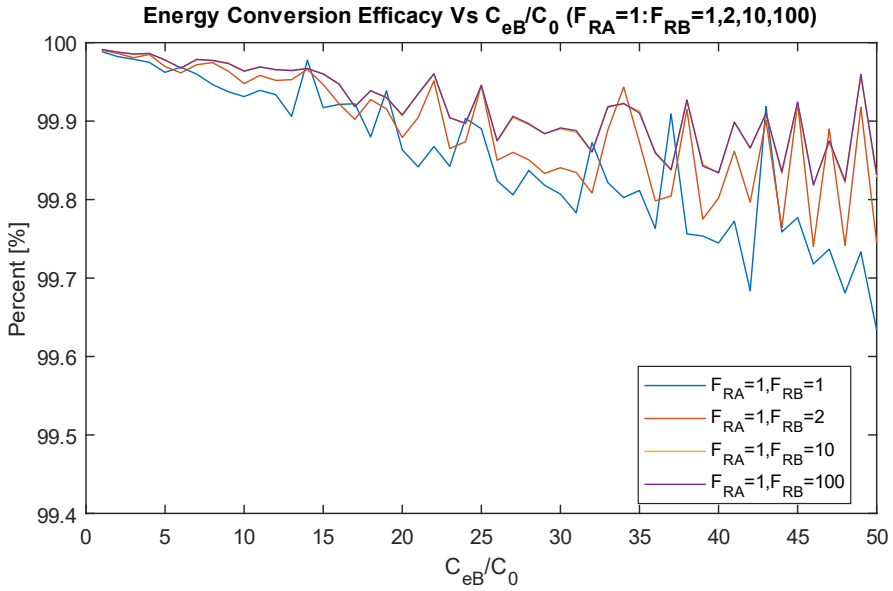


Figure 6-30: Energy Conversion Efficacy vs. Self-Capacitance (FFGIMD)

Similar to the ideal energy manipulation case where FFGMD was used as the principle *Fragmentation* generation method, the maximum electrical and magnetic energies present on both Line A and Line B exhibit robustness in the face of changing self-capacitances. Similarly, this is evidenced by the ECE in Figure 6-30. From these results, we can surmise that increases in *Fragmentation Ratio* and the self-capacitance of the inductor L_B do little to disrupt the efficacy of the energy manipulation processes. It must be however cautioned that if the self-capacitance of the inductor starts to approaches values that are comparable to the primary capacitor C_A. The principle operation of the LC Resonant tank will change as the TL segment that once represented the inductor L_B will now better approximate a capacitor. Consequently, this means the cascaded TL setup can now be classified as the case of two similar transmission lines.

6.3.2 Noise Implications

The noise implications of *Fragmentation* in the LC Resonant tank will be assessed by taking the difference of the waveforms generated by the *Fragmentation* process and the reference or predicted sinusoidal waveforms given by (6.31) and (6.32). This difference in waveforms gives rise to a delta waveform. The delta waveforms for the voltage ($\Delta v(z,t)$) and current ($\Delta i(z,t)$) are given by the following equations

$$\Delta v(z_0,t) = v_f(z_0,t) - v_r(z_0,t) \tag{6.34}$$

$$\Delta i(z_0,t) = i_f(z_0,t) - i_r(z_0,t) \tag{6.35}$$

In equation (6.34) and (6.35) the subscripts f and r speak to whether the waveform has been generated from the *Fragmentation* process (f) or the reference waveforms (r). If minimal noise exists in the system because of *Fragmentation* generation the magnitude of the delta waveform should be relatively small. The simulated parameters in Table 6.4 are used with modifications being made to the propagation delay τ_B and the characteristic impedance Z_B. The updated simulation parameters for the various *Fragmentation Ratios* are represented in Table 6.5. In the LC Resonant tank, the boundary conditions present at z_{B_f} represents that of a short circuit whilst the boundary conditions at z_{A_0} still represent open-circuits conditions. Observing these conditions $i_A(z_{A_0},t)$ and $v_B(z_{B_f},t)$ will be omitted from the analysis and do not form part of the generated figures. The generated waveforms arising from the modified simulation parameters in Table 6.5 as well as the associated difference waveforms are given in Figure 6-31-Figure 6-42.

Table 6.5: LC Resonant Tank FFGIMD Simulation Parameters

$C_A = 100nF, L_B = 100\ \mu H$								
$F_{RA}:F_{RB}$	k	$t_A[ns]$	$t_B[ns]$	$Le_A[nH]$	$C_{eB}[nF]$	$Z_A[\Omega]$	$Z_B[k\Omega]$	ΔZ_{AB}
1:1	1	10	10	1	1	1	10	9999
1:2	2	10	20	1	4	1	5	4999
1:10	10	10	100	1	100	1	3.333	3332.3
1:50	50	10	500	1	2500	1	0.2	199
1:100	100	10	1000	1	10000	1	0.1	99

In attempts to standardise, the analysis for the various *Fragmentation Ratios* presented in Table 6.5 classification of the results will be split into three categories in accordance with the number of generated fragments in the system. These categories are: shallow, moderate and excessive. Shallow fragmentation will classify systems that have fewer than ten generated fragments i.e. $1:1 \leq F_{RA}:F_{RB} < 1:10$. Moderate fragmentation will be classified as systems that contain fragments anywhere in the range between ten and one hundred i.e. $1:10 \leq F_{RA}:F_{RB} < 1:100$. Lastly excessive fragmentation will classify systems that have generated fragments of one hundred and greater i.e. $F_{RA}:F_{RB} \geq 100$. For all the fragmentation categories a FFGIMD generation method is used.

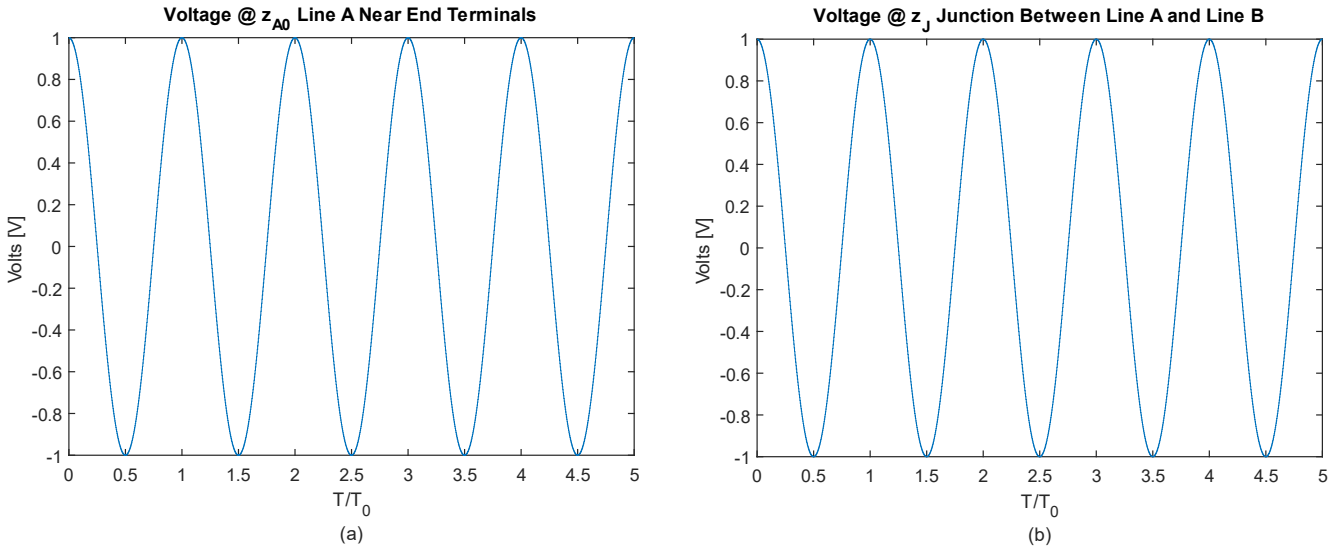


Figure 6-31: Generated Voltage Waveforms a) $v_A(z_{A_0}, t)$ b)$v(z_J, t)$ ($F_{RA} = 1, F_{RB} = 1$)

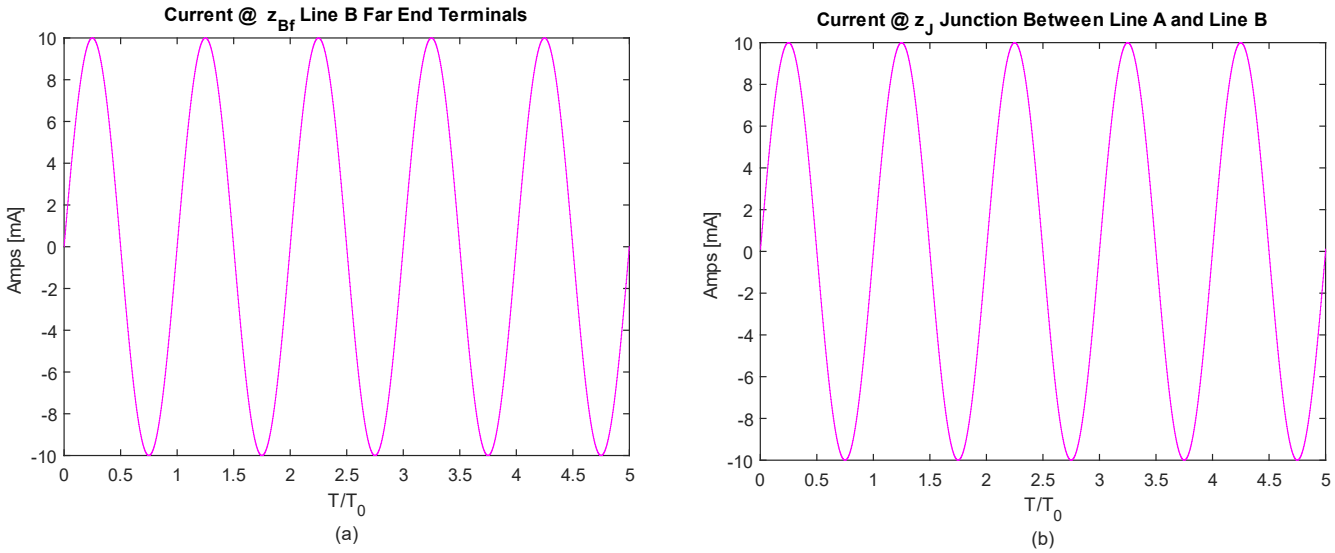


Figure 6-32: Generated Current Waveforms a) $i_B(z_{B_f}, t)$ b) $i(z_J, t)$ ($F_{RA} = 1, F_{RB} = 1$)

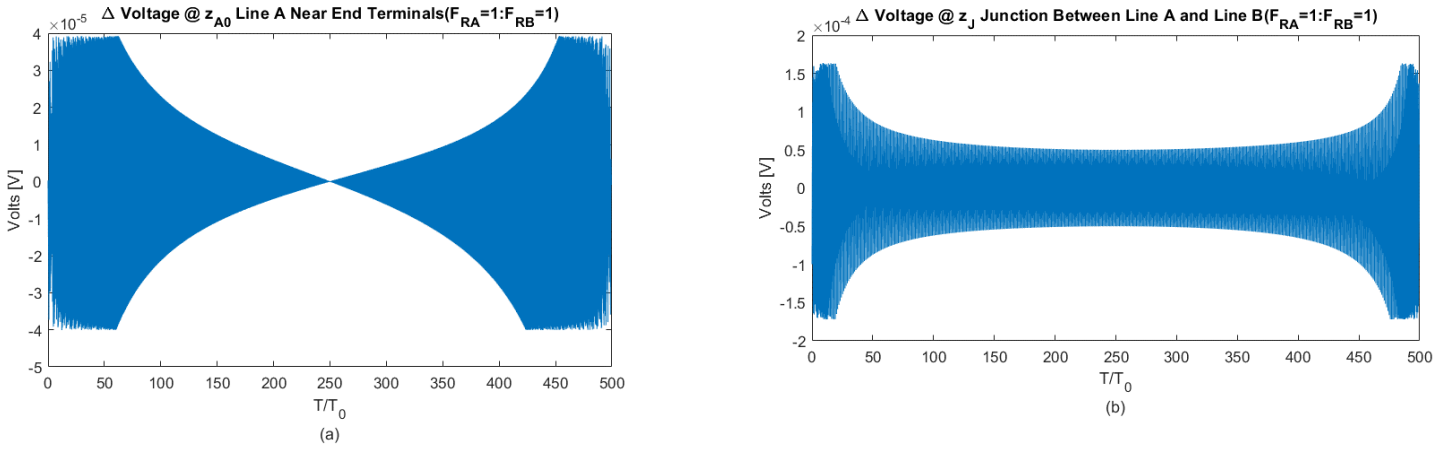


Figure 6-33: Voltage Differences at z_{A_0} and z_J a)$\Delta v(z_{A_0}, t)$ b)$\Delta v(z_{B_f}, t)$ ($F_{RA} = 1, F_{RB} = 1$)

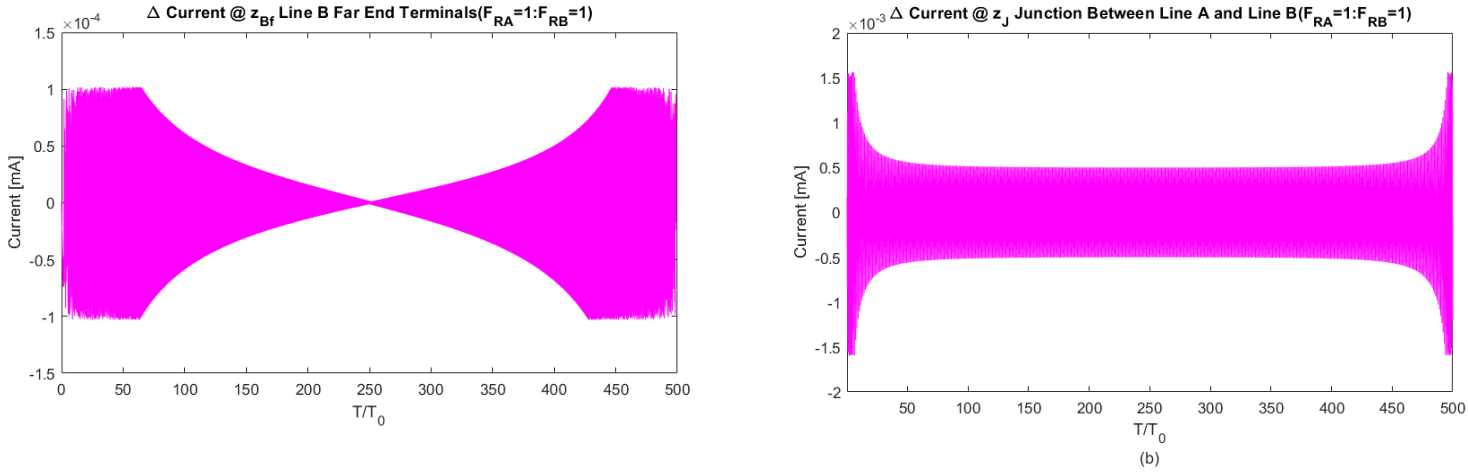


Figure 6-34: Current Differences at z_{B_f} and z_J a)$\Delta i(z_{B_f}, t)$ b) $\Delta i(z_J, t)$ ($F_{RA} = 1, F_{RB} = 1$)

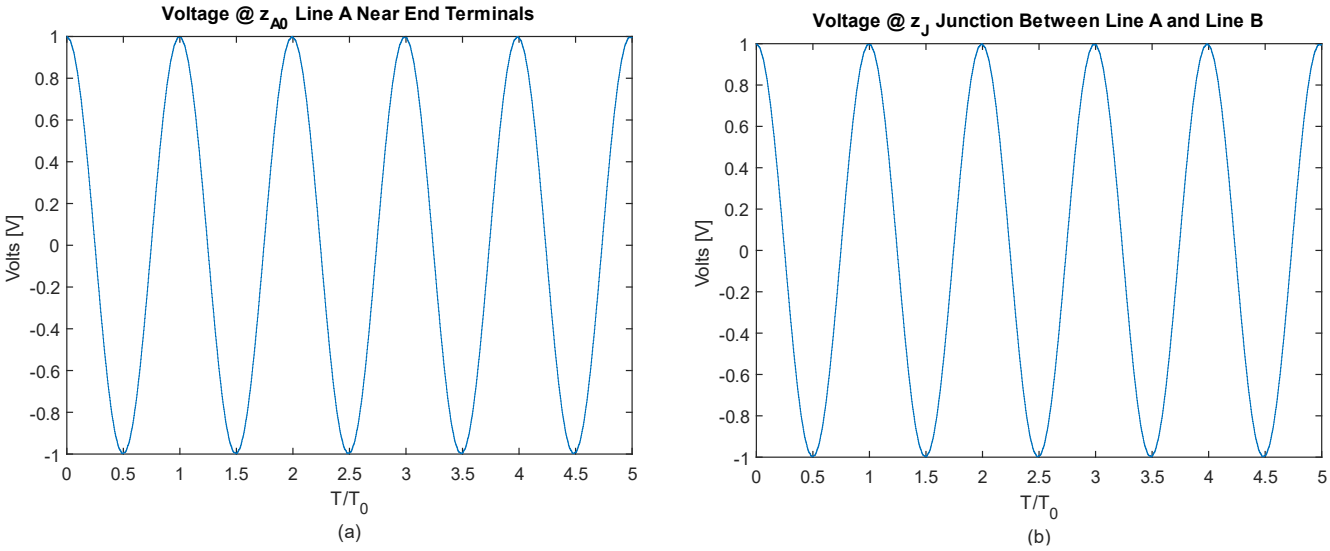


Figure 6-35: Generated Voltage waveforms a)$v_A(z_{A_0}, t)$ b)$v(z_J, t)$ ($F_{RA} = 1, F_{RB} = 10$)

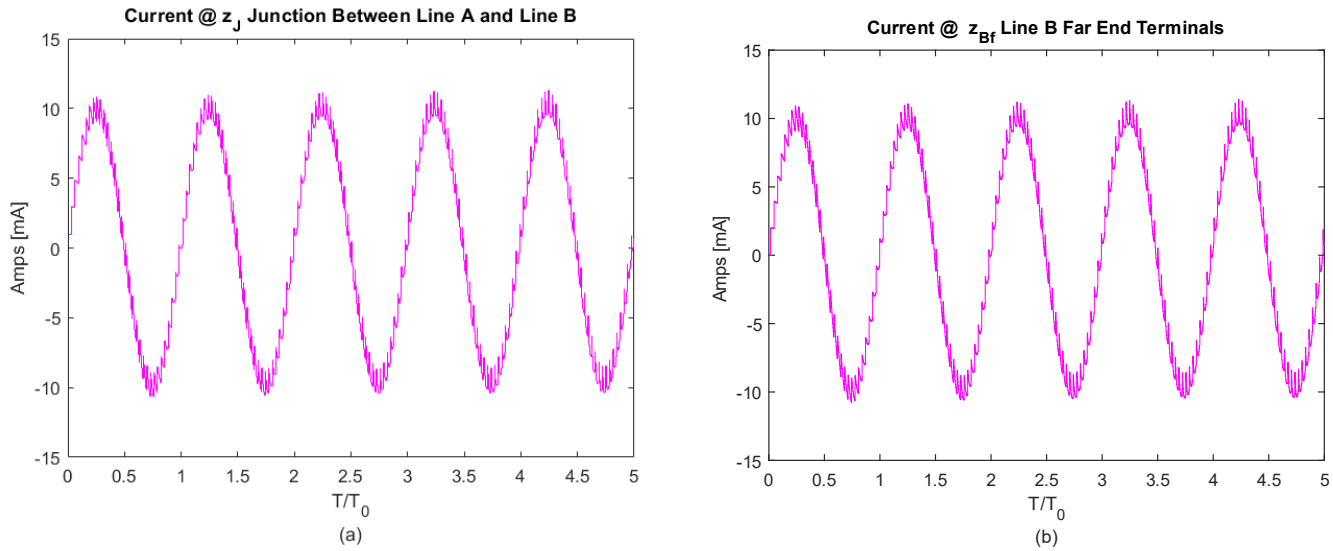


Figure 6-36: Generated Current Waveforms a) $i(z_J, t)$ b) $i_B(z_{B_f}, t)$ ($F_{RA} = 1, F_{RB} = 10$)

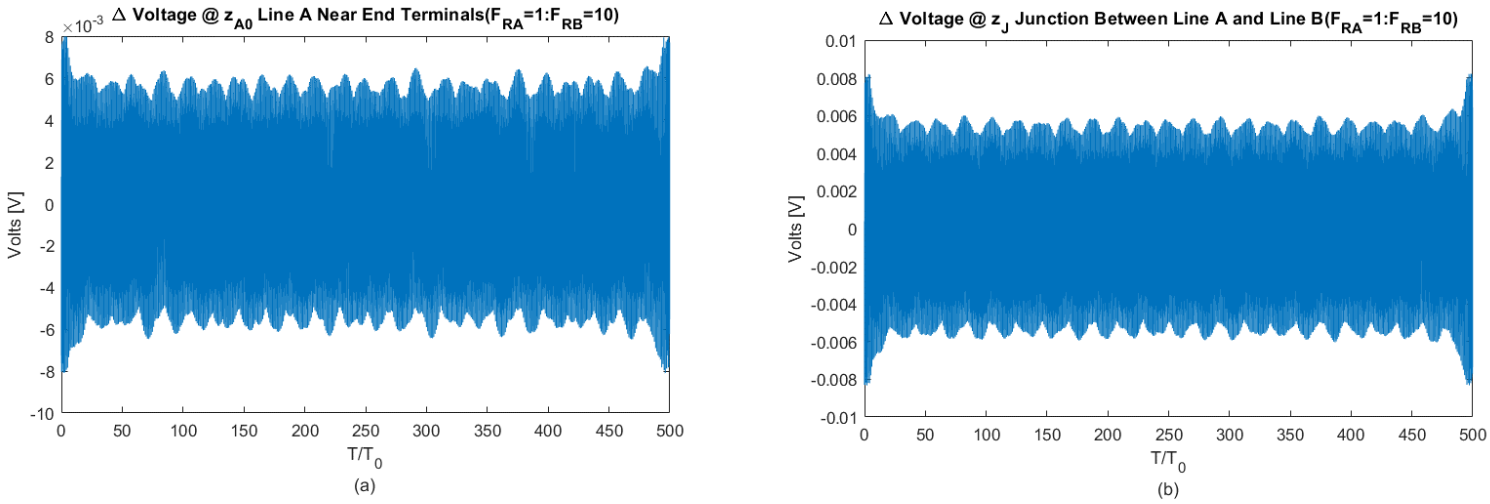


Figure 6-37: Voltage Differences at z_{A_0} and z_J a)$\Delta v(z_{A_0}, t)$ b)$\Delta v(z_{B_f}, t)$ ($F_{RA} = 1, F_{RB} = 10$)

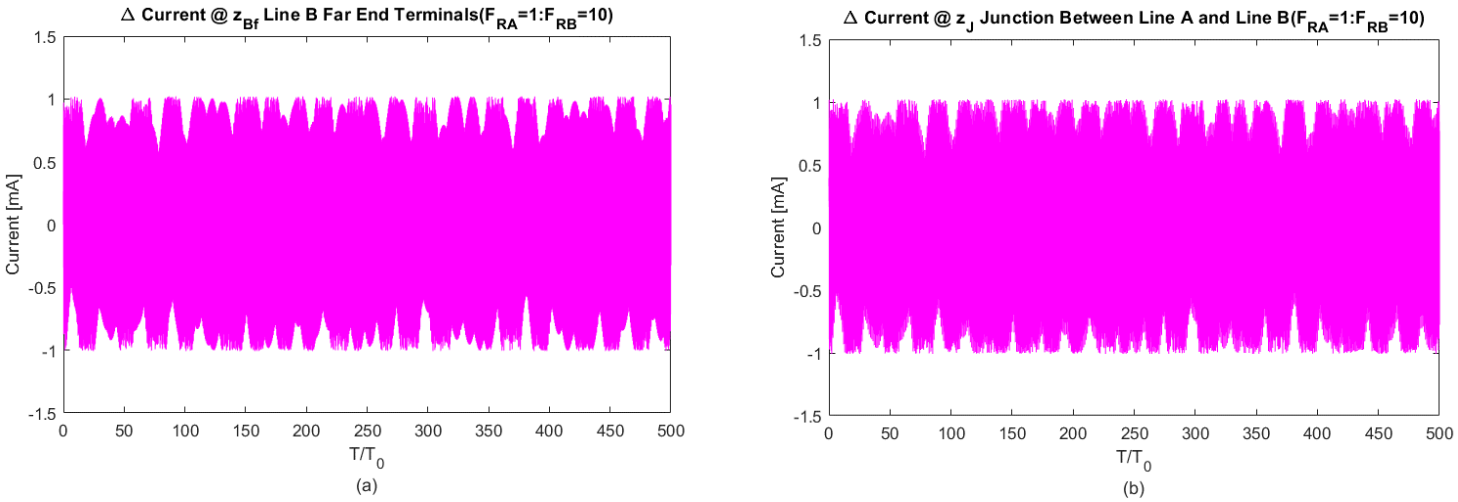


Figure 6-38: Current Differences at z_{B_f} and z_J a)$\Delta i(z_{B_f}, t)$ b) $\Delta i(z_J, t)$ ($F_{RA} = 1, F_{RB} = 10$)

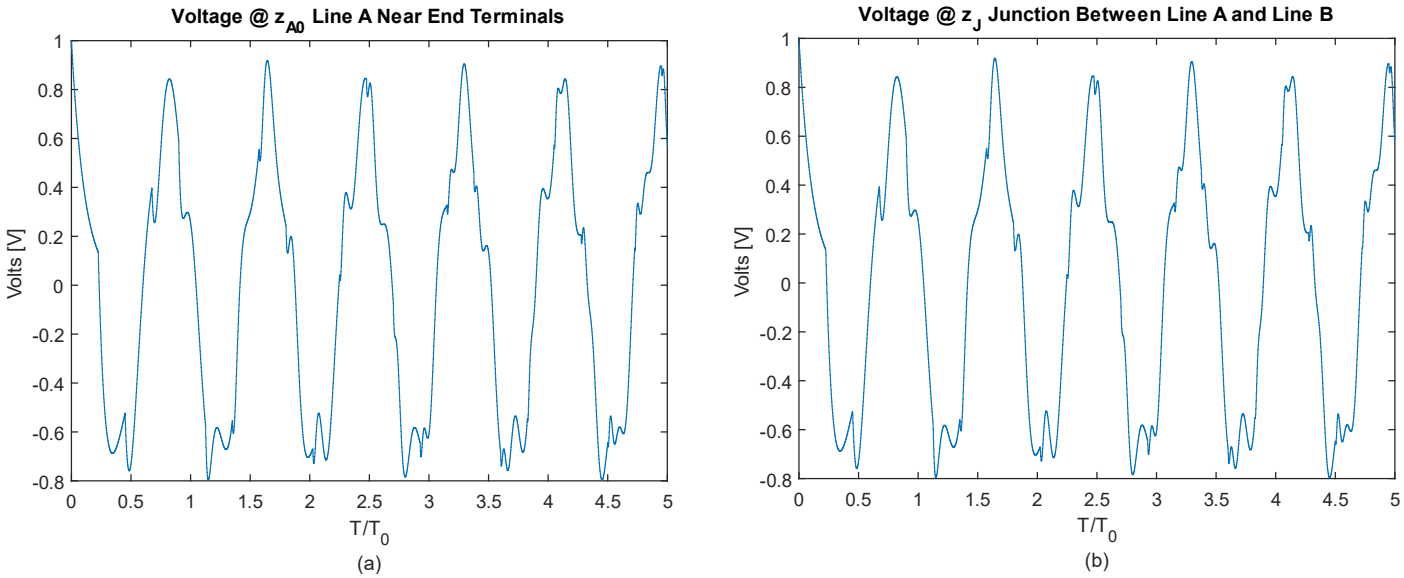


Figure 6-39: Generated Voltage waveforms a)$v_A(z_{A_0}, t)$ b)$v(z_J, t)$ ($F_{RA} = 1, F_{RB} = 100$)

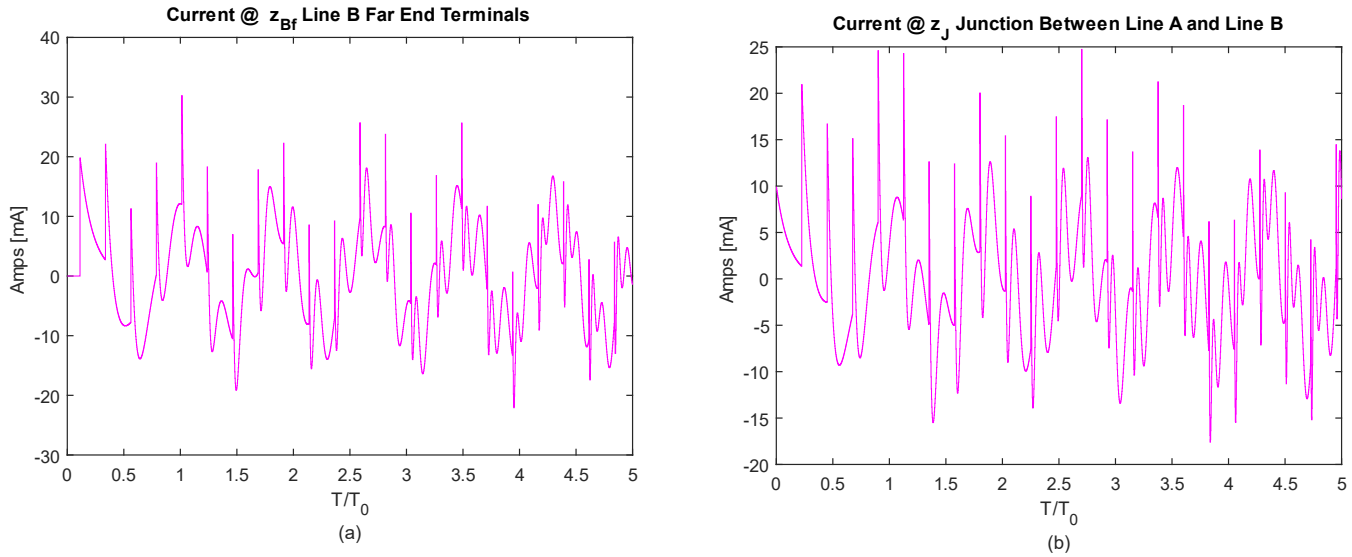


Figure 6-40: Generated Current Waveforms a) $i_B(z_{B_f}, t)$ b) $i(z_J, t)$ ($F_{RA} = 1, F_{RB} = 100$)

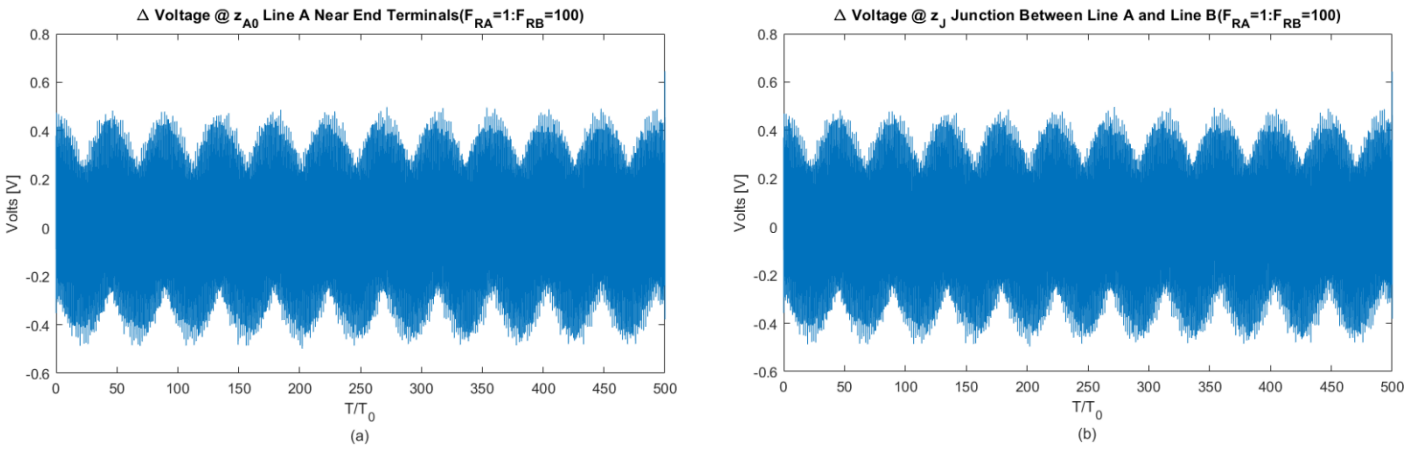


Figure 6-41: Voltage Differences at z_{A_0} and z_J a)$\Delta v(z_{A_0}, t)$ b)$\Delta v(z_{B_f}, t)$ ($F_{RA} = 1, F_{RB} = 100$)

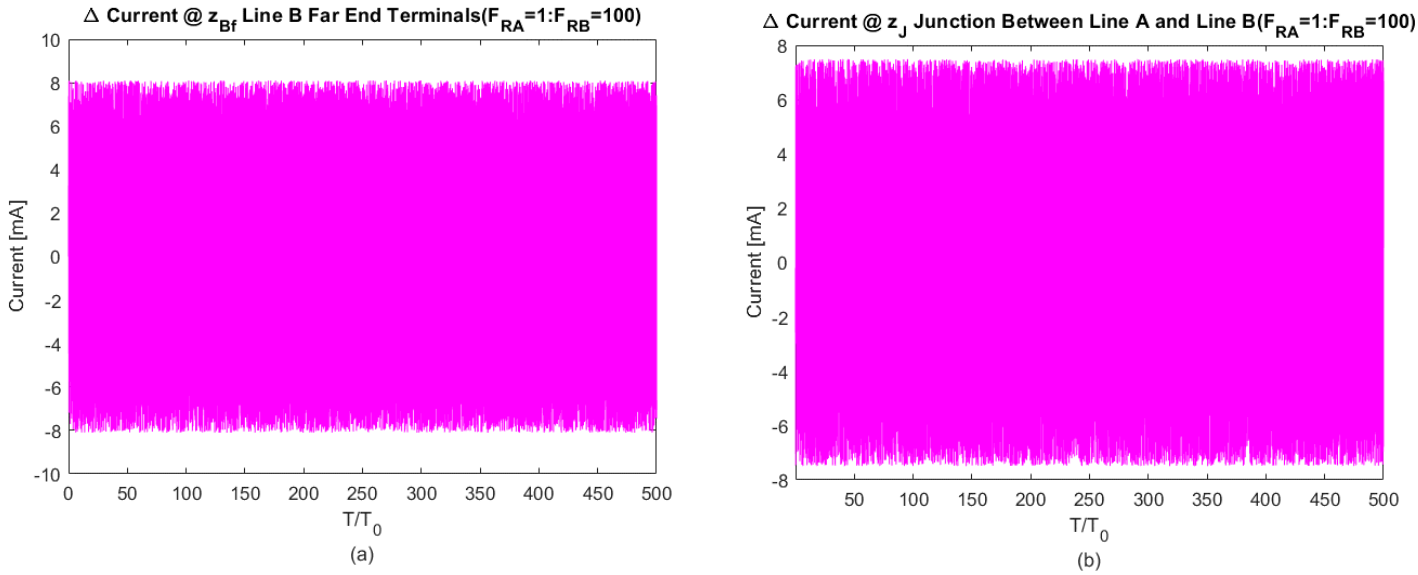


Figure 6-42: Current Differences at z_{B_f} and z_J a)$\Delta i(z_{B_f}, t)$ b) $\Delta i(z_J, t)$ ($F_{RA} = 1, F_{RB} = 100$)

6.3.2.1 Shallow Fragmentation

The generated voltage and current waveforms depicted in Figure 6-31 and Figure 6-32 are smooth sinusoids that closely resemble the idealistic reference waveforms. This is evident by looking at the delta voltage and current waveforms in Figure 6-33 and Figure 6-34. The maximum difference in the voltage at Line A's Near End terminals is $\approx 0.4\mu V$ i.e. $\left|\Delta v\left(z_{A_0}, t\right)\right| \cong \left|0.4uV\right.$ whilst at the junction a maximum of $\approx 150\mu V$ i.e. $\left|\Delta v\left(z_J, t\right)\right| \cong \left|150uV\right.$ is observed. For the delta current waveforms peak noise values of . $\left|\Delta i\left(z_{B_f}, t\right)\right| \cong 100nA$ and $\left|\Delta i\left(z_{B_f}, t\right)\right| \cong 2\mu A$ are observed at Line B's Far End terminals and the junction respectively.

6.3.2.2 Moderate Fragmentation

Increasing the *Fragmentation Ratio* to $1:10$ effectively reduces the differences in characteristic impedances (ΔZ_{AB}) of the two TL segments by approximately half as evidenced in Table 6.5. Observing the generated current waveforms in Figure 6-36 it is noted that the once *"clean"* sinusoid (Figure 6-32) appears to have a noise component superimposed onto it. Observing the delta voltage and current waveforms given in Figure 6-37 and Figure 6-38 reveals the following. The delta or difference waveforms for the *Fragmentation Ratio* of $1:10$ show dramatic increases in noise when compared to their shallow fragmentation counterparts (Figure 6-33 and Figure 6-34). Considering the peak current of the reference sinusoid is $10mA$ the upper and lower bounds of the delta current waveforms at the junction or discontinuity are approximately $1mA$. These bounds are representative of exactly 10% of the full scale or peak amplitude of the reference current waveform i.e. $\left|\Delta i\left(\mathrm{z}_{B_f},\mathrm{t}\right)\right| = \left|\Delta i\left(\mathrm{z}_J,\mathrm{t}\right)\right| = 0.1I_0$. Considering the delta voltage waveforms in Figure 6-37 it is also quite evident that significant increases in the peak noise are seen when compared to the shallow fragmentation delta voltage waveforms. For the delta voltage waveform in Figure 6-37 a maximum or peak voltage of $8mV$ is seen at the terminals of Line A as well as the junction.

6.3.2.3 Excessive Fragmentation

Excessive *Fragmentation* is observed for the generated voltage and current waveforms in Figure 6-39 and Figure 6-40. Upon observation it is readily apparent that the shape of the generated sinusoids have become severely distorted. Considering the delta waveforms for the voltages and currents in Figure 6-41 and Figure 6-42 the following observations are noted. The delta voltage waveform appears to now exhibit some form of oscillatory behaviour within the upper and lower noise bounds of $-0.4V$ and $0.4V$. The presence of this oscillatory motion could speak to the fact that the *Fragmentation* process may introduce various different modes into the generated waveform and only when a large number of fragments are present in the system can these effects be seen. At this point this is pure conjecture or speculation and more rigorous frequency domain techniques would be required to either verify or disprove the hypothesis. Looking at the current delta waveform in Figure 6-42 the noise appears to be bounded in a symmetrical range between $8mA$ and $-8mA$ with no oscillatory motion being seen. The peak noise current values at this point are equal to $\approx 80\%$ of the peak current of the reference waveform. These high noise current values are not surprising if one considers the fact that current spikes of as high as $30mA$ and $26mA$ are seen in Figure 6-40.

6.4 Conclusion

From the simulated results presented in this chapter the implications of *Fragmentation* generation on system energies and noise have been investigated. It has been shown that increases in the number of fragments present in the system adversely effects the ECE of the system. The *Twin Capacitor* topology is severely affected by the inclusion of additional fragments into the system. Additionally, it is shown that energy in the system is able to be fully reconstituted into the primary or main energy store provided the difference in characteristic impedances is zero. For the LC Resonant tank, it is shown that 100% ECE is not realisable in the system as the very act of initiating the electric to magnetic energy manipulation process exhibits a form of energy taxation. This energy taxation occurs because of residual currents and voltages that are left after energy is extracted or converted from the TL segment. The noise implications of *Fragmentation* generation for both topologies showed a steady increase in noise until what appears to be an upper bound or threshold is approached.

7 CONCLUSIONS AND RECOMMENDATIONS

In this work a novel quantification metric that establishes the quality of the various energy manipulation processes that occur between reactive components at a base or fundamental level in a lossless environment is presented. The development of such a metric is necessary because operating under lossless conditions the quantification of system performance in terms of traditional efficiency does not provide much insight. This is because under lossless conditions energy conservation in the system will always hold true. To address this a novel quantification metric called *Energy Conversion Efficacy* is developed. *Energy Conversion Efficacy* seeks to establish how well (i.e. the efficacy) a primary energy store can transfer and convert energy from a secondary energy store in the desired or intended form. Additionally, the metric also speaks to how well the initially transferred energy can be reconstituted back into the primary energy store. In order to properly assess the various energy manipulation interactions from a truly fundamental level a transmission line approach is adopted as opposed to traditional network paradigms and circuit theory.

Transmission line theory is favoured because it provides an intermediary electromagnetic modelling paradigm that is fully capable of obtaining results due to higher-level network abstractions such as voltages and currents whilst maintaining fundamental wave propagation and field quantity effects. The reactive components are therefore modelled using 1-D TLM Link Line equivalent models. In order to fully explore the impact of multiple internal reflection and transmission effects that can arise due to incident TEM waves of various propagation delays the 1-D TLM framework requires modification. This is primarily because traditional TLM modelling enforces model synchronism, which effectively means the propagation delays of all segments are required to be the same length. This is done in efforts to ensure pulses arrive at local nodes at synchronised intervals. In order to better explain the various scattering and diffusion effects that may take place if the propagation delays of the TL segments are not matched the verbiage of *Fragmentation* is developed. *Fragmentation* can essentially be defined as the effective splitting or fissioning of a propagating waveform that takes place at a junction or discontinuity ultimately giving rise to new propagating waveforms. The development of *Fragmentation*, *Fragmentation Ratio* and *Energy Conversion Efficacy* provided the necessary research framework in order to facilitate the answering of the research question.

"Utilising transmission line equivalent models for reactive components, what effect do multiple successive internal reflections and transmissions at an interface or discontinuity have on the quality of the energy manipulation processes?"

In attempts at answering the research question the *Twin Capacitor* and LC Resonant tank topologies are examined and the fundamental electric to electric and electric to magnetic energy manipulation processes assessed. The energy manipulation processes in this work are assessed using the *Energy Conversion Efficacy* metric and the effect of various *Fragmentation Ratios* and *Fragmentation* generation techniques such as FFGMD and FFGIMD. The implications this has on energy as well as noise generation are then subsequently established. Upon application of the various *Fragmentation* generation methods two principal energy manipulation cases are established. These are the ideal and non-ideal energy manipulation cases. The conditions for ideal and non-ideal energy manipulations are identified and it is found that the predominant factors are the *Fragmentation Ratio* and principle differences in characteristic impedances of the two TL segments.

Applications of the *Energy Conversion Efficacy* metric and the various *Fragmentation* generation methods and *Fragmentation Ratios* in the *Twin Capacitor* and LC Resonant tank topologies yields a number of key observations and results. A summary of the major results or findings are represented below:

- An alternative solution to the *Twin Capacitor Paradox* that identifies the perceived energy loss or *"Missing Energy"* in the system to be fully contained within the associated self-inductors of the capacitors. In addition, the notion of an equilibrium state is disproven as both capacitors are in perpetual charge and discharge cycles.
- In the *Twin Capacitor* topology, the entirety of the system energy can be reconstituted into the primary capacitor irrespective of the size of the secondary capacitor provided that FFGMD *Fragmentation* generation (minimal *Fragmentation*) is maintained.
- For both the *Twin Capacitor* and LC Resonant tank topologies an increase in the number of propagating fragments in the system will bring with it an accompanying decline in ECE. From these results it can be concluded that the ECE and *Fragmentation Ratio* are inversely proportional. The adverse effects of an increased *Fragmentation Ratio* on *Energy Conversion Efficacy* are exacerbated by increases in the associated self-inductance and self-capacitance quantities on the TL segment (L_e or C_e).
- In a cascaded transmission line setup that consists of only two links or segments the only fragments or propagating waves that are capable of creating new fragments are the origin propagating waves or fragments.
- In the *Twin Capacitor* topology, it is seen that the generated EMI or noise is proportional to increases in the *Fragmentation Ratio* up until a plateau or threshold point is reached. This is attributed to the increased activity at the terminal nodes and junction due to the presence of multiple propagating fragments on the TL segment. This is established by taking the variance at particular nodes or terminals.
- In the LC Resonant topology, a proportional increase in generated noise or EMI is also seen with an increase in *Fragmentation Ratio*, the effects of which are exacerbated by the subsequent increases in associated self-inductance and self-capacitance quantities. The generated or produced noise appears to be bounded between symmetrical upper and lower bounds.

Overall the findings in this dissertation provided a new quantification metric for establishing the quality of a given energy manipulation process in reactive components.

7.1 Recommendations

The simulated results and observations obtained using ECE and various *Fragmentation Ratios* are achieved based solely on the interaction of two cascaded transmission lines. Although quite useful the fact that only two Link-Line equivalent models can be utilised within the simulated environment restricts the number of examinable topologies to very simplistic topologies such as the *Twin Capacitor* and LC Resonant tank. If the concepts of ECE and *Fragmentation* are to be applied to more complex topologies with the goal of being able to examine a complete power electronic converter topology with multiple reactive components this limitation needs to be addressed in future work. This provides a possible line of extension for the work on *Fragmentation* and the accompanying *Fragmentation* generation methods. In order to do this the simulator framework needs to be extended to account for the modelling of reactive components in a fully 3-D environment. At present, the reactive components are being modelled solely in a 1-D simulation environment.

In order for the ECE metric to be used in a 3-D environment which is more representative of real-life conditions and environments where the propagation of waves and hence energy flux is not confined to a singular dimension. The *Fragmentation* simulator will need to be extended to deal with more than one dimension. The principle first step towards this goal is the expansion of the *Fragmentation* generation methods to deal with an N-link transmission line structure in at least one dimension. In order to facilitate this, it is necessary to modify the various *Fragmentation* generation methods to account for an N-link cascaded transmission line setup. Conventional 1-D TLM modelling at present is capable of achieving this however, it makes use of model synchronism and the principle of locality. The locality principle states that only interactions that occur immediately to at the left and right nodes i.e. local nodes need be considered.

This method of analysis is only permissible because the propagation delays of the individual TL segments in the N-links all have the same propagation delays i.e. model synchronism is enforced. This is only applicable in the most simplistic of *Fragmentation* generation methods such as FFGMD. If any other *Fragmentation* method is used it will require a derivation that is capable of accommodating a TL setup that consists of N arbitrary cascaded TL segments each with arbitrary propagation delays. Before the derivation of the N-link *Fragmentation Ratios* and *Fragmentation* generation methods are derived the internal bounce cycles of the respective Reverse and Forward propagating waveforms needs to be expressed solely in terms of the origin Reverse and Forward waves. This is necessary in order to ensure that the interactions due to a *Fragmentation Initiation* event can be completely characterised by the waveform that starts the *Fragmentation* process i.e. the origin propagating waves or fragments. Representation of fragments in this manner will facilitate computation methods such as parallelization. In using parallelization dedicated threads on CPU cores can be dedicated to computing all the Reverse or Forward waveforms that occur on a given TL segment. Processing in this manner will greatly reduce the computational time and increase the simulator efficiency, which will enable a greater number of fragments to be simulated which in turn facilitates the simulation of more complex topologies in a timeous manner.

The simulation framework could also be expanded to deal with AC signals because at present only linear combinations of Heaviside unit step functions are exclusively considered. The inclusion of AC sources is a critical next step because it will allow the simulation of various periodic waveforms by way of the Fourier series.

Lastly the effect of various *Fragmentation* generation methods on the harmonic content on of the generated waveforms should be considered. Additional insight into how the number of fragments influences the spectral content could prove to be a useful tool in identifying how many additional fragments a system can accommodate before undesirable effects such as Total Harmonic Distortion become prevalent. Questions such as whether or not the generated fragments all exhibit commensurable modes and frequency content should also be looked at.

REFERENCES

[1] T. G. Wilson, "The evolution of power electronics," *IEEE Trans. Power Electron.*, vol. 15, no. 3, pp. 439–446, May 2000.
[2] J. D. van Wyk and J. A. Ferreira, "Some present and future trends in power electronic converters," in *and Automation Proceedings of the 1992 International Conference on Industrial Electronics, Control, Instrumentation*, 1992, pp. 9–18 vol.1.
[3] pSemi, "PE29102 is an integrated high-speed driver," *PE29102 High-speed FET Driver*, 27-Sep-2018.[Online].Available:https://www.psemi.com/products/gan-fet-driver/pe29102. [Accessed: 27-Sep-2018].
[4] J. A. Ferreira and J. D. V. Wyk, "Electromagnetic energy propagation in power electronic converters: toward future electromagnetic integration," *Proc. IEEE*, vol. 89, no. 6, pp. 876–889, Jun. 2001.
[5] J. D. van Wyk and F. C. Lee, "On a Future for Power Electronics," *IEEE J. Emerg. Sel. Top. Power Electron.*, vol. 1, no. 2, pp. 59–72, Jun. 2013.
[6] J. A. Ferreira, I. W. Hofsajer, and J. D. van Wyk, "Exploiting the third dimension in power electronics packaging," in *Proceedings of APEC 97 - Applied Power Electronics Conference*, 1997, vol. 1, pp. 419–423 vol.1.
[7] J. W. Kolar, J. Biela, S. Waffler, T. Friedli, and U. Badstuebner, "Performance trends and limitations of power electronic systems," in *2010 6th International Conference on Integrated Power Electronics Systems*, 2010, pp. 1–20.
[8] R. Chen, "Integrated EMI Filters for Switch Mode Power Supplies," Nov. 2004.
[9] J. A. Ferreira, "Engineering science considerations for integration and packaging," in *2000 IEEE 31st Annual Power Electronics Specialists Conference. Conference Proceedings (Cat. No.00CH37018)*, 2000, vol. 1, pp. 12–18 vol.1.
[10] D. Maksimovic and S. Dhar, "Switched-capacitor DC-DC converters for low-power on-chip applications," in *30th Annual IEEE Power Electronics Specialists Conference. Record. (Cat. No.99CH36321)*, 1999, vol. 1, pp. 54–59 vol.1.
[11] Y. Beck and S. Singer, "Capacitive Transposed Series-Parallel Topology With Fine Tuning Capabilities," *IEEE Trans. Circuits Syst. Regul. Pap.*, vol. 58, no. 1, pp. 51–61, Jan. 2011.
[12] R. W. Erickson and D. Maksimovic, *Fundamentals of Power Electronics*, 2nd ed. Springer US, 2001.
[13] J. A. Ferreira, "Application of the Poynting vector for power conditioning and conversion," *IEEE Trans. Educ.*, vol. 31, no. 4, pp. 257–264, Nov. 1988.
[14] F. Blaabjerg, A. Consoli, J. A. Ferreira, and J. D. van Wyk, "The future of electronic power Processing and conversion," *IEEE Trans. Power Electron.*, vol. 20, no. 3, pp. 715–720, May 2005.
[15] M. Buzdugan and H. Balan, "Hidden schematics of EMI filters," *Renew. Energy Power Qual. J.*, pp. 835–840, May 2016.
[16] A. K. Singal, "The Paradox of Two Charged Capacitors -- A New Perspective," *ArXiv13095034 Phys.*, Aug. 2013.
[17] K. T. McDonald, "A Capacitor Paradox." Princeton University, 05-Jul-2018.
[18] S. Y. R. Hui and C. Christopoulos, "Modeling non-linear power electronic circuits with the transmission-line modeling technique," *IEEE Trans. Power Electron.*, vol. 10, no. 1, pp. 48–54, Jan. 1995.
[19] C. Jackson, "Modeling of a Circuit Using Transmission Line Elements," in *2007 IEEE Radio and Wireless Symposium*, 2007, pp. 121–124.

[20] M. C. Smit, J. A. Ferreira, and J. D. V. Wyk, "Application of transmission line principles to high frequency power converters," in *, 23rd Annual IEEE Power Electronics Specialists Conference, 1992. PESC '92 Record*, 1992, pp. 1423–1430 vol.2.
[21] C. R. Sullivan and A. M. Kern, "Capacitors with fast current switching require distributed models," in *2001 IEEE 32nd Annual Power Electronics Specialists Conference (IEEE Cat. No.01CH37230)*, 2001, vol. 3, pp. 1497–1503 vol. 3.
[22] P. Hammond, "Electromagnetic energy transfer," *Proc. IEE - Part C Monogr.*, vol. 105, no. 8, pp. 352–358, Sep. 1958.
[23] J. H. Poynting, "XV. On the transfer of energy in the electromagnetic field," *Philos. Trans. R. Soc. Lond.*, vol. 175, pp. 343–361, Jan. 1884.
[24] E. T. (Edmund T. Whittaker, *A history of the theories of aether and electricity : from the age of Descartes to the close of the nineteenth century*. London ; New York : Longmans, Green [etc., etc.], 1910.
[25] C. Christopoulos, *The Transmission-Line Modeling (TLM) Method in Electromagnetics*. Morgan & Claypool, 2006.
[26] V. G. Endean and C. J. Carpenter, "Electromagnetic energy and power in terms of charges and potentials instead of fields," *IEE Proc. - Sci. Meas. Technol.*, vol. 139, no. 6, pp. 338–342, Nov. 1992.
[27] J. Slepian, "Energy and Energy Flow in the Electromagnetic Field," *J. Appl. Phys.*, vol. 13, no. 8, pp. 512–518, Aug. 1942.
[28] R. F. Wang, "The Dynamical Mechanism of the Aharonov-Bohm Effect," p. 13.
[29] W. E. Sumpner, "Radiation and electrical power transmission," *J. Inst. Electr. Eng.*, vol. 75, no. 454, pp. 512–526, Oct. 1934.
[30] J. J. (Joseph J. Thomson and J. C. Maxwell, *Recent Research in Electricity and Magnetism*. Oxford, The Clarendon press, 1893.
[31] R. J. Gutmann, "Application of RF Circuit Design Principles to Distributed Power Converters," *IEEE Trans. Ind. Electron. Control Instrum.*, vol. IECI-27, no. 3, pp. 156–164, Aug. 1980.
[32] "Transmission Lines in Digital Systems for EMC Practitioners," *Wiley.com*. [Online]. Available:https://www.wiley.com/enus/Transmission+Lines+in+Digital+Systems+for+EMC+Practitioners-p-9781118145562. [Accessed: 18-Oct-2018].
[33] A. F. Peterson and G. D. Durgin, "Transient Signals on Transmission Lines: An Introduction to Non-Ideal Effects and Signal Integrity Issues in Electrical Systems," *Synth. Lect. Comput. Electromagn.*, vol. 3, no. 1, pp. 1–144, Jan. 2008.
[34] P. Enders, "Huygens' principle in the transmission line matrix method (TLM). Global theory," *Int. J. Numer. Model. Electron. Netw. Devices Fields*, vol. 14, no. 5, pp. 451–456, Sep. 2001.
[35] S. Y. R. Hui and C. Christopoulos, "Numerical simulation of power circuits using transmission-line modelling," *Manag. Educ. IEE Proc. - Phys. Sci. Meas. Instrum.*, vol. 137, no. 6, pp. 379–384, Nov. 1990.
[36] J. W. Bandler, P. B. Johns, and M. R. M. Rizk, "Transmission-line modeling and sensitivity evaluation for lumped network simulation and design in the time domain," *J. Frankl. Inst.*, vol. 304, no. 1, pp. 15–32, Jul. 1977.
[37] S. Y. R. Hui and C. Christopoulos, "A discrete approach to the modelling of power electronic switching networks," in *20th Annual IEEE Power Electronics Specialists Conference*, 1989, pp. 130–137 vol.1.
[38] S. Y. R. Hui and C. Christopoulos, "Computer simulation of a converter-fed DC drive using the transmission-line modeling technique," *IEEE Trans. Power Electron.*, vol. 6, no. 4, pp. 636–644, Oct. 1991.
[39] S. Y. R. Hui, K. K. Fung, and C. Christopoulos, "Decoupled simulation of multi-stage power electronic systems using transmission-line links," in *PESC '92 Record. 23rd Annual IEEE Power Electronics Specialists Conference*, 1992, pp. 1324–1330 vol.2.

[40] L. D. Smith, D. Hockanson, and K. Kothari, “A transmission-line model for ceramic capacitors for CAD tools based on measured parameters,” in *52nd Electronic Components and Technology Conference 2002. (Cat. No.02CH37345)*, 2002, pp. 331–336.
[41] S. Y. R. Hui and C. Christopoulos, “Discrete transform technique for solving nonlinear circuits and equations,” *IEE Proc. - Sci. Meas. Technol.*, vol. 139, no. 6, pp. 321–328, Nov. 1992.
[42] P. B. Johns and M. O’Brien, “Use of the transmission-line modelling (t.l.m.) method to solve non-linear lumped networks,” *Radio Electron. Eng.*, vol. 50, no. 1.2, pp. 59–70, Jan. 1980.
[43] C. Thompson, “A STUDY OF NUMERICAL INTEGRATION TECHNIQUES FOR USE IN THE COMPANION CIRCUIT METHOD OF TRANSIENT CIRCUIT ANALYSIS,” *Dep. Electr. Comput. Eng. Tech. Rep.*, Apr. 1992.
[44] L. O. Chua and P. Y. Lin, *Computer-Aided Analysis of Electronic Circuits: Algorithms and Computational Techniques*. Prentice Hall Professional Technical Reference, 1975.
[45] K. K. Fung, S. Y. R. Hu, and C. Christopoulos, “Parallel Simulation of Electric Circuits Using the TLM Technique,” *Trans. Eng. Sci.*, vol. 3, pp. 21–28.
[46] N. Ida, *Engineering Electromagnetics*, 3rd ed. Springer International Publishing, 2015.
[47] J. H. Poynting, G. Barlow, and G. A. Shakespear, *Collected scientific papers*. London : Cambridge University Press, 1920.

APPENDIX A

A.1. Overview

In this appendix an additional numerical example of the electric to magnetic energy manipulation processes are presented. The numerical example parameters for the experimental prototype are given in Table A-1 as seen in [20]. The prototype is designed for direct application in parallel LLC resonant converters. However, other use cases for the integrated structure can be found in DC power filters and Snubber circuits [20].

A.2. Parallel LC Resonant Structure

The geometrical structure for the planar parallel LC resonant tank is presented in Chapter 2.4.2 (Figure 2-5). Similarly, the accompanying 1-D Link-Line equivalent model is given in Chapter 3.5.2 (Figure 3-19 and Figure 3-20). However, Figure 2-5 as well as Figure 3-19 and Figure 3-20 are reproduced here for convenience.

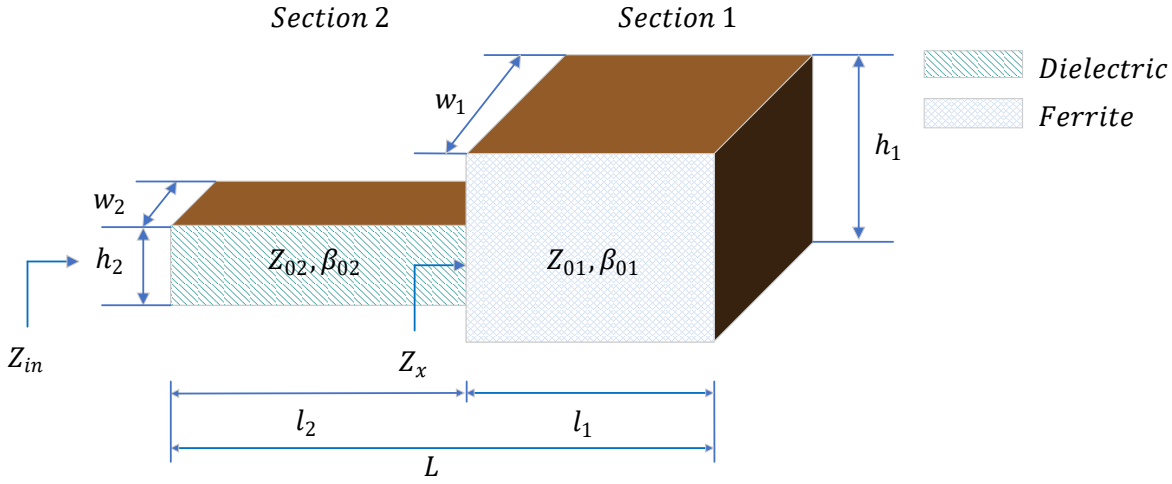


Figure A-1: Parallel Planar LC Resonant Structure (Adapted from [20])

Table A-1: Parallel LC Resonant Structure Parameters (Adapted from [20])

	$Capacitor (Line\ A)$	$Inductor (Line\ B)$
$Width\ [mm]$	28	28
$Height\ [mm]$	1	12
$Length\ [mm]$	44	44
ϵ_R	1000	1
μ_R	1	1000
ϵ_{eff}	675	1
Z_0	≈ 0.457	≈ 2560
$\tau\ [ns]$	≈ 0.147	≈ 0.147
$C\ [nF]$	≈ 0.320	$\approx 0.0573 \times 10^{-3}$
$L\ [nH]$	≈ 0.0671	≈ 375.588
$Resonant\ Frequency\ [rad/sec]$	3707079.331	

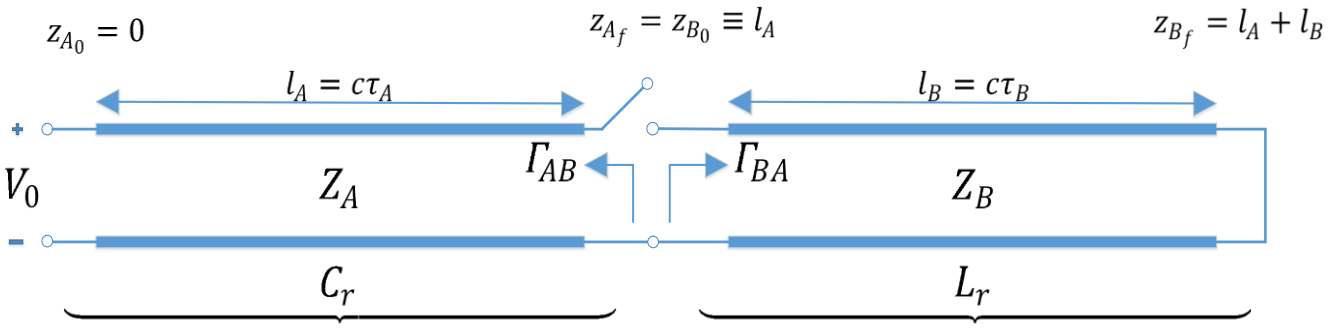


Figure A-2: Resonator Tank Link-Line Equivalent Model (Switch Open)

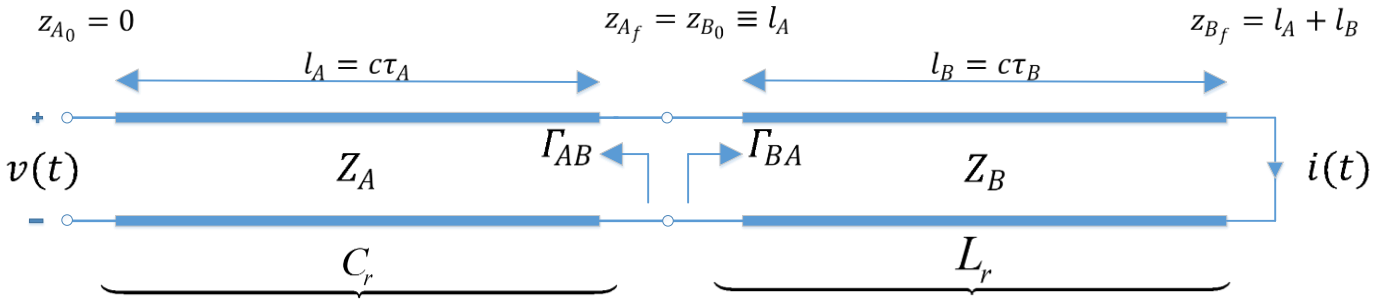


Figure A-3: Resonator Tank Link-Line Equivalent Model (Switch Closed)

As seen in Chapter 3 the horizontal planar lengths l_1 and l_2 correspond to the length dimensions l_A and l_B (seen in Figure A-2 and Figure A-3) as these are the dimensions in which assumed current flow takes place. It then follows that the length dimensions l_A and l_B are the dimensions which will be spatially discretised in the 1-D TLM Link-Line models.

From the parameters given in Table A-1 the FFGMD simulation parameters given in Table A-2 are derived.

Table A-2: Parallel LC Resonant FFGMD Simulation Parameters

Parameter	*Value*
U_0	$4020\ pJ$
V_0	$5\ V$
I_0	$146\ mA$
ΔZ_{AB}	$2.559\ k\Omega$
l_A	$44\ mm$
l_B	$44\ mm$
C_A	$0.320\ nF$
L_{eA}	$67\ pH$
L_B	$376\ nH$
C_{eB}	$0.0573\ pF$
C_0	$0.0573pF$
ω_0	$1180000\pi\ rad/sec$
n_{seg}	10000

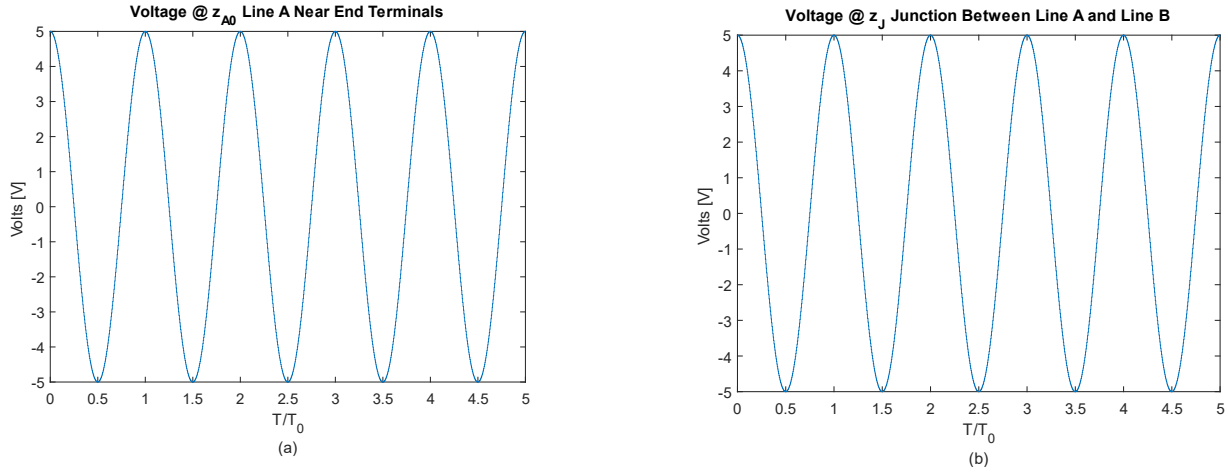


Figure A-4: LC Resonator Terminal and Junction Voltages a) $v_A(z_{A_0}, t)$ b) $v_A(z_J, t)$

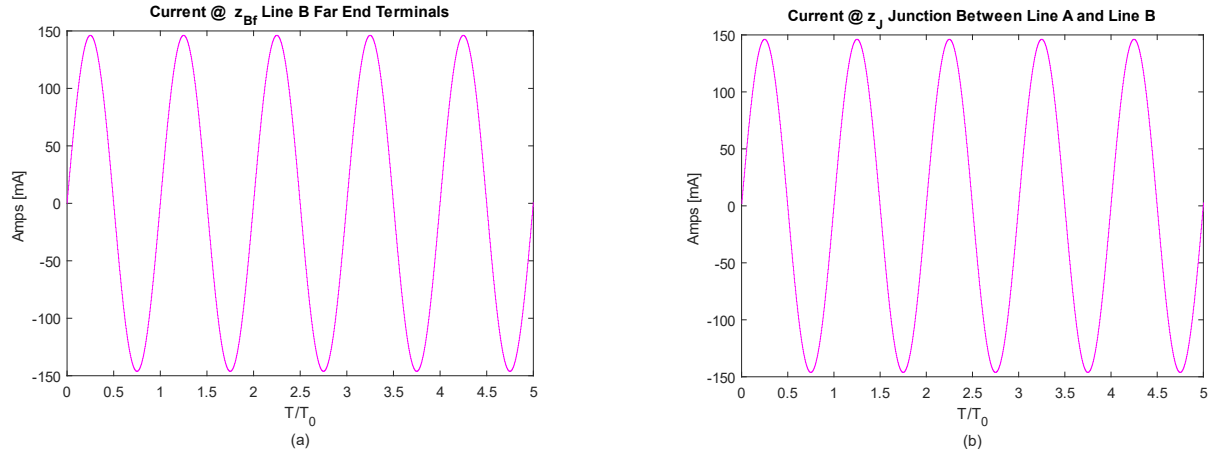


Figure A-5: LC Resonator Junction and Terminal Currents a) $i_B(z_{B_f}, t)$ b) $i_B(z_J, t)$

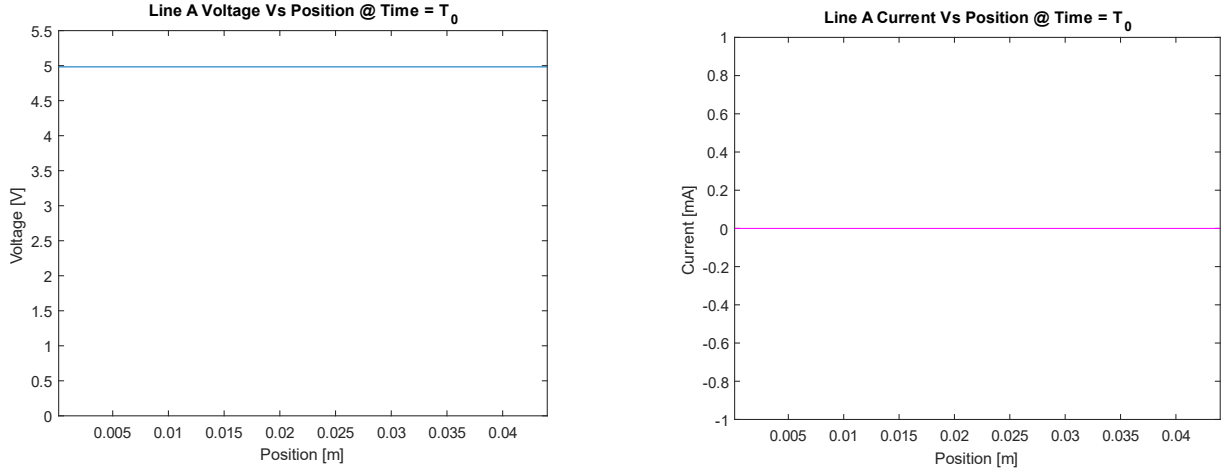


Figure A-6: LC Resonator Line A Voltage and Current @ T_0 ($v_A(z, T_0)$, $i_A(z, T_0)$)

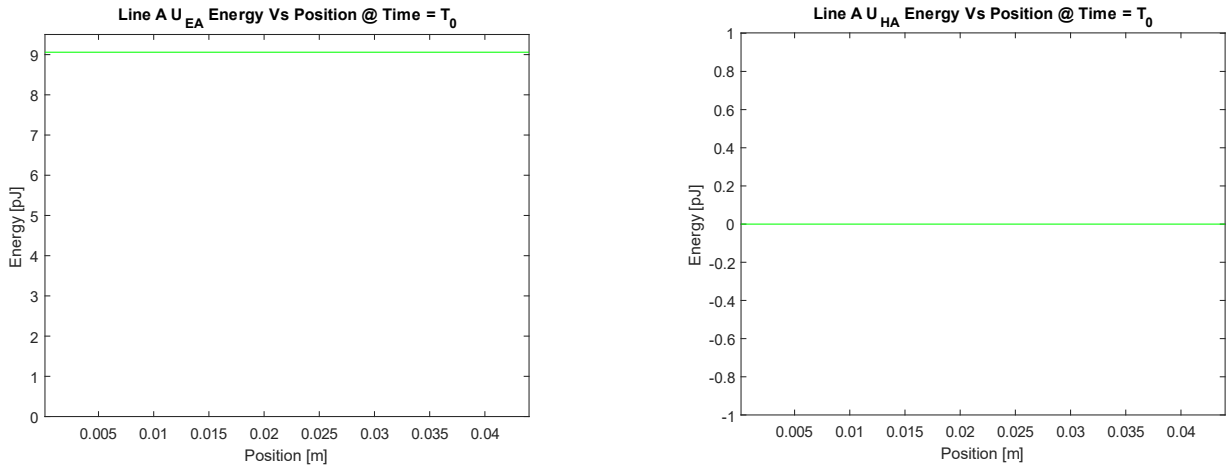


Figure A-7: LC Resonator Line A Electric and Magnetic Energies @ T_0 ($U_{EA}(z,T_0)$, $U_{HA}(z,T_0)$)

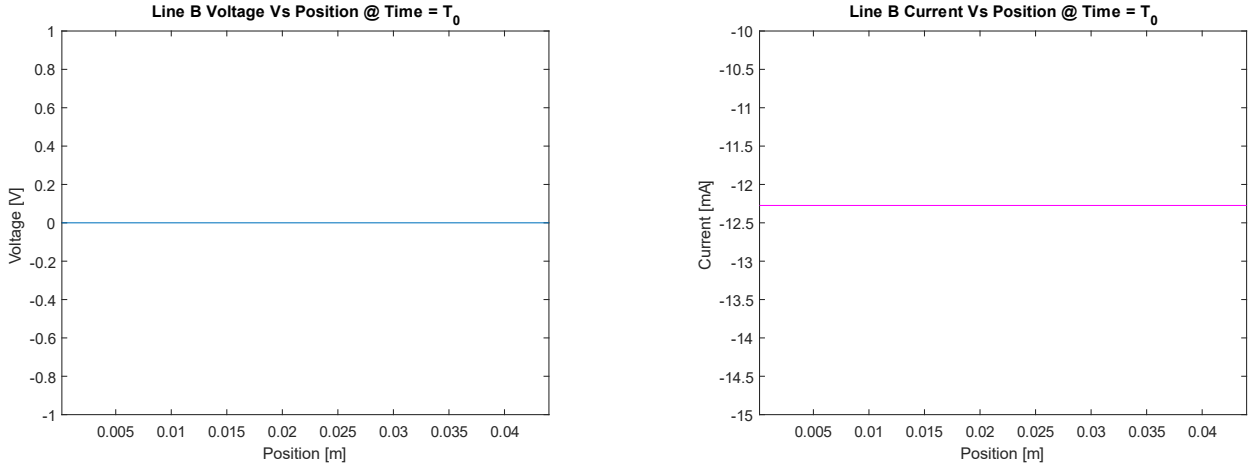


Figure A-8: LC Resonator Line B Voltage and Current @ T_0 ($v_B(z,T_0)$, $i_B(z,T_0)$)

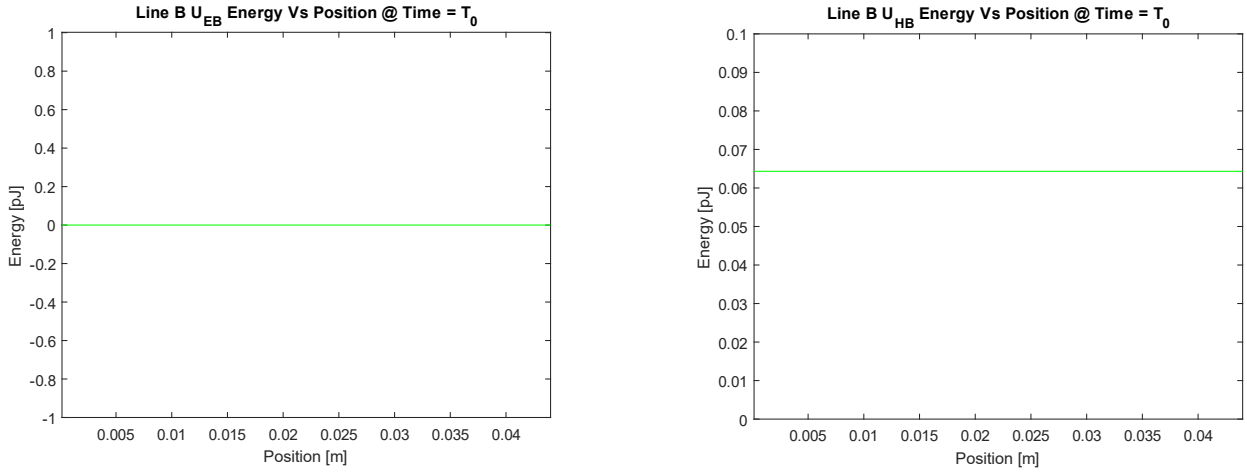


Figure A-9: LC Resonator Line B Electric and Magnetic Energies @ T_0 ($U_{EB}(z,T_0)$, $U_{HB}(z,T_0)$)

As previously seen in Chapter 6 the maximum magnetic energy (stored in L_B) is seen on Line B at time instances $T = \frac{2n-1}{2}T_0, n \in \mathbb{Z}$. Conversely, maximum electrical energy (stored in C_A) is seen on Line A at time instances $T = nT_0, n \in \mathbb{Z}$. Assuming that C_A is initially charged at $T = 0$ (with system energy U_0) after one complete period i.e. $T = T_0$ it is to be expected that the entirety of the system energy U_0 will be electric in nature and stored on Line A. Observing Figure A-6a it can be seen that the voltage on Line A ***appears*** to be equal to the rated or initial charge voltage i.e. $|v_A(z, T_0)| \cong V_0$. However, a small deficiency in the line voltage, and hence electrical energy exists on Line A i.e. $|U_{EA}(z, T_0)| \neq U_0$. This deficiency in line voltage and electrical energy can be attributed to the fact that a non-zero residual line current and hence magnetic energy is present on Line B as seen in Figure A-8b and Figure A-9b respectively. This essentially means that the entirety of the initial system energy U_0 stored on Line A at $T = 0^-$ can never be fully recovered. This is due to the fact that at all instances of $T = nT_0, n \in \mathbb{Z}$ a residual current will always be present on Line B. The magnitude of this deficiency in energy can be quantified by calculating the residual magnetic energy left on Line B. Using(6.33) the total magnetic energy on Line B $U_{H_BT}(z, T_0) \cong 28.3\ pJ$.

Expressing U_{H_AT} as a percentage of the initial energy U_0 present in the system.

$$U_{H_BT}\ \% = \frac{U_{H_BT}}{U_0} = \left(\frac{28.3 \times 10^{-12}}{4020 \times 10^{-12}}\right) \times 100 = 0.70\%$$

Considering the total stored magnetic energy as a percentage of the initial system energy U_0 it is readily apparent that whilst still relatively small in magnitude the energy taxation on the energy manipulation process due to the presence of this residual current is almost 1%. The implications of this mean that the theoretical best-case efficacy of the system is 99% in a completely lossless an ideal environment.

Further analysis of this apparent deficit or energy taxation reveals that it is a function of the self-capacitance (C_{eB}) on Line B as well as the residual line current ($i_B(z,t)$) and the absolute difference in characteristic impedances (ΔZ_{AB}) of Line A and Line B. The magnitude of this residual magnetic energy is directly proportional to the line current ($i_B(z,t)$) and the difference in characteristic impedances (ΔZ_{AB}) between the two lines. In order to explore the implications of an increasing residual current and hence magnetic energy on the energy manipulation process, and the ramifications this has on *Energy Conversion Efficacy* Z_B needs to be lowered. In order to lower Z_B whilst maintaining minimal *Fragmentation* (i.e. $F_{RA} = 1$ and $F_{RB} = 1$) conditions in the system, the self-capacitance C_{eB} must be increased as per equation (3.27).The effects of the increasing C_{eB} w.r.t the initial self-capacitance C_0 are expressed as the ratio C_{eB}/C_0 in order to establish a comparative base line to compare the initial self-capacitance with the various increased self-capacitance values on Line B. This ratio is then plotted against the maximum and minimum electric and magnetic energies on the respective transmission lines as seen in Figure A-10 and Figure A-11, with the effects on ECE seen in Figure A-12.

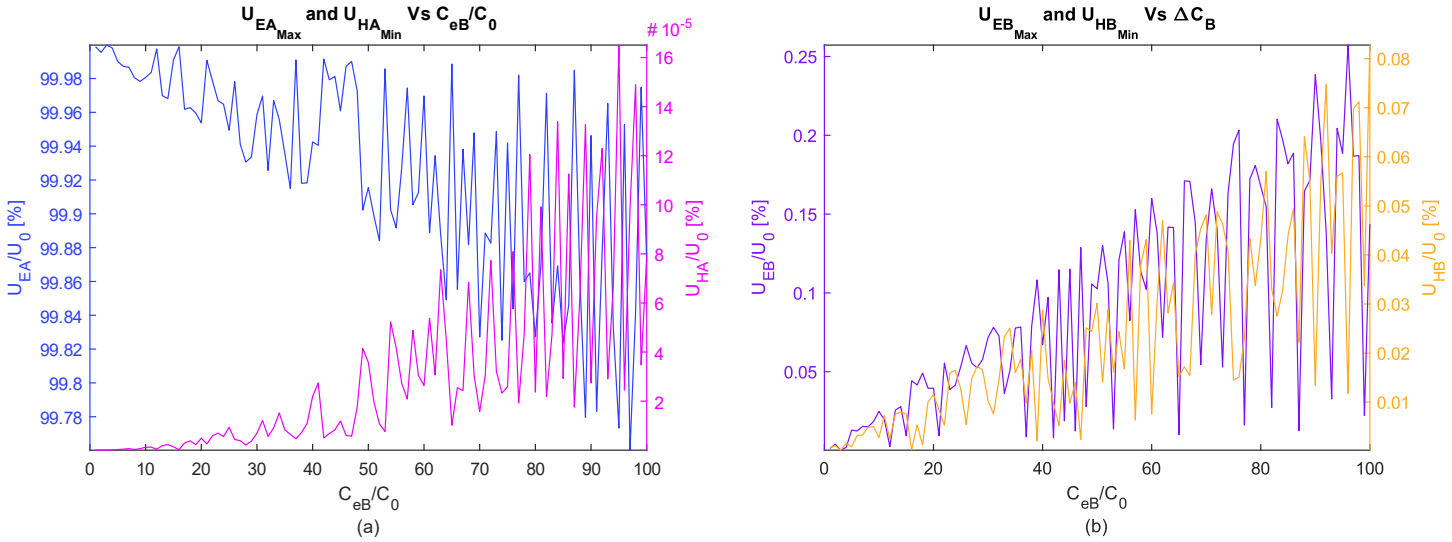


Figure A-10: LC Resonator Max Electrical and Min Magnetic Line Energies Vs. Self-Capacitance

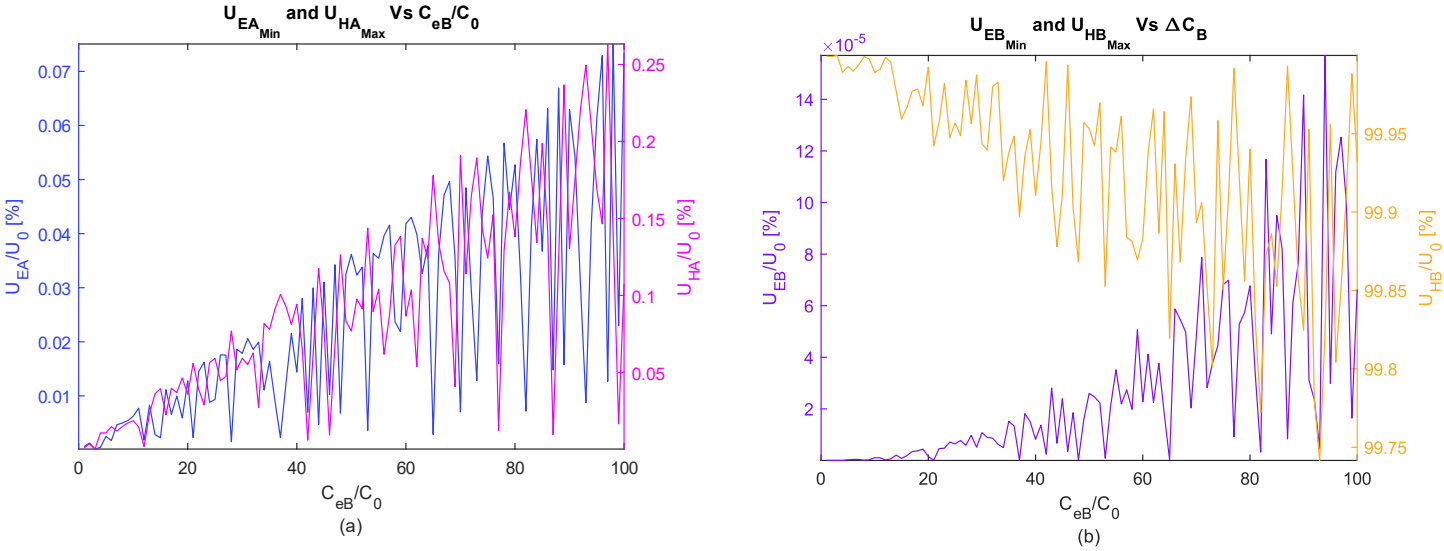


Figure A-11: LC Resonator Min Electrical and Max Magnetic Line Energies Vs. Self-Capacitance

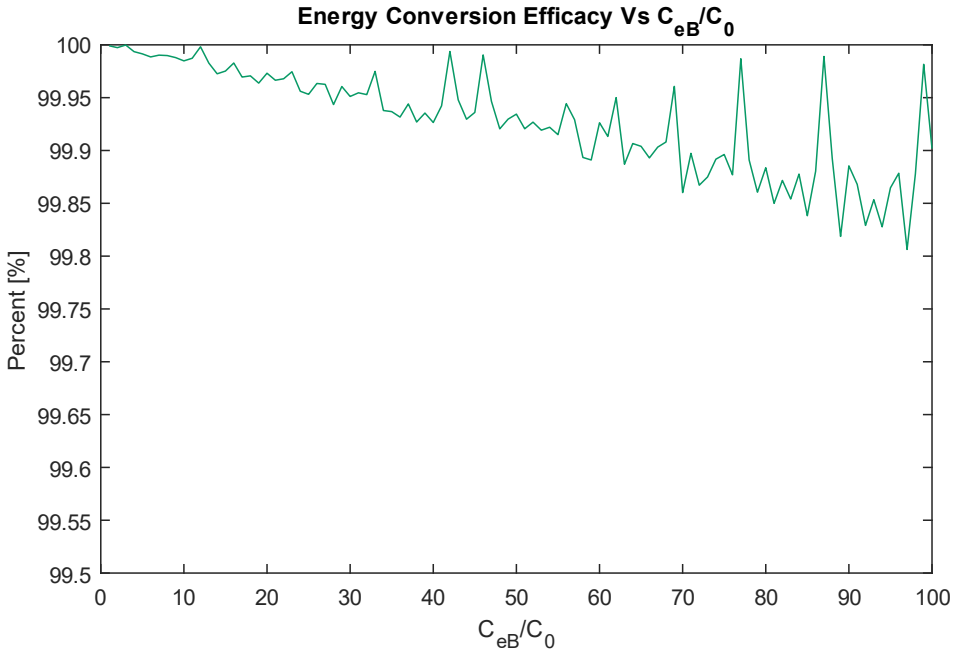


Figure A-12: LC Resonator Energy Conversion Efficacy Vs. Self-Capacitance

From the maximum electrical and magnetic energies seen in Figure A-10 and Figure A-11 the following observations are noted. Considering the maximum electrical energy present on Line A ($U_{EA_{Max}}$) first, it can be seen that despite C_{eB} increasing by over two orders of magnitude i.e. $C_{eB} \approx 100C_0$ from the original self-capacitance seen on Line B $U_{EA_{Max}}$ remains virtually unchanged. The most significant drop in $U_{EA_{Max}}$ occurs when $C_{eB} = 94C_0$. This corresponds to a $\Delta Z_{AB} = 184.811\Omega$ and a $Z_B = 185.265\Omega$. The reason $U_{EA_{Max}}$ starts to see changes (albeit minutiae) in energy at this stage are because the differences in characteristic impedances is approaching the lower impedance boundary for dissimilar transmission lines i.e. $\Delta Z_{AB} \rightarrow 100\Omega$. If C_{eB} continues to increase the accompanying decrease in ΔZ_{AB} will result in the impedances of Line A and Line B becoming comparable. In this instance the cascaded setup will be more representative of the *Twin Capacitor* topology rather than the desired LC Resonant tank.

Looking at the minimum magnetic energy $U_{HA_{Min}}$ it is readily seen that with an increasing C_{eB} accompanying increases in magnetic energy are seen. This is due to the increase in line currents that arise due to reductions in the ΔZ_{AB} and Z_B. The subsequent increase in current however does not manifest as an appreciable increase in magnetic energy because the self-inductance (L_{eA}) of Line A remains relatively small i.e. $L_{eA} = 67pH$ and is consistent for the entirety of the simulated range. What is telling however is that the notion of increasing C_{eB} leads to the presence of a small residual current on Line A when ideally this should be zero. The trend observed at this stage is that $U_{HA_{Min}}$ is directly proportional to increases in C_{eB} i.e. $U_{HA_{Min}} \alpha C_{eB}$.

Considering Figure A-10b now, it can be seen that as C_{eB} increases, accompanying increases in $U_{EB_{Max}}$ as well as $U_{HA_{Min}}$ occur. This is due to the fact that as C_{eB} increases a residual amount of voltage as well as current will be present on Line B at time instances of $T = nT_0$. Ideally both the line voltage and current present on Line B should be zero at instances of $T = nT_0$. However, if a non-zero voltage is present on Line B then increases in C_{eB} will manifest as increases in $U_{EB_{Max}}$ as per equation (3.57).

Additionally, considering the fact that with an increasing C_{eB} the characteristic impedance Z_B is lowered (for reasons explained earlier) it stands to reason that the magnitude of the residual current on Line B will also be increased. This results in an accompanying increase in $U_{HA_{Min}}$ as per equation (3.58).

Looking at Figure A-11a it is the dual of the situation described in Figure A-10b with the minimum and maximum electrical and magnetic energies interchanged. The time instances where minimum electrical energy can be experienced occur at $T = \frac{2n-1}{2}T_0$, ideally both $U_{EA_{Min}}$ as well as $U_{HA_{Max}}$ should be zero. However, increases in C_{eB} result in residual line voltages and currents being left on Line A which lead to the non-zero electric and magnetic energies $U_{EA_{Min}}$ and $U_{HA_{Max}}$ respectively.

Similarly Figure A-11b is the dual of the case described and seen in Figure A-10a. This time the maximum and minimum electric and magnetic energies are interchanged. The maximum magnetic energy $U_{HA_{Max}}$ appears to be virtually at 100% for the entirety of the simulated range. However, as C_{eB} is increased an associated residual voltage develops on Line B. This associated voltage although minutiae means that a minimum amount of electric energy $U_{EB_{Min}}$ will always be present whenever maximum magnetic energy is reached on Line B. By the very fact of its existence this along with the residual line voltage and current seen on Line A mean that the entirety of the initial electrical system energy stored in C_A can never be converted to purely magnetic energy stored in L_B as desired.

Lastly considering the *Energy Conversion Efficacy* presented in Figure A-12 reveals the following. It can be seen that the general trend of the ECE is downward. This is because increases in C_{eB} exacerbate the residual line voltages and currents present on Line A and Line B at time instances of $T = nT_0$ and $T = nT_0$ respectively. This leads to reductions in $U_{EA_{Max}}$ and $U_{EB_{Max}}$ which adversely affect the reconstituted and desired energy. Reductions in these quantities lead to an overall reduction in overall ECE as is seen in Figure A-12.